Measurement of Meningeal Motion Using B-Mode Ultrasound as a Step Toward Understanding the Mechanism of Subdural Hematoma

DISSERTATION

Presented in Partial Fulfillment of the Requirements for the Degree Doctor of Philosophy in the Graduate School of The Ohio State University

By

Ann Elizabeth Mallory, M.S.

Graduate Program in Mechanical Engineering

The Ohio State University

2014

Dissertation Committee:

Rebecca Dupaix, Advisor

Necip Berme

John Bolte

Jun Liu

Abstract

Head injuries to older motor vehicle crash occupants are of increasing importance because of the growing number of older occupants on the road and their elevated vulnerability to injury compared to younger occupants. Crash data analysis to understand head injuries of particular importance among aging crash victims identified subdural hematomas from bridging vein bleeding as particularly frequent and life-threatening for older occupants. Ultimately, in order to quantify the age-dependent relationship between whole head motion and risk of subdural hematoma from bridging vein bleeding, experimental test methods are needed to measure the potential for bridging vein stretch as a function of head kinematics. To that end, methods were developed to use high-frequency, high-speed, Brightness-mode (B-mode) ultrasound to image motion of the meninges and peripheral brain in head rotation tests using *post mortem* human subjects. Results of preliminary low-rate rotation tests using the developed methods suggest that motion relative to the skull resulted from deformation of the cortex, rather than from sliding of the meningeal layers. High-rate testing confirmed the potential effectiveness of the developed methods, which represent a first essential step in the definition of age-dependent estimates of the risk of subdural hematoma from bridging vein bleeding in motor vehicle crashes.

Dedication

In memory of my mother, Beverley Caithness Mallory (1936-2010), who could have made an excellent engineer herself except for a high school guidance counselor who told her that the higher education options for a young lady were Languages or Home Economics. She chose Languages, and then went on to raise four engineers and a high school guidance counselor.

Acknowledgments

I am very grateful to the many people who made the completion of this project possible. First, I would like to thank Rod Herriott, my colleague at the Transportation Research Center Inc. He was involved in nearly every step of the project, from collecting surgical reports in case studies for the early epidemiology work to development of test equipment and execution of tests. His steadfast commitment to this project and determination to make it succeed are deeply appreciated. I would also like to thank many other colleagues at the Transportation Research Center Inc. Brian Suntay and Jim Stricklin worked long test days and helped to solve many experimental issues. Jim Clevenger contributed to the design of test fixtures, prepared drawings of all equipment, and assisted with FARO point digitization. Ralph Fout fabricated several of the fixtures used in testing. Ron Puckett and Will Millis assisted with preliminary tests. My supervisors, Alena Hagedorn and Ron Burton, were tremendously supportive throughout the stages of my doctoral work. Alena Hagedorn also took several of the test fixture photographs in Chapter 4. Other TRC Inc. staff who contributed include Dr. Tom Ranney, Tim Cleland, Jared Dowdy, Dave Hyder, Greg Stevens, Jeff Gruber, Brian Crabtree, and Kevin Watkins.

My dissertation committee was extremely supportive throughout this effort: Professors Rebecca Dupaix, Jun Liu, John Bolte, and Necip Berme. Jun Liu contributed

significantly to the development of ultrasound techniques. John Bolte was generous with his lab facilities and provided invaluable assistance in subject preparation. I count myself lucky to have had not just one, but two exceptional advisors during the course of my doctoral work: Professors Jim Schmiedeler and Rebecca Dupaix were unfailingly encouraging and kept me and the project on track.

The head rotation testing reported in Chapters 4 through 6 could not have been completed without the help of the staff and students of the Ohio State University Injury Biomechanics Research Center. In particular, I thank Dr. Yun-Seok Kang, Colleen Mismas, Michelle Murach, Kyle Icke, and Alex Redrow for their hard work, creative ideas, and willingness to work the long hours needed to perform these tests.

I want to thank Heather Rhule of NHTSA, who was a tireless champion for this project, helping to overcome every obstacle the project faced, both technical and logistical. On test days, and in the years that preceded them, she was willing to do anything that was needed to make the project a success. I am also deeply grateful to Dr. Bruce Donnelly of NHTSA who was a mentor throughout my doctoral studies: he asked hard questions and pushed me to think of unconventional solutions, making me a better engineer along the way.

I learned much from the following researchers and physicians of the Ohio State Wexner Medical Center who provided advice, hands-on assistance, or both: Dr. Anna Bratasz, Peter Boyer, Dr. Petra Schmalbrock, Dr. David Bahner, Dr. Danny Prevedello, Dr. Ali Jamshidi, Susie O'Connor Butler, Dr. Lynne Gauthier, and Dr. Amanda Agnew.

Other experts who answered my questions, provided valuable ideas and helped to shape my thinking in discussions during the course of this project include the late Dr. Helmut Maxeiner of the Charité - Universitätsmedizin Berlin, Dr. Bart Depreitere of the Katholieke Universiteit Leuven, Fangfang Sun of the Ohio State University Department of Statistics, Dr. Peter Letarte of the Edward Hines Jr. VA Hospital, Professor Phil Bayly and Aaron Feng of the University of Washington at St. Louis, Professor Duane Cronin of the University of Waterloo, Dr. Louise Mallory of Quality Assurance Inc., Dr. Jacqueline Paver, Professor Matt Maltese of The Children's Hospital of Philadelphia, Professor Robert Anderson of the University of Adelaide and Stephen Buttars and Dr. Anna Trujillo of VisualSonics Inc. I would also like to thank Professor Pat Bishop and Dr. Carley Ward who were teachers and mentors to me earlier in my career.

Previously published material in Section 2.1 of this dissertation is used with the permission of the Association for the Advancement of Automotive Medicine. Material in Section 2.2 is reprinted with the permission of co-authors Rod Herriott and Heather Rhule. I am grateful to donors to the Ohio State University Anatomy Body Donation Program, whose generosity made the experimental work reported in this dissertation possible.

While my doctoral work could not have been completed without the support and hard work of many colleagues and collaborators, I could not have even considered beginning it without the support and hard work of my family and friends. I am indebted to Bridget Murphy, Louise Mallory, Penny McGill, George Mallory, Bev Mallory, Emily Moersdorf, Heather Rhule, Mark & Amy Spears, and all the other friends who helped me

and my family through the last six years. To my husband Dave Gnas, whose boundless belief in me has been matched only by his heroic efforts to take care of all of us, and to my son Duncan Gnas who has been patiently waiting for me to finish work for as long as he can remember, thank you with all of my heart. And to my son Stuart Gnas, who was born in the final days of this effort, thank you for waiting.

Vita

1971.....Born Hamilton, Ontario, Canada

1995.....B.A.Sc., Systems Design Engineering, University of Waterloo, Canada

2001.....M.S., Biomedical Engineering, University of Southern California

1994.....Ergonomist, CAMI Automotive, Ingersoll, Ontario, Canada

1995-2003 .....Biomechanics Engineer, Biodynamics Engineering Inc., California

2003-present.....Research Engineer, Transportation Research Center Inc., Ohio

Publications

Mallory, A. and H. Rhule (2013). Injury Risk Estimates: A Method for Determining Equivalent Increase in Risk of Death for Older and Younger Occupants. Proceedings of IRCOBI Conference, pp. 328-329.

Mallory, A., S. Duffy and H. Rhule (2013). Head Injuries to Helmeted and Unhelmeted Motorcyclists in US Trauma Data. Proceedings of IRCOBI Conference, pp. 443-444.

Kang, Y.S., J. H. Bolte, K. Moorhouse, B. Donnelly, R. Herriott and A. Mallory (2012). Biomechanical Responses of PMHS in Moderate-Speed Rear Impacts and Development of Response Targets for Evaluating the Internal and External Biofidelity of ATDs. Stapp Car Crash Journal, Vol. 56, pp. 105-170.

Mallory, A., R. Fredriksson, E. Rosen and B. Donnelly (2012). Pedestrian Injuries By Source: Serious and Disabling Injuries in US and European Cases. Annals of Advances in Automotive Medicine, Vol. 56, pp. 13-24.

Ott, K., J. Wiechel, D. Guenther, J. Stammen and A. Mallory (2012). Assessment of the Simulated Injury Monitor (SIMon) in Analyzing Head Injuries in Pedestrian Crashes. SAE Technical Paper: 01-0569.

Mallory, A. (2010). Head injury and aging: the importance of bleeding injuries. Annals of Advances in Automotive Medicine, Vol. 54, pp. 51-60.

Mallory, A. E. (2001). The Relationship Between the Material Properties of Femoral Cortical Bone and Bone Density, Master's Thesis, University of Southern California.

Field of Study

Major Field: Mechanical Engineering

Table of Contents

List of Tables

List of Figures

List of Acronyms and Abbreviations

AIS	Abbreviated Injury Scale
BEV	barrier equivalent velocity
B-mode	Brightness mode
c	rotation cage center of rotation
CDS	Crashworthiness Data System
CFC	Channel Filter Class
CIREN	Crash Injury Research and Engineering Network
CSF	cerebrospinal fluid
e	tracking error
E_{max}	maximum rotation energy
EVA	ethylene vinyl acetate
F_{min}	minimum number of frames to be tracked
FR	frame rate
g	acceleration due to gravity
I	moment of inertia
ICP	intracranial pressure
m	mass of head, cage, and positioning fixture shaft
MR	magnetic resonance

NASS	National Automotive Sampling System
N	total number of lines in ultrasound image frame
NHTSA	National Highway Traffic Safety Administration
n_{ij}	line number corresponding to lateral position of point j in frame i
R	radius of gyration
r	radius of curvature of dural surface
SDH	subdural hematoma
SE	standard error
T	time to construct one frame of ultrasound image
T_{adj}	period of oscillation, adjusted for large angle
T_o	period of oscillation
t_{ij}	true time of point j in frame i
$t_{Start(i)}$	frame start time for frame i
x_{ij}	lateral position of point j in image i
x_{width}	full lateral width of ultrasound image
Δ_{Dist}	change in distance between two points in consecutive frames
ΔV	Delta V (change in velocity)
θ	misalignment angle
θ_o	angle of oscillation
σ_e^2	variance of tracking error
υ_{max}	maximum linear velocity
ω_{max}	maximum rotational velocity

Chapter 1: Motivation and Background

1.1 Motivation for Studying Subdural Hematoma in Older Crash Occupants

The safety of older motor vehicle occupants in crashes is of increasing importance as the US population ages. Between 2000 and 2050, the number of people age 65 and older in the US is projected to increase by 135% and by 350% for the age group 85 and older (Wiener and Tilly 2002). Injury prevention in motor vehicle crashes for this older population is of particular interest because of their vulnerability to injury compared to younger adult motor vehicle occupants: given similar crash conditions, every year of age increases the risk of serious injury by 2.3% (Kahane 2013). The consequences of head injury for older motor vehicle occupants are compounded by the worsening of head injury outcomes for aging patients (Vollmer, Torner et al. 1991; Mosenthal, Lavery et al. 2002; Hukkelhoven, Steyerberg et al. 2003). Jane and Francel reported that traumatic coma patients over age 55 had more than double the rate of death of adults younger than age 36, while the rate of "good recovery" for the younger adults was more than 30 times that of the older patients (1996).

Epidemiological studies have shown that older trauma patients sustain different types of head injuries than younger patients, with an overall increase in intra-cranial bleeding with age (Vollmer, Torner et al. 1991; Coronado, Thomas et al. 2005). As a precursor to the experimental work in this dissertation, a more detailed analysis of head

injuries by age group in motor vehicle crashes was performed to determine which head injuries are most important among older vehicle occupants by identifying types of injuries that become more likely for aging occupants in crashes (Mallory 2010). In particular, specific intra-cranial bleeding injuries were compared, taking into consideration previous reports on the severity and potential outcome of those injuries for an older population. Analysis showed that older occupants had particularly elevated rates of extra-axial bleeding (bleeding within the skull but outside the brain tissue), especially in lower-severity crashes that make up the majority of all crashes. The age-related increase in extra-axial bleeding resulted from elevated odds of sustaining subdural hematoma (collection of blood between the dura and arachnoid) and subarachnoid hemorrhage (bleeding into the subarachnoid compartment) compared to younger occupants. To assess the relative importance of subdural hematoma and subarachnoid hemorrhage, these injuries were compared relative to outcome for older patients. Although the subdural mortality rate has been reported to be as high as 50% or higher in comatose patients or surgery cases (Seelig, Becker et al. 1981; Gennarelli, Spielman et al. 1982; Haselsberger, Pucher et al. 1988; Marshall, Gautille et al. 1991; Servadei 1997; Sawauchi and Abe 2008; Taussky, Widmer et al. 2008), Perel reported an overall subdural hematoma mortality rate of 33% (Perel, Roberts et al. 2009), which is a more appropriate estimate to compare to motor vehicle crash cases which include non-surgical and non-comatose cases. After adjusting for the contribution of other injuries, Perel reported the odds of mortality from large subdural hematomas was still greater than for other space-occupying bleeding injuries, which is consistent with reports that subdural

hematoma is especially lethal among bleeding head injuries (Seelig, Becker et al. 1981; Marshall, Gautille et al. 1991) and responsible for as many as 43.5% of head injury deaths (Gennarelli, Spielman et al. 1982). Subdural hematomas present an increased rate of mortality and poor outcome for older patients (Hukkelhoven, Steyerberg et al. 2003; Raju, Gupta et al. 2004; Stitzel, Kilgo et al. 2008; Hanif, Abodunde et al. 2009). Age 54 has been identified as the age threshold for increased mortality for subdural hematoma (Stitzel, Kilgo et al. 2008). The combination of the increased incidence of subdural hematoma for occupants aged 50 and older (Mallory 2010) and the previously-reported increased mortality rate for subdural hematoma over age 54 presents a double risk for older occupants.

Subarachnoid hemorrhage, also identified in the Mallory study (2010) as more frequent among older occupants, has been linked to increased risk of poor outcome after head injury (Vollmer, Torner et al. 1991; Greene, Marciano et al. 1995; Servadei, Murray et al. 2002; Mattioli, Beretta et al. 2003; Chieregato, Fainardi et al. 2005), but this increased risk is not related to subarachnoid hemorrhage as a primary injury. Instead, the relationship between subarachnoid hemorrhage and poor outcome has been attributed to subarachnoid hemorrhage as an indicator of more severe underlying mechanical injury or on the negative effect subarachnoid hemorrhage can have on the resolution of primary head injuries. While subarachnoid hemorrhage may not be as important as subdural hematoma as a primary cause of mortality, it may be aggravating injury outcomes.

Exploration of age-related changes in tolerance to subdural hematoma is therefore urgently needed. Ultimately, a better understanding of why older motor vehicle

occupants have reduced tolerance to subdural hematoma will contribute to the definition of age-adjusted injury thresholds for head injury and to the development of injury prevention countermeasures for older occupants.

1.2 Subdural Hematoma Injury Mechanism

The original source for the bleeding that produces subdural hematoma can be from adjacent brain contusions, lacerations or intracerebral hematomas; from ruptured cortical vessels on the surface of the brain; or from the bridging veins that cross the meninges en route to the dural sinuses (Lee, Melvin et al. 1987; Graham 1996; Miller, Piper et al. 1996; Miller and Statham 2000; Toyama, Kobayashi et al. 2005; Depreitere, Van Lierde et al. 2006; Mallory, Herriott et al. 2011).

1.2.1 Subdural Hematoma Originating from Bridging Veins

Experimental studies exploring injury mechanism and tolerance for subdural hematoma have primarily focused on those that originate with the rupture of parasagittal bridging veins. Holbourn proposed that rotational motion of the brain relative to the skull stretched the bridging veins that cross the meningeal layers (1943). Ommaya et al. produced subdural hematoma in rhesus monkeys by simulating a rear impact and attributed the bleeding to veins draining into the sagittal sinus, i.e. bridging veins (1968). In a subsequent review of this work, Ommaya reported that subdural hematoma was produced with rotation at 500 degrees/second, and 10,000 radians/second^2 for a 5-6 millisecond duration (2002). Löwenhielm produced bridging vein rupture in frontal sled tests with *post mortem* human subjects, and estimated rotational injury tolerance of 4,500 radians/second^2 and 60 radians/second (1974). Gennerelli and Thibault produced

subdural hematoma in rhesus monkeys by applying anterior-posterior acceleration in a 60 degree arc, with demonstrable damage to bridging veins underlying the hematomas (1982). Subsequent scaling of their results yielded an estimated human injury limit of 12,500 radians/second^2 (Newman 1998). Depreitere et al. documented parasagittal bridging vein failure in *post mortem* human subjects by pressurizing the superior sagittal sinus with radiopaque fluid and identifying bridging vein rupture after impact with radiographs *post mortem* (2005; 2006). Predicted tolerance to sagittal plane rotation/acceleration was approximately 10,000 radians/second^2 for durations shorter than 10 milliseconds or lower for longer pulses.

Experimental studies of the failure of isolated bridging veins have shown a mean ultimate stretch of 1.50 to 1.55 (Lee and Haut 1989; Monson, Goldsmith et al. 2005). The bridging vein and superior sagittal sinus complex has also been tested as a unit and shown to have a mean ultimate strain corresponding to an elongation of the sinus-vein complex of 4.95 mm±1.8 mm (Delye, Goffin et al. 2006).

Age-related brain atrophy is thought to contribute to bridging vein failure in older individuals because it can lead to more relative motion between the skull and brain, resulting in increased tension in the bridging veins (Yamashima and Friede 1984; Meaney 1991; Hanif, Abodunde et al. 2009). Modeling studies have predicted a tripling of bridging vein strain in frontal impacts with modeled increase in the thickness of the subdural space to simulate age-related atrophy (Kleiven and von Holst 2002).

A study of subdural hematoma cases in motor vehicle crashes was done in preparation for the experimental work reported in this dissertation (Mallory, Herriott et

al. 2011). That analysis of US motor vehicle crash data in NASS CDS (National Automotive Sampling System Crashworthiness Data System) and CIREN (Crash Injury Research Engineering Network) datasets showed that older occupants in frontal impacts were particularly vulnerable to isolated subdural hematoma without other bleeding sources coded, and that these isolated subdural hematomas were more often associated with bridging vein bleeding than with other bleeding sources. Although the odds of subdural hematoma increased with age regardless of accompanying injuries, this study supported that age-related increases in the frequency of subdural hematoma may be especially dramatic with bridging vein failure. That increase in subdural hematoma frequency with bridging vein failure was especially notable among women and in frontal impacts with anterior-posterior head motion.

1.2.2 Subdural Hematoma from Sources Other than Bridging Veins

In contrast to the body of work on subdural hematoma resulting from bridging vein failure, there is limited documentation on the mechanism of subdural hematoma as a result of other bleeding sources, or on how tolerance to subdural hematoma from sources other than bridging veins changes with age. Studies that have addressed subdural hematoma from sources other than bridging veins have focused on the conditions under which subdural hematoma from sources other than bridging veins occur rather than the mechanical loading required to produce both the original bleeding injury and the subdural hematoma.

A long-term study of surgically-treated subdural hematoma cases found that in 40.5% of cases there was a laceration, intracerebral clot, or “exploded” temporal pole that

was a cause of the subdural hematoma (Jamieson and Yelland 1972). These were categorized as "complicated" subdural hematoma and were more common among males but less common for adults over age 60. These complicated subdural hematomas were more frequent in motor vehicle crashes than "simple" subdural hematomas that were not associated with a surface contusion or laceration. In complicated subdural hematoma cases, the head impact was lateral 55% of the time. Among those lateral head impact cases, the impact and subdural hematoma were on the same side in 53% of cases and on contralateral sides in 47%.

While previous studies suggest that there are differences in the head impact conditions that produce subdural hematoma by bridging vein failure versus by other sources (Jamieson and Yelland 1972; Maxeiner 1998; Mallory, Herriott et al. 2011), none address the mechanical loading that results in subdural hematoma from sources other than bridging veins. However, given that age-related increases in subdural hematoma appear to be primarily linked to bridging vein bleeds, the mechanism of subdural hematoma from other sources is less urgent for older motor vehicle crash occupants than questions related to tolerance to bridging vein subdural hematomas.

1.2.3 Importance of Meningeal Motion in Subdural Hematoma Associated with Bridging Veins

Since epidemiological results suggest that the impact conditions and patient characteristics associated with subdural bleeding sourced from either bridging veins or from other bleeding sources may vary significantly (Jamieson and Yelland 1972; Maxeiner 1998; Mallory, Herriott et al. 2011), strategies to explore the mechanism of

subdural hematoma from different bleeding sources will also differ. To better understand subdural hematoma in older crash occupants, the increase in frequency of subdural hematoma from bridging vein bleeding with age supports an experimental focus on the loading and motion that results in bridging vein failure. Since the age-related increase in subdural hematoma associated with bridging vein failure is especially prominent in frontal crashes with anterior-posterior head motion in motor vehicle crashes (Mallory, Herriott et al. 2011) head motion in the anterior-posterior direction is of particular interest in investigation of bridging vein failure.

While previous in vivo animal studies (Ommaya, Faas et al. 1968; Gennarelli and Thibault 1982) and post-mortem human impact studies (Löwenhielm 1974; Depreitere, Van Lierde et al. 2005; Depreitere, Van Lierde et al. 2006) have reported the relationship between gross head kinematics and the risk of subdural hematoma in anterior-posterior head motion, these studies have reported a wide range of kinematic thresholds for injury and have not quantified any relationship between injury tolerance and aging. To develop an age-tolerance relationship with whole body testing such as the experiments reported by Depreitere (Depreitere, Van Lierde et al. 2005; Depreitere, Van Lierde et al. 2006) would require head impact testing of an impractically large number of *post mortem* human subjects to determine injury risk as a function of both head kinematics *and* subject age or an age-linked parameter such as brain atrophy.

Therefore, as a first step to determining the relationship between gross head kinematics and risk of subdural hematoma resulting from bridging vein failure, the relationship between head kinematics and the intracranial brain motion associated with

bridging vein stretch needs to be better understood. Since bridging veins cross from the surface of the brain, through the arachnoid and dura into the superior sagittal sinus, it is the motion of these layers relative to the skull that determines the magnitude of bridging vein stretch during head motion. Therefore, motion of these layers at the periphery of the brain needs to be quantified to predict the corresponding magnitude of associated bridging vein stretch, which could in turn be compared to risk of bridging vein failure and subdural bleeding. Specifically, the relative motion of the meningeal layers (the membrane layers at the periphery of the brain) needs to be defined as a function of gross kinematic motion of the head. Ultimately, if the relationship between motion of the head and relative motion of these peripheral layers were defined, this motion could be compared to the stretch limits of bridging veins to predict the corresponding likelihood of bridging vein failure and subdural hematoma under given head motion conditions.

Practically, characterizing the relative motion of the meningeal layers as a function of gross kinematic motion of the head and of age would require parametric measurement of the motion of the meningeal layers under a variety of loading directions, rates, and conditions, with test subjects covering a wide range of age or an age-linked characteristic such as brain atrophy. While such a parametric study could be supplemented with computational or physical modeling, initial experimental measurement of meningeal motion under a variety of loading conditions with a set of subjects representing a wide range of brain atrophy is required to first establish suitable boundary conditions and validation data.

Background on the anatomy of the meningeal layers and bridging veins is presented in Section 1.3 and a review of previous experimental and modeling efforts to track the motion of the peripheral brain and meninges is in Section 1.4 and 1.5.

1.3 Meningeal Anatomy

The cranial meninges are three membrane layers that surround the brain: dura, arachnoid, and pia (Figure 1.1). Subdural hematomas are collections of blood that form in the dural border cell layer (Figure 1.2) between the dura and the arachnoid, the two outer membranes of the meninges (Haines, Harkey et al. 1993).

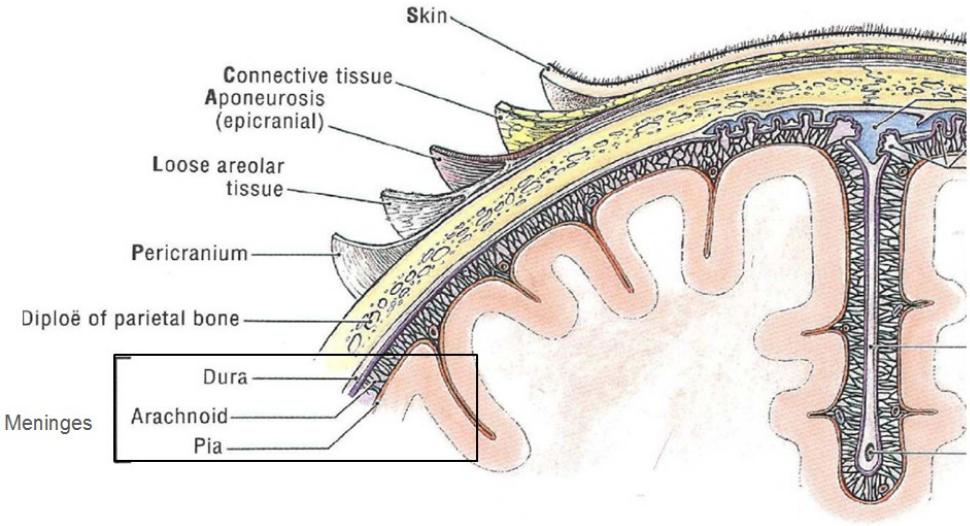

Figure 1.1. Meningeal membranes (dura, arachnoid, pia) between the brain and skull. Reprinted with permission from Moore (1992). Copyright © 1992 Williams and Wilkins.

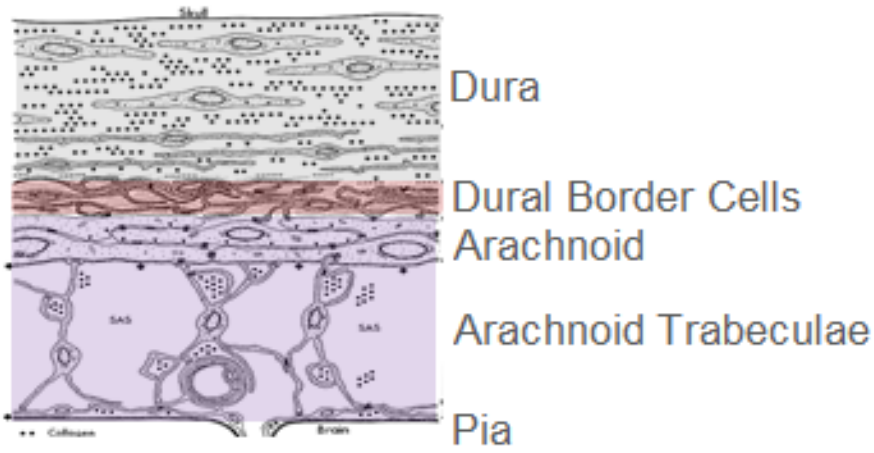

Figure 1.2. Dural border cell layer connecting the dura and arachnoid.
Reprinted with permission from Haines et al. (1993). Copyright © 1993 The Congress of Neurological Surgeons; permission conveyed through Copyright Clearance Center, Inc.

The connections among the meningeal membranes are essential to understanding potential relative motion of these layers. Dura is firmly attached to the skull (Moore 1992) although it can be peeled off surgically or at autopsy. The dural border cells between the dura and arachnoid form the weakest connection among the layers, with a propensity to shear open (Haines, Harkey et al. 1993). As a result, the dura is easily separated from the arachnoid when the overlying skull is removed in surgery or the dura is manipulated during dissection. The arachnoid is partly separated from the pia by the subarachnoid space containing cerebrospinal fluid (CSF) (Yaşargil 1984; Moore 1992), but the arachnoid trabeculae, the web-like connective tissues that connect the arachnoid to the pia, keep those two layers in close contact (Figure 1.3). The pia itself, which is just cell-layers thick, cannot be differentiated from the cortex beneath, either visually or in ultrasound images. Therefore, motion of the dura and arachnoid will be discussed in relation to the surface of the cortex rather than to the pia in this study.

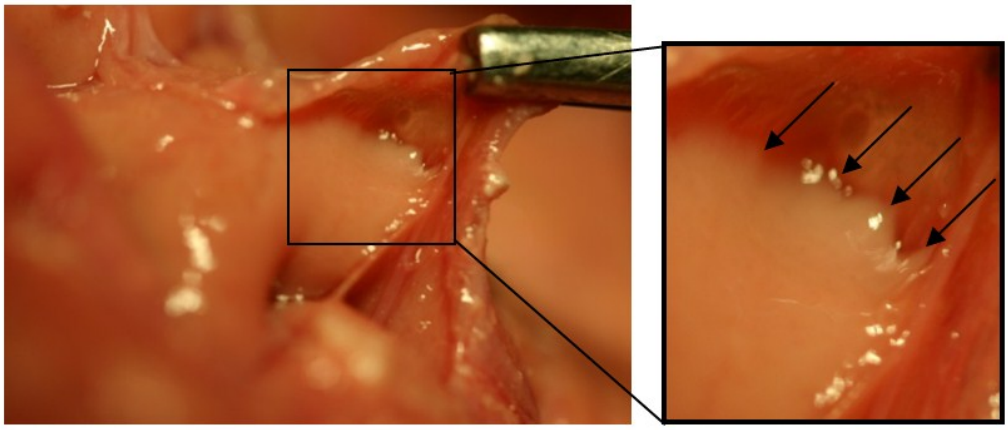

Figure 1.3. *Post mortem* arachnoid being peeled away from brain.
(Inset shows how tightly arachnoid trabeculae adhere the arachnoid to the brain surface.)

1.3.1 Bridging Vein Anatomy and Properties

Monson reported on the dimensions of 11 bridging veins harvested from *post mortem* subjects (Monson, Goldsmith et al. 2005). Mean cross-sectional area was 0.799 mm^2. Mean outer diameter was 1.84 mm, and mean wall thickness was 0.12 mm. In Lee and Haut's study of 139 bridging veins from 8 *post mortem* subjects, vein length varied from 2 to 25 mm with a mean of 6.2 mm (Lee and Haut 1989). Mean circumference was 4.4 mm and wall thickness was 0.05 mm on average. Wall thickness increased with circumference but there was no significant correlation between length and circumference. Vessel dimensions did not vary with location.

In a detailed study of the dural entrance of bridging veins into the superior sagittal sinus, Han et al. documented the properties of bridging veins on both sides of 30 adult *post mortem* subjects (Han, Tao et al. 2007). An average of 11 bridging veins per side were identified, with a mean diameter of 2.5 mm (range 0.4-7.0mm) at approximately 5 mm from the dural entrance. In 74% of the bridging veins examined, the vein was

positioned at an acute angle against blood flow in the sinus, i.e. they were angled from a posterior location on the cortex toward an anterior location on the sinus (Figure 1.4). This forward angle was more pronounced in the cluster of bridging veins posterior to the coronal suture (where mean angle between the bridging veins and sinus was 35 degrees) than in the cluster anterior to the coronal suture (mean angle 86 degrees).

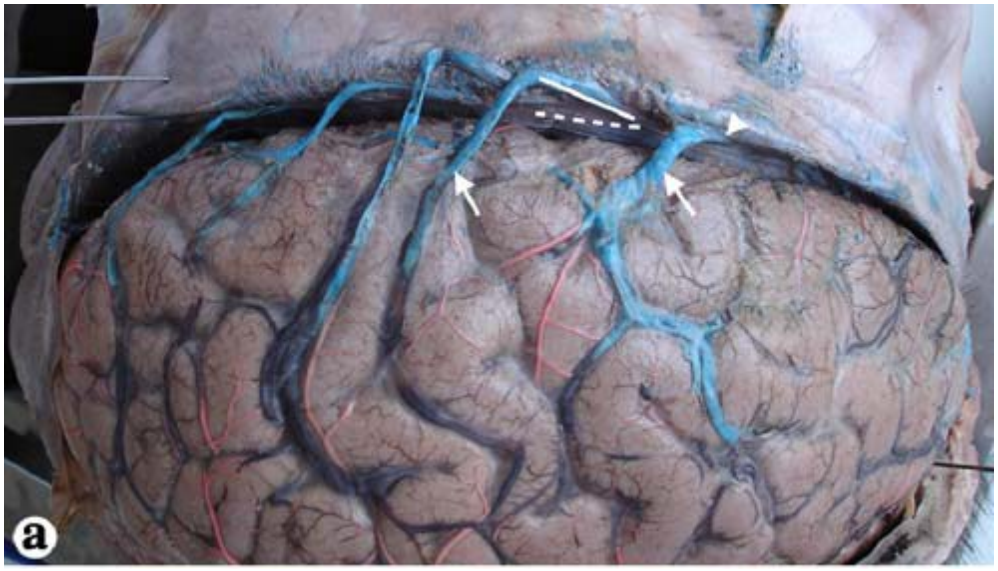

Figure 1.4. Dural entrances of bridging veins into the superior sagittal sinus on a lateral image of a cadaver.
Reprinted from Han, Tao et al. (2007) with kind permission of Springer Science and Business Media. Copyright © Springer-Verlag 2007.

Failure limits of bridging veins. There are substantial contradictions among previous studies of the failure properties of parasagittal bridging veins.

Löwenhielm investigated the stress and strain properties of isolated parasagittal bridging veins with uniaxial tension tests at reported strain rates from 1 to 1000 per

second (1974). Löwenhielm's 22 tests from 11 *post mortem* subjects showed a strong dependence on rate for both elongation at failure, and maximum stress.

In a subsequent analysis of the sensitivity of bridging vein failure properties to strain rate, Lee and Haut tested bridging veins from 8 *post mortem* subjects (1989). After freezing and thawing the tissue, tensile testing was performed at strain rates from 0.1 per second to 250 per second. Ultimate stretch ratios averaged between 1.5 and 1.6 for low and high strain rates with no significant effect of strain rate on measured failure properties. In a discussion of the contradiction with previous results, Lee and Haut suspected possible error in Löwenhielm's results as a result of indirect strain measurement and possible specimen slippage at the clamps.

In his 1991 dissertation, Meaney reported on the effects of perfusion and subject age as well as loading rate in uniaxial tension tests of *post mortem* human bridging veins (1991). Failure properties did not vary significantly with either perfusion of the vein during testing or with subject age at time of death. Consistent with Lee and Haut and in contrast to Löwenhielm, Meaney found that the effect of strain rate on bridging vein failure properties was statistically insignificant over a strain rate range from 0.4 to 241 per second.

In a comparison of the failure properties of veins obtained from surgery patients and *post mortem* human veins tested within 48 hours *post mortem*, Monson et al. tested 11 bridging veins obtained *post mortem* (Monson, Goldsmith et al. 2005). In uniaxial tension testing without perfusion, the veins were reported with a mean yield and ultimate stretch (λ) of 1.29 (standard deviation 0.09) and 1.50 (standard deviation 0.19)

respectively. Although no bridging veins were obtained surgically, other veins tested suggested that yield stretch for veins from autopsy was significantly lower with 25% less extension than for fresher veins obtained surgically from living patients. However, the time elapsed *post mortem* before testing reportedly had no effect on tensile test properties.

1.4 Experimental Studies of Motion at the Surface of the Brain

1.4.1 Direct Observation Studies of Motion

Early investigations demonstrated motion at the surface of the brain during impact by replacing the skull and dura over the calvaria of live primates with transparent caps (Sheldon, Pudenz et al. 1944; Pudenz and Shelden 1946; Gosch, Gooding et al. 1970). Although interpretation of the results is limited by removal of the dura, these studies qualitatively demonstrated motion of the parietal surface of the brain relative to the transparent cap replacing the skull. More recently, Ibrahim et al. reported on motion in a horizontal plane just superior to the orbits and lateral ventricles in axial rotation using horizontally-transected *post mortem* piglet heads (Ibrahim, Natesh et al. 2010). Motion was tracked at the transected surface through a layer of lubricant and a Plexiglas cover plate. Although peak strains were reported based on motion of ink tracking points on the transected surface, displacements at the brain-skull interface were not estimated. Possible alteration of the brain-skull interface during subject preparation was listed as a study limitation.

1.4.2 Radiographic Studies of Motion

Several studies have used x-ray techniques to track motion of brain tissue during skull motion. Radio-opaque markers and intravascular contrast fluid have been used to demonstrate central brain motion in animal testing (Hodgson, Gurdjian et al. 1966; Sass, Corrao et al. 1971). Contrast fluid in primate (mucaca mulatta monkeys) testing was used to show motion of vessels on the surface of the brain, presumably associated with similar cerebral parenchymal displacements (Shatsky, Alter et al. 1974; Shatsky, Evans et al. 1974). High-speed radiography has also been used to study motion of the *post mortem* human subject brain, to show gross motion of the brain (Stalnaker, Melvin et al. 1977) and motion of lines of injected radiopaque gel (Nusholtz, Lux et al. 1984). The tests by Nusholtz et al. demonstrated differential motion between the brain and the skull by comparing the motion of points on the curve closest to the skull, with relative motion reported only in tests with skull fracture. Nusholtz described the adhesion of the brain to the skull as a "stick-slip" condition, allowing relative motion at this surface only when overlying skull fracture occurred.

More recently, Hardy's studies used x-ray tracking of neutral density targets implanted within the brain tissue, resulting in the most comprehensive description to date of brain motion during impact (Al-Bsharat, Hardy et al. 1999; Hardy, Foster et al. 2001; Hardy 2007; Hardy, Mason et al. 2007). In an analysis of Hardy et al.'s (2001) tests, brain motion was separated into rigid body displacement and deformation (Zou, Schmiedeler et al. 2007). In low severity impacts in the sagittal plane, 4-5 mm of rigid body translation and 5 degrees of rigid body rotation was estimated. However, given the

deep placement in the brain of neutral density targets in Hardy et al.'s (2001) tests, Zou et al. cautioned that the rigid body motion results did not predict brain motion at the boundary between the brain and skull. In Hardy's later results (2007), he did report results for one specimen with a tracking target near the surface of the cortex that moved approximately 9 to 11 mm relative to the skull, and one approximately 10 mm below the cortex that showed only 2-3 mm relative motion. Differences between the two tests cited as possible reasons for these apparently paradoxical results included pressurization deficiencies or inconsistent lateral positioning of the targets. Hardy concluded that the relative motion phenomena at the cortex required further investigation.

1.4.3 MR Imaging of Motion

Magnetic resonance (MR) imaging has been used to capture brain motion in living humans during normal pulsatile cardiac cycles, with results ranging from less than 0.3 mm to 5 mm of brain motion in healthy volunteers (Poncelet, Wedeen et al. 1992; Maier, Hardy et al. 1994; Zhong, Meyer et al. 2009). The magnitude of pulsatile motion varied by region, and was relatively small at the cerebral periphery (Poncelet, Wedeen et al. 1992). To understand interface conditions between the skull and brain at the base of the skull, MR imaging has also been used to track brain motion during flexion (Ji, Zhu et al. 2004). Results showed 1-3 mm of brain motion relative to the base of the skull during voluntary head motion, but did not specify where the motion interface was located.

Brain motion in volunteers during mild head deceleration has been reported in a series of MR studies reported by Philip Bayly and colleagues at Washington University at St. Louis (Bayly, Cohen et al. 2005). Time resolution suitable for capturing rapid motion

was obtained by repeating the impact and acquiring a subset of image data for each repetition. In occipital impacts producing 2 to 3 g of linear head deceleration, angular brain motion was attributed to tethering forces at the periphery of the brain, changing the angular momentum of the brain about its mass center. Subsequent studies included angular acceleration of the head and focused on peripheral motion of the brain relative to the skull. These studies show that while the brain does "slide" relative to the skull (Sabet, Christoforou et al. 2008; Abney, Feng et al. 2010), the relative displacement at the cortical surface of the brain is small, with the tangential motion of the brain surface apparently being constrained by the skull (Feng, Abney et al. 2010). Larger displacements were seen deeper in the cortex.

1.4.4 Other Measurement Efforts

Other methods developed for measuring brain motion relative to skull motion that have been reported but have not yielded definitive results include implantation of accelerometers (Trosseille, Tarriére et al. 1992; King, Ruan et al. 1995). In a review of experimental methods (Viano, Aldman et al. 1997), Ono was reported to have inserted fine wires through the skull and brain and Tarriére reportedly inserted needles through the skull into the brain so that fine tears in the brain tissue could be measured in dissection to quantify motion of the brain relative to the skull.

In summary, direct observation studies of motion at the surface of the animal brain showed only qualitative motion of the cortical surface, relative to a transparent skull replacement. The dura was removed, and relative motion of the arachnoid could be not visualized. Radiographic studies of motion in trauma-level loading have tracked motion

near the surface of the brain but have lacked the resolution to differentiate motion of the meningeal layers from deformation deeper in the cortex. Volunteer studies of response to low-level impact have come closer to tracking motion near the surface of the brain in the cortex, but cannot predict response to trauma-level impact and could not identify motion of the meningeal layers.

1.5 Modeling of Motion at the Surface of the Brain

1.5.1 Physical Models of Brain Motion

Physical models used to explore brain motion have been inconsistent in predicting motion at the surface of the brain because of the variation in how the brain-skull interface has been represented. This interface has been modeled as a pure-slip interface (Margulies 1987; Viano, Aldman et al. 1997; Anata, Miyazaki et al. 2010; Cheng, Howard et al. 2010) or a no-slip interface (Margulies 1987; Margulies, Thibault et al. 1990). Pure-slip interfaces have been described as representative of the CSF layer of the brain, although the arachnoid and cortex between which CSF is located are, anatomically, quite well connected by arachnoid trabeculae. Margulies et al. concluded that the influence of the skull-brain interface was attenuated for locations central in the brain, and recommended limiting motion conclusions from physical models to the study of central brain motion (1990).

1.5.2 Computational Models of Brain Motion

Computational models have also used a variety of brain-skull interfaces to represent meningeal connections. Ward and Thompson (1975) first accounted for motion

at the subarachnoid space in a finite element model by introducing boundary elements that resulted in motion at the surface of the brain in good agreement with motion observed in rotational primate testing through windows cut in the skull and dura (Pudenz and Shelden 1946). Subsequent efforts included linear elastic solid elements with low shear modulus or complex contact algorithms ranging from fixed to frictionless connections between brain and skull, as summarized in reviews by Claessens, Sauren, et al. (1997), Kleiven and Hardy (2002), Horgan and Gilchrist (2004), and Ji, Roberts, et al. (2009). Most of these models have been validated against experimental data on pressure or motion measurements deeper in the brain, and used to predict and study motion and loading centrally in the brain. In comparisons of tied (no-slip) and sliding (free-slip) interfaces at the meningeal surfaces, Claessens et al. (1997) concluded that relative motion at the skull-brain interface had a large effect on pressures measured deeper in the brain, while Kleiven et al. (2002) concluded that relative motion deeper in the brain was less sensitive to the meningeal contact definitions than to brain tissue properties. Kleiven and Holst (2002) used a sliding contact definition to represent motion of the arachnoid relative to the brain to explore relative motion of the surface of the brain with varying levels of brain atrophy, where atrophy was simulated by varying the thickness of the subarachnoid space. Their results showed up to 16.5 mm of motion of the surface of the brain. Although they validated their model using motion of neutral density targets in the brain (Al-Bsharat, Hardy et al. 1999; Hardy, Foster et al. 2001), there was no experimental data to confirm the motion estimated at the brain surface, making it difficult to assess the accuracy of their modeled displacements at the periphery of the brain.

More recently, Coats, Eucker et al. evaluated the effectiveness of solid elements or spring connectors between the skull and brain in a piglet model (2012). Compared to injury results from tests under the same loading conditions with live piglets, the spring connector representation of the brain-skull interface yielded the best predictive capability for intracranial hemorrhage. However, when compared to motion in the experimental results of Ibrahim et al.'s transected piglet rotations (2010), either boundary connection could effectively match the experimental results. These findings are consistent with Margulies et al.'s conclusion that central motion in the brain may not be affected substantially by boundary conditions at the skull-brain interface (Margulies, Thibault et al. 1990), but suggest that intracranial bleeding can be influenced by these peripheral boundary conditions.

As summarized above, many physical and computational models represent the relative sliding motion of the meningeal layers with a single interface or element layer. The use of sliding surfaces in this interface has been suggested to be representative of the sliding allowed by CSF (Kleiven 2006; Cheng, Howard et al. 2010), which is located between the arachnoid membrane and the surface of the brain. Models reported to date have not accounted for how tightly the arachnoid is adhered to the surface of the brain by the arachnoid trabeculae, or the relatively weaker connection between the dura and the arachnoid at the dural border cell layer. Without data to validate the motion of the surface of the brain in physical or computational models, it is unclear whether a simplified single-layer sliding interface can accurately model the combined motion of the arachnoid relative to the dura and of the surface of the brain relative to the arachnoid.

1.6 Selection of Methods for Motion Measurement in the Current Study

An experimental model of peripheral motion of the human brain was developed for the current study, since there is insufficient data to develop or validate a physical or computational model of the relative motion of the meningeal tissues during motion. *Post mortem* human subjects were used for the current study.

The primary constraint for selection of a method to observe and measure motion of the meningeal layers during high-rate head motion was that the imaging or measurement method be non-invasive. Among previously reported and novel methods for tracking brain motion, several involved penetrating the meningeal layers, thus disrupting the very structures to be observed. These invasive methods (including direct observation studies of the inner meninges with the dura and skull removed, radiographic imaging that involved placement of radio-opaque markers, implantation of accelerometers or ultrasonic displacement sensors, and use of wires and needles to document maximum displacement) were excluded from consideration for the current experimental effort.

Additional candidate methods were evaluated against the criteria that (1) data be collected at a sufficiently high rate to allow measurement of motion in impact-level head motions and (2) that observation of individual meningeal tissue layers be possible. MR imaging, which has been used to track motion near the surface of the brain in human volunteers, was excluded because it was determined to be neither sufficiently fast to image motion in high-rate impacts nor to have sufficient resolution adjacent to the skull to track individual tissue layers. High-speed radiographic imaging with vascular contrast

was rejected because while it was expected to be able to capture high-rate motion, it did not offer a way to differentiate motion of the meningeal layers. The most promising method of non-invasive measurement of the meningeal layers during head motion was determined to be high-frequency Brightness-mode (B-mode) ultrasound. B-mode ultrasound is capable of producing 2-dimensional images at frame rates up to 1000 frames per second, and axial resolution up to 40 microns, offering the potential to differentiate the dura (approximately 500-1000 microns thick), the arachnoid (approximately 100-300 microns thick) and the surface of the cortex.

1.7 Experimental Plan for the Current Work

Since epidemiological results suggest that the impact conditions and patient characteristics associated with subdural bleeding sourced from either bridging veins or from other bleeding sources may vary significantly (Jamieson and Yelland 1972; Maxeiner 1998; Mallory, Herriott et al. 2011), different strategies are needed to explore the mechanism of subdural hematoma from different bleeding sources. The mechanism of subdural hematoma from sources other than bridging veins, including adjacent brain contusions, lacerations, hematomas, or cortical vessels on the surface of the brain is poorly understood and should be explored, particularly considering the frequency of subdural hematoma from non-bridging-vein sources among young and mid-age adults. However, as the emphasis of the current study is ultimately on prediction of age-adjusted injury thresholds for subdural hematoma, an improved understanding of older occupants' reduced tolerance to subdural hematoma will require deeper understanding of the mechanism of subdural hematoma from bridging vein failure, and how that mechanism

changes in the aging brain. Therefore, the experimental work in the current study will be focused on the motion typically associated with bridging vein failure, specifically in anterior-posterior head impacts.

As a first step toward determining the relationship between gross head kinematics and risk of subdural hematoma resulting from bridging vein failure, the current study is focused on the development of methods to define the relationship between head kinematics and the intracranial motion associated with bridging vein stretch. Specifically, the current experimental effort aims to develop procedures to track and quantify the relative motion of the meningeal layers and peripheral brain relative to the skull. Ultimately, it is expected that it will be possible to compare the measured motion of these layers to the stretch limits of bridging veins to predict the corresponding likelihood of bridging vein failure and subdural hematoma in a given *post mortem* motion test. With such a test procedure, it would be possible to parametrically measure the motion of the meningeal layers under a variety of loading directions, rates, and conditions. The effect of subject age, or age-associated parameters such as brain atrophy in the tested subjects, could also be evaluated in order to quantify the change in subdural injury risk with age.

Additionally, results of meningeal motion measurements in controlled head motion testing could be used to better define and validate boundary conditions between these layers in computational models in order to improve the biofidelity of head impact models for adults of all ages.

In summary, this current research effort is targeted at developing methods to better understand motion at the periphery of the brain during high-rate rotation. While no direct relationship to head injury is made in this study, an improved understanding of motion of these peripheral tissues is needed in order to define head injury tolerance for motor vehicle occupants as a function of age, given the expected dependence of brain motion on age and the relationships between brain motion and risk of the subdural hematoma.

This dissertation describes the work done to develop methods to quantify motion at the periphery of the brain, toward the ultimate goal of defining head injury tolerance as a function of age. Chapter 2 includes two background epidemiology studies. An initial epidemiological study of US crashes was undertaken to explore which head injuries are most important among older vehicle occupants by identifying types of injuries that become more likely for aging occupants. When that study indicated the importance of subdural hematoma for older crash occupants, a second epidemiological study was done to compare crash and injury characteristics for subdural hematoma in different adult age groups, with a focus on determining the original source of bleeding most common among older occupants.

As discussed in Section 1.6 high-frequency B-mode ultrasound was selected as the most promising method to observe and measure motion of the meningeal layers. A preliminary study was run to develop methods needed to accurately track tissue displacement as a function of time in B-mode ultrasound images at high-speed. The

tracking methods developed, along with dura motion tests run to validate the tracking and time-displacement calculations, are presented in Chapter 3.

Ultrasound imaging was then used to track meningeal and peripheral brain motion in anterior-posterior head acceleration using *post mortem* human subject heads. The heads were prepared by exposing the meninges for ultrasound imaging through an opening cut in the skull, pressurizing the vasculature with saline to replicate normal intracranial pressure, and perfusing the subarachnoid space with artificial cerebrospinal fluid. Methods were developed to grip and rotate the *post mortem* heads so that the exposed meningeal surfaces could be accelerated past the ultrasound probe such that they stayed in view throughout the event. Meningeal motion was imaged in both low-rate (130 to 155 radians/second^2) and high-rate (7400 to 7750 radians/second^2) rotational accelerations, as well as in one mid-rate acceleration test (1230 radians/second^2). Because of the links between age, brain atrophy, and brain motion, efforts were made to estimate atrophy in each subject using MR imaging methods. Chapter 4 describes subject preparation and experimental methods used for the rotation testing and motion tracking and Chapter 5 reports the results of the preliminary experimental efforts.

The effectiveness of the developed ultrasound motion measurement methods was evaluated for low-rate and high-rate tests in Chapter 6, along with recommendations for improvements in procedures for future rotational brain motion testing. Chapter 6 also discusses the challenges presented by the methods developed to measure meningeal motion and a discussion of its ultimate use as a tool to quantify relationships between head motion and subdural hematoma injury risk as a function of age and rotational skull

motion. Chapter 7 summarizes the implications of the results of preliminary ultrasound and rotation tests, and highlights areas of future work needed to refine the methods developed in this dissertation and to more fully understand subdural hematoma in motor vehicle crash occupants.

Chapter 2: Epidemiology of Subdural Hematoma in Older Motor Vehicle Occupants

As discussed in Chapter 1, the experimental work presented in this dissertation was motivated by crash data that showed subdural hematoma was particularly important among head injuries sustained by older motor vehicle crash occupants. The focus of the experimental efforts on understanding the mechanism of subdural hematoma sourced to bridging vein bleeding in particular was driven by crash data analysis that suggested that the increase in vulnerability to subdural hematoma with aging was linked to bridging vein bleeds in particular. Two of the crash-data studies cited in Chapter 1 that formed the fundamental motivation for the experimental work in this dissertation were prepared specifically as preliminary work to the current study. These two studies are presented in additional detail in this chapter. The first study in Section 2.1 is an analysis of the types of head injuries sustained by adult motor vehicle crash occupants by age, identifying subdural hematoma as particularly important among head injuries sustained by older occupants (Mallory 2010). The second study in Section 2.2 is an analysis of available data on the bleeding source and associated injury conditions for subdural hematoma among older crash occupants (Mallory, Herriott et al. 2011).

2.1 Head Injuries by Age Among Motor Vehicle Crash Occupants (Mallory 2010)

Previous epidemiological studies have shown that older trauma patients sustain different types of head injuries than younger patients, with an overall increase in intra-cranial bleeding with age (Vollmer, Torner et al. 1991; Coronado, Thomas et al. 2005). A more detailed analysis of head injuries by age group in motor vehicle crashes was performed to determine which head injuries are most important among older vehicle occupants by identifying types of injuries that become more likely for aging occupants in crashes. In particular, specific intra-cranial bleeding injuries were compared, taking into consideration previous reports on the severity and potential outcome of those injuries for an older population.

2.1.1 Methods for Study of Motor Vehicle Crash Head Injury by Age

Source data. The data for the study were drawn from cases in the NHTSA (National Highway Traffic Safety Administration) NASS CDS national crash database from 1993 to 2007. Analysis was performed using SAS, Version 9.1 (SAS Institute Inc., Cary NC).

Rollover and ejection cases were eliminated because of the possible confounding differences in crash conditions between young and older occupants in these crashes. Rollovers were excluded by eliminating cases where the primary type of damage was attributed to rollover/overturn. Ejection and partial ejection cases were excluded by the limitation that the EJECTION variable was equal to 0 for all included cases. Cases were limited to adults aged 20 and older. Fatal cases were not excluded from the study.

Although non-injury cases were retained in order to calculate injury rates, cases were excluded if the total number of injuries was coded as '97', which indicated that the occupant was injured but with details unknown. Occupants in all seat positions were included regardless of restraint use. Cases with unknown crash severity, indicated by estimated vehicle change in velocity (ΔV) or impact direction were only excluded from analyses that included those variables.

Head injury classification. All serious head injuries were included based on AIS (Abbreviated Injury Scale) severity codes 3 to 6. Multiple injuries were included for occupants with more than one serious injury coded. The AIS codes used in NASS CDS were based on the Association for the Advancement of Automotive Medicine's AIS-90 (AAAM 1990) from 1993 to 1999, and on AIS-90/98 Update (AAAM 1998) from 2000 to 2007. Head injuries were classified by seven-digit AIS code into broad categories (Table 2.1). For additional analysis of extra-axial bleeding injuries, this category was further classified into sub-categories: subdural hematoma, epidural hematoma, and subarachnoid hemorrhage.

Table 2.1. Broad head injury categories used in analysis

Injury Category	Specific Injuries Included
Intra-axial bleeding (Within the brain)	• Cerebellum or cerebrum contusion/hematoma/hemorrhage • Intra-ventricular hemorrhage • Cerebrum or cerebellum laceration • Penetrating injury • Vessel injury deep to the meninges
Extra-axial bleeding (Outside the brain)	• Epidural hemorrhage • Subdural hematoma • Subarachnoid hemorrhage • Subpial hemorrhage
Bleeding, location unknown	• Cerebrum/cerebellum hematoma or hemorrhage, location not further specified
Fracture	• Crush, fracture
Closed head injury	• Loss of consciousness or concussion • Diffuse axonal injury • Closed head injury/blunt head injury/traumatic brain injury not further specified
Swelling and other sequelae	• Swelling • Ischemia • Pneumocephalus
Brain stem injuries	• Any injury to the brain stem
Other	• Any other injury to the AIS head region not included in the categories above, such as pituitary injury or serious scalp injury

Data analysis. The first step of the hierarchical analysis was calculation of relative injury frequency to determine which broad injury types were most common for different adult age groups by decade. Bleeding injuries, identified in the relative frequency analysis as common among older occupants, were the focus of the second step of analysis: injury rate and the effect of speed. Step three of the analysis, odds ratio analysis, focused in still further on extra-axial bleeding injuries by estimating the increased odds of specific extra-axial injuries for older occupants.

Relative injury frequency by age. Relative frequency of serious head injuries of different broad categories was compared for age groups by decade. The SAS SURVEYFREQ procedure was used to calculate the proportion of head injuries by

category for each age decade. SAS survey analysis procedures account for the stratified probability sampling procedure used in NASS CDS and produce estimates based on weighted NASS CDS data.

For each age group, the weighted proportions of serious injuries in each injury category type were plotted. Analysis was performed on counts of all serious injuries, not on the number of seriously injured occupants.

Injury rate and the effect of speed for bleeding injuries. Injury rates were estimated for bleeding injuries, which were identified in the relative injury frequency analysis as more frequent among older occupants. The injury rate represents the total number of occupants in a selected dataset with at least one head injury of a given type divided by the total number of occupants in the same dataset. Three adult age groups were selected (20-49, 50-69, 70+) based on the results of the relative injury frequency analysis that suggested shifts in head injury patterns at these approximate age thresholds.

Three speed-change categories were used, based on the NASS CDS ΔV variable DVTOTAL: 0-19 km/h, 20-39 km/h, and 40+ km/h. The SAS SURVEYFREQ procedure was used to estimate injury rate for each of the three age groups at different levels of crash ΔV. Injury rate and crash frequency at different levels of ΔV were compared, and presented along with the total proportion of bleeding injuries occurring to occupants in different age groups. Occupants in crashes with unknown ΔV were excluded from the analysis of the effect of speed.

Odds ratio analysis for extra-axial bleeding injuries. For extra-axial bleeding head injuries, identified in the relative frequency analysis and injury rate analysis as

frequent among older occupants, an odds ratio analysis was performed. Increased odds of injury for specific extra-axial injuries among the older age groups relative to the youngest age group were estimated.

The SAS SURVEYLOGISTIC procedure was used to estimate odds ratios for sub-categories of extra-axial bleeding injuries: subdural hematoma, epidural hematoma, and subarachnoid hemorrhage. A model was developed for each specific type of bleeding injury, where the dependent variable was a dichotomous categorical variable equal to one for occupants with a given injury and zero otherwise. Categorical variables for age group (age 50-69 and age 70+) were compared to a baseline 20-49 year-old group. For example, the SAS logistic model for extra-axial bleeding injury was EAXIAL(EVENT='1') = AGEGROUP. Ninety-five percent confidence limits for the odds ratios were based on variance calculated by the Taylor series. In order to correct for simultaneous estimation of six confidence intervals for odds ratios (two age groups for three different injuries), Bonferroni correction was applied by dividing the significance level of 0.05 by 6 so that alpha was equal to 0.0083.

To account for possible confounding differences between crash and vehicle conditions for younger and older vehicle occupants, an adjusted logistic regression model was developed with additional independent variables: ΔV, vehicle age, impact direction, and vehicle body type. The dependent variable remained a categorical variable for the presence of injury, and age group remained a categorical variable to compare two age groups of older occupants to the baseline 20 to 49 age group. ΔV and vehicle age in years at the time of the crash were continuous variables and vehicle body type and impact

direction were modeled as categorical variables. Vehicle body type was a categorical variable set to zero for passenger cars, and one for all trucks, light trucks, and vans using the BODYTYPE variable. Impact direction was set to zero for frontal impacts and one for side impacts, where frontal impacts were defined by a direction of force 11 to 1 o'clock or 10/2 o'clock with general area of damage to the front. Side impacts were defined as all other cases with direction of force from 2-4 o'clock and 8 to 10 o'clock. Rear impacts were excluded from the adjusted model in the odds ratio analysis, which accounted for impact direction, because of a limited number of rear impact injury cases. Cases where vehicle body type, impact direction, or ΔV was unknown were also excluded for the adjusted odds ratio analysis.

2.1.2 Results of Study of Motor Vehicle Crash Head Injury by Age

Relative injury frequency by age. After exclusion of 10,562 NASS CDS occupants documented as injured but with injury details unknown, there were 131,885 NASS CDS case occupants remaining in the dataset. Of these, 5093 NASS CDS case occupants had at least one serious head injury, with a total of 10,242 serious head injuries. These cases represented 345,000 weighted occupants with 574,000 serious head injuries or an annual average of 23,000 included cases with serious head injuries.

Distribution of the serious head injuries in the dataset is shown by broad injury type (Table 2.2) and by age group (Table 2.3). Among the youngest adults included (age 20-29) there were an estimated weighted total of 179,000 serious head injuries (Table 2.3). The total number of head injuries estimated for each age decade was progressively lower up to the age group of 60 to 69 where there was an estimated 42,000 serious head

injuries. Those in the 70 to 79 age group had an estimated 56,000 serious head injuries, and those aged 80 and older had an estimated 35,000 serious head injuries.

Relative frequency of serious head injuries of different types was compared for age groups by decade in Figure 2.1, which shows, for example, that 49% of serious injuries in the oldest age group are extra-axial bleeding and 30% are intra-axial bleeding. Not all age groups add to 100% because "Other" injuries are not shown.

Table 2.2. Number of raw and weighted serious head injuries (AIS 3+) by broad injury type

	Injury categories							
	Intra-axial bleeding	Extra-axial bleeding	Bleeding, Location unknown	Fracture	Closed Head Injury	Swelling and other sequelae	Brain Stem Injury	Other
n (raw)	2462	3578	147	1438	1186	738	674	19
n (weighted) 1000's	155	190	12	74	80	37	24	2

Table 2.3. Number of raw and weighted serious head injuries (AIS 3+) by age group

	Age group (years)						
	20-29	30-39	40-49	50-59	60-69	70-79	80+
n (raw)	3719	1995	1617	1023	754	678	456
n (weighted) 1000's	179	101	96	66	42	56	35

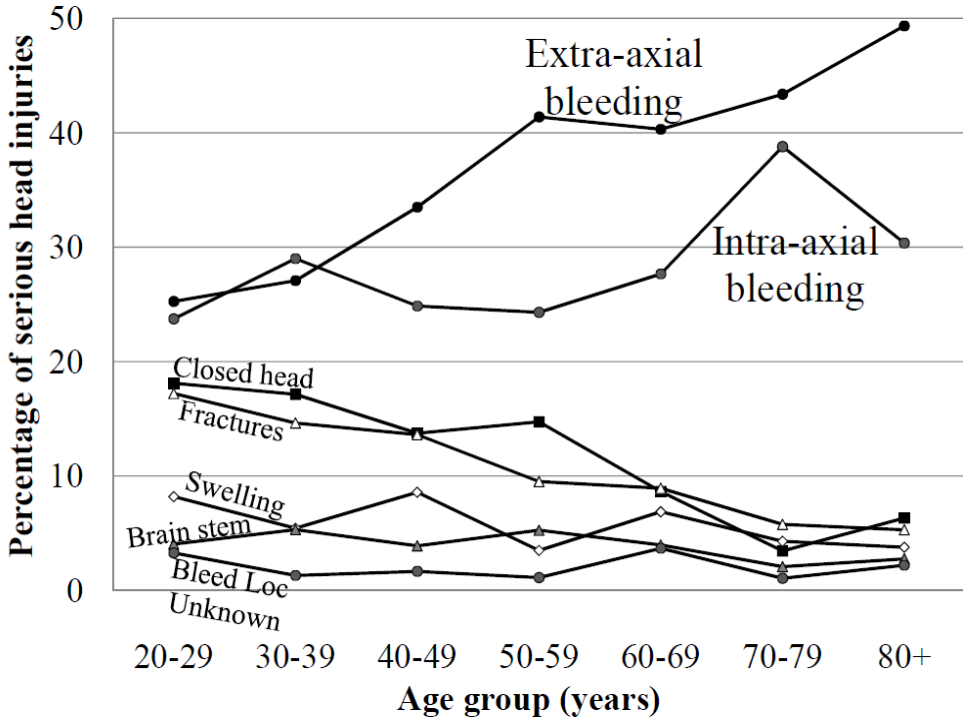

Figure 2.1. Proportion of serious head injuries of each type, for each age group.

Injuries that accounted for a lower proportion of head injuries in the older occupants than in younger occupants included swelling and other sequelae, closed head injury and fracture (Figure 2.1). Closed head injuries made up 17 to 18% of serious head injuries among adults under age 40, but only 3 to 9% of head injuries for those age 60 and older. Seventeen percent of head injuries in occupants aged 20-29 were fractures. This percentage declined for every decade up to age 80 or greater, where the percentage of serious head injuries attributed to fractures was only 5%.

Bleeding injuries were more frequent, relative to other injuries, among older occupants than among younger occupants. The proportion of extra-axial bleeding among serious head injuries began increasing as early as the 30's decade and exceeded 40% by the 50's decade. Extra-axial bleeding injuries accounted for 49% of the serious head

injuries in the oldest age group. The increase in the proportion of intra-axial bleeding with age appeared to start at an older age and was less steady, remaining between 24% and 29% for occupants younger than 70.

When the percentages of serious head injuries in each age group that involved bleeding in any location were combined, the majority of serious head injuries were bleeding injuries in all age groups (Figure 2.2). Bleeding injuries accounted for approximately 52% of head injuries for adults in their 20s, and a gradually increasing proportion for older occupants. In age groups age 70 or older, more than 80% of serious head injuries were bleeding injuries. While there was a steady increase in the proportion of injuries that were bleeding injuries, the steepest increases in the combined percentage of the two types of bleeding injuries occurred for occupants at approximately the 70's decade and, to a lesser extent, in the 50's decade, where there was also a steep increase in the percentage of extra-axial injuries. The shifts at these age thresholds were used for binning age groups in subsequent analyses in this study. No more than 1.2% of injuries in any age group were in the "other" category, indicating that the broad categories used in this analysis captured most serious injuries in the data.

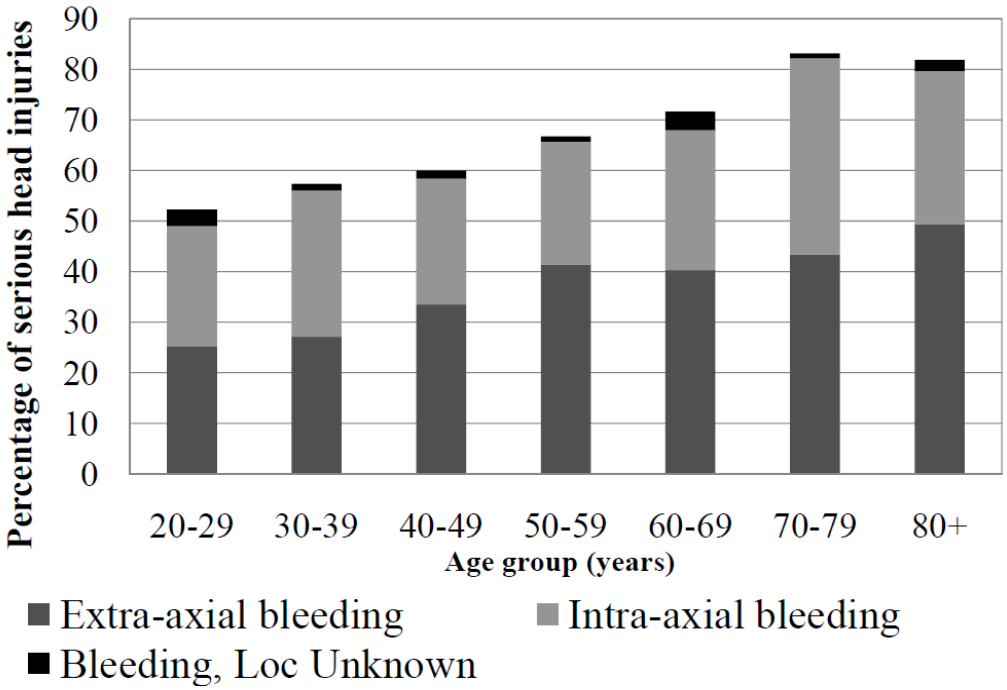

Figure 2.2. Bleeding injuries as percentage of all serious head injuries by age group.

Injury rate and the effect of speed. Bleeding injuries, identified in relative frequency analysis as increasingly frequent with age, were further analyzed. Injury rates for bleeding injuries were calculated by age group and by ΔV, using three age groups: adults aged 20-49, 50-69, and older adults (age 70+).

Injury rate for crashes at all speeds combined is shown in Figure 2.3. For intra-axial bleeding injury, the oldest group (70+) had an injury rate more than three times that of the youngest group (20-49). The difference in injury rate by age group was even greater for extra-axial injury: the 50-69 age group had twice the injury rate of the youngest group and the oldest group had more than 5 times the injury rate of the youngest group.

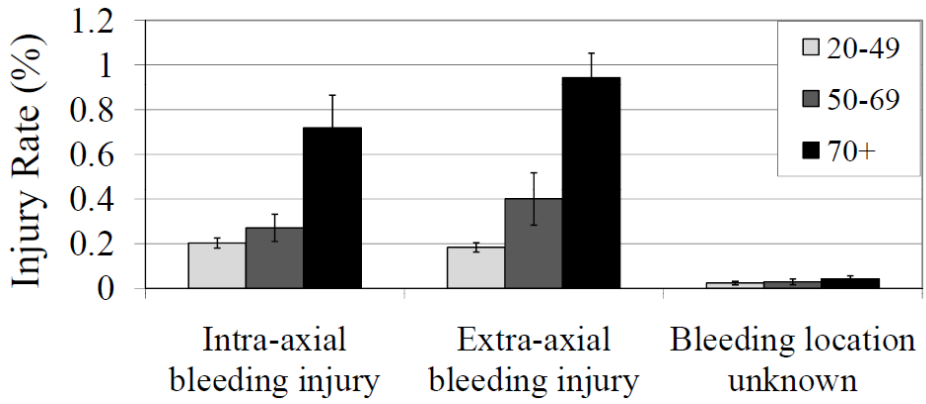

Figure 2.3. Injury rate for types of bleeding injuries by age group. (Standard error (SE) shown by error bars.)

The total number of bleeding injuries sustained by occupants in different age groups was affected by the number of crashes that occurred in each speed range, as well as by the rate of injury in each speed range. Figure 2.4 shows the distribution of ΔV for all crashes with known ΔV in each age group. These data represent exposure to crashes and include all occupants, with or without injury. As shown in Figure 2.4, the majority of weighted NASS CDS crashes are below a ΔV of 30 km/h for all age groups.

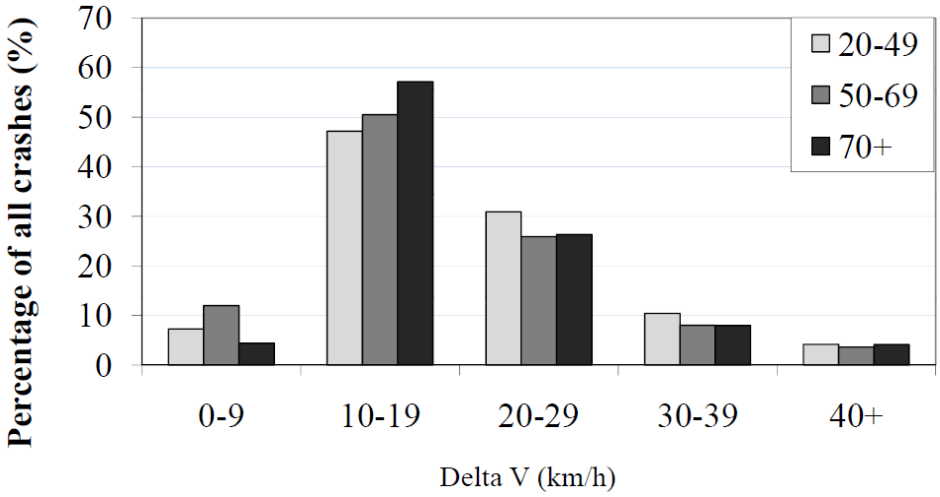

Figure 2.4. Distribution of ΔV for all crashes, by age group.
(Each age group sums to 100%.)

In order to understand the effect of age at different crash severity levels, the rates of intra-axial bleeding injury and extra-axial bleeding injury by age group were sub-divided by ΔV range as shown in Figure 2.5 and Figure 2.6. For *intra-axial* bleeding injury, the most notable difference in injury rate with age was in crashes with ΔV over 40 km/h where the oldest age group (age 70 and older) showed a rate of injury more than three times the rate for either of the two younger groups. In contrast, injury rate variation by age for *extra-axial* bleeding injury was greatest for lower ΔV crashes. In crashes at ΔV 20 to 29 km/h, the extra-axial bleeding injury rate for occupants age 70 and older was estimated to be 21 times higher than the rate for occupants younger than age 50.

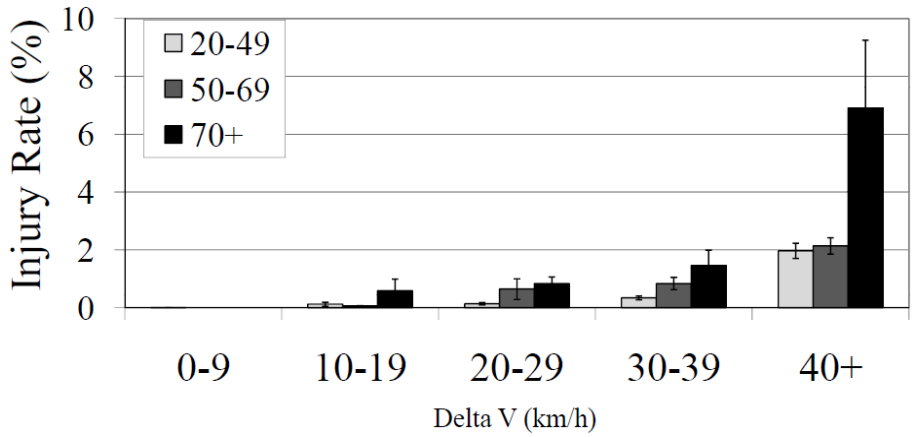

Figure 2.5. Injury rate for *intra-axial* bleeding injury by ΔV and age group. (SE shown by error bars.)

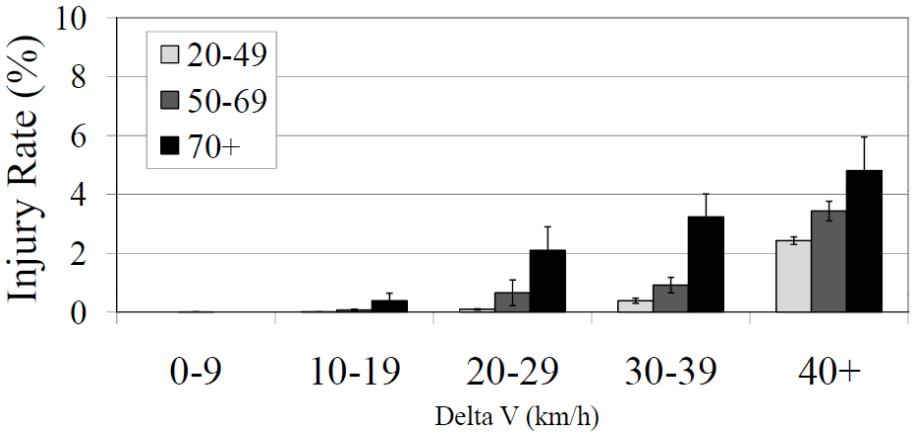

Figure 2.6. Injury rate for *extra-axial* bleeding injury by ΔV and age group. (SE shown by error bars.)

The combination of an elevated rate of extra-axial bleeding injury for older occupants in relatively low ΔV crashes along with the high frequency of crashes at these lower severity levels leads to a disproportionately high number of extra-axial injuries in older occupants, as illustrated in Figure 2.7 and Figure 2.8. Figure 2.7 shows age distribution of occupants in crashes of known ΔV, compared to the age distribution of occupants with intra-axial and extra-axial bleeding injuries. Occupants in the oldest age

group (70+) make up 24% of occupants with intra-axial bleeding injuries and 30% of occupants with extra-axial bleeding injuries in the included crashes, in spite of accounting for only 7% of the total number of occupants in these crashes. When narrowed to include only crashes with ΔV less than 30 km/h (Figure 2.8), older occupants are especially over-represented in the group of occupants who sustained extra-axial bleeding injury in low- to mid-speed crashes. Occupants in the 70+ age group accounted for 47% of the extra-axial bleeding injuries reported in these relatively low-speed crashes, while again only accounting for 7% of the crashes in this ΔV range.

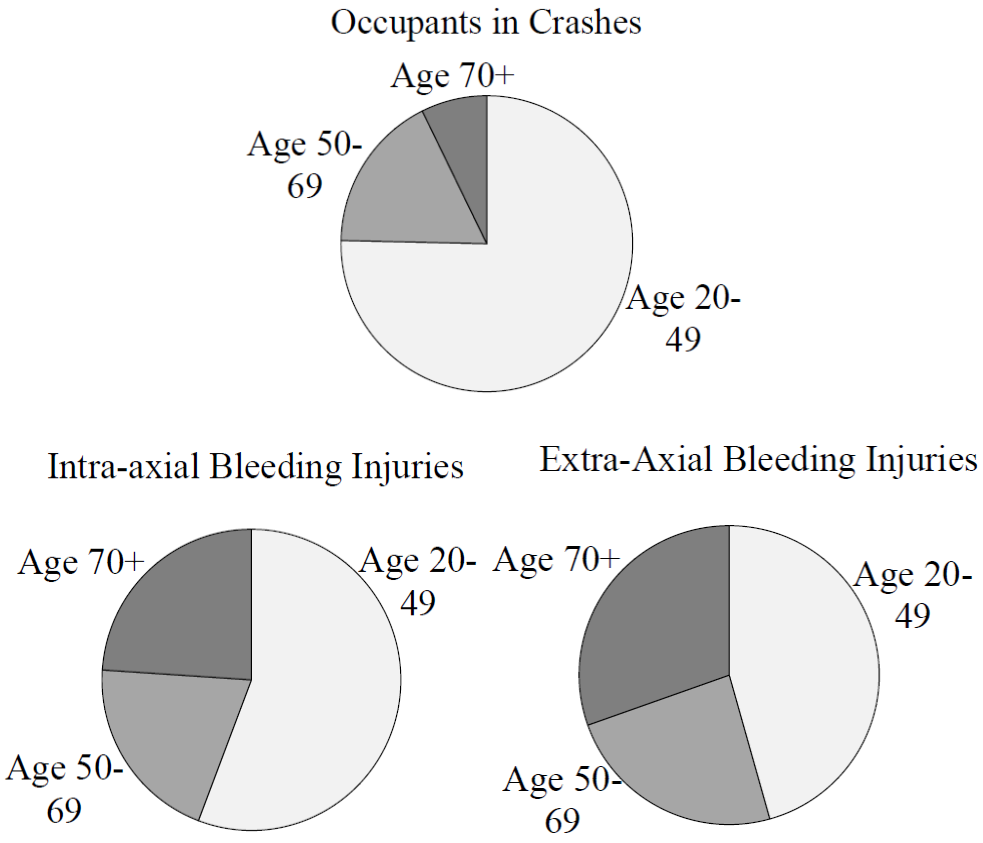

Figure 2.7. Proportion of occupants in crashes (known ΔV) compared to proportion of intra-axial and extra-axial bleeding injuries by age.

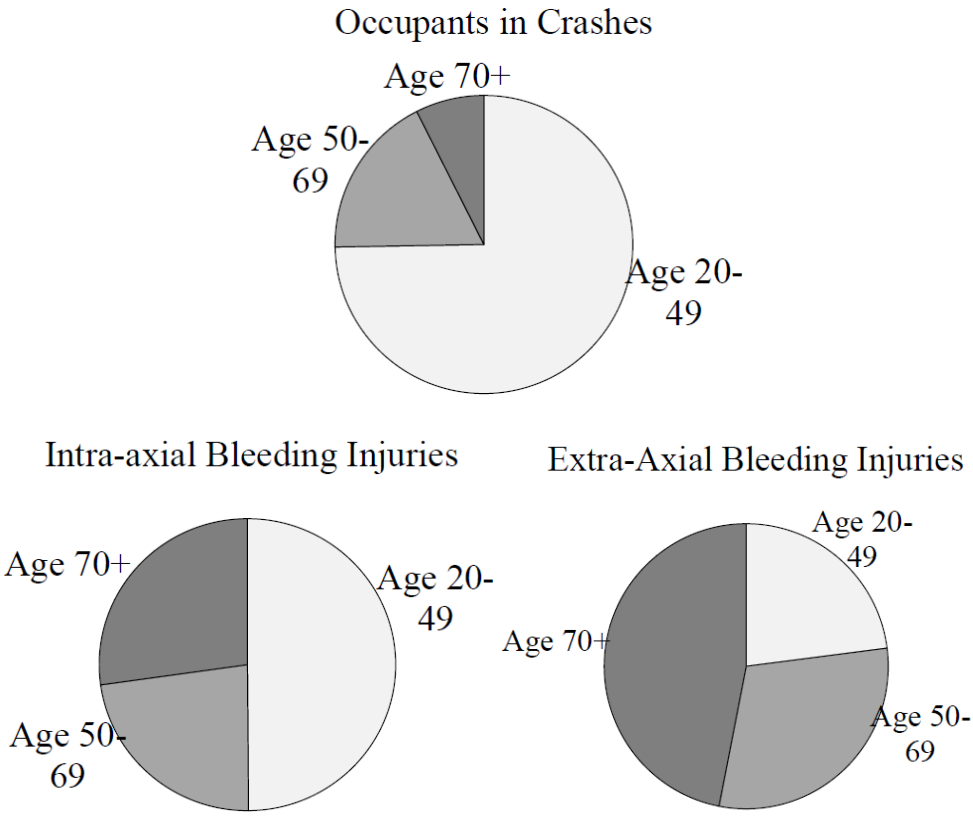

Figure 2.8. Proportion of occupants in crashes at *ΔV less than 30 km/h* compared to proportion of intra-axial and extra-axial bleeding injuries by age.

Odds ratio analysis. Odds ratios were calculated to compare the odds of sustaining specific extra-axial bleeding injuries for older age groups compared to the 20-49 age group. Subpial hemorrhage was excluded from odds ratio analysis because there were only three cases in the included dataset. Table 2.4 shows odds ratios calculated with a model that accounts only for the effects of age on injury odds, and Table 2.5 shows odds ratios calculated with an adjusted model that accounts for potentially confounding variables ΔV, vehicle age, impact direction, and vehicle body type, as well as for age group.

In this comparison of injury odds for older occupants compared to young adults, injuries that had a point estimate odds ratio greater than 1.0 and that did not include 1.0 in the Bonferroni-corrected 95% confidence interval (alpha= 0.05/6=.0083) are shown in bold font indicating significantly increased odds of injury for the older age groups. The resulting adjusted odds ratios for subdural hematoma, for example, estimates that the odds of injury for an individual in the oldest age group were 9.38 times the odds of injury for a young adult *in a crash at the same ΔV and impact direction and in the same age and body type of vehicle* (Table 2.5).

With or without adjustment for possible confounding variables, both the 50 to 69 and the 70 and older age groups showed increased odds of subdural hematoma and of subarachnoid hemorrhage. Neither age group showed increased odds of epidural hematoma over younger occupants, either with or without accounting for possible confounding variables.

Table 2.4. Odds ratios for extra-axial bleeding head injuries, without adjustment for possible confounding variables
(Significant point estimates in bold font. Baseline young adult group age 20 to 49.)

	Point Estimate of Odds Ratio	**95% Confidence Limits**	
Subdural hematoma			
Age 50-69 compared to young adults	**2.93**	1.16	7.39
Age 70+ compared to young adults	**6.71**	4.26	10.59
Epidural hematoma			
Age 50-69	0.79	0.31	1.99
Age 70+	0.40	0.11	1.48
Subarachnoid hemorrhage			
Age 50-69	**1.70**	1.40	2.08
Age 70+	**4.15**	2.75	6.25

Table 2.5. Odds ratios for extra-axial bleeding head injuries, accounting for ΔV, vehicle age, body type, and impact direction in model
(Significant point estimates in bold font. Baseline young adult group age 20 to 49.)

	Point Estimate of Odds Ratio	**95% Confidence Limits**	
Subdural hematoma			
Age 50-69	**3.73**	1.11	12.49
Age 70+	**9.38**	3.74	23.48
Epidural hematoma			
Age 50-69	0.81	0.25	2.66
Age 70+	0.50	0.12	2.05
Subarachnoid hemorrhage			
Age 50-69	**2.12**	1.46	3.08
Age 70+	**5.18**	2.60	10.32

2.1.3 Discussion of Study of Motor Vehicle Crash Head Injury by Age

Bleeding injuries accounted for at least half of serious head injuries reported among adult occupants in all age groups, and made up an increasing proportion of head injuries among older occupants. More than 80% of serious head injuries among those aged 70 and over were bleeding injuries. While the oldest occupants (age 70 and older) have the highest rates of intra-axial and extra-axial bleeding injuries compared to younger occupants, the age-related increase in extra-axial bleeding injuries was substantial even for occupants as young as those in their 50s and 60s.

The effect of age on rate of *extra-axial* injury was greatest in lower ΔV crashes (Figure 2.6), while the effect of age on rate of *intra-axial* injury was predominant in high ΔV crashes (Figure 2.5). Given that less than 15% of crashes in any age group occurred at over 30 km/h (Figure 2.4), the elevated intra-axial injury rate in high ΔV crashes would not be expected to result in a substantial increase in injuries to older occupants.

However, the elevated extra-axial injury rate for older occupants in lower ΔV crashes is especially important because this speed range is where most crashes occur (Figure 2.4).

The combination of an elevated rate of extra-axial bleeding injury for older occupants in relatively low ΔV crashes along with the high frequency of crashes at these lower severity levels led to a disproportionately high number of extra-axial injuries to older occupants. Occupants in the oldest age group (70+) make up 47% of those with extra-axial bleeding injuries reported in crashes with ΔV less than 30 km/h, while accounting for only 7% of the occupants in crashes in this ΔV range.

With or without adjustment for possible confounding variables, both the 50 to 69 age group and the 70 and older group showed increased odds of subdural hematoma and subarachnoid hemorrhage relative to the youngest adult age group. Conversely, the odds of epidural hematoma showed no increase for the older age groups, indicating that the age-related increases in extra-axial bleeding injuries identified in this study were driven largely by subdural and subarachnoid bleeding.

To assess the relative importance of subdural hematoma and subarachnoid hemorrhage, these injuries were evaluated in the context of outcome, in particular for older patients.

As discussed in Chapter 1, mortality can range from 33 to 50% of cases, making subdural hematoma especially lethal among head injuries. Subdural hematomas present an especially increased rate of mortality and poor outcome for older patients (Hukkelhoven, Steyerberg et al. 2003; Raju, Gupta et al. 2004; Stitzel, Kilgo et al. 2008; Hanif, Abodunde et al. 2009). The increased incidence of subdural hematoma for

occupants aged 50 and older from the current study, combined with the previously-reported increased mortality rate for subdural hematoma for older patients presents a double risk for older occupants for this already life-threatening injury.

Subarachnoid hemorrhage, also identified in the current study as more frequent among older occupants, has been linked to increased risk of poor prognosis after head injury (Vollmer, Torner et al. 1991; Greene, Marciano et al. 1995; Servadei, Murray et al. 2002; Mattioli, Beretta et al. 2003; Chieregato, Fainardi et al. 2005), but this increased risk is not related to subarachnoid hemorrhage as a primary injury, but as an aggravating injury with a negative effect on the outcome of other injuries. While subarachnoid hemorrhage injuries are frequent, especially for older occupants, they do not present the threat to life associated with subdural hematoma.

2.2 Subdural Hematoma in Older Occupants (Mallory, Herriott et al. 2011)

The original source for the bleeding that produces subdural hematoma can be from bridging veins; adjacent brain contusions, lacerations or intracerebral hematomas; or from ruptured cortical vessels on the surface of the brain (Lee, Melvin et al. 1987; Graham 1996; Miller, Piper et al. 1996; Miller and Statham 2000; Toyama, Kobayashi et al. 2005; Depreitere, Van Lierde et al. 2006). Few studies have quantified the frequency of subdural hematoma from specific sources. In post-mortem studies of fatal traumatic subdural cases, Maxeiner showed that as many as two thirds of subdural hematoma were the result of brain contusions (Maxeiner 1997) and in the remaining third of cases, bleeding was attributed to bridging vein rupture and torn cortical arteries with equal frequency (Maxeiner and Wolff 2002). Previously, in a study of surgically-treated

subdural hematoma cases, bleeding from cerebral lacerations or intracranial hematoma was identified as the cause of subdural hematoma in 40.5% of cases (Jamieson and Yelland 1972).

Bleeding sources for subdural hematoma. No previous epidemiology studies have directly compared the injury or patient characteristics of subdural hematoma associated with bridging vein bleeding versus other bleeding sources. However, as summarized in Chapter 1, two previous authors have compared subdural hematoma cases with accompanying bleeding injuries to cases of isolated subdural hematoma (Jamieson and Yelland 1972; Maxeiner 1998). In the cases with accompanying bleeding injuries, such as adjacent contusions, lacerations, or intracerebral hematomas, the subdural hematoma was potentially sourced from these original bleeds. In contrast, the cases with isolated subdural hematoma in the absence of other bleeding injuries more likely resulted from bridging vein bleeding. Both studies reported differences in the direction of head impact for subdural hematoma cases with versus without accompanying bleeding injuries. The study based on surgical cases from two hospitals reported that cases with accompanying bleeding injury were less common over age 60 (Jamieson and Yelland 1972), while the study based on autopsy cases made no conclusions related to patient age (Maxeiner 1998). While these two previous studies suggested that there are differences in the head impact conditions that produce subdural hematoma by bridging vein failure versus by other sources, they did not address the mechanical loading that results in subdural hematoma from sources other than bridging veins or address how tolerance might be affected by age.

To better understand how tolerance to subdural hematoma changes with age, specifically for motor vehicle trauma patients, the bleeding sources for subdural hematoma among different age groups need to be identified in motor vehicle crash data. With bleeding source information by age group, it can be determined if either bridging vein ruptures or other bleeding sources are primarily responsible for the increase in subdural hematoma for older occupants. Therefore, as foundation for the work in this dissertation, a study of available US crash data was performed to explore how crash and injury characteristics for occupants who sustain subdural hematoma change with age. Specifically, crash data was analyzed to look for evidence that older occupants may be more susceptible to subdural hematoma as a result of bridging vein failure versus as a result of contusions or ruptured vessels on the surface of the brain.

2.2.1 Methods for Study of Subdural Hematoma in Older Occupants

In order to understand how the risk and mechanism of subdural hematoma changes for motor vehicle crash occupants as they age, US databases were used to compare crash and injury characteristics for adult subdural hematoma cases in different age groups, with a focus on evidence of the original bleeding source. The two motor vehicle crash databases used were the NHTSA NASS CDS database and the NHTSA CIREN database.

Medical information available in the CIREN dataset was used for detailed review of cases where the probable bleeding source in subdural hematoma cases could be identified. Cases were categorized by the bleeding source: *bridging veins*, *brain contusions*, or *other bleeding sources*.

Because NASS CDS does not contain the detailed medical information included in CIREN, a different approach was used to identify possible bleeding sources for subdural hematoma. Crash data from NASS CDS was compiled to determine the frequency of different serious bleeding head injuries that accompany subdural hematoma. Subdural hematoma cases were sorted into three categories. Those sustained in the absence of other serious head injuries were identified as *isolated*. The remaining cases were categorized as subdural hematoma *with contusion* or subdural hematoma *with other serious head injury*. In the absence of specific information on bleeding sources in NASS CDS cases coded with subdural hematoma, it was assumed that isolated cases with no other serious head injury documented were more likely than other cases to be associated with bridging vein failure directly into the subdural border cell region since bridging veins are the only potential bleeding source that pass through the dural border cell layer. Similarly it was assumed that subdural cases that also had a documented brain contusion were the injury category most likely to include subdural hematoma sourced to contusions. Other potential subdural bleeding sources were combined in a third category with all other serious head injuries.

CIREN case review. All subdural hematoma cases in NHTSA's CIREN crash database up to August 2010 were selected. Those with recorded intracranial surgery for evacuation of subdural hematoma were reviewed individually. Operative reports were evaluated for documentation of bleeding source for each of these cases. Subdural hematoma cases with operative reports were categorized into those associated with (1) bridging vein rupture, (2) brain contusions, or (3) other specified bleeding sources.

After categorizing the CIREN cases by associated bleeding source using the detailed medical descriptions available in the operative reports, the cases were also sorted by the accompanying injury categories used for the NASS CDS analysis using only the AIS-coded injuries: *isolated, with contusion,* or *with other serious injury*. A case-by-case comparison was made to determine if the NASS CDS accompanying injury categories, determined from AIS code only, were consistent with the CIREN categories based on the probable bleeding sources identified in the detailed records. This comparison was used to confirm the suitability of using the accompanying injuries in NASS CDS cases as surrogate variables for probable bleeding sources in the absence of explicitly coded information on bleeding source in NASS CDS.

NASS CDS analysis. Subdural hematoma cases in NASS CDS from 1993 to 2008 were selected based on seven-digit AIS codes. The AIS codes used in NASS CDS were based on the Association for the Advancement of Automotive Medicine's AIS-90 (AAAM 1990) from 1993 to 1999, and on the AIS-90/98 Update (AAAM 1998) from 2000 to 2008. Serious injuries are those with an AIS score of 3 to 6.

All analyses compared three adult age groups: 20-49 years, 50-69 years, and age 70 and older. Occupants under age 20 were excluded. Occupants in all seat positions were included. Cases with unknown impact direction or velocity change were excluded only from analyses that included those variables. Weighted data was used for all NASS CDS analyses. Analysis was performed using survey analysis procedures in SAS, Version 9.2 (SAS Institute, Cary NC).

Accompanying head injuries. The percentage of occupants in NASS CDS with subdural hematoma who also had other types of serious head injuries was estimated by age group. AIS 3+ head injuries were initially classified by their seven-digit AIS code into categories as listed in Table 2.6, while subdural hematoma cases with no other serious injuries were classified as Isolated Subdural Hematoma.

Table 2.6. Categories for accompanying head injuries (AIS 3+)

Injury Category	Specific injuries included
Skull fracture	Including crush
Subarachnoid hemorrhage	
Contusions	
Intraventricular hemorrhage	
Epidural hematoma	
Other intracranial bleeding injury	Including blood vessel injury, hematoma or hemorrhage not further specified, subpial hemorrhage, laceration or penetration, sinus bleeding, intracerebellar or intracerebral bleeding
Closed head injury	Including loss of consciousness or concussion, diffuse axonal injury, or closed head injury/blunt head injury/ traumatic brain injury not further specified
Sequelae	Including swelling, ischemia, pneumocephalus
Brain stem injury	Including any injury to the brain stem
Other intracranial injury	Any other injury to the AIS head region not included in the categories above, such as pituitary injury or serious scalp injury

Relative Frequency of Isolated Subdural Hematoma. For the purpose of comparing the crash characteristics of subdural hematoma cases that were isolated to cases where the subdural hematoma was accompanied by a contusion or by other serious head injury, subdural hematoma cases were grouped as shown in Table 2.7.

Table 2.7. Subdural hematoma injury categories (AIS 3+)

Injury grouping in NASS CDS	Injuries accompanying subdural hematoma
Isolated	No other documented AIS 3+ head injury
With contusion	Subdural hematoma combined with AIS 3+ brain contusion
With other serious injury	Subdural hematoma combined with AIS 3+ head injuries other than contusion

The frequency of isolated subdural hematoma was compared to the frequency of subdural hematoma accompanied by contusion or other serious injuries for different types of occupant and impact conditions. Frequency of each sub-type of subdural hematoma case was calculated as a percentage of all subdural hematoma cases among each occupant or crash type. Data is presented by sex, age group, vehicle impact direction, and head contact location.

Vehicle impact directions are defined by the direction of force variable in NASS CDS. Frontal impacts included those from 11 o'clock to 1 o'clock, as well as those at 10 or 2 o'clock only if the general area of damage was to the front of the vehicle. Side impacts were defined as all other cases with direction of force from 2 to 4 o'clock and 8 to 10 o'clock. Rear impacts included those from 5 to 7 o'clock and rollovers were any crash where the primary damage variable indicated overturn damage. Head contact locations were estimated based on the location of cutaneous and fracture injuries coded to the head and face. Injuries coded to the frontal aspect of the head were classified as frontal contacts and to the left or right aspects were classified as lateral contacts. Any face contact injury in combination with a frontal head contact, or without any other contact injuries to the head was classified as a frontal head contact. If face contact injuries were coded to the left or right aspect and were combined with a lateral head contact injury, the case was classified as a lateral head contact.

For vehicle side impact cases, the location of the subdural hematoma was compared to the vehicle impact direction. Cases where the vehicle impact and subdural hematoma were on the same side were categorized as ipsilateral, and those on opposite sides were contralateral. Side impact cases with documented subdural hematoma on both sides of the brain were classified as bilateral.

Injury rate analysis. For each of the three AIS-based accompanying injury categories (isolated, with contusion, and with other serious injury), injury rate was estimated by dividing the weighted number of injured occupants by the total weighted number of NASS CDS occupants in each age and impact direction category. The only cases excluded from the rate calculations were those where the occupant was listed as injured, but with details unknown (INJNO=97) since inclusion of these cases would increase the denominator of the rate calculations even though it was unknown whether they would be included in the numerator.

Injury rates were presented by age group for all occupants, then separately by impact direction for impact directions with sufficient numbers of cases to present rates by age group.

Odds ratio analysis. Odds ratios were calculated to compare the odds of sustaining either isolated subdural hematoma or subdural hematoma with contusion for the oldest age group compared to the youngest age group. Subdural hematoma cases with other serious head injuries were not included in the odds ratio analysis.

The SAS SURVEYLOGISTIC procedure was used to estimate odds ratios by age group separately for male and female occupants in frontal and side impacts. For each age

and impact direction, a multinomial logistic regression model was developed, where the dependent injury variable could take on one of four values: no subdural hematoma, isolated subdural hematoma, subdural hematoma with contusion, or subdural hematoma with other serious injury. Categorical variables for age group were used to compare the 70 years and older group to a baseline 20 to 49 year-old group. To account for possible confounding differences in crashes for different age groups, independent variables reflecting potential differences in crash conditions and crash severity between young and old motor vehicle crash victims were included. The regression models for each sex and impact condition combination were built using a backward elimination stepwise procedure until the multinomial regression model contained only significant explanatory variables. Variables in the final models included a continuous variable for ΔV, dichotomous variables for the presence of a skull fracture and air bag deployment, and a categorical variable for seat position with possible values of driver, front seat passenger, or rear seat passenger.

Ninety-five percent confidence limits for the odds ratios were based on variance calculated by the Taylor series. In order to correct for simultaneous estimation of confidence intervals for each group (two-sided confidence interval for two injury types), Bonferroni correction was applied by dividing the significance level of 0.05 by 4 so that alpha was equal to 0.0125.

2.2.2 Results for Study of Subdural Hematoma in Older Occupants

CIREN search results. A search of the CIREN database identified 277 cases with subdural hematoma. Case occupant age ranged from 4 days to 96 years, with a

mean age of 37 years. Eighty-one cases were fatal, with the mean age of the fatal cases being 44 years. Operative reports were available for 37 individuals who underwent surgical evacuation of the subdural hematoma. These operative reports were reviewed for documentation of the source of subdural bleeding in each case.

In fourteen of the 37 cases with surgical records, a specific source of adjacent bleeding was identified. Two of these cases involved children and were excluded from the current analysis. The remaining 12 CIREN cases with documented bleeding sources adjacent to the evacuated subdural hematoma are summarized in Table 2.8 and Table 2.9. Included are occupant age and sex, as well as CIREN-estimated impact direction and ΔV or barrier equivalent velocity (BEV) for the primary impact. The location of the impact on the head and the head contact surface were drawn from CIREN investigation conclusions. Cases involving bridging vein bleeding sources are listed in Table 2.8, and cases involving only other bleeding sources are in Table 2.9.

In *four* of the twelve adult CIREN cases with documented bleeding source adjacent to the evacuated subdural hematoma, a bridging vein was the only identified bleeding source. In *two* of the twelve cases, bleeding was documented from a bridging vein as well as from cortical vessels: the vein of Labbé in the case involving a 46 year-old woman and a posterior parietal superficial cortical vein in the case involving a 27 year-old woman (Table 2.8). In the remaining *six* adult CIREN cases with bleeding sources listed in the operative reports, bridging veins were not involved (Table 2.9). In three of those cases, documented bleeding adjacent to the evacuated subdural hematoma was attributed to contusions. Of the remaining three cases attributed to other bleeding

sources, two documented intracerebral hematomas and the third documented an adjacent arterial bleed on the brain surface.

The CIREN cases with information on subdural bleeding source were also reviewed to determine how they would have been categorized under the AIS-based accompanying injuries system used to sort cases in the NASS CDS analysis (Table 2.10). The objective was to determine whether the AIS-based categories to be used as surrogate variables for bleeding sources were consistent with the actual bleeding source identified in CIREN cases with additional medical information.

Table 2.8. CIREN cases with operative report documentation of *bridging vein bleeding* adjacent to surgically-evacuated subdural hematoma

Age, Sex & Seat Position	**Impact Direction (PDOF)**	**Crash Severity**	**Head impact**	**SDH location**	**Adjacent Bleeding Source Identified in Operative Report**	**Other Serious Head Injuries**	**Accomp. Injury Category**
26 y.o. female driver	11 o'clock	BEV= 49 km/h	Roof/side rail with left head	Left panhemispheric and over tentorium	*Bridging vein:* Two lacerated bridging veins near midline	Left cerebral swelling AIS 4 Left subcortical hemorrhage AIS 4 Left subarachnoid hemorrhage AIS 3	Other serious injuries
85 y.o. female right front	12 o'clock	ΔV= 22 km/h	Passenger-side frontal air bag with left face	Left frontotemporal	*Bridging vein:* Torn bridging vein "was cause of hematoma"	**(Fatal)** Cerebral edema AIS 3	Other serious injuries
16 y.o. female right rear	3 o'clock	ΔV= 53 km/h	Left forehead to seatback, right occiput to unknown surface	Left temporal to convexity and over tentorium	*Bridging vein:* Hole in superior sagittal sinus from an evolved bridging vein	Right intracranial vessel laceration AIS 4	Other serious injuries
18 y.o. female driver	2 o'clock	ΔV= 59 km/h	Right door impact documented	Right	*Bridging vein:* Torn parasagittal vein	None	Isolated
46 y.o. female right front	3 o'clock	ΔV= 27 km/h	Right parietal / temporal to door interior or striking vehicle	Right frontal temporal and parietal	*Bridging vein & other:* Torn vein of Labbé, petrosal vein, and sylvian bridging vein	Subarachnoid hemorrhage AIS 3	Other serious injuries
27 y.o. female driver	1 o'clock	ΔV= 32 km/h	Left face and occiput to A-pillar and roof	Left frontal, parietal	*Bridging vein & other:* Bleeding from bridging vein and superficial cortical vein	None	Isolated

Table 2.9. CIREN cases with operative report documentation of bleeding adjacent to subdural hematoma from sources *other than bridging veins*

Age, Sex & Seat Position	Impact Direction (PDOF)	Severity	Head impact	SDH location	Adjacent Bleeding Source Identified in Operative Report	Other Serious Head Injuries	Accomp. injury category
76 y.o. female Driver (FATAL)	2 o'clock, (rotated to 3 o'clock by time of head impact)	BEV= 38 km/h	Right passenger door with right forehead	Bilateral (surgery on left)	Left temporal/parietal intracerebral hematoma	(Fatal) Right temporal hinge fracture AIS 4 Right white matter hemorrhage and left temporoparietal intracerebral hematoma AIS 4 Right subarachnoid hemorrhage AIS 3	Other serious injuries
23 y.o. male driver	10 o'clock	ΔV= 28 km/h	B-pillar with left head, seat with right head	Right temporal and along tentorium	Temporal and parietal surface contusions and bleeders	Right epidural hematoma AIS 4 Basilar and right vault fractures AIS 4 Hemorrhagic contusions under SDH AIS 4 Right subarachnoid hemorrhage AIS 3	Contusion
21 y.o. female driver	4 o'clock	ΔV= 26 km/h	B-pillar with right occiput	Left frontal/ temporal	Temporal bleeders and bruises with contusions	Bilateral cerebral swelling AIS 5 Subarachnoid hemorrhage AIS 3 Left frontal-temporal hemorrhagic contusion AIS 4	Contusion
76 y.o. female driver	10 o'clock	ΔV= 12 km/h	B-pillar with left side of head	Left parietal/ occipital	Small arterial bleeder on the brain surface	No other head injuries coded	Isolated
29 y.o. male driver	2 o'clock	ΔV= 44 km/h	A-pillar-handle with right head	Right convexity	Temporoparietal intracerebral hematoma with bleeders	Right parietal skull fracture AIS 4 Right cerebral edema AIS 3 Right intracerebral hematoma not coded	Other serious injuries
49 y.o. female driver (FATAL)	3 o'clock	ΔV= 44 km/h	Tree with right head and face	Left frontal/parietal/ temporal	Underlying hemorrhagic contusion	Cerebral hematoma/hemorrhage AIS 4 Fractures basilar skull, right vault and orbit AIS 3 Left subarachnoid hemorrhage AIS 3 Bilateral frontal lobe contusions AIS 3	Contusion

Table 2.10. Number of CIREN cases in each injury source category sorted by how they would have been categorized under AIS-based accompanying injury system used in NASS CDS analysis

		Bleeding Source (from operative report)		
		Bridging Vein	**Contusion**	**Other**
Categorized by AIS-based accompanying injury	**Isolated**	**2 cases**	**0**	1 case
	With Contusion	**0**	**3 cases**	0
	With Other Serious Injury	4 cases	0	2 cases

Of the CIREN cases, two of the three cases that would have been categorized as isolated using the AIS-based system were confirmed to be associated with bridging vein failure in the CIREN operative report (Table 2.10). All three cases that would have been categorized as "With contusion" using the AIS-based system were confirmed to be associated with contusion in CIREN records. This correspondence provides support for the use of isolated and with contusion injury categories as surrogate variables for subdural hematoma originating from bridging vein rupture and contusion, respectively. Of the CIREN cases that would have been categorized as with other serious injury by the AIS-based system, four were actually associated with bridging vein failure, and two were attributed to adjacent hematomas. Thus, the other serious injury category was not used as a surrogate variable for any specific bleeding source.

NASS CDS search results. In NASS CDS 1993-2008, there were 1,943 adult occupants coded with subdural hematoma, representing a weighted total of 105,980

cases. Among these, 46,907 cases were occupants age 20-49, 41,578 were age 50-69, and 17,494 were age 70 or older.

Accompanying head injuries. The percentage of adult subdural hematoma cases where there were also other serious head injuries documented are shown in Figure 2.9. The percentages for each age group sum to greater than 100% since each subdural hematoma case may have multiple accompanying serious head injuries.

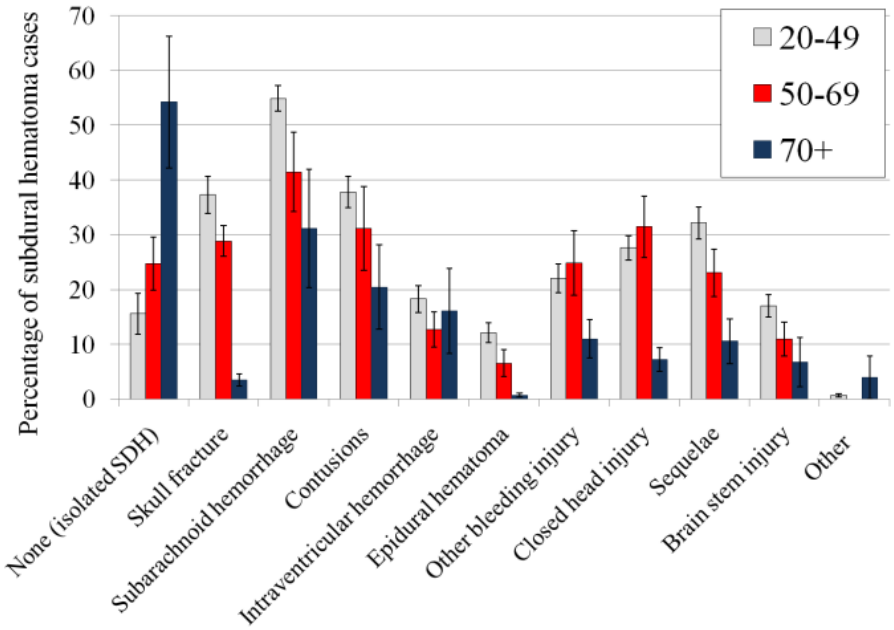

Figure 2.9. Percentage of subdural hematoma (SDH) cases in each age group where other serious head injuries are also present.
(SE shown by error bars.)

Among the youngest age group, 16% of those with subdural hematoma sustained no other serious head injuries. In the oldest age group, 54% of subdural hematoma cases were isolated. For adults in all age groups, subarachnoid hemorrhage and contusions were among the most common serious injuries to accompany subdural hematoma. For

those younger than 70, skull fracture and closed head injury were recorded in more than 25% of subdural cases. In contrast, among the oldest group of occupants with subdural hematoma, skull fractures were documented in fewer than 3% of cases and closed head injuries in fewer than 10% of cases. For the youngest age group, injuries in the sequelae category were also common.

Relative frequency of isolated subdural hematoma. The frequency of isolated subdural hematoma versus subdural hematoma with contusion or with other serious injury was compared for occupants by age group and sex (Figure 2.10) as a percentage of all subdural hematoma cases. The percentage of subdural cases that are isolated among younger occupants is similar for men (15%) and women (17%). Among older occupants, however, the percentage of subdural hematoma that are isolated among men increases to only 33% while for women isolated subdural hematoma make up 65% of all subdural cases.

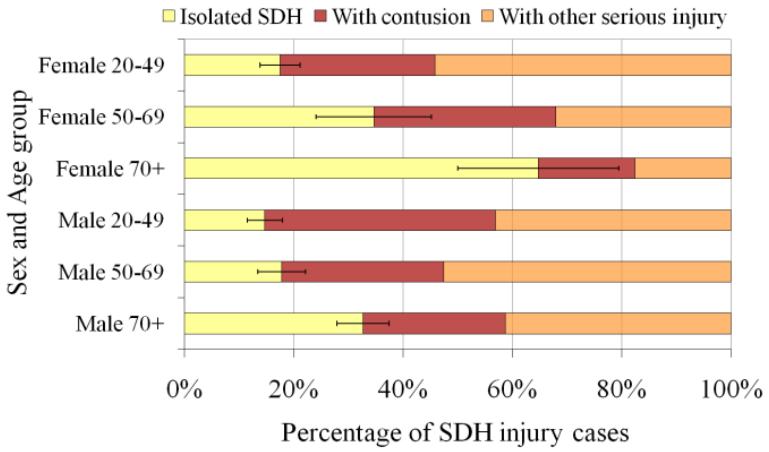

Figure 2.10. Percentage of SDH cases by sex and age group that are isolated versus with contusion or other serious head injury.
(SE shown for percentage of isolated only.)

The frequency of isolated subdural hematoma compared to subdural hematoma with contusion or subdural hematoma with other serious head injury is compared by crash impact direction in Figure 2.11. Of the vehicle impact directions, frontal impacts showed the highest percentage of isolated subdural hematoma, with over 30% of frontal subdural hematoma cases having no other serious head injuries.

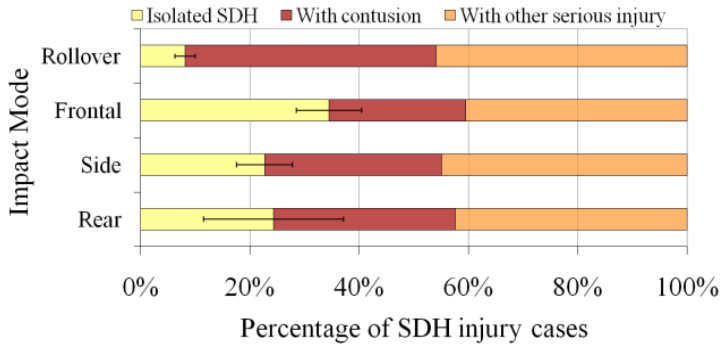

Figure 2.11. Percentage of SDH cases by impact direction that are isolated versus with contusion or other serious head injury.
(SE shown for percentage of isolated only.)

Broken down by head impact location where cutaneous or bone injuries were present, Figure 2.12 shows that cases with isolated subdural hematoma were more likely to be associated with evidence of only frontal contact while cases with contusion were more likely to have evidence of a head impact on the side, either alone or with frontal contact.

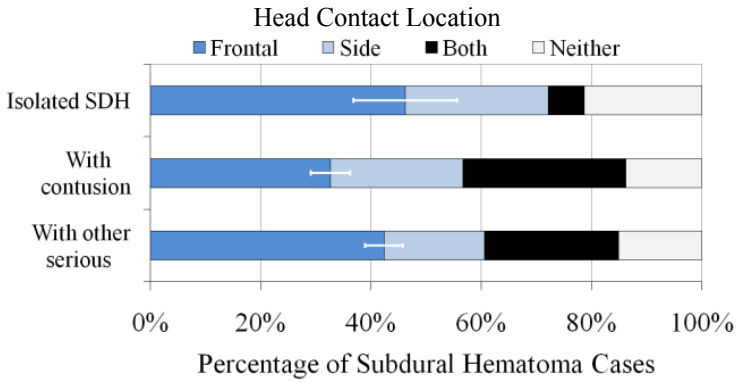

Figure 2.12. Percentage of SDH cases by accompanying injury category that have evidence of head contact location.
(SE shown for frontal cases only.)

For side impact cases with subdural hematoma, the vehicle impact direction was compared to the side of the subdural hematoma (Figure 2.13). Cases where the vehicle impact and subdural were on the same side were categorized as ipsilateral, and those on opposite sides were contralateral. Cases with isolated subdural hematoma were rarely bilateral (7%) compared to cases with subdural and contusion (41% bilateral) or subdural and other serious injury (32% bilateral). Isolated subdural hematoma were predominantly contralateral (69%). In subdural cases with contusion or other serious head injury, ipsilateral or contralateral subdural hematoma occurred with similar frequency.

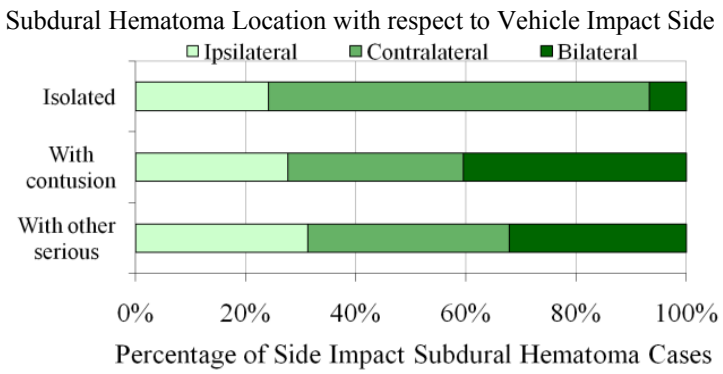

Figure 2.13. Percentage of side impact SDH cases by type (isolated versus accompanied by contusion or other serious head injuries) where SDH is ipsilateral or contralateral to vehicle impact side

Injury rate analysis. The rate of subdural hematoma injury goes up with age, regardless of whether the injury is isolated or in combination with contusion or other serious head injuries (Figure 2.14), but the increase in injury rate for occupants age 70 and older is especially dramatic for isolated subdural hematoma. The oldest group had a rate of isolated subdural hematoma that was 15 times higher than the rate of injury for younger occupants. For younger occupants, the rate of subdural hematoma in combination with contusion or other serious head injury is higher than the rate of isolated subdural hematoma. The opposite is true for older occupants, who are twice as likely to sustain an isolated subdural hematoma as one accompanied by contusion or other serious head injury.

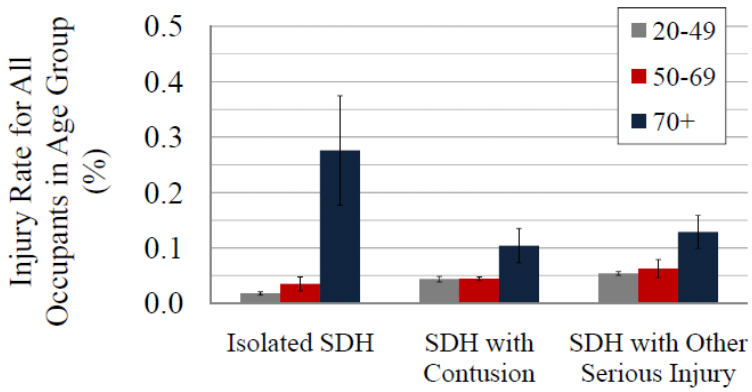

Figure 2.14. Injury rate for each type of SDH as percentage of all included occupants in all crash directions in each age group.
(SE shown by error bars.)

When injury rates are calculated by impact direction (Figure 2.15), the age-related increase in rate of isolated subdural hematoma is especially notable in frontal impacts, while side impacts show a consistent increase in all types of subdural hematoma for the oldest occupants. The rate of subdural hematoma with contusions is higher in side impact than in frontal impact for all age groups.

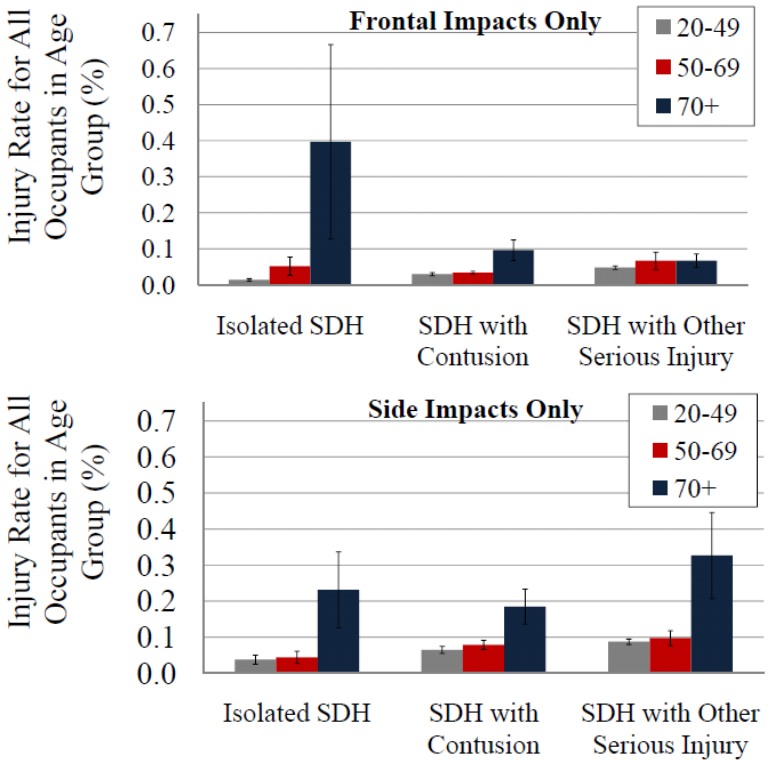

Figure 2.15. Injury rate for each type of SDH as percentage of all included occupants in frontal and side impact crashes.
(SE shown by error bars.)

Odds ratios. Odds ratios were calculated to compare the odds of sustaining either isolated subdural hematoma or subdural hematoma accompanied by contusion for the oldest age group compared to the youngest age group. Regression models developed using backward elimination for males and females in frontal impacts included the potential confounding variables ΔV, skull fracture, and occupant seat location (driver, front passenger or rear passenger). Models for side impact for both males and females additionally included the potential confounder of air bag deployment.

Table 2.11 shows the point estimate for each odds ratio for males and females and for impact direction separately. To compare odds of each type of injury for older

occupants versus younger adults, injuries that have a point estimate odds ratio greater than 1.0 and do not include 1.0 in the Bonferroni-corrected 95% confidence interval are shown in **bold** font to indicate significantly increased odds of injury for the older age groups. The resulting odds ratio for males in frontal crashes, for example, estimates that the odds of isolated subdural hematoma for an individual in the oldest age group were 11.4 times the odds of injury for a young adult *under the same conditions.* Since the entire confidence interval is greater than 1.0, this difference is significant at the 95% confidence level. As shown in Table 2.11, odds of injury for subdural hematoma are especially elevated for older occupants in frontal crashes. The age-related increases in injury odds in frontals are particularly notable for isolated subdural hematoma and for women.

Table 2.11. Odds ratios for types of SDH for 70+ age group compared to age 20 to 49. (Significant point estimates in bold.)

			Odds Ratio	95% CI
Frontal	**Male**	Isolated SDH	**11.4**	2.0 - 64.9
		With Contusion	**2.6**	1.03 - 6.7
	Female	Isolated SDH	**118.4**	11.9 - >999
		With Contusion	**11.5**	2.4 - 54.5
Side	**Male**	Isolated SDH	2.1	0.4 - 12.5
		With Contusion	2.4	0.7 - 7.8
	Female	Isolated SDH	4.5	0.7 - 30.4
		With Contusion	**3.9**	1.6 - 9.4

2.2.3 Discussion of Study of Subdural Hematoma in Older Occupants

Previously, the focus in subdural hematoma tolerance research has been on those originating from bridging vein failure. To begin to explore how tolerance to subdural hematoma changes with age, it needs to be determined whether bridging vein failure is the dominant injury mechanism for adults of all ages, or whether certain bleeding sources are particularly associated with the increase in subdural hematoma for older occupants.

Although autopsy and surgery studies have shown that subdural hematoma are commonly caused by bleeding from sources other than bridging veins (Jamieson and Yelland 1972; Maxeiner 1998), no large scale crash data set includes bleeding source information for subdural hematoma to evaluate the proportion of motor vehicle crash subdural hematoma cases that are caused by bleeding sources other than torn bridging veins for different age groups.

CIREN results. The current analysis of the CIREN database revealed a small number of cases where surgical reports documented adjacent bleeding that was identified as the probable source of bleeding in each case. Subdural hematoma cases in CIREN were associated with surface contusions, intracerebral hematoma, and bleeding vessels on the surface of the brain as well as with bridging vein bleeding (Table 2.8 and Table 2.9). The results of the CIREN search were consistent with previous studies that showed that subdural hematoma was not exclusively associated with bleeding from bridging veins and that subdural hematoma from non-bridging vein sources were relatively common in motor vehicle crashes (Jamieson and Yelland 1972; Maxeiner 1998).

Although review of the CIREN cases showed that bleeding sources other than bridging veins can contribute to subdural hematoma, that database has too few cases with documentation on bleeding sources to analyze the distribution of age or crash conditions among cases originating either with bleeding from the bridging veins or from other bleeding sources.

Comparison of probable bleeding source by categories in CIREN and NASS CDS analyses. In contrast to CIREN, NASS CDS has a large number of occupants coded with subdural hematoma, but no detailed medical information to specifically attribute those injuries to individual sources of bleeding. Therefore, the current study used available information on accompanying head injuries in NASS CDS to categorize the cases according to other serious head injuries present. In the absence of specific information on bleeding sources in cases coded with subdural hematoma, the accompanying injuries were used as surrogate variables for potential bleeding sources for the subdural hematoma in each case.

CIREN cases were used to evaluate the suitability of categorizing NASS CDS occupants into isolated subdural hematoma cases and subdural hematoma cases with contusion as surrogate variables for bridging-vein sourced subdural cases and contusion-sourced subdural hematoma cases, respectively. The CIREN cases with documented probable bleeding sources were reviewed and sorted by the same categories used in the NASS CDS search based on AIS codes (Table 2.10). The objective was to confirm whether the information drawn from AIS codes was consistent with the more detailed information available in operative reports. A good match would support use of the AIS-

based categories as surrogate variables for probable bleeding source in NASS CDS which has no narrative injury detail.

Of the three CIREN cases that would have been classified as isolated from the categories used in the NASS analysis, two were indeed associated with bridging vein failure and one with a torn artery on the surface of the brain. Of the three cases that would have been classified as subdural with contusion, all three were associated with a contusion in the operative report. Among the six cases that would have been classified as subdural with other serious injury, operative reports indicated that two were associated with intracerebral hematoma, and four were associated with bridging vein failure or bridging vein failure as well as failure of other surface veins. This comparison suggests that cases categorized as isolated subdural hematoma are more likely to be associated with bridging vein rupture than with other sources and that cases in the subdural hematoma with contusion category are more likely to be from contusions than from bridging veins or other sources. The other serious head injury category may contain cases caused by bridging vein rupture or from bleeding sources on the surface of the brain. Therefore, although the injury categories used are only surrogates for variables describing the original source of bleeding, it is reasonable to use the trends in the isolated subdural hematoma and the subdural hematoma with contusion categories to approximate trends between cases where the subdural hematoma was produced by bridging vein bleeding versus by brain contusions, respectively. Since the true source of subdural bleeding is not available in NASS CDS or any other large-scale crash database, these data represent the best available estimate.

NASS CDS results. Based on the assumption that the injury categories used are reasonable surrogate variables for bleeding source for subdural hematoma, the increased tendency for older occupants to sustain isolated subdural hematoma (Figure 2.9) potentially reflects an increased frequency of subdural hematoma caused by bridging vein damage. Although the rate of subdural hematoma increases with age, regardless of accompanying injuries (Figure 2.14), cases with isolated subdural hematoma are 15 times more frequent among those aged 70 and older than among adults younger than 50. In comparison, subdural hematoma with contusion or other serious injury is only about 2.4 times as frequent among the oldest group compared to the youngest group.

The age-associated increase in isolated subdural hematoma is especially prominent for women and in frontal impacts (Table 2.11). Although isolated subdural hematomas make up about the same proportion of subdural hematoma cases in women and men in the age 20 to 49 age group (15% and 17% respectively), subdural hematoma in the 70 and older age group are isolated in 65% of female cases but only 33% of male cases (Figure 2.10). Subdural hematoma is isolated in 34% of cases sustained in frontals, compared to 23% of cases in side impacts (Figure 2.11). For the oldest age group, the injury rate for isolated subdural hematoma in frontals is almost twice that in side impacts (Figure 2.15). These results suggest that the age-related increase in bridging vein-associated subdural hematoma may especially affect women and those in frontal impacts.

Odds ratio analysis (Table 2.11) shows that the age-related increase in subdural hematoma in frontal crashes is present even after accounting for variables related to crash

and head impact severity (ΔV, air bag deployment, skull fracture), especially for isolated subdural hematoma, and for women.

Assuming that isolated subdural hematomas are most likely to be associated with bridging vein bleeding, the current findings that the age-related increase in isolated subdural hematoma may be more frequent in frontal impacts are consistent with studies that have linked anterior-posterior motion to bridging vein failure (Ommaya, Faas et al. 1968; Löwenhielm 1974; Gennarelli and Thibault 1982; Depreitere, Van Lierde et al. 2006) and consistent with the explanation that older individuals are more prone than younger individuals to subdural hematoma by bridging vein failure due to the increased relative brain motion and bridging vein tension induced by atrophy in the aging brain (Yamashima and Friede 1984; Meaney 1991; Kleiven and von Holst 2002).

The case conditions for the subdural hematoma cases with contusion in the current study were compared to previous findings on cases with subdural hematoma with contusion (Maxeiner 1998), or caused by bleeding sources that were intracerebral or on the surface of the brain rather than by bridging vein failure (Jamieson and Yelland 1972). In Jamieson and Yelland, the subdural hematoma cases with intracerebral or surface bleeds were more common among males. In the current study, subdural hematoma were accompanied by contusion more often among men than women, especially for *young* males under age 50 who sustained contusion with subdural hematoma more than twice as often as they sustained isolated subdural hematoma (Figure 2.10). Jamison and Yelland also reported that subdural hematoma caused by intracerebral or surface bleeding was *less* common for adults over age 60. In the current study, although the injury rate for

subdural hematoma with contusion increases for older occupants (Figure 2.14), the proportion of subdural hematoma that were accompanied by contusions decreased with age: only 20% of subdural cases among those age 70 and older were associated with contusion, compared to 38% of subdural cases for adults under age 50 (Figure 2.9). The reason for the reduction in the proportion of subdural injuries with contusion is that the age-related increase in rate of isolated subdural hematoma outpaced the age-related increase in rate of subdural hematoma with contusion. In previous studies, subdural hematomas associated with sources other than bridging veins were more frequently from lateral impact than those associated with bridging veins. In Jamieson and Yelland, 55% of complicated subdural hematoma cases were from lateral head impacts, while only 32% of isolated subdural hematoma cases were from lateral head impacts. Maxeiner reported 44% of subdural hematoma associated with contusion were confirmed to involve lateral head impacts while only 12% of bridging vein subdural hematoma were lateral head impacts. In the current study, 29% of cases with contusion were lateral vehicle impacts compared to 23% of isolated subdural hematoma cases which were lateral vehicle impacts.

Overall, the crash conditions most often associated with isolated subdural hematoma are different from those associated with subdural hematoma combined with contusion. While the rates of both types of subdural hematoma increased with age, the age-related increase is greater for isolated subdural hematoma, especially among women. For the oldest group of occupants, the rate of isolated subdural hematoma is almost twice as high in frontals as in side impacts, while subdural hematoma with contusions occur at

a higher rate in side impacts than in frontals for all age groups. Isolated subdural hematoma occur bilaterally in only 7% of cases, compared to subdural with contusion cases which are bilateral in 41% of cases (Figure 2.12). Among the isolated subdural cases, the hematoma is contralateral to the vehicle impact side in 69% of cases, while contralateral subdural hematoma are documented in only 32% of subdural cases with contusion (Figure 2.13). These differences between cases with isolated subdural hematoma and subdural hematoma combined with contusion support that these two injury categories are representative of two different patterns of injury. Assuming that these injury categories generally correspond to subdural hematoma caused by bridging vein failure and subdural hematoma caused by contusions or other bleeding sources, the results suggest that the mechanism of injury for these two types of subdural hematoma may be quite different.

The types of motion and loading required to produce subdural hematoma from bleeding sources on the surface of the brain have not been addressed. Although bleeding from cortical contusions or ruptured cortical vessels into the subdural border cell region would only be possible with rupture of the arachnoid, the loading required to produce this combination of bleeding injury and arachnoid damage has not been explored experimentally, nor have the effects of age on this process been explored. Research on the tolerance of occupants of all ages to subdural hematoma would benefit from a better understanding of the mechanism of subdural hematoma from sources other than bridging veins.

Older occupants appear to be particularly vulnerable to isolated subdural hematoma, which suggests that the increase in subdural hematoma rate in older occupants may be more dependent on decreased tolerance to subdural hematoma associated with bridging vein failure than to those associated with other bleeding sources. Further research on how tolerance to bridging vein failure changes with age may explain and help to quantify the increase in incidence of subdural hematoma among older occupants.

2.3 Summary and Implications of Epidemiological Studies

Motor vehicle crash data shows that older head injury victims are more likely to sustain bleeding injuries than younger head injury victims (Mallory 2010). In particular, the rate of extra-axial injury appears to increase with age, and is substantial for occupants as young as those in their 50's. The increase in extra-axial injury rate with age is especially prominent in relatively low-severity crashes, which represent the majority of all crashes.

Subdural hematoma is of primary importance among the extra-axial bleeding injuries that have increased odds of injury for older occupants because of the combination of increased incidence and previously-reported increase in mortality for those as young as the 50s decade.

The increase in the rate of isolated subdural hematoma with age among adult crash occupants potentially reflects an increase in the frequency of subdural hematoma caused by bridging vein bleeding (Mallory, Herriott et al. 2011). This age-related increase is especially notable among women and in frontal impacts.

The results of these epidemiological studies provide the motivation for the experimental work described in this dissertation. Specifically, the results suggest that exploration of the mechanism of subdural hematoma in older crash occupants is needed to define age-adjusted injury tolerance and to develop head injury countermeasures for older occupants. Determination of age-specific injury tolerance for subdural hematoma will require evaluation of the increasing risk of bridging vein failure in older occupants, specifically focusing on the increased potential for stretch of the bridging veins for older individuals in anterior-posterior head motion.

Additionally, the epidemiological results suggest that the head loading required to produce subdural hematoma from bleeding sources other than bridging veins may differ significantly from the loading needed to produce subdural hematoma associated with bridging vein failure. Given the frequency of subdural hematoma from non-bridging-vein sources among occupants younger than 70, future research is also needed on the mechanism of subdural hematomas that result from contusions and vessels on the surface of the brain.

Chapter 3: Preliminary Study on the Application of B-Mode Ultrasound to Measure High-Speed Tissue Displacement

The development of high-frequency Brightness-mode (B-mode) ultrasound has led to increases in frame rate (temporal resolution) that offer opportunities for imaging high-speed motion. In the field of injury biomechanics, where an understanding of tissue dynamics in high-rate loading is essential to understanding injury mechanism and tolerance, high-frequency ultrasound is a potentially valuable new tool. Two-dimensional B-mode ultrasound was selected as the measurement method for the current study because of its ability to image the meninges and peripheral brain non-invasively without breaching the dura. Additionally, B-mode ultrasound has the potential to collect images at a high enough rate to allow tracking of motion in impact-level head motions, with sufficient resolution to observe individual tissue layers. However, B-mode ultrasound had not been previously used to track tissue motion in injury biomechanics and needed to be evaluated for its effectiveness in high-speed, relatively large-displacement testing. The primary objective of this preliminary study was to evaluate the potential of B-mode ultrasound for motion tracking of the meningeal tissues and peripheral brain during rotation testing and to define the limitations of this experimental approach in terms of the tissue motion that could be effectively tracked and measured. Secondarily, the results of this preliminary study were used to evaluate the potential use

of high-frequency B-mode ultrasound in high-speed, large displacement tissue testing in injury biomechanics research more generally.

3.1 Distortion of High-speed Motion and Proposed Correction Method

Current clinical B-mode ultrasound technology typically uses frequencies of 2-20 MHz. In contrast, current high-frequency ultrasound technology uses frequencies up to 70 MHz. Because such high frequencies are heavily attenuated and do not penetrate deeply, the time between image lines can be reduced, leading to reduced image refresh time and increased frame rates in an image sequence.

However, very high frame rates necessitate a narrow horizontal or lateral field of view across the width of the image, as well as a shallow vertical image height (Figure 3.1), and these limitations need to be considered when determining potential use of B-mode ultrasound in high-speed, large-displacement testing. Additionally, the sequential line-by-line nature of the construction of conventional 2-dimensional B-mode images necessarily means that image lines on the leading edge of the image are produced earlier in time than image lines on the trailing edge of the image. As a result, images are expected to be temporally distorted, showing features on one side of the image frame at a different point in time than the features captured on the other side of the frame. This distortion must be accounted for to analyze tissue motion quantitatively.

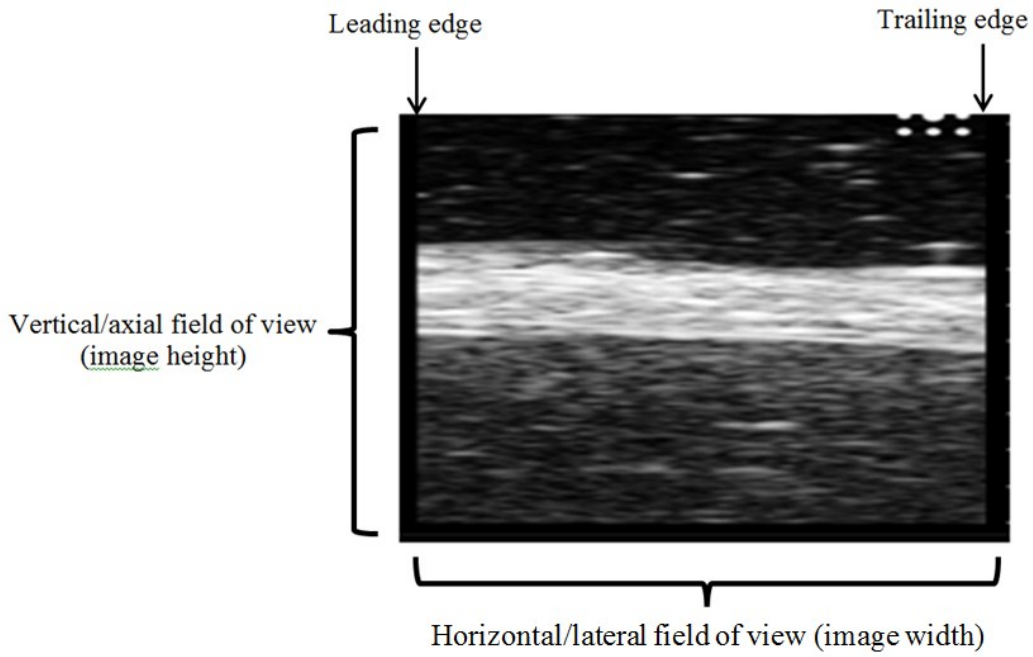

Figure 3.1. Ultrasound image frame illustrating field of view.

To analyze tissue motion, the position-time history of individual points needs to be known, i.e. the position of the imaged points in the tissue has to be identified at known points in time. While the time at which the ultrasound image frame was started or completed can be calculated from the image sequence frame rate, determining the precise time at which a given tissue point was imaged also requires knowing when each line of the image was produced during the formation of the image.

Because each vertical line of the ultrasound image is constructed sequentially as every transducer across the array sends and receives ultrasound signal, it is hypothesized that the true time at which each point in the ultrasound image is captured can be calculated as a function of its position across the width of the image. If each line of the image is constructed at a time proportional to its lateral position across the ultrasound

array, the true time at which a given point was imaged in a frame can be calculated. A method for calculating the true time for each point imaged was proposed and evaluated in this preliminary study in order to account for the temporal distortion in uncorrected ultrasound images. In order to effectively use B-mode ultrasound in the analysis of high-speed, large-displacement tissue tests, the proposed method for adjusting for temporal image distortion to calculate the position-time history of individual points in a tissue image sequence needs to be validated under test conditions with known tissue motion. In this preliminary study, the accuracy of the proposed algorithm for analyzing tissue motion was evaluated and the limitations on the motion that can be analyzed using these methods were explored.

3.2 Experimental Methods for Preliminary Study

Motion testing with samples of *post mortem* human cranial dura was performed to compare ultrasound-tracked motion of the tissue with measured kinematics of the tray on which the tissue was mounted.

3.2.1 Sample Preparation

Post mortem human cranial dura was obtained through the Anatomy Body Donation Program at the Ohio State University. Dura was harvested from a human autopsy subject at 8 days *post mortem*. The sample had not undergone freezing or preservation. All testing was complete within 6 hours of harvest. *Post mortem* human tissue testing was performed with the approval of the Ohio State University Institutional Review Board.

An aluminum tray was prepared for the specimen with a well (25x825x12.5 mm) for ultrasound gel. An ultrasound gel pad, trimmed to fit, extended 1 to 2 mm above the surface of the tray and additional gel was spread over the surface of the gel pad (Figure 3.2). The dura sample was fixed to the aluminum tray using cyanoacrylate around the periphery of the well, and the dura edges trimmed with a scalpel. The prepared sample was covered with saline-soaked toweling until tested.

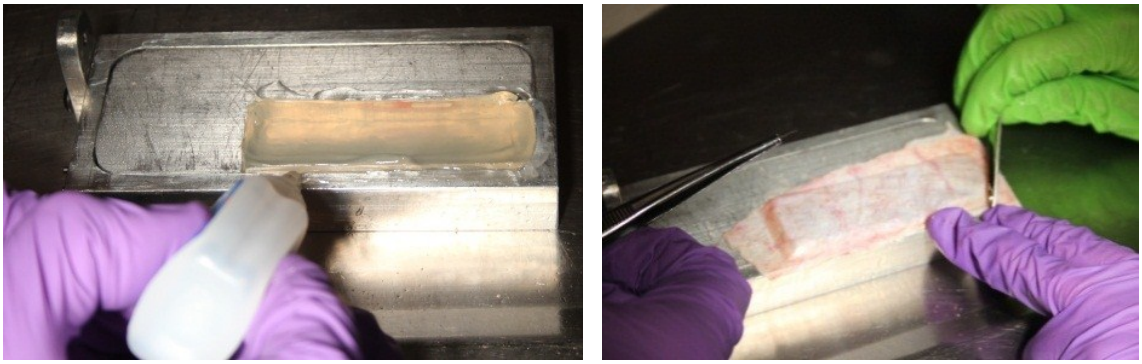

Figure 3.2. Preparation of tray-mounted sample of cranial dura.

Motion setup. The tray on which the dura sample was mounted was accelerated along an aluminum track using a slingshot-powered mass (Figure 3.3). The velocity of the 423 gram mass was varied by modifying its initial position, the number of elastic bands used, and the mounting location of the elastic bands. The mass accelerated the tray up to speed before the motion of the mass was arrested by contact with the track base, allowing the tray to continue along the aluminum track. The sliding tray was brought to a stop by friction and by a rubber brake-stop after approximately 65 mm of tray travel. Target tray velocity was 0.2 to 2.0 m/s.

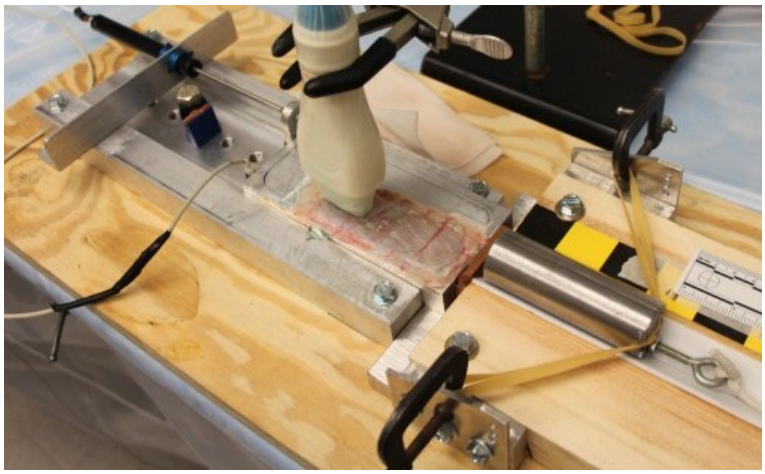

Figure 3.3. Dura sample mounted to sliding tray.

3.2.2 Kinematics Instrumentation

Kinematic data was collected using a DTS G5 data acquisition system (*DTS, Seal Beach, California, USA*). Tray displacement with respect to time was measured using a linear potentiometer (Servo Model 08TC1-2778, Baraboo, Wisconsin, USA) mounted to the tray and to a stationary mount on the track fixture. An Endevco 7264 linear accelerometer (Meggitt Sensing Systems, San Juan Capistrano, California, USA) was also mounted to the tray.

Kinematic data was collected at 20 kHz, and processed using DIADEM 2012 data analysis software (National Instruments, Rockville, Maryland, USA). Offset was removed before filtering displacement and acceleration data with a Channel Frequency Class (CFC) 180 filter, defined in the Society of Automotive Engineers (SAE) standard J211 as a digital Butterworth low-pass filter with a 3 dB limit frequency of 300 Hz (SAE 2007). Acceleration was integrated to calculate a velocity time history.

3.2.3 Ultrasound Data Collection

B-mode ultrasound images were collected using a Vevo 2100 Imaging System (VisualSonics Inc., Toronto, Ontario, Canada) with an MS550D ultrasound probe at 40 MHz. Images were collected at a frame rate of 865 frames per second with a vertical or axial image height of 10 mm and a lateral image width of 4.08 mm. Image resolution was 40 μm axially and 80 μm laterally at the geometric focus. Sensor spacing was 55 μm for 74 transducers across the ultrasound array, resulting in 74 image lines.

The ultrasound probe was fixed in a stationary position over the dura sample with the ultrasound array parallel to the tissue direction of motion, using ultrasound gel as a surface medium. Tests were performed with the ultrasound probe in two configurations. Tests with the transducer array sequence direction aligned with the direction of tissue motion will be referred to as *co-directional* and with the transducer array sequence in the opposite direction as the tissue motion will be referred to as *contra-directional*.

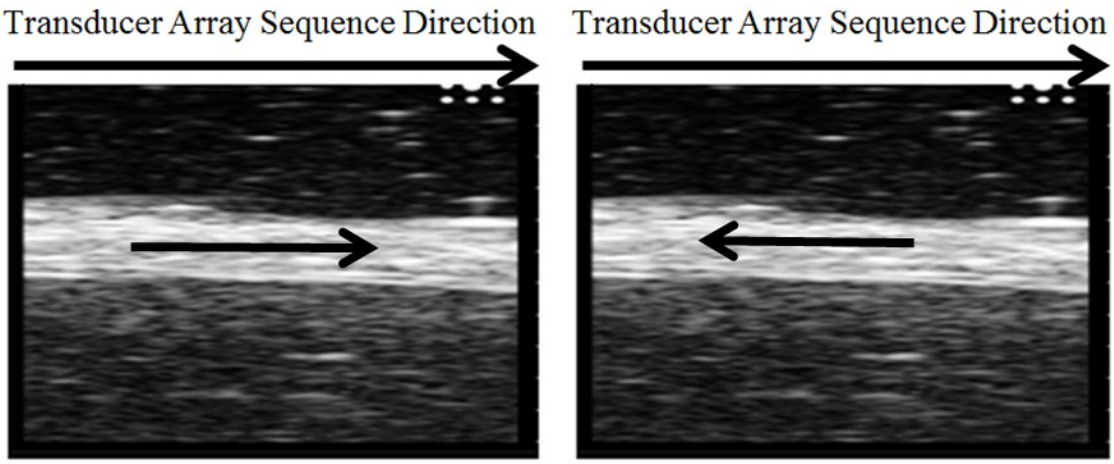

Figure 3.4. Tissue motion aligned with direction of transducer array sequence is co-directional (left) and in opposite direction to transducer array sequence is contra-directional (right).

3.2.4 Ultrasound Data Analysis

Image scaling. The VevoStrain post-processing utility for the Vevo 2100 was used to determine dimensional scaling for the B-mode images. Using the FreeCurve tool in VevoStrain, arbitrary motion points on the dura were selected for analysis and the exported data file included the image scaling factor in mm/pixel.

Image conversion. Vevo 2100 cine-images were exported as DICOM image files and converted to avi image format using Philips DICOM Viewer (Philips, Best, The Netherlands, Version R2.6L1-SP1). The converted video files of each motion test were analyzed using TEMA Version 3.7 image analysis software (Image Systems, Linköping, Sweden). In TEMA, the manual scaling factor was set to the VevoStrain-determined scaling factor. The scaling factor was confirmed for each test image sequence by using TEMA to measure the width of the image to check that its scaled width matched the nominal collection width of 4.08 mm.

Motion tracking. Motion tracking was performed with semi-automated point registration in TEMA. Tissue features were identified manually and semi-automated tracking in subsequent frames was performed with the "correlation" tracking setting in TEMA. The co-ordinate system was defined with x representing lateral position across the width of the frame of the image and y representing vertical or axial position in the image.

Images collected in the co-directional configuration, where tissue motion was in the same direction as the sequence of ultrasound sensors across the transducer array, resulted in left-to-right motion of tissue in the frame of the B-mode image sequences (Figure 3.5). Images collected in the contra-directional configuration, where tissue motion was in the opposite direction as the sequence of ultrasound sensors across the transducer array, resulted in right-to-left motion of tissue in the frame of the B-mode video images. For both relative directions of tissue motion, tissue motion was tracked starting with the frame immediately before motion could be detected, which was defined as frame number 0.

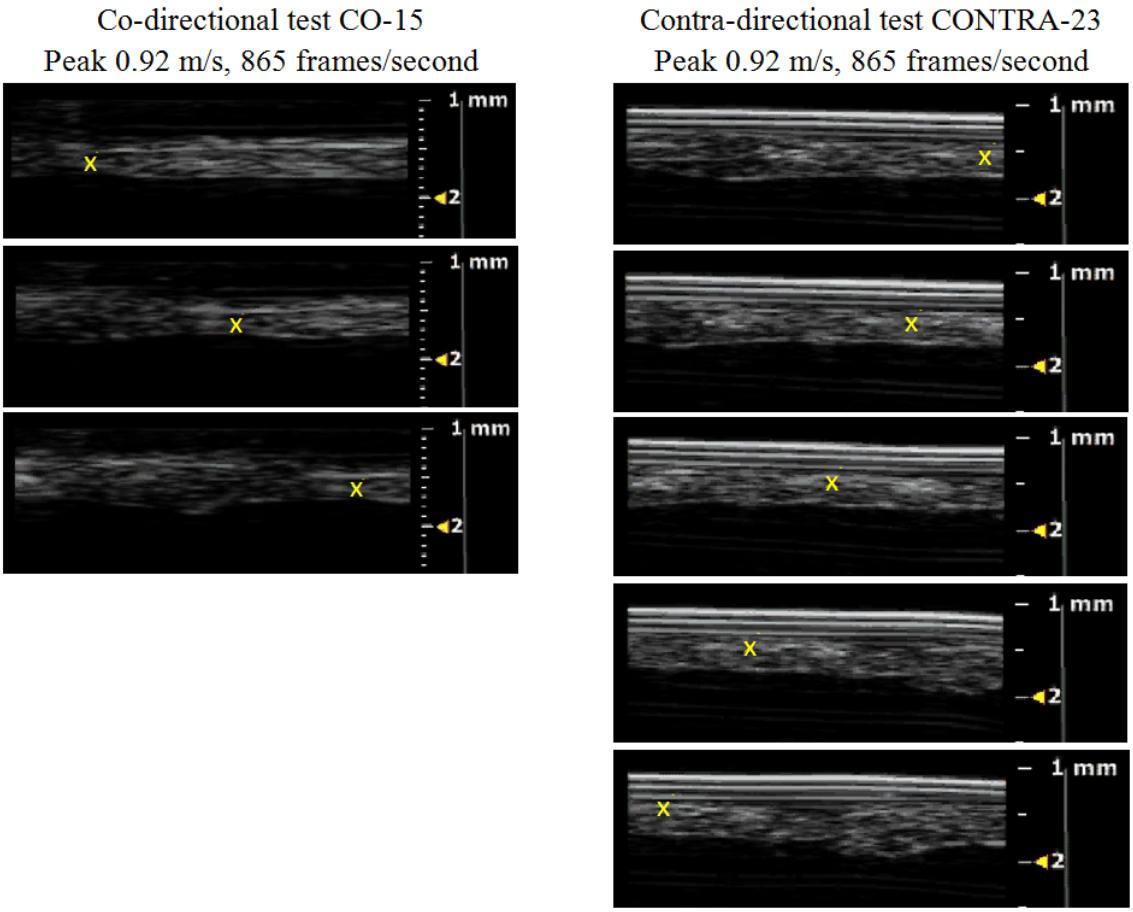

Figure 3.5. Tracking of consecutive frames in co-directional and contradirectional tests.

For tracking of motion in co-directional tests, tracking targets were placed on features in the dura near the left edge of the frame. As each point moved across the image in subsequent frames, TEMA was used to track the x-y co-ordinates of each point. When a point reached the right edge of the image, tracking was manually suspended. Each tracked point was confirmed by the operator for each frame. Similarly for tracking of motion in contra-directional tests, in each frame points were initially placed at the right edge of the image, tracked by TEMA as they moved across the image in subsequent frames, and disabled when they reached the left edge of the image.

For each test, x and y coordinates for each tracked point were exported by image sequence frame number, starting with frame 0. All remaining analysis and correction of the exported ultrasound co-ordinate data was performed using Matlab R2012 (The MathWorks Inc., Natick, Massachusetts, USA). Start timing was applied to each frame number *i*, calculated as shown in Equation 3.1 with frame rate (FR) in seconds^{-1}. The inverse of frame rate is the frame period (T), or the length of time it takes to construct one entire image. For the current series of tests in this preliminary study, FR was 865 seconds^{-1} so that the frame period T was 1.156 milliseconds.

$$Frame\ start\ time\ (frame\ i) = t_{Start(i)} = (i) \times \frac{1}{FR} \tag{3.1}$$

Proposed method for calculation of true point time. Since each vertical line of the ultrasound image is constructed sequentially as each transducer across the array sends and receives ultrasound signal, the image does not reflect the true position of all points visible in the frame at the frame start time. If the image is formed over time period T, then points at the leading edge of the image are imaged first near the beginning of time period T and points at the trailing edge of the image are formed near the end of the time period T. Therefore, it is proposed in Equation 3.2 that the true time at which point j is imaged in frame i (t_{ij}) can be calculated as a function of a point's lateral position in the image frame. Since each image is constructed from a number of sequential vertical image "lines" across the image width, that lateral position in the image width corresponds to the line number (n_{ij}) in which point j is imaged in frame i (Equation 3.3). Thus,

$$t_{ij} = t_{Start(i)} + \frac{1}{FR} \times \left(\frac{n_{ij}}{N}\right) \quad (3.2)$$

$$n_{ij} > \frac{x_{ij}}{x_{width}} N \quad (3.3)$$

where:
N is the total number of vertical image lines used to construct the entire image,
n_{ij} is the lowest integer that satisfies the given inequality
x_{ij} is the lateral "x" position of point j in image i, and
x_{width} is the full lateral width of the image (4.08 mm in current test series)

Estimation of cumulative displacement. Since it could be assumed for this validation testing that the dura fixed to the sliding tray moved as a rigid body, the position-time history of the tray-mounted dura was tracked during the entire time-period of the motion by summing the displacement calculated throughout the motion sequence. The initial position assigned to each point in the first frame in which it was tracked was estimated from the total displacement of the tissue up to that time. For points tracked from time 0 (i.e. the frame immediately before motion starts), the initial position was set to 0 mm. For all subsequent tracked points that appeared in the ultrasound image in frames after motion started, initial displacement was estimated based on the cumulative motion of the tissue up to that time. That cumulative displacement was interpolated from a time-displacement curve based on all points tracked previously. The time-displacement curve of all previously-tracked points was curve-fit using the Matlab weighted linear least-squares "loess" smoothing function, which uses local regression on a quadratic model.

3.3 Results of Preliminary Study

Twelve tests were conducted in each of two configurations. The co-directional configuration resulted in rightward motion of tissue in the frame of the B-mode video images. In the contra-directional configuration, where the probe was rotated 180 degrees, the tissue motion was toward the left in the B-mode images.

3.3.1 Tray Kinematics

For co-directional tests, tray time-displacement history from the linear potentiometer and time-velocity history from integrated acceleration results are shown in Figure 3.6. Peak tray velocity in co-directional tests ranged from 0.2 to 1.1 m/s. Displacement and velocity time histories for contra-directional are shown in Figure 3.7. Peak tray velocity in contra-directional tests ranged from 0.3 to 2.3 m/s. In lower-speed tests, the tray was slowed by friction before reaching the rubber stop. In higher-speed tests, when the tray traveled as far as the rubber stop, the tray bounced back from the stop, resulting in negative velocity. Peak tray velocity for each test is in the legends of Figure 3.6 and Figure 3.7.

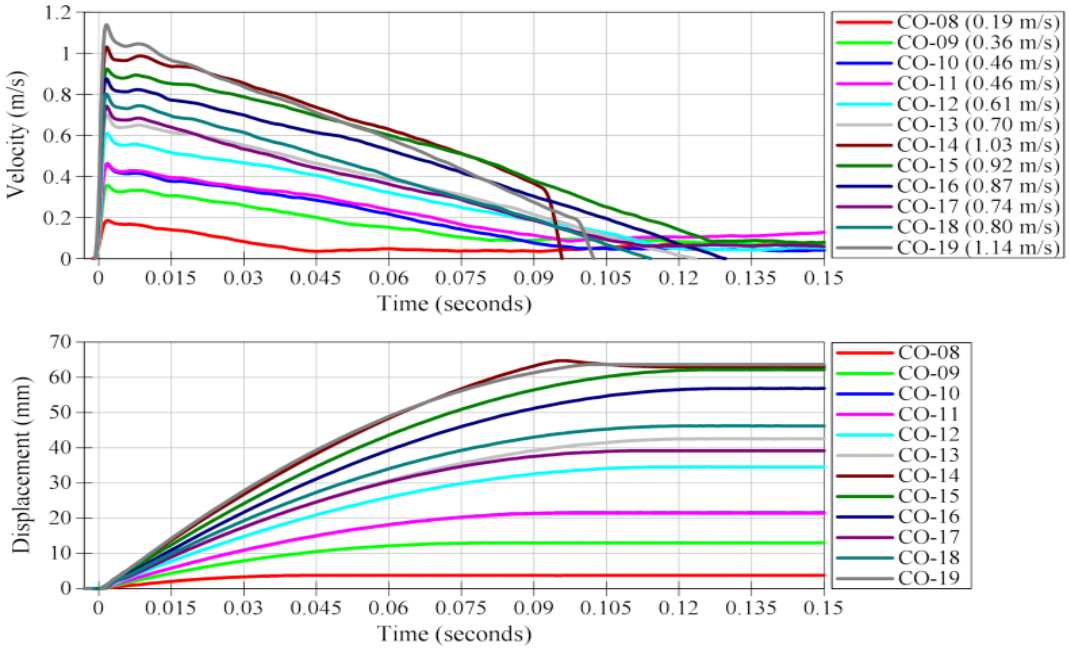

Figure 3.6. Co-directional motion time history of the tray: velocity (peak velocity listed in legend) and displacement.

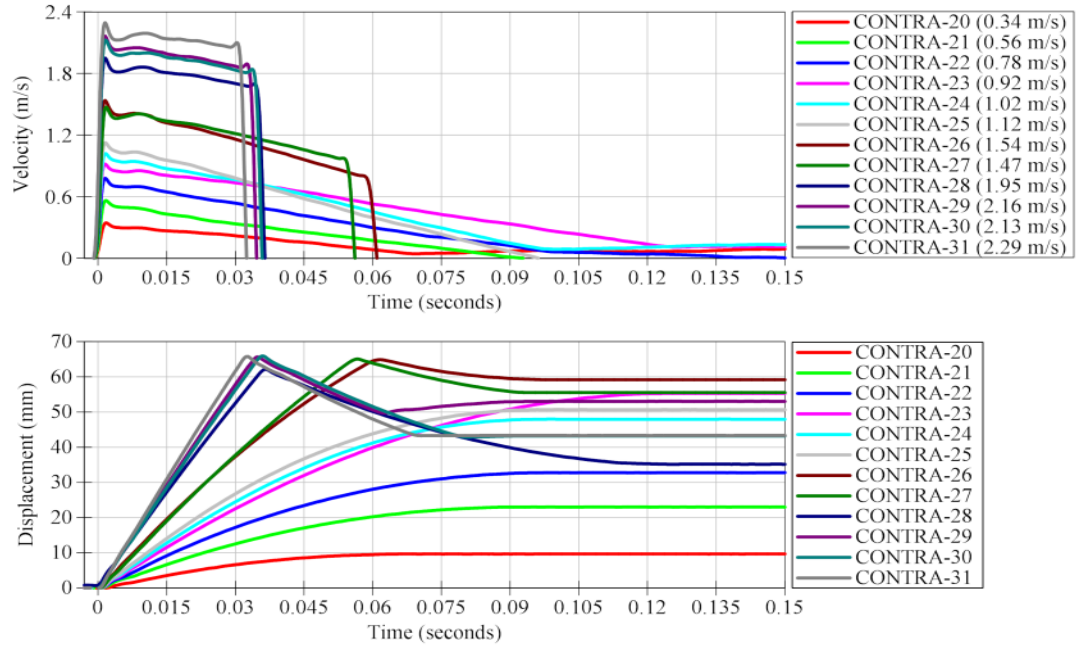

Figure 3.7. Contra-directional motion time history of the tray: velocity (peak velocity listed in legend) and displacement.

3.3.2 Ultrasound Motion

Using the ultrasound image scale factor, determined by the VevoStrain Analysis measurement utility in the Vevo 2100 software, the resulting scaled width of the processed images was within 0.001 mm of the nominal image width of 4.08 mm. Tissue motion was tracked for each trial using semi-automated tracking. Trackable ultrasound images were not collected for tests CONTRA-28 and CONTRA-29 so no further analysis was performed on either of these tests.

Figure 3.8 and Figure 3.9 show examples of tissue motion analysis results for co-directional test CO-12 and contra-directional test CONTRA-22. Both uncorrected and corrected displacement time histories for the tracked ultrasound results are compared to the displacement time history measured using the tray-mounted potentiometer in the same test. For the uncorrected displacement-time history, the cumulative displacement of each tracked point was plotted versus the frame start time ($t_{Start(i)}$). The corrected displacement-time history plots cumulative displacement of each tracked point versus its true point time (t_{ij}) calculated using Equation 3.2.

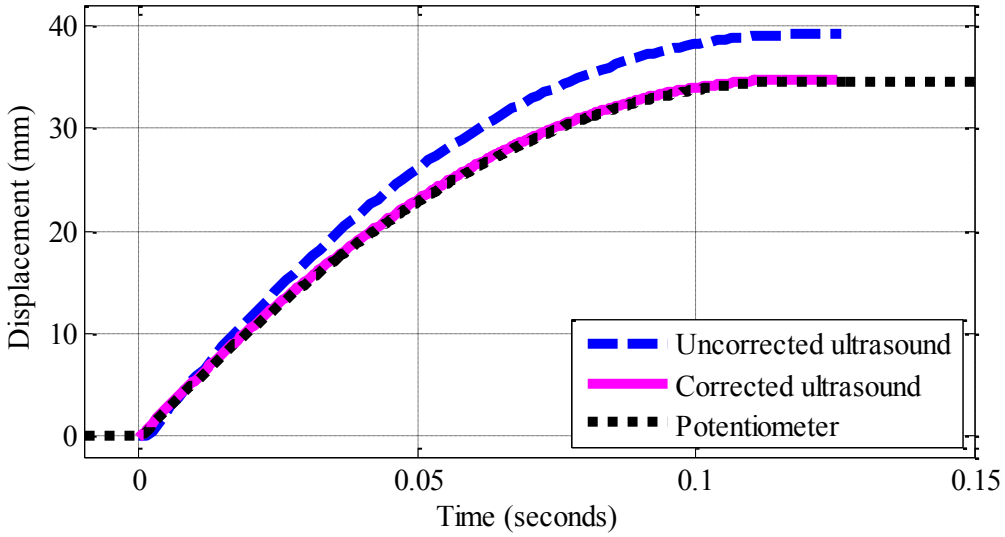

Figure 3.8. Co-directional motion test CO-12, comparison of time-corrected displacement of tissue to potentiometer measured displacement-time history and to uncorrected tissue displacement.

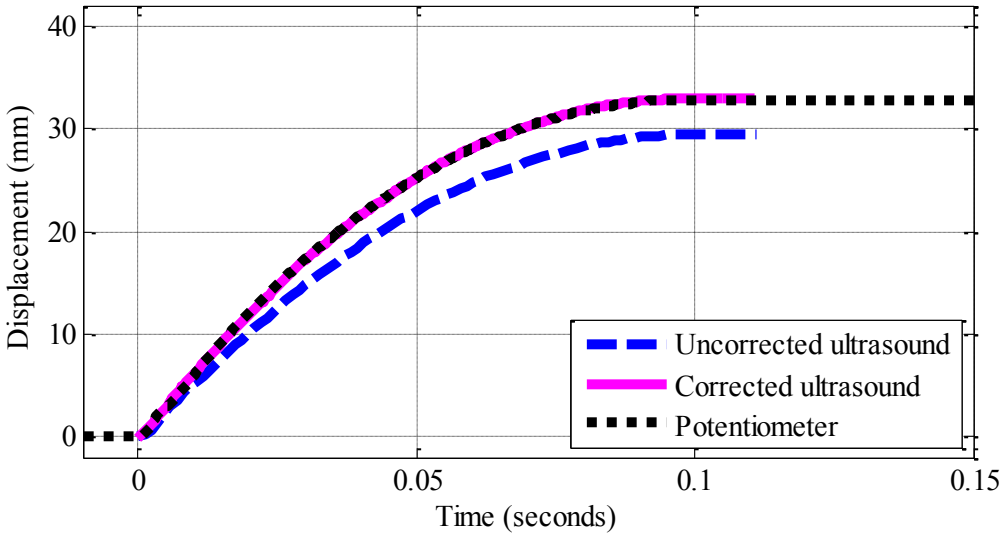

Figure 3.9. Contra-directional motion test CONTRA-22, comparison of time-corrected displacement of tissue to potentiometer measured displacement-time history and to uncorrected tissue displacement.

In co-directional test CO-12, the total cumulative displacement of the tray was 34.6 mm when it came to a stop at 0.12 seconds. Cumulative displacement estimated by uncorrected ultrasound tracking of points on the tissue *overestimated* the total displacement by 4.5 mm, while the corrected estimate using the corrected true time t_{ij} proposed in Equation 3.2 resulted in a displacement estimate within 0.20 mm of that measured by the linear potentiometer. In contra-directional test CONTRA-22, the total cumulative displacement was 32.8 mm at 0.11 seconds. Uncorrected ultrasound tracking *underestimated* the total displacement by 3.4 mm, while the corrected estimate using the true point time was within 0.15 mm of the measured displacement. Estimated total cumulative displacement calculated from ultrasound image tracking with, and without, correction is compared to direct measurement of tray displacement in Table 3.1 and Table 3.2 for all tests in which motion was tracked. Without correction, calculated displacement of the dura overestimated measured tray displacement in co-directional tests by 8 to 30% and underestimated tray displacement in contra-directional tests by 1 to 42% for an overall mean difference from measured displacement of 16.8%. With correction for true point time, calculated displacement of the dura was within 0.4 to 5% of the measured displacement (mean 2.0%).

Table 3.1. Cumulative displacement of dura by direct measurement of tray displacement and calculated in co-directional tests using ultrasound methods
(Bracketed value is percentage difference from direct measurement)

	CO-08	CO-09	CO-10	CO-11	CO-12	CO-13	CO-14	CO-15	CO-16	CO-17	CO-18	CO-19
Direct Measurement (mm)	3.8	13.0	21.6	21.4	34.6	42.5	64.8	62.2	56.9	39.2	46.2	63.7
Uncorrected ultrasound (mm) *(Difference from measured)*	4.1 *(9%)*	14.0 *(8%)*	23.6 *(9%)*	23.7 *(11%)*	39.1 *(13%)*	48.2 *(13%)*	75.8 *(17%)*	77.0 *(24%)*	65.8 *(16%)*	44.9 *(15%)*	54.9 *(19%)*	83.0 *(30%)*
Time-corrected ultrasound (mm) *(Difference from measured)*	4.0 *(5%)*	13.1 *(1%)*	21.7 *(0.5%)*	21.7 *(1%)*	34.7 *(0.5%)*	42.1 *(-1%)*	62.9 *(-3%)*	62.8 *(1%)*	56.6 *(-0.5%)*	39.1 *(-0.1%)*	46.9 *(1%)*	64.9 *(2%)*

Table 3.2. Cumulative displacement of dura by direct measurement of tray displacement and calculated in contra-directional tests using ultrasound methods
(Bracketed value is percentage difference from direct measurement)

	CONTRA-20	CONTRA-21	CONTRA-22	CONTRA-23	CONTRA-24	CONTRA-25	CONTRA-26	CONTRA-27	CONTRA-30	CONTRA-31
Direct Measurement (mm)	9.7	23.0	32.8	55.3	48.0	50.7	64.9	64.2	63.4	59.7
Uncorrected ultrasound (mm) *(Difference from measured)*	9.5 *(-1%)*	21.2 *(-8%)*	29.4 *(-10%)*	48.6 *(-12%)*	40.9 *(-15%)*	43.6 *(-14%)*	50.8 *(-22%)*	46.8 *(-27%)*	41.3 *(-35%)*	34.8 *(-42%)*
Time-corrected ultrasound (mm) *(Difference from measured)*	10.1 *(5%)*	23.3 *(1%)*	32.9 *(0.4%)*	56.8 *(3%)*	48.3 *(1%)*	52.4 *(3%)*	67.6 *(4%)*	63.1 *(-2%)*	66.4 *(5%)*	57.3 *(-4%)*

3.3.3 Comparison by Scanning Direction

Comparison of tests performed at approximately the same speed in each direction consistently showed that tracked points on the tissue appeared in more consecutive

ultrasound frames in tests with contra-directional motion than in tests with co-directional motion. For example, the tray reached the same velocity in tests CO-15 and CONTRA-23 (peak velocity 0.92 m/s for both tests) but the orientation of the probe affected the number of frames in which an individual tracking point was visible (Figure 3.5). Over the first 10 milliseconds of tracking in co-directional test CO-15, points were only visible for an average of 3 consecutive images. In contrast, contra-directional test CONTRA-23 allowed points on the tissue to be tracked in an average of 5 consecutive image frames.

Correspondingly, the maximum tissue speeds that could be tracked in each motion direction varied. In co-directional tests, semi-automated tracking was effective for motion up to speeds of 1.1 m/s, while contra-directional tests allowed semi-automated tracking in speeds up to 2.3 m/s. Approaching these speeds, point registration became increasingly difficult: at higher speeds, the distance traveled between frames approached the width of the frame so that points needed to be registered at the leading edge of the frame and then at the trailing edge of the frame in the subsequent frame.

3.4 Discussion of Preliminary Ultrasound Study

3.4.1 Distortion of B-mode Ultrasound Images with High-Speed Motion

Although recent advances in high-frequency, high frame-rate B-mode ultrasound have made it possible to capture high-speed tissue motion, the sequential nature of B-mode image construction can produce distorted time-series results. Because each vertical line of the ultrasound image is constructed sequentially, a single image frame does not reflect the stop-motion position of all points at the same time. Tissue points at the leading edge of the image are imaged first, near the beginning of frame construction

period T, while points at the trailing edge of the image are formed near the end of the frame construction period T.

In motion analysis applications involving displacements that are small relative to the frame width, this temporal distortion may be negligible. However, where displacements are large relative to the frame width, as in high-speed testing, the resulting error can be substantial. In the current series of tests, cumulative displacements calculated using uncorrected time series data were up to 42% different than measured displacements (Tables 3.1 and 3.2). Therefore, for the analysis of high-speed tissue motion in traumatic loading for injury biomechanics research, it is essential to understand and correct the temporal distortion that results from sequential construction of B-mode ultrasound images.

Theoretical effectiveness of time-series distortion correction. The algorithm developed to correct for time-series distortion of B-mode ultrasound relies on the premise that *position* data can be accurately tracked, but that the *time* associated with each tracked point must be calculated as a function of the position of the point in the B-mode image frame and the start time of the frame. The correction is a proportional function of the position of the tracked point across the width of the B-mode image (Equation 3.1).

The accuracy of this correction method relies on the timing of the image construction by the sequenced array of ultrasound transducers across the face of the probe. The correction scheme assumes that the entire frame period T (the reciprocal of the frame rate) is used to construct the image and that construction of each line across the image takes an equal proportion of the frame period. It is also assumed that any delay

between the completion of the final line of an image and the start of the first line of the next image is negligible.

Effectiveness of distortion correction in validation testing. The accuracy of the time-series distortion correction was tested by comparing results of ultrasound image analysis of dura motion to the motion of the mounting tray in the tests presented in this study. Application of the proposed correction procedure to ultrasound tracking results in tests where the displacement time history could be directly measured showed that the time correction improved error in calculation of cumulative displacement from an average of 17% to within an average of 2%. This level of accuracy suggests that the assumptions made regarding the timing of the image construction were reasonable for the ultrasound equipment used.

3.4.2 Contribution of Tracking Procedure to Potential Error

Potential error from the point registration and tracking procedures for the ultrasound image analysis can result from (1) limitations in initial ultrasound image spatial resolution, (2) image degradation in image file type conversion from the VEVO 2100 to the image analyzed by TEMA, (3) inaccurate feature-based tracking, and (4) misalignment of the ultrasound probe and the motion of the tissue leading to changes in shape and appearance of tissue features between frames.

The magnitude of potential error from the first source, spatial resolution, can be estimated from the manufacturer's lateral resolution estimate of 80 μm (Visualsonics 2009). While it is difficult to quantify the error from each of the other three sources of error, the potential error from image degradation (2) and feature based tracking (3) would

likely be consistent between tests with the same tissue and test conditions, but the error from probe misalignment (4) could potentially vary between tests and be improved with careful probe setup technique.

The effect of probe misalignment in the current test configuration was evaluated. The thickness of tissue imaged in the z-dimension at the geometric focus of the ultrasound beam is expected to be equal to the lateral resolution of one element of the ultrasound array across the x-dimension of the image (Figure 3.10). The probe used in the current study had a reported lateral resolution at the geometric focus of 80 μm so that the tissue in view for a single image line at the geometric focus was 80 μm in either the x direction (lateral image width) or the z direction (thickness of imaged tissue). If the direction of motion is not aligned with the probe, then points in the tissue at one side of the image frame (i.e. at x=0), may no longer be visible in the B-mode image when that point on the tissue moves across the width of the frame where x= x_{width} (Figure 3.11). If the tangent of the misalignment angle θ is equal to $\frac{z}{x_{width}}$, then a point visible at one frame edge is not expected to be visible in a subsequent frame when the tissue has moved a distance of $x_{width.}$ At misalignment angles less than $\tan^{-1}\left(\frac{z}{x_{width}}\right)$, the loss of trackable points is expected to vary with misalignment. Any improvement in alignment angle will improve tracking success.

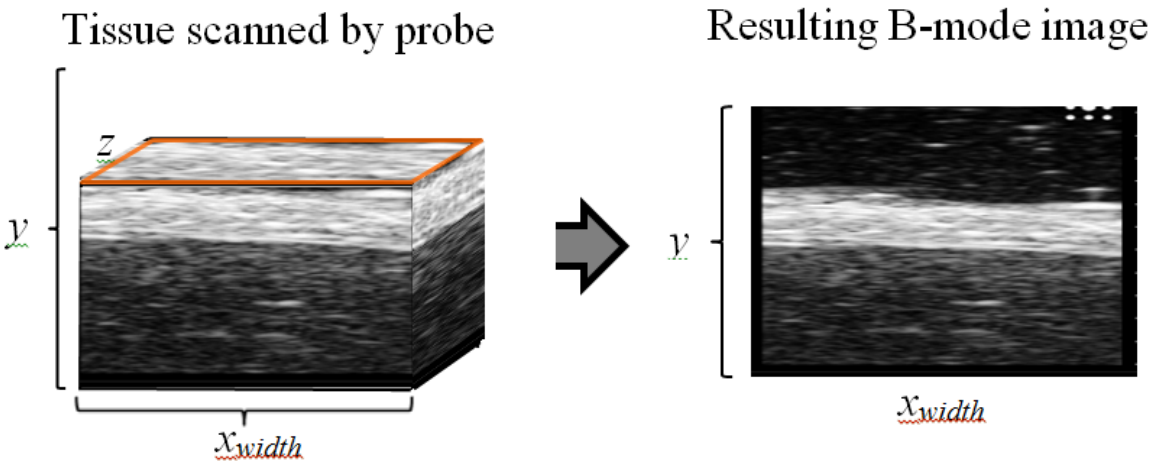

Figure 3.10. Conceptual illustration of the dimensions of 3-dimensional tissue segment scanned to form a 2-dimensional B-mode image.

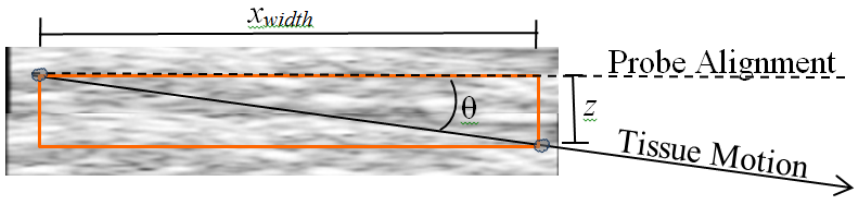

Figure 3.11. Illustration of the misalignment angle (θ) showing that a tissue point on one side of the frame will no longer be visible when it moves to the other side of the frame.

In the current tests, with x_{width} of 4.08 mm and image depth z of 80 μm, an angle of 1.1 degrees would result in complete loss of tracking for points traveling from one edge of the frame to the other. Alignment of the probe with tissue motion is therefore expected to play a major role in reducing error in motion tracking.

Of the four sources of potential error considered, it appeared that none resulted in error as substantial as the error from temporal distortion that results from sequential image-building in tracking high-speed tissue motion for which a correction procedure

was proposed. However, any reduction in errors during tracking and processing can improve accuracy and allow tracking of tissue at higher motion speeds.

3.4.3 Co-directional and Contra-directional Sensor Array Position

Experimentally, this study demonstrated that for tissue moving at a given velocity, imaging motion by aligning the ultrasound probe in a co-directional configuration with the tissue moving in the same direction as the ultrasound array sequence resulted in tracked points on the tissue being visible for fewer frames than when the probe was aligned so that motion was contra-directional. This difference results from tissue at the trailing edge of the frame being imaged late in the image construction period T and tissue at the leading edge of the frame being imaged early in the image period T. Accordingly, a tissue point that appears at the trailing edge of the image (as in contra-directional motion) can be captured one frame earlier than one that appears at the leading edge of the image. Similarly in contra-directional motion, the tissue point will leave the image boundary at the leading edge of the image, and be captured for one additional frame that would not be captured if a tissue point were leaving the image boundary at the trailing edge as in co-directional motion. As a result, given tissue motion at the same speed, a tissue point will typically appear in two more consecutive frames when imaged in a contra-directional configuration than in a co-directional configuration.

Because of the additional frames in which a point is visible in contra-directional motion, this configuration has significant advantages over co-directional motion for analyzing high-speed tissue motion.

3.4.4 Maximum Trackable Tissue Speed

Theoretically, tissue points must appear in at least two consecutive B-mode images to track tissue motion, since between-frame displacement motion can only be quantified if the same tracked point appears in both frames. In co-directional motion, theoretical maximum tissue speed at which points can be imaged in at least two consecutive frames corresponds to traveling the width of image frame over the time it takes to complete two images (Equation 3.4) since the point is imaged at the beginning of frame period T in the first image and at the end of frame period T in the second image.

$$Max\ Theoretical\ Speed_{codirectional} = \frac{x_{width}}{2 \times \mathrm{T}} \tag{3.4}$$

In contra-directional motion, the maximum theoretical speed at which a tissue point would appear in at least two consecutive frames corresponds to the image frame width over the time to complete the final line of one image and the first line of the next image. Assuming for this idealized case that the time to build each of the N lines in an image is proportional and that there is no delay between frames, this theoretical maximum speed could be estimated as in Equation 3.5.

$$Max\ Theoretical\ Speed_{contradirectional} = \frac{x_{width}}{2 \times {}^{\mathrm{T}}/_{N}} \tag{3.5}$$

In practical terms, however, more than two consecutive frames per tracked point are necessary in order to effectively quantify motion. Tracking motion at the maximum theoretical speeds listed in equations 3.4 and 3.5 would require tracking of the tissue

points at the very periphery of the frame, which is problematic in either automatic or manual tracking because the image patterns to the left and right of the point cannot be used to help identify the point. Any conditions that contribute to poor image quality exacerbate the difficulty in identifying tissue points.

The practical effective maximum tissue speed at which motion can be captured is therefore a function of the minimum number of frames in which each point realistically needs to be visible to track motion under a given set of test conditions (Equations 3.6 and 3.7). For both configurations, this maximum tissue speed is calculated by dividing the distance travelled to cross the entire width of the image frame (x_{width}) by the time that corresponds to the number of frames (F_{min}) in which the point needs to be tracked. For co-directional tests, this time is equal to frame period T multiplied by the minimum number of frames in which the point is to be tracked, since the point will be tracked at the beginning of the frame period T in the first frame it is tracked and the end of the frame period T in the last frame it is tracked. For contra-directional tests, the denominator time is equal to the frame period T multiplied by the minimum number of frames to be tracked minus 2: since the point will be tracked at the *end* of frame period T in the first frame it is imaged and at the *beginning* of frame period T in the last frame it is imaged, thus reducing the travel time of the contra-directional point by 2 frame periods.

$$MaxSpeed_{codirectional} = \frac{x_{width}}{F_{min} \times T} \tag{3.6}$$

$$MaxSpeed_{contradirectional} = \frac{x_{width}}{(F_{min} - 2) \times T} \tag{3.7}$$

Empirically for the current set of validation tests, the number of frames in which each tracked point needed to be visible was 3; however tracking was not possible if the point was adjacent to the image periphery in the first or last frame in which it was visible. At a fractional F_{min} between 3 and 4, tissue points were visible in three consecutive frames with each point sufficiently far from the image periphery that the pattern surrounding the point could be used to effectively identify it. Therefore, under the current imaging conditions with x_{width} of 4.08 mm, T of 865^{-1} seconds, and F_{min} of 3.5, the estimated maximum trackable tissue speed for contra-directional motion is estimated to be 2.4 m/s. Under the same conditions, tissue speed would be limited to approximately 1.0 m/s in co-directional motion. Degradation of image quality or of alignment of the ultrasound array with tissue motion will reduce the maximum trackable tissue speed by increasing the number of frames needed, while improvement of image tracking methods that allow identification of points near the periphery of the image will decrease the additional fractional number of frames needed.

3.5 Limitations and Challenges of B-mode Ultrasound in Injury Biomechanics

Although B-mode ultrasound has excellent potential as an experimental tool, this method also has limitations for use in experimental injury biomechanics and other large-displacement, high-speed applications. In addition to the limitations with respect to tissue speed, the physics and hardware for high-frequency ultrasound imaging present further challenges.

Frame dimensions. Using sequential-array B-mode ultrasound technology, the high frame rates needed for trauma-type experimental testing necessitate a narrow

horizontal or lateral (x-dimension) field of view and a shallow axial or vertical (y-dimension) image range. The narrow lateral field of view limits the maximum tissue speed that can be captured by an off-board, stationary probe. The shallow axial image range limits use of this technique to studying superficial tissues and introduces challenges in keeping the tissue of interest close to the probe face throughout the event. The dimensional limits of the field of view are driven by the physics of B-mode ultrasound, which sends sequential ultrasound pulses from each sensor across the array. Since each array fires only after reflected sound waves have returned to the previous sensor, the speed of the image collection is restricted by the speed of sound. Overcoming these limitations without decreasing spatial resolution will require innovations that allow simultaneous firing of multiple transducer elements.

Ultrasound probe fragility. In experimental injury biomechanics, use of B-mode ultrasound is further limited by the fragility of currently available equipment, which necessitates mounting the probe in a stationary position and protecting it from excessive acceleration or tissue impact. If the ultrasound probe were ruggedized so that it could be accelerated with the tissues of interest, there would be many more potential applications for B-mode ultrasound in experimental high-speed testing. For example, to study relative motion of brain and dura through a window in the skull in experimental head rotation, mounting the probe to the skull would keep the tissues in a shallow field of view throughout the event. Additionally, this configuration would substantially increase the maximum head rotation rate possible since the tissues would not be moving as fast relative to the probe as they would in an off-board probe setup. Other applications for

imaging of deep structures may also be possible if the probe could be positioned within the body during impact testing, thus overcoming the limitation that high-frequency ultrasound be used only for superficial tissues.

Two-dimensional motion. Since sensor alignment with the direction of motion is essential to the capture of high-speed motion, only motion within the plane of the B-mode image can be tracked so that out-of-plane motion cannot be analyzed.

Imaging medium. Use of B-mode ultrasound carries other challenges for experimental setup in injury biomechanics research, including the need for a fluid or gel imaging medium. It is expected that most experimental applications involving an off-board, stationary probe will require a fluid medium in order to prevent introduction of air between the probe and the tissue. The fluid medium presents challenges for experimental design and for other electronic instrumentation. With a ruggedized probe that could be accelerated with the tested structure, a gel standoff could be used between the probe and the tissue of interest.

In summary, high-frequency, high frame-rate B-mode ultrasound has potential as an imaging tool to improve understanding of tissue dynamics in experimental injury biomechanics. The sequential nature of B-mode image construction can produce temporal distortion when displacements are large relative to the frame width, and this distortion can result in substantial errors in motion characterization. However, relying on the assumption that the entire frame period is used to construct the image and that construction of each line across the image takes an equal proportion of the frame period, the resulting error can be easily corrected. The corrected *time* at which each tracked

point was imaged is calculated as a proportional function of the position of the tracked point across the width of the B-mode image. Verification testing in the current study showed that tissue motion could be effectively characterized using a stationary off-board high-frequency ultrasound probe and the proposed correction algorithm.

Although the maximum tissue velocity that can be tracked using high-frequency, high frame-rate B-mode ultrasound is limited by the frame width and frame rate available, a contra-directional configuration with the ultrasound sensor array sequence in the opposite direction as the tissue motion allowed tracking of higher tissue speeds than did a co-directional configuration. The maximum trackable tissue velocity is also dependent on the number of consecutive frames in which a point needs to be identified to be effectively tracked. This minimum number of frames is specific to a given test configuration and depends on image quality, alignment of the tissue motion with the ultrasound sensor array, and on the effectiveness of the image registration procedure.

In addition to tissue speed limitations, the challenges involved in using high-frequency, high frame-rate B-mode ultrasound in experimental injury biomechanics or other large-displacement, high-speed applications include limited image width and axial height, restriction to two-dimensional motion, probe fragility, and the need for a fluid or gel imaging medium.

3.6 Summary of Preliminary Study Implications for Head Rotation Study

Overall, the preliminary study showed that B-mode ultrasound had the potential to measure motion of the meninges in high-speed testing, subject to the limitations discussed in the previous section. In a test configuration that allows the head to be

rotated past the stationary probe in a fluid bath, a small window of tissue at the surface of the brain can be imaged as it moves past the probe. However, the results of the preliminary study had several specific implications for the experimental use of B-mode ultrasound in head rotation tests that needed to be incorporated into the methods used for head rotation testing.

Temporal distortion correction. For the high-speed, large-displacement motions expected in rotation testing, the cumulative effects of time-series distortion are expected to be substantial, making it essential to correct the timing of each tracked point. Results of the preliminary study showed that the algorithm proposed in in Equation 3.2 effectively corrected this potential source of error in high-speed tests.

Other sources of potential error. The preliminary study showed that misalignment of the probe with the direction of tissue motion was the next largest potential source of preventable error in motion tracking, suggesting that precise alignment of the ultrasound probe with tissue motion in head rotation testing is key to effective image tracking in high-rate testing.

Orientation of ultrasound sensor array relative to tissue motion. When the ultrasound probe is oriented so that tissue motion is in the opposite direction of the ultrasound array sequence across the probe face, i.e. a contra-directional orientation, tissue points appear in more consecutive frames than if the probe is positioned in a co-directional orientation. To optimize imaging of high-rate tissue motion in rotation testing, the probe should be positioned in contra-directional orientation relative to motion of the imaged tissues on the head.

Maximum tissue speed in rotation testing. Maximum trackable tissue speed for a given lateral frame width (x_{width}), frame period (T), and minimum number of frames in which each point needs to be visible (F_{min}) can be calculated using Equation 3.7. Based on processing of the tests in the current preliminary study, a conservative estimate of the number of frames needed per tracked point for cranial dura is between 3 and 4 for effective and reliable motion analysis. The maximum rate of rotation in head testing needs to be calculated based on the image dimensions and timing used for ultrasound data collection.

Chapter 4: Methods of Head Rotation Study

This chapter describes the experimental procedures used for rotation testing of *post mortem* human subject heads. The experimental setup consisted of a rotating frame to move the head past a stationary ultrasound probe. In this way the meningeal tissues could be imaged during head rotation through a parasagittal window cut through the skull. Methods are described for the preparation and testing of *post mortem* heads including pre-test magnetic resonance (MR) imaging, fluid perfusion, cutting and alignment of the parasagittal window of the skull; the design of the rotation fixture; instrumentation used to track head kinematics; and the collection and analysis of ultrasound images.

4.1 *Post Mortem* Subjects

Post mortem human subjects for this testing were obtained from the Ohio State University's Anatomy Body Donation Program, and testing was performed with the approval of the Ohio State University Institutional Review Board. Acceptance constraints for *post mortem* subjects were:

- Subject access at no more than 48 hours *post mortem*,
- Body mass less than 90 kg to allow manual lifting of the body required for pre-test imaging, and

- Head width at tragions no greater than 16.5 cm to accommodate test fixture dimensions.

Subjects were not accepted if there was a known history of major head trauma or primary or secondary brain cancer, or where the cause of death was strangulation. Patient selection was *not* limited by age, sex, or by history of neurological disease associated with brain atrophy such as Alzheimer's Disease, Parkinson's Disease, or Multiple Sclerosis.

4.2 MR Imaging of Head for Estimation of Atrophy

After acceptance of the test subject and confirmation of suitability for the test program, the body was transported to the Wright Center of Innovation in Biomedical Imaging at The Ohio State University's Martha Morehouse Medical Plaza for MR imaging. Scanning of the head was performed using a Philips Achieva ultra-high-field 7 Tesla MR scanner (Philips, Andover, MA). Segmentation of T1 images for both subjects was attempted using SPM8 (Wellcome Trust Center for Neuroimaging, UK), a voxel-based suite of Matlab tools and procedures for interpretation of neuroimaging data. Using SPM8, an attempt was made to isolate CSF from grey matter and white matter in each slice so that atrophy could be estimated by dividing the total volume of CSF by the summed volume of CSF, grey matter, and white matter in the cranial space.

4.3 Initial Preparation of Head

After completion of MR imaging of the head, the subject was transported to the Injury Biomechanics Research Laboratory at The Ohio State University for the remainder of the subject preparation for testing. Initial preparation included removal of the scalp to

expose the cranial vault, and inspection of dentition. Since rotation loading was applied through the jaw as well as to the skull, a well-aligned bite was necessary to ensure direct rotation loading of the head.

4.3.1 Ligation of Cervical Vasculature

Prior to separation of the head and neck from the body, the external carotids were ligated to reduce bleeding into the neck musculature and scalp vessels when the vasculature was later pressurized. The bifurcation of each common carotid into the internal and external carotids was identified through a vertical incision to the anterior neck medial to the sternocleidomastoid. The external carotids were ligated proximal to the first branch (Figure 4.1).

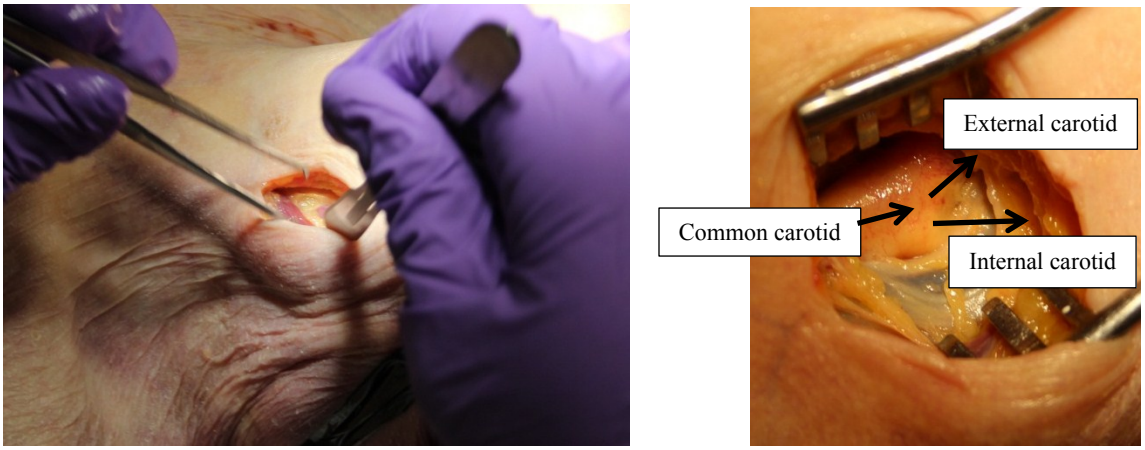

Figure 4.1 Access to the external carotid for ligation.

Vasculature at the base of the neck was accessed by cutting along the clavicle and through the surface musculature to expose the internal jugulars, common carotids, and

vertebral arteries. These vessels were ligated and severed immediately distal to the ligation for later connection for pressurization.

4.3.2 Separation of Head

To separate remaining structures of the neck, the skin was reflected back along the clavicle, and anterior structures severed to expose the C7 and T1 vertebrae. The spine was separated at this level by cutting through the C7-T1 intervertebral disc and separating the facet joints and vertebral processes, before making a final cut through the spinal dura and cord to remove the head and neck.

4.3.3 Plugging of Space Between Spinal Dura and Arachnoid

Immediately following separation of the head and neck from the body between the C7 and T1 vertebrae, the space between the cervical vertebral dura and the underlying arachnoid was plugged in order to limit the introduction of air or fluid between the cranial dura and arachnoid. The plug was constructed with a layer of petroleum jelly inserted via veterinary feeding tubes followed by yarn coated in a 1:10 mixture of paraffin and petroleum jelly, and an additional layer of petroleum jelly.

4.3.4 Perfusion of Artificial Cerebrospinal Fluid

The cranial subarachnoid space was perfused with artificial cerebrospinal fluid (CSF) prepared with distilled water according to the recipe of Sugawara, Atsuta et al. (1996). Since the artificial CSF is isotonic to physiological CSF, it is expected to minimize diffusion of fluid into or out of the brain and therefore prevent the swelling or dehydration of brain tissue that can result from parenchyma contact with water or saline.

The artificial CSF was introduced into the cranial subarachnoid space via the spinal subarachnoid space at the transected C7-T1 level. A Foley catheter (size 6French) was inserted into the subarachnoid space, posterior to the spinal cord and guided to the upper cervical spine using fluoroscopic guidance, if available, to ensure that it did not extend past the cervical spinal canal into the skull. For subject PM01, placement of the subarachnoid catheter was guided by a conservative estimate of the length of the cervical spine. For subject PM02, the fluoroscope images were used to estimate the distance from inferior C7 to C2 to determine the insertion depth of the catheter. The catheter was then anchored in place at the transected surface of the neck, and the catheter connected to a reservoir of artificial CSF with a fluid level approximately 55cm above the level of the upper cervical spine. This height difference resulted in a nominal fluid column pressure of approximately 40 mmHg, allowing the artificial CSF to perfuse into the cranial subarachnoid space throughout the remainder of the subject preparation procedure. Although perfusion was interrupted during individual preparation procedures, each subject was intended to undergo at least 20 hours of perfusion prior to testing. Post-test, green RIT dye was added to the artificial CSF perfusate to allow visualization of the extent of subarachnoid perfusion at post-test dissection.

4.3.5 Sealing of Exposed Tissues

Tissues left exposed after transection of the neck and removal of the scalp were sealed in order to prevent blood flow from reducing vascular pressure in the head and to reduce spray of blood and saline during testing. Following connection of artificial CSF at the cervical spinal canal, all exposed tissues at the neck were sealed using gel

cyanoacrylate (Loctite 426 Instant Adhesive, Loctite, Henkel Corporation, Düsseldorf, Germany) and nylon panty hose. Openings in the hose were made at the spinal canal for the artificial CSF plumbing and at the ligated cervical blood vessels to be used for vascular pressurization.

4.3.6 Opening of Cranial Viewing Window

A window was opened through the cranial vault in order to expose the dura parasagittally along the anterior-posterior path to be imaged. In test PM01, the opening was nominally 25 mm wide, and centered 35 cm from the midline of the head. In test PM02, the opening was nominally 19 mm wide and centered 31 mm from midline. The anterior-posterior cuts of the opening were pre-marked using a laser positioned parallel to the sagittal suture line (Figure 4.2). The opening was cut using a surgical craniotome (Model 6516-01-378-A176, Aesculap, Center Valley, Pennsylvania), by perforating the skull around the periphery of the opening using a size 302 craniotome drill and a craniotome cutting blade with dura guard to cut around the periphery of the opening and to cut the piece of skull to be removed into smaller segments. For subject PM02, additional efforts were made to separate the dura from the skull prior to cutting the opening by enlarging burr holes using Kerrison rongeurs and a Penfield surgical elevator to separate the dura between burr holes. The cut segments of skull were removed individually from the opening using a surgical elevator to separate each bone segment from the underlying dura (Figure 4.3).

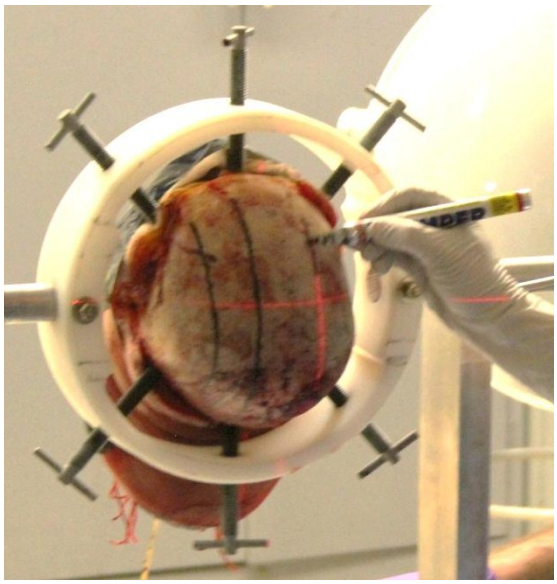

Figure 4.2. Marking of viewing window in cranial vault using laser aligned parallel with sagittal suture.

Figure 4.3. Removal of bone segments to expose dura.

When the dura was inadvertently cut during the window cutting procedure (subject PM01), the opening was repaired using sutures, patched using duct tape, and sealed with gel cyanoacrylate (Figure 4.4).

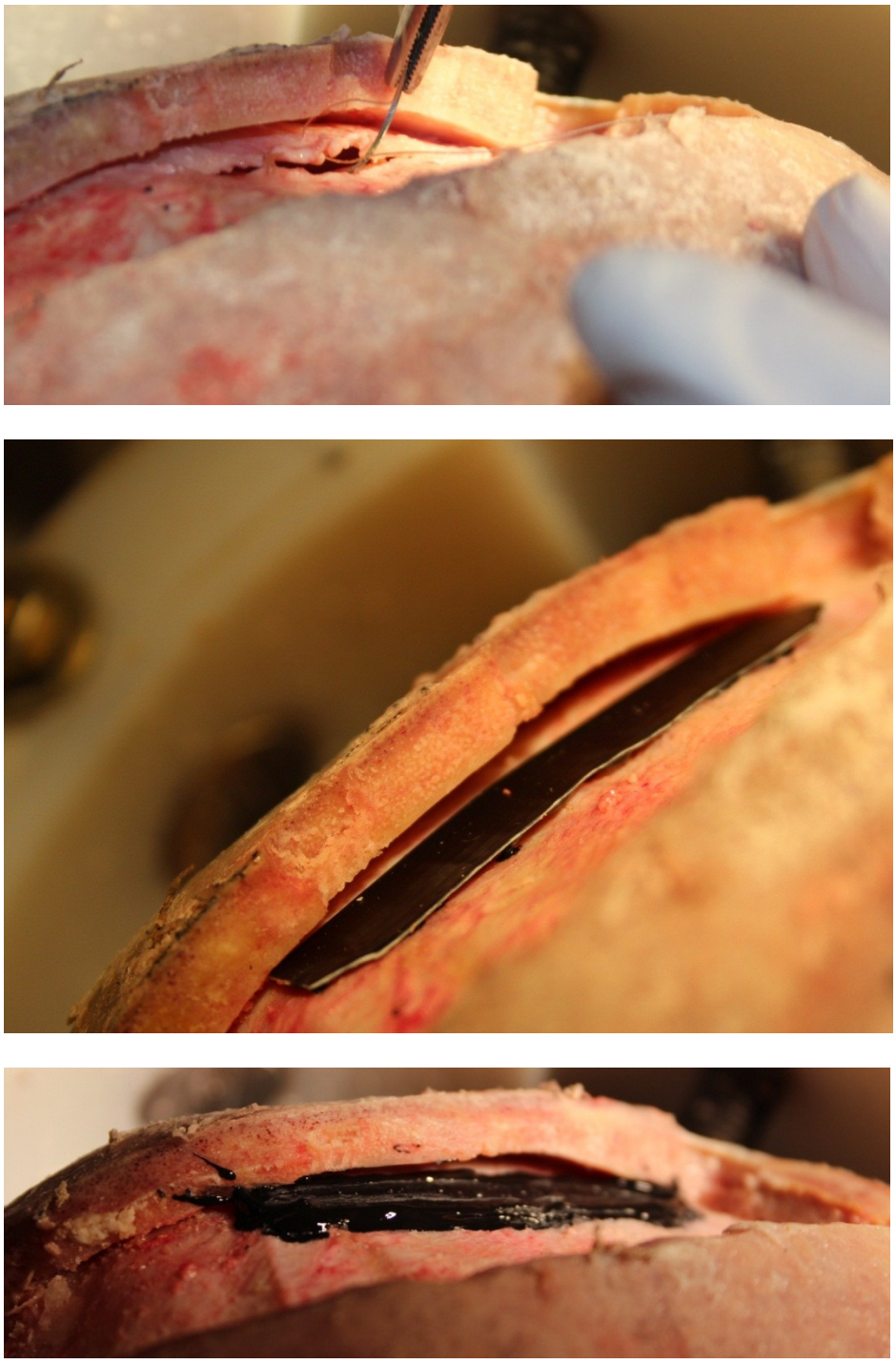

Figure 4.4. Suturing, patching, and sealing of cut in dura.

For subject PM02, the skull opening was buttressed along the edges with moldable two-part plumbing epoxy (Wet Weld, JB Weld, Sulphur Springs, Texas) so that the window width was narrowed to approximately 10 mm (Figure 4.5).

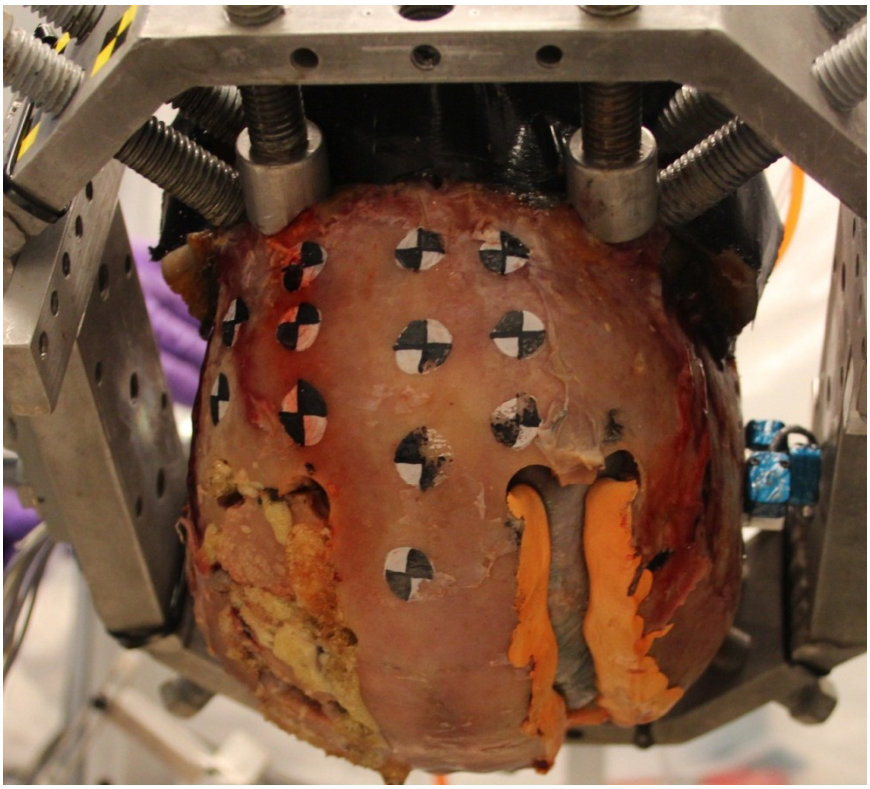

Figure 4.5. Buttressing of dura at edges of skull window with plumbing epoxy (PM02).

The exposed dura was kept hydrated during the remaining preparation procedures by covering it with gauze sponges soaked in artificial CSF.

4.3.7 Arterial Pressurization

The cranial arterial system was pressurized for testing with saline, prepared using 9 grams sodium chloride per liter water. The arterial system was pressurized via the internal carotid arteries, which were fitted with size 14French to 16French Foley

catheters connected to a gravity-fed saline source. On initial connection of the saline to each common carotid artery, the vertebral arteries were left open to flow until clear outflow of saline confirmed that the system was flushed. Flushing was accomplished using a fluid reservoir mounted approximately 125 cm above the arterial catheter openings for a nominal fluid pressure of 92 mmHg. After system connection and flushing, the arterial system pressure was closed off until immediately before testing. Pre-test pressure was resumed with the saline source at a fluid column height of 400 mm (PM01) or 370 mm (PM02) above the opening of the carotid artery catheters for nominal input pressure of 30 mmHg in PM01 and 27 mmHg in PM02.

4.3.8 Venous Pressurization

The venous system was pressurized via the internal jugular veins using 16French Foley catheters connected to a gravity-fed saline source, prepared using 9 grams sodium chloride per liter water, tinted orange using Sunshine Orange RIT clothing dye (Quality Brands, Stamford, Connecticut) at a concentration of 25 to 40 mL dye per gallon saline.

Initial flushing of the venous system was done by connecting the internal jugular veins one at a time and allowing orange-dyed saline to flow freely from the other internal jugular at an initial nominal fluid pressure of 92 mmHg. Once flow of orange-tinted saline from each jugular vein confirmed sufficient flushing of the system, both veins were connected to pressurization catheters and venous pressure closed off until immediately before testing. Pre-test pressure was resumed with the orange-tinted fluid source at a fluid column height of 600 mm (PM01) or 590 mm (PM02) above the connection to the jugular veins for nominal input pressure of approximately 45 mmHg.

4.3.9 Evaluation of Intracranial Pressure (ICP)

Following motion testing, the effectiveness of the vascular pressurization was evaluated by measuring parenchymal ICP with the vascular pressurization fluids turned on as they were during testing. ICP was measured with a Codman Microsensor ICP Transducer (Codman & Shurtleff Inc., Raynham, Massachusetts, USA) with a manufacturer-supplied calibration value of 5 μV/V/mmHg at 5 V input voltage. Calibration was confirmed prior to each use by submersion in a column of water up to 408 mmH_2O (30 mmHg).

Post-test, the Codman ICP Transducer was inserted through the dura and into the parenchyma along the mid-pupillary line (approximately 3 cm from the mid-sagittal plane) on the ultrasound-tested side of the head, adjacent to the vertex of the head (Figure 4.6). For test PM01, the ICP transducer was inserted to a depth of 5 cm, and for PM02 a depth of 2 cm was used. During ICP evaluation, the head was inverted to the start position used for rotation testing, and vascular and subarachnoid fluids were turned on and placed at the same heights used for testing in order to best approximate the intracranial pressure achieved during testing. The reference range for comparison to normal physiological intracranial pressure was 5 to 15 mmHg (Raboel, Bartek et al. 2012).

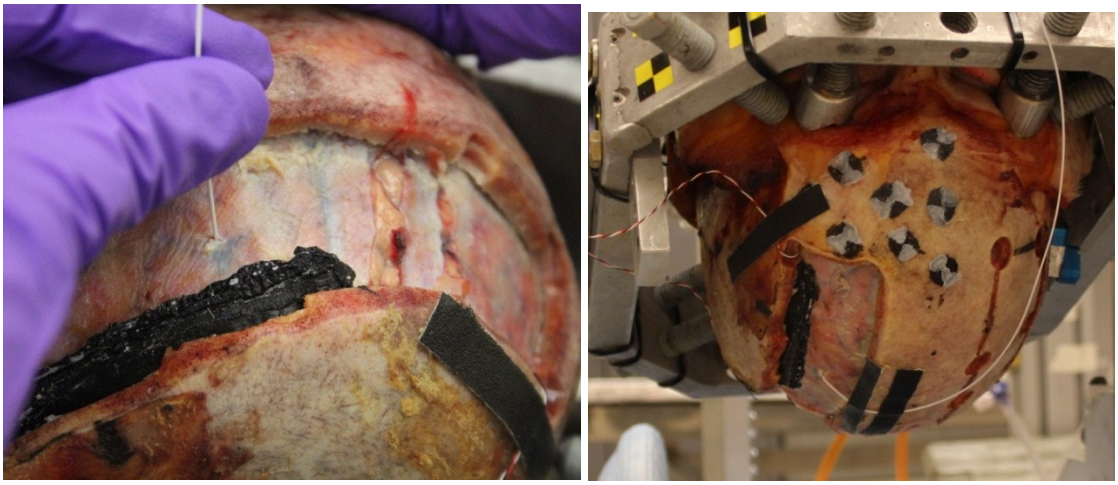

Figure 4.6. Post-test placement of Codman Microsensor through dura.

4.4 Design of Rotation Fixture

The head was enclosed in a purpose-designed rotation cage for testing. The skull was gripped in place in the cage using threaded locator bolts that positioned the head without penetrating the skull.

4.4.1 Cage Design

The cage was constructed of welded aluminum, with an internal opening of 23.5 by 18 cm. Bolt holes around the periphery of the cage were arranged in columns of three so that bolt position could be selected to accommodate heads of different sizes to optimize perpendicular placement of the bolts against the skull. A flange at the cage posterior allowed for approximately perpendicular placement of bolts at the occiput of the subject (Figure 4.7). Threaded bolts were customized with a (45 degree) rounded end-point (Figure 4.8). For subjects where the available bolt positions in the anterior cage

would not allow solid perpendicular bolt contact with the frontal bone, aluminum brow fittings were used in place of bolts to grip the supraorbital ridge (Figure 4.9).

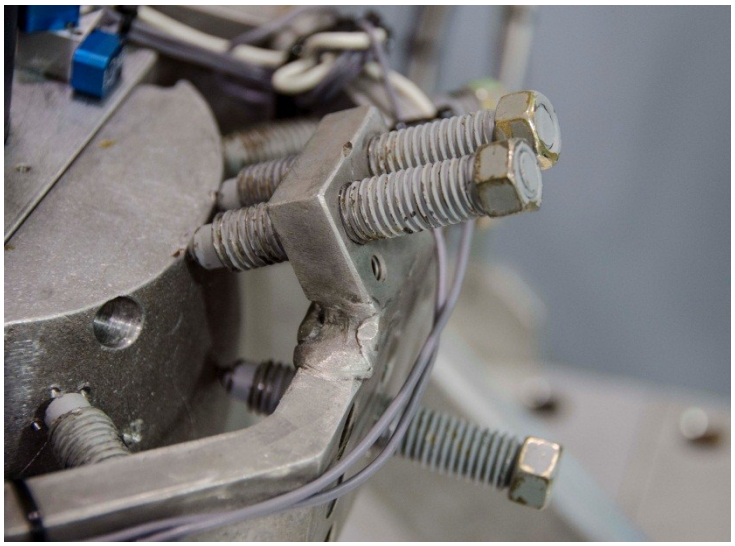

Figure 4.7. Flange at occiput of cage to allow approximately perpendicular placement of bolts to subject occiput, shown above with aluminum dummy head in place of subject.

Figure 4.8. Customized cage bolts with angled endpoint.

Figure 4.9. Customized alternative bolt grips for engaging the supraorbital ridge.

A height-adjustable chin bar was fitted with a rectangular plate that rested directly on the inferior surface of the mandible. The plate was tightened in place by five bolts (Figure 4.10).

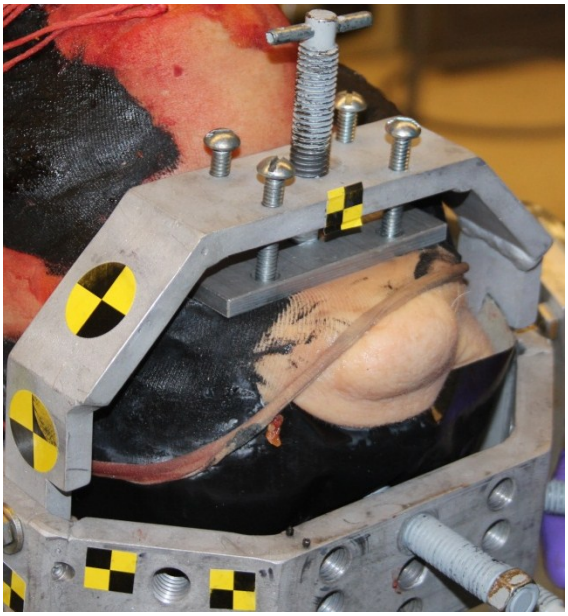

Figure 4.10. Chin bar with mandible plate tightened in place against inferior edge of mandible.

A removable bar over the crown of the cage was fitted with flat-end bolts that were used to help support the weight of the head during positioning in the cage (Figure 4.11). The crown bar was removed prior to testing.

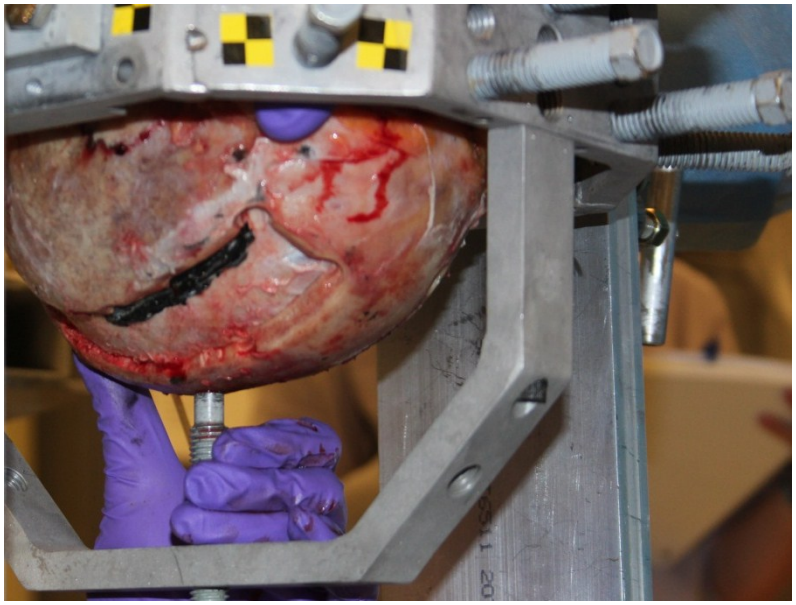

Figure 4.11. Crown bar and positioning bolt used to support weight of head during positioning in the rotation cage.

4.4.2 Rotation Fixture

The rotation cage was mounted on a steel shaft in a rotation fixture (Figure 4.12). To the right side of the subject's head, the cage was mounted to a 2 inch steel shaft supported by 2 cast iron flange-mounted ball bearings. Extending from the shaft between the two bearings were an 11 cm aluminum arm for load application and a 22 cm aluminum arm for braking. On the opposite side of the cage, a 1" shaft was supported by a third bearing. Each of the three bearings was centered at 24 cm above a cart-mounted fixture table surface by aluminum support plates.

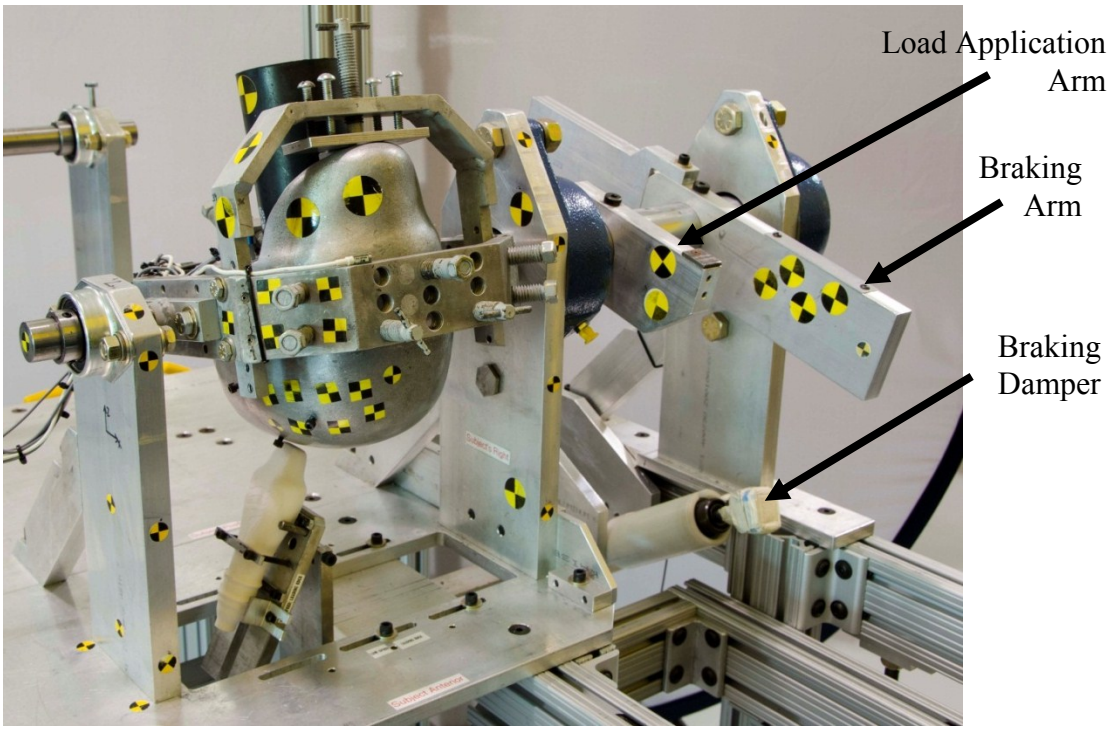

Figure 4.12. Shaft-mounted rotation fixture with arms for braking and load-application.

4.5 Positioning of the Head in the Rotation Fixture

4.5.1 Location of the Rotation Axis

To keep the surface of the dura adjacent to the ultrasound probe throughout the rotation, the head was positioned so that the axis of rotation was aligned through the center of curvature of the targeted viewing path in the parasagittal window. The first step of the procedure to locate the center of curvature was to estimate the radius of curvature of the dural surface to be scanned using a set of Lexan templates cut with inner radii of 8 cm to 13 cm (Figure 4.13). Next, the radius template that best fit the radius of curvature of the dural surface was inserted into a purpose designed tool to locate the center of radius relative to the head. With the radius template in place adjacent to the dura on the

targeted path of the ultrasound probe (Figure 4.14), the axis of rotation locator pins were used to identify the ideal rotation axis. The head was inverted in test position throughout the procedure. Soft tissue was removed from this location and shallow divots were drilled at the pinned locations using a brad-point bit (Figure 4.15). These divots were used as locator marks for positioning the head so that the center of curvature of the dura on the targeted viewing path was aligned with the shaft of the rotation fixture.

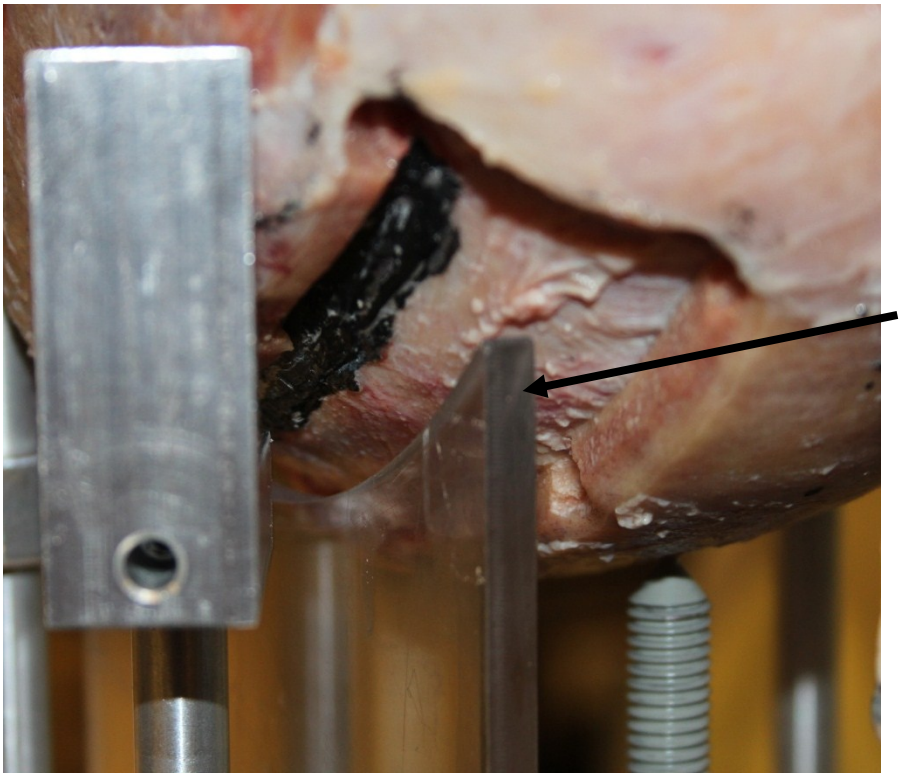

Figure 4.13. Lexan radius of curvature template in place against dura.

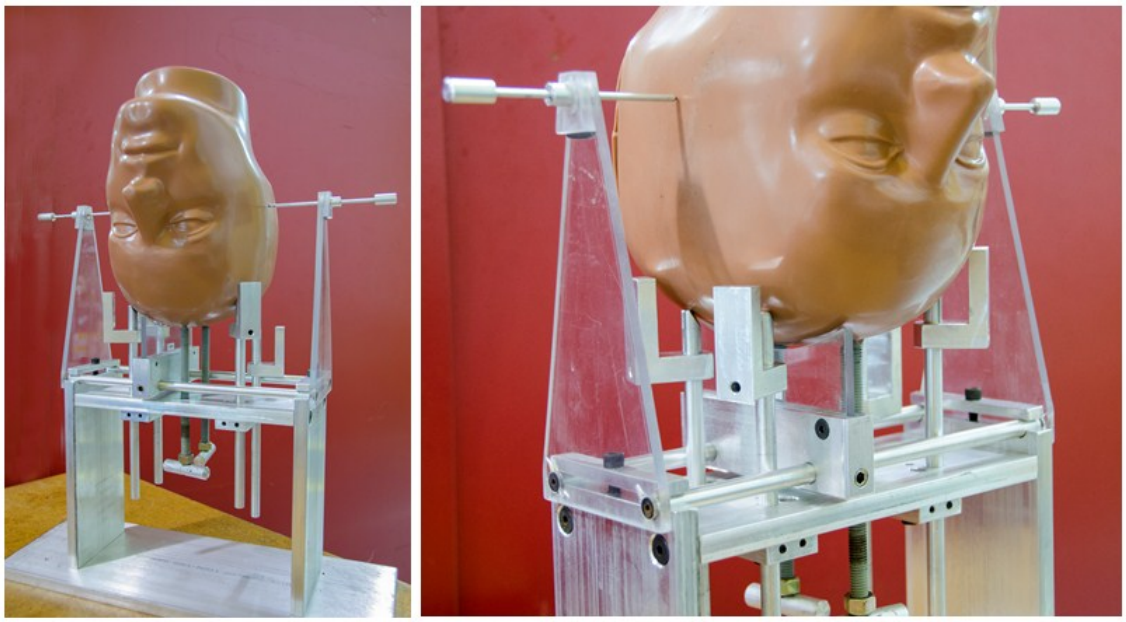

Figure 4.14. Fixture for location of the center of curvature.

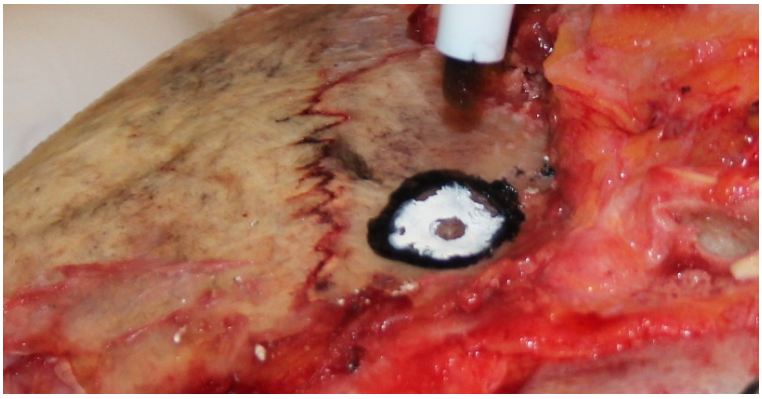

Figure 4.15. Divot at identified center of curvature, to be aligned with the fixture axis of rotation.

4.5.2 Placement of the Head in the Rotation Fixture

To fasten the head in the rotation cage, the cage was mounted in an intermediate positioning fixture. That intermediate positioning fixture had rotation bearings so that the cage could rotate freely about the axis of rotation, but was equipped with threaded

positioning pointers through the bearing center of rotation such that the positioning pointers could be used to align the markings on the skull at the target center of rotation with the fixture's shaft (Figure 4.16).

Figure 4.16. Divot at center of curvature aligned with the fixture axis of rotation using positioning pointers.

With the cage mounted in the positioning fixture, the head was placed into the cage and manually guided while the threaded positioning pointers were aligned with the target center of rotation divots on the head and tightened in place. Next, the head was manually rotated within the cage to find the best alignment of the cage's brow positioning bolts and occipital positioning bolts with the supraorbital ridge and occipital skull respectively. These bolts were tightened until they were just engaged with the skull. Next, bolts across the rear of the cage, the front of the cage and in all oblique positions were manually tightened until each was just engaged with the skull. If there was

remaining soft tissue under any bolts, the bolts were individually backed out and the soft tissue removed with a scalpel before reinserting the bolt. Final tightening of the bolts was done sequentially, confirming at each stage that the divots at the target center of rotation were still centered at the shaft center threaded positioning pointers.

After tightening of all cage positioning bolts, mandible position was checked to ensure that the jaw was closed and the upper and lower dentition engaged. The mandible bar was fastened to the cage, and the mandible plate screwed down so that the cage was firmly engaged under the mandible. The plate angle was variable to ensure full engagement with the mandible. The threaded positioning pointers were removed from the shaft center (Figure 4.17) and prior to testing all bolts on the cage and chin strap were tightened and the crown strap was removed.

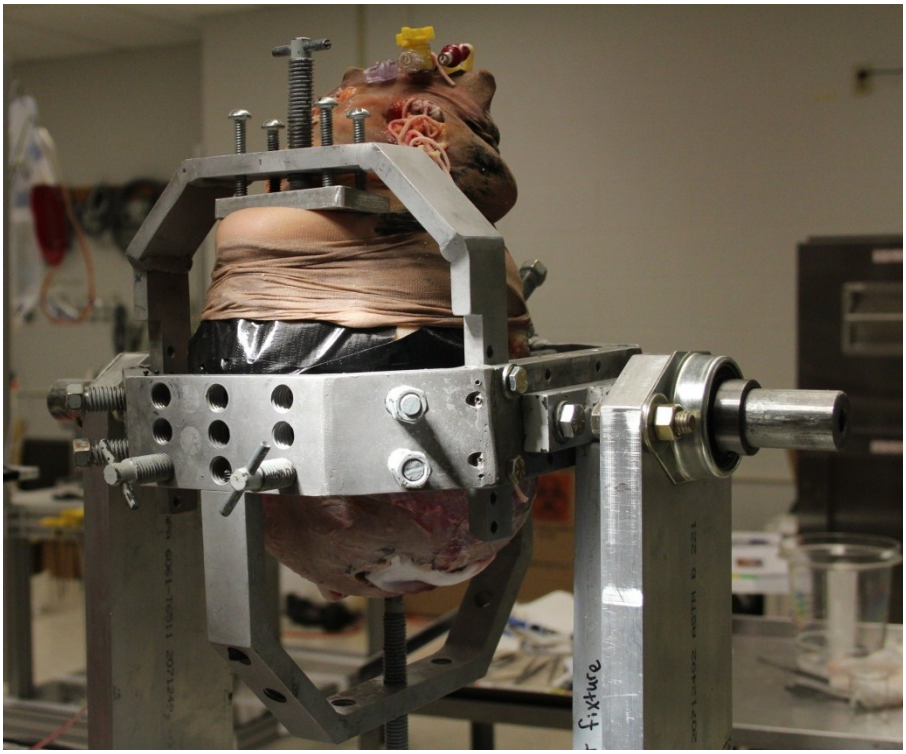

Figure 4.17. Intermediate positioning fixture with positioning pointers removed from the shaft center.

4.6 Estimation of Mass Properties of Head and Rotation Fixture

Inertial mass properties of the head and cage were estimated for each subject prior to testing in order to determine the energy needed for rotational loading as discussed in Section 4.6.1. Moment of inertia of the head and cage was estimated using pendulum rotation tests. Moment of inertia of the remaining rotating portions of the fixture, including the shaft, load arm, and braking arm, were calculated based on their geometry and material properties.

4.6.1 Moment of Inertia of Cage and Head

Moment of inertia (I) of the head and cage was estimated in pendulum tests, since the oscillation period (T_o) of a compound pendulum is a function of its moment of inertia, as well as its mass (m), gravitational acceleration (g), and the radius of gyration (R) of the pendulum (Equation 4.1). Although that relationship only holds for small oscillation angles (θ_o), the period T_o measured in large oscillations can be adjusted by the empirical relationship in Equation 4.2 so that T_{adj} can be used in place of T_o in Equation 4.1.

$$T_o = 2\pi\sqrt{\frac{I}{mgR}} \; for \; small \; \theta_o \tag{4.1}$$

$$T_{adj} = \frac{T_o}{1 + \frac{1}{16}\theta_o^2 + \frac{11}{3072}\theta_o^4 + \cdots} \tag{4.2}$$

Thus the moment of inertia for an oscillating system can be calculated by rearranging Equation 4.1 and substituting T_{adj} for T_o as in Equation 4.3.

$$I = mgR\left(\frac{T_o}{2\pi\left(1 + \frac{1}{16}\theta_o^2 + \frac{11}{3072}\theta_o^4 + \cdots\right)}\right)^2 \tag{4.3}$$

The mass of the head and cage were measured directly. The radius of gyration was determined as described in the next paragraph. To measure the period, T_o, of the head-cage system in oscillation tests, the head and cage were rotated posterior-to-anterior

on the end of the positioning fixture shaft, and then released to swing freely. The cage was instrumented with an angular rate sensor (ARS-18K, DTS, Seal Beach, CA, USA) that was used to determine T_o. The peak angle of oscillation (θ_o) was calculated for each oscillation by integration of measured angular rate. The moment of inertia of the rotating portions of the position fixture (0.0003 kg-m^2) was subtracted from the total calculated moment of inertia of the oscillating system in order to determine the isolated moment of inertia of the head and cage only. To estimate the total moment of inertia of the head, cage, shaft, and all rotating parts of the rotation fixture, the moment of inertia of the rotation fixture's shaft and attached braking arms (0.0120 kg-m^2) was added to the calculated moment of inertia of the head and cage.

Measurement of Radius of Gyration (R). After final positioning of the head in the cage, the left side of the cage was mounted to the shaft of the positioning fixture so that the right side was visible. The head and cage were allowed to hang under gravity from two different positions on the cage, such that the center of mass would locate itself vertically below the shaft center (Figure 4.18). In each position, a vertically-aligned laser line was aligned with the shaft center. The planar distance from the shaft center to the point where the two lines intersected was used to estimate the radius of gyration, i.e. the distance from the axis of rotation to the combined center of mass of the head, cage, and positioning fixture shaft.

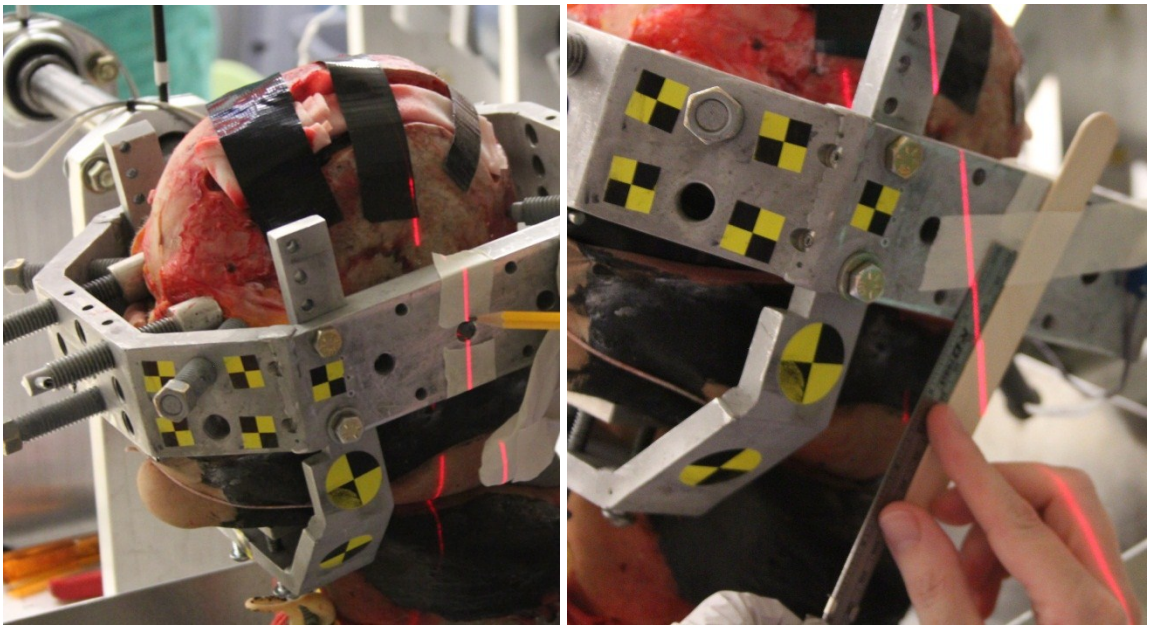

Figure 4.18. Intersection of the vertical lines through the shaft center indicate the planar location of the combined center of mass of the head, cage, and positioning fixture shaft.

4.7 Kinematic Instrumentation of the Head and Cage

4.7.1 Coordinate System

The Y-axis of the fixture-based coordinate system corresponded to the axis of rotation of the rotation fixture (Figure 4.19). The X-axis was positive toward the front of the fixture (toward the subject face) and the Z-axis was positive in the vertical up direction. The origin was aligned with the cage axis of rotation, where it intersected the plane of the inner surface of the vertical support for the shaft bearing on the subject's left side.

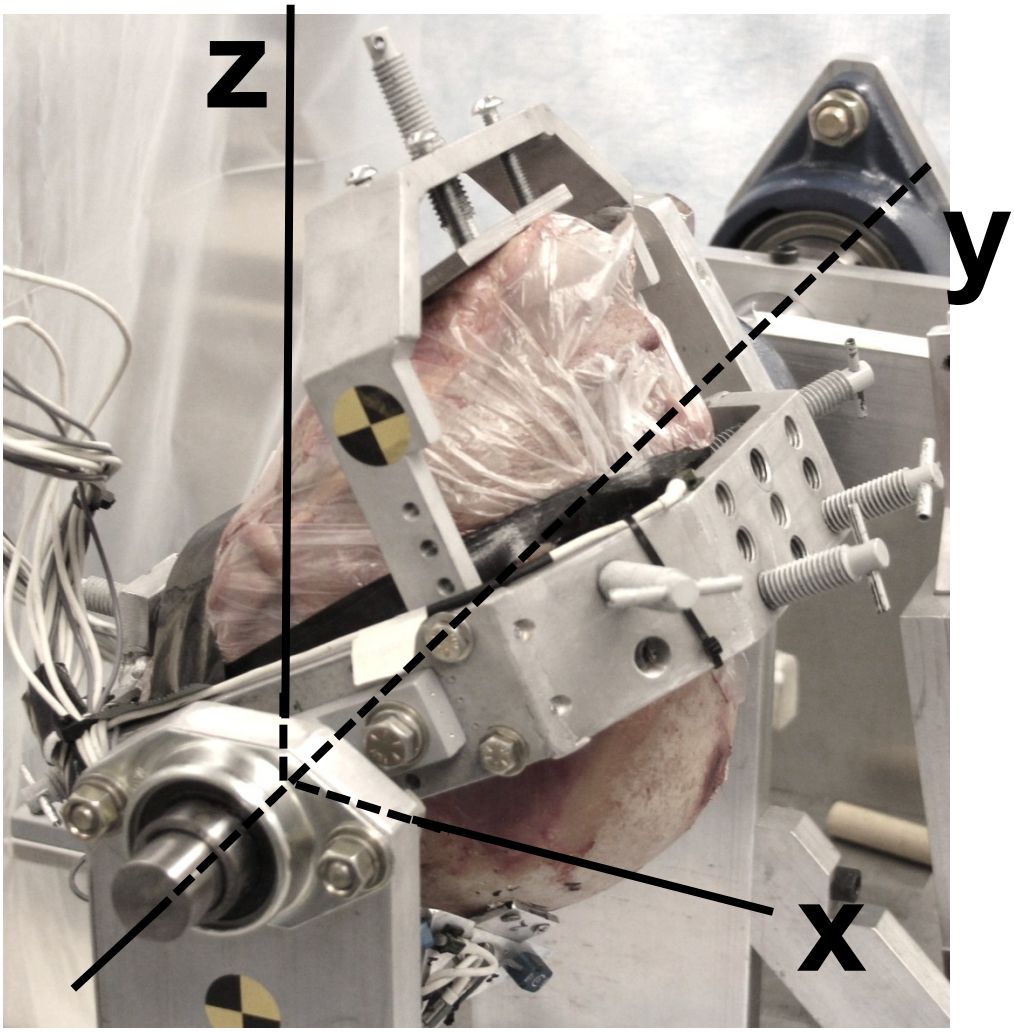

Figure 4.19. Fixture-based co-ordinate system.

4.7.2 Instrumentation of the Cage

The shaft and both sides of the cage were instrumented with angular rate sensors (ARS PRO-18K, DTS, Seal Beach, California, USA) to track rotational velocity about the Y-axis. In PM02, an additional angular rate sensor was mounted to the flange used to mount the cage to the rotating shaft on the subject's right side (Figure 4.21). Cage-mounted Endevco 7264 uniaxial accelerometers (Meggitt Sensing Systems, San Juan

Capistrano, California) were mounted on the anterior and posterior cage and were used to calculate rotational acceleration about the Y-axis.

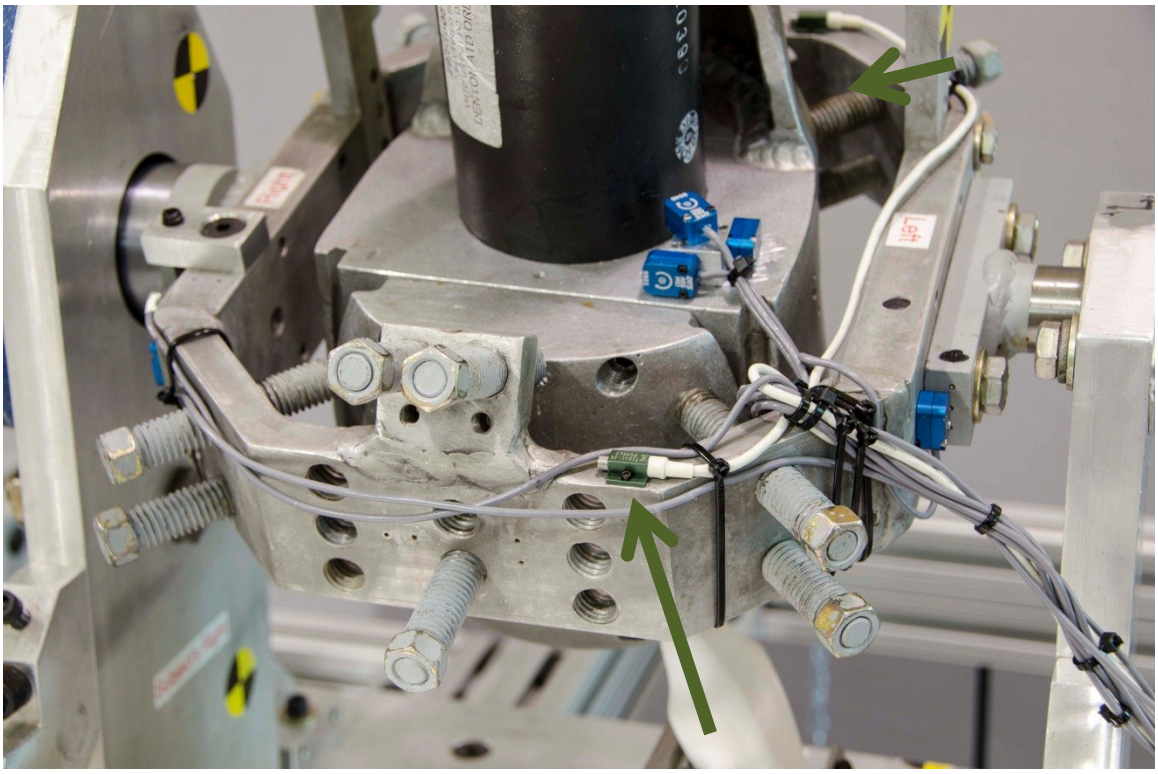

Figure 4.20. Cage-mounted accelerometers at front and rear of cage (indicated by arrows).

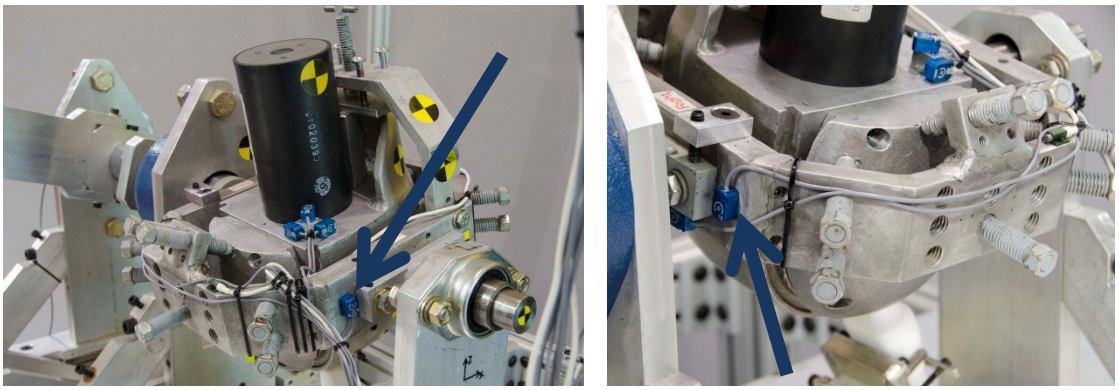

Figure 4.21. Cage-mounted angular rate sensors on left and right and additional angular rate sensor on cage-mounting flange (indicated by arrows).

4.7.3 Instrumentation of the Head

Each skull was instrumented with three orthogonally-mounted angular rate sensors (ARS-18K, DTS, Seal Beach, CA, USA). The scored base of the aluminum mounting block was glued to the temporal skull, which was prepared and flattened with a wood rasp. The angular rate sensor mounting block was located as close to the center of rotation as possible to avoid submersion in ultrasound fluid medium (Figure 4.22).

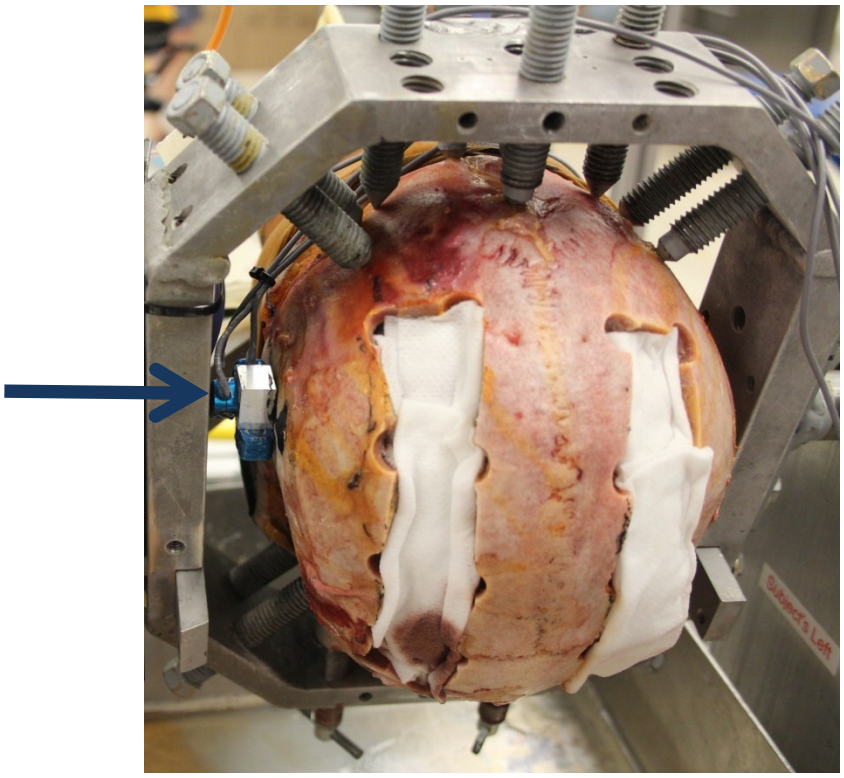

Figure 4.22. Head-mounted angular rate sensors.

4.7.4 3-D digitization

The location and orientation of each sensor and of anatomical landmarks on the head were documented relative to the rotation fixture following testing using a FaroArm 3-dimensional point digitizer (Model/version, Lake Mary, Florida, USA).

4.8 Ultrasound Image Collection

High-speed, high-frequency motion images were collected using a Vevo 2100 ultrasound imaging system (VisualSonics Inc., Toronto, Ontario, Canada) with software version 1.4.1 in the Wexner Medical Center Small Animal Imaging Core. A solid-state

550D ultrasound probe was used for all imaging, with sound wave center frequency of 40 MHz.

4.8.1 Ultrasound Probe Mount

The ultrasound probe was mounted to the test fixture so that the imaging elements were aligned perpendicular to the rotation shaft, and thus aligned with the plane of rotation. This precise positioning, necessary to minimize misalignment of the probe with the motion of the tissue, as discussed in Section 3.3.2, was achieved by allowing the probe mount to slide laterally on a plate mounted between slotted tracks. Perpendicular alignment of the rotating cage and the slotted tracks was confirmed each time the fixture was re-assembled using point digitization with a FaroArm. The cage's true axis of rotation was established by digitizing pairs of points (a and b) on the exterior cage at two locations in its rotation arc. Each pair of points was in the same X-Z plane so that Y was constant. The center of rotation (c) of the cage at the given location along the Y axis was determined using the intersection of the perpendicular lines from the mid-point between arc positions for each point (Figure 4.23). The axis of rotation of the cage was determined by the center of rotation determined in two planes perpendicular to the Y-axis.

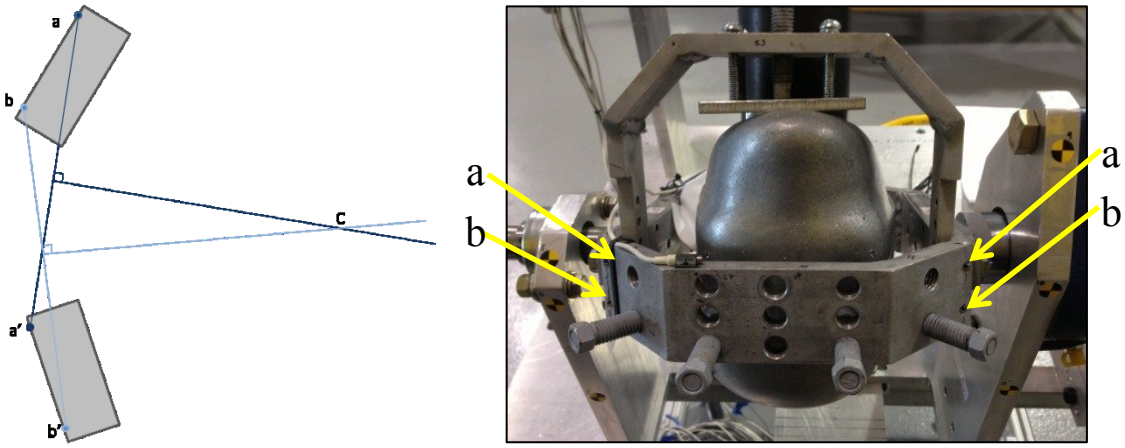

Figure 4.23. Points used to determine true axis of rotation of cage.

The probe's leading edge is defined relative to the imaging sequence with the elements at the leading edge activated prior to those at the trailing edge. For all testing, the probe was oriented so that the transducer array sequence was contra-directional, relative to the direction of tissue motion. For high-rate testing, the probe was positioned in the fixture with its leading edge toward the posterior head to capture the anterior-posterior motion. In low-rate testing, the probe was positioned with its leading edge toward the posterior head in anterior-posterior motion tests and toward the anterior head in posterior-anterior motion tests. For all tests, this contra-directional configuration resulted in right-to-left tissue motion in real-time B-mode ultrasound images.

4.8.2 Ultrasound Fluid Medium

The dural surface to be imaged was submerged in artificial CSF as an imaging medium. A rubber baffle was fixed to an open pedestal in the base of the fluid pan to allow the probe to extend into place adjacent to the submerged dura, while keeping the probe dry. The pan and baffle pedestal were constructed of clear acrylic (Figure 4.24).

The baffle material was cut from a condom (Trojan Magnum XL, Church & Dwight, Annapolis, Maryland, USA) that was fixed in place across the pedestal opening with an aluminum frame and sealed with silicone sealant (All-Purpose Adhesive 100% Silicone Sealant, DAP Products, Inc., Baltimore, MD). To reduce artifact from entrained air in the artificial CSF imaging medium, the CSF for PM02 was prepared using degassed distilled water and was poured into the fluid pan more than 24 hours prior to testing to reduce any entrained air or other gasses in the fluid.

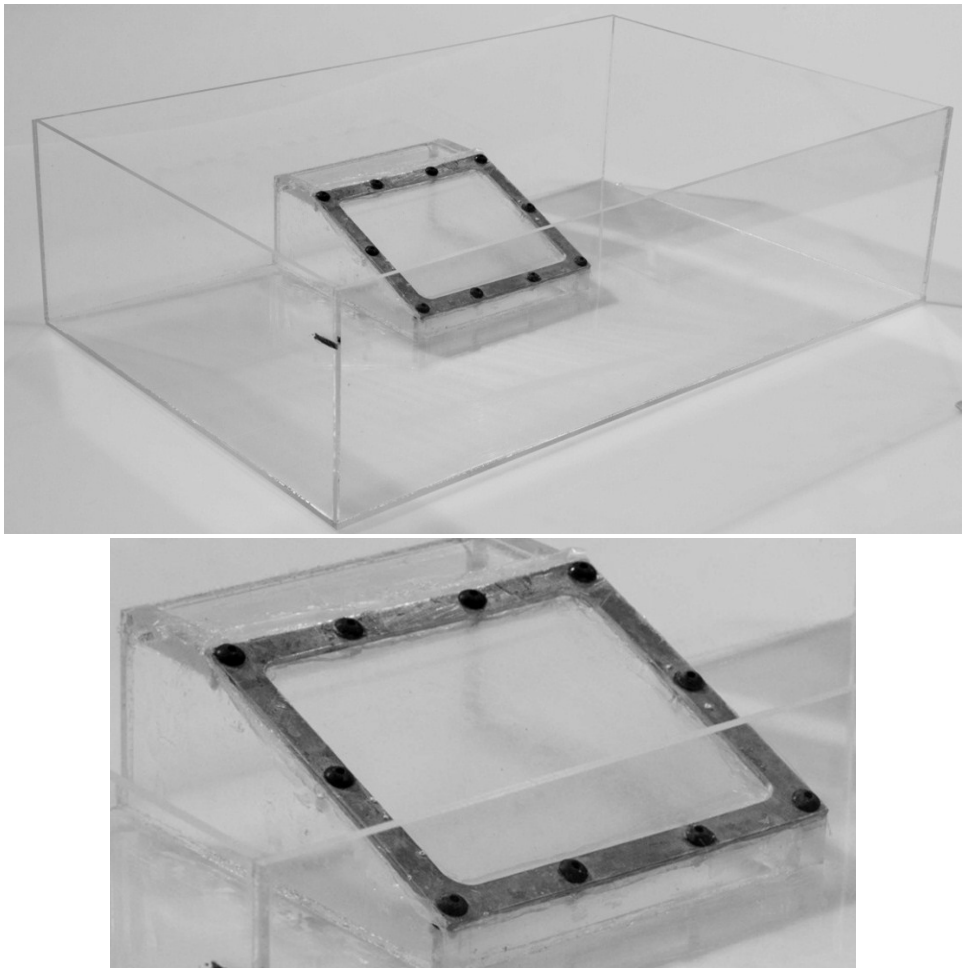

Figure 4.24. Fluid pan for CSF with baffle for placement of ultrasound probe.

The ultrasound probe was positioned below the baffle, and then allowed to stretch the baffle as it was pushed vertically into place adjacent to the dura to be imaged (Figure 4.25). To ensure that the space between the dura and the probe along the imaging path remained filled with fluid, the fluid pan was filled with artificial CSF to a height approximately 2 cm higher than the dural surface adjacent to the probe.

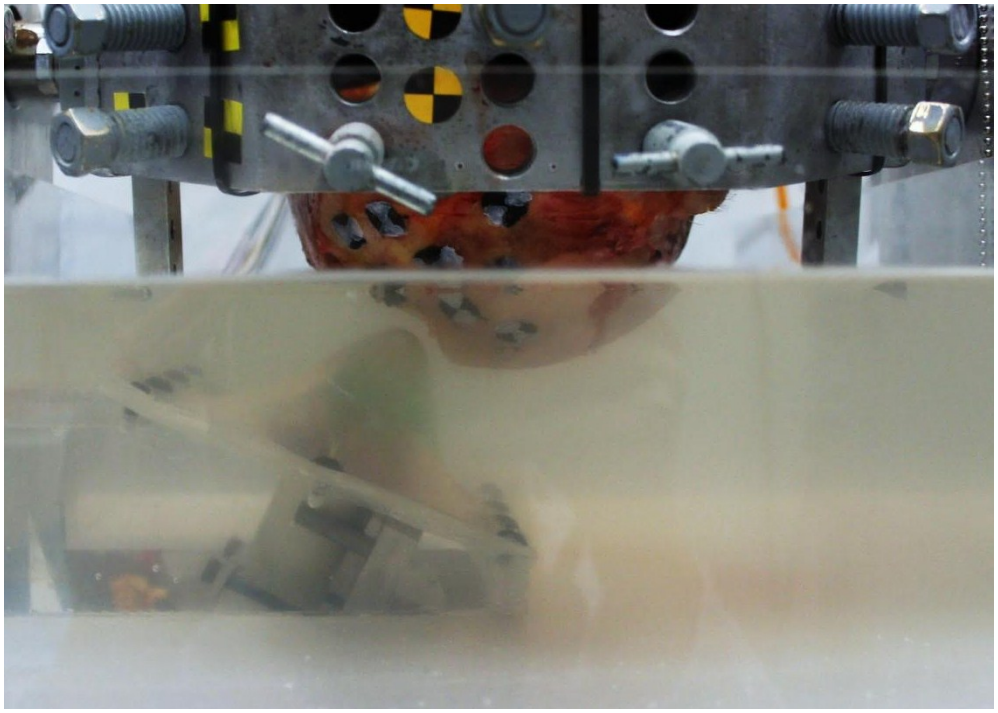

Figure 4.25. Ultrasound probe in position adjacent to dura, stretching fluid pan baffle.

4.8.3 Ultrasound Image Settings

B-mode ultrasound images were collected using a 550D ultrasound probe, which has a center frequency of 40 MHz. Image frame width was 4.08 mm and axial/vertical image height was 13 mm. For each test, 1000 frames were collected at a frame rate of

693 frames per second, the maximum allowable for the given frame dimensions. Timing was targeted to collect the entire motion sequence from acceleration through deceleration.

4.8.4 Stationary Images of Meningeal Layers

Following testing of subject PM01, two openings were made in the meninges in the area that was in view during acceleration in high-rate testing. In one opening, dura was removed, leaving the underlying arachnoid intact and in the second opening, both dura and arachnoid were removed exposing the cortex (Figure 4.26). Stationary ultrasound images were taken of these locations, using the same image settings used for motion tests to aid in identification of each meningeal layer in dynamic test images.

Figure 4.26. Openings cut in meninges for stationary images, through dura only (lower) and through dura and arachnoid (upper).

4.9 Control of Head Motion

4.9.1 High-Speed Loading

The head test fixture was accelerated by applying a linear force to the 11 cm load arm, which initiated rotational acceleration of the head cage via the fixture shaft (Figure 4.27).

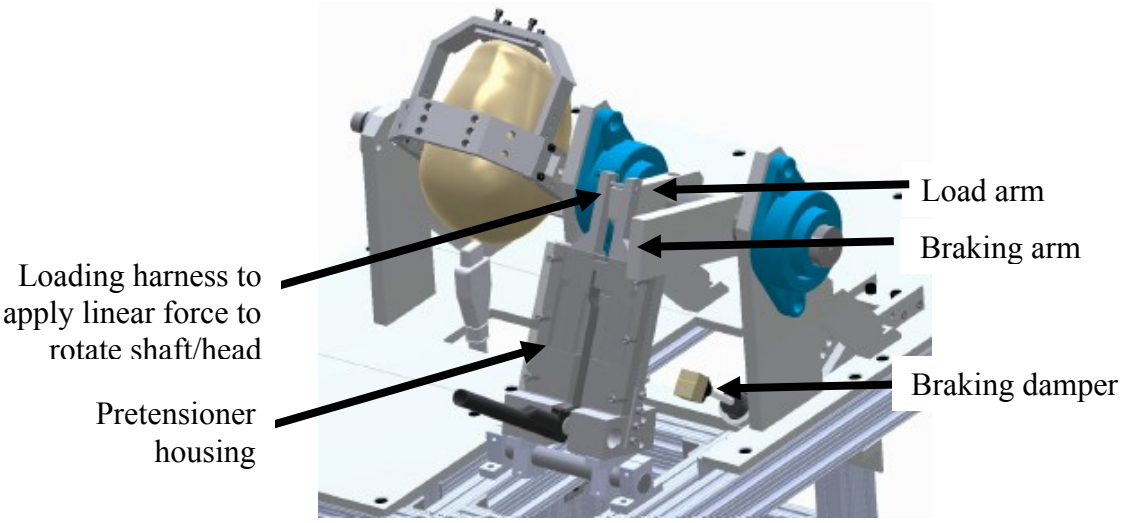

Figure 4.27. Acceleration of the head by a linear force applied to load arm.

The energy for the applied force was supplied by a production passenger car seat-belt pretensioner (TRW 5F13-5461202-AAW, TRW, Livonia, Michigan) positioned to apply a linear force to the end of the load-arm. The pretensioners were mounted with the stalk end of the pretensioner connected to a loading harness that was retracted when the pretensioner was fired. The retracting end of the pretensioner and the loading harness were confined by the pretensioner housing which guided the motion of the pretensioner. The pretensioner housing was fit with custom-cut wood blocks for each test to limit

stroke of the pretensioner as a method of controlling the energy applied. Nominal energy to be applied was estimated to target a maximum rotational velocity corresponding to the maximum linear meningeal velocity (υ_{max}) calculated using Equation 3.7. At a frame width of 4.08 mm, a frame rate of 693 frames per second, and targeting each point to be visible for at least 3.5 frames, maximum linear meningeal velocity was 1.9 m/s at the dural surface. The maximum corresponding rotational velocity (ω_{max}) was calculated with Equation 4.4, using the measured head radius of curvature (r), defined by the distance from the center of rotation to the dural surface for each test subject. In Equation 4.5, maximum energy (E_{max}) was calculated using the moment of inertia of the head and cage, estimated as described in Section 4.6. Pretensioner stroke length was then selected based on the empirical relationship between energy (E) and stroke length determined in 22 trials of the rotation fixture using the same model of pretensioner and dummy head configurations with moment of inertia ranging from 0.053 kg-m^2 to 0.096 kg-m^2. Because this empirical relationship was imprecise and not well defined, stroke length was selected conservatively, to ensure that tissue speed did not exceed υ_{max} of 1.9 m/s.

$$\omega_{max} = \frac{v_{max}}{r} \tag{4.4}$$

$$E_{max} = \frac{1}{2} I \omega_{max}^2 \tag{4.5}$$

Motion of the head was slowed to a stop using a braking damper with a padded face against the 22 cm anterior braking arm (Figure 4.27). Both the starting and stopping position for head rotation could be adjusted by repositioning the pretensioner mount and

the braking damper, respectively. The starting and stopping position for each head were adjusted based on the arc length over which there was a consistent radius of curvature of the dura in the skull window.

4.9.2 Low-Speed Loading

For lower-rate loading the rotation shaft was allowed to accelerate from rest under the force of gravity and then decelerated to a stop using a padded brake-stop for the 22 cm braking arm. For subject PM01, the motion was in the anterior-posterior direction so that the deceleration was in a direction simulating an occipital impact. For subject PM02, an additional 22 cm braking arm was added to the shaft, extending in the opposite direction as the load arm so that head motion for low-rate loading was in the posterior-anterior direction and deceleration in a direction simulating a frontal head impact (Figure 4.28). The start position for the motion was selected to maximize viewing of motion over the vertex of the head. The brake-stop position was selected after a speed-shot demonstrated the angle at which the head exceeded a rotational velocity of 120 degrees per second (Figure 4.29). The padding on the braking stop was adjusted for subsequent impacts until the appropriate padding was identified to produce peak rotational acceleration during the stopping phase within a target range of 124 to 143 rad/sec^2. The dimensions and characteristics of the padding materials determined to produce the desired acceleration pulse are identified for each test in Chapter 5.

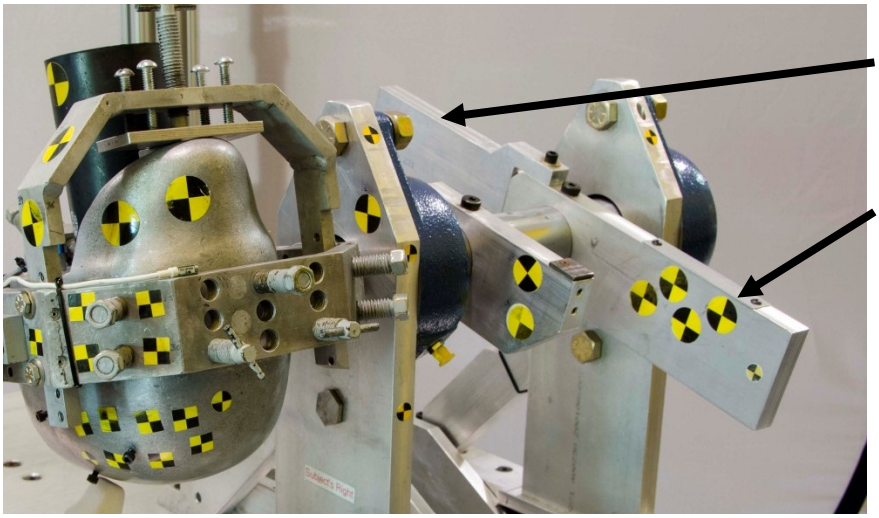

Figure 4.28. Braking arms for stopping motion in low-rate tests.

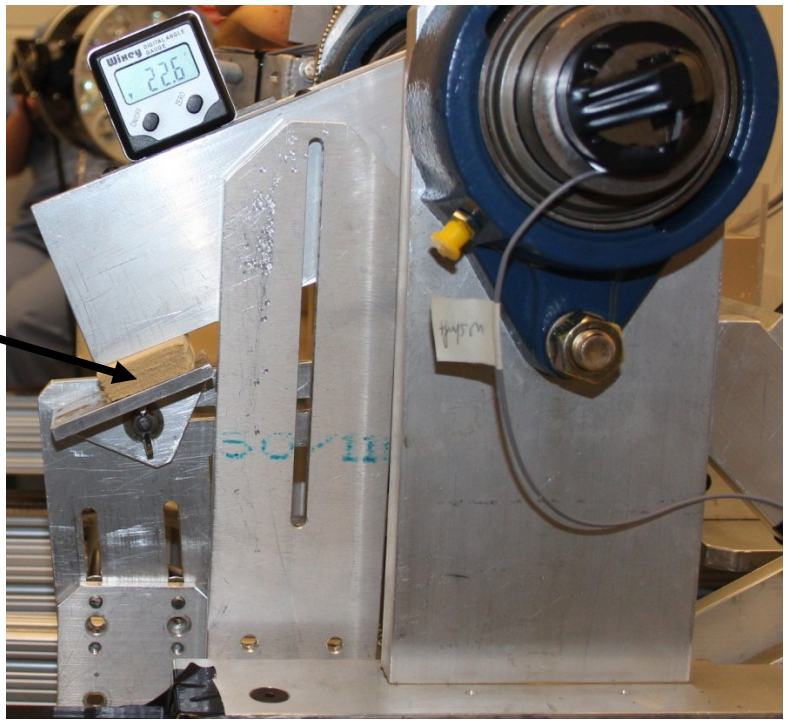

Figure 4.29. Adjustable-position brake stop with padding in place.

4.10 Kinematic Analysis

Acceleration and rotational velocity results were processed by removing offset prior to motion and filtering with a low-pass CFC 180 filter (300 Hz) using DIAdem Version 12 (National Instruments, Austin, Texas). Head rotational velocity, measured using orthogonal angular rate sensors mounted to the head were transformed to the fixture co-ordinate system to yield rotational velocity of the head about the fixture's X-, Y-, and Z-axes. Rotational acceleration of the cage was estimated by dividing the difference between the output of two cage-mounted accelerometers by the distance between them. Head angle was estimated by integration of cage- and head-mounted angular rate sensors.

4.11 Ultrasound Motion Analysis

4.11.1 Image Processing

The image scale factor, in mm/pixel, was determined using the FreeCurve tracking tool in the VevoStrain post-processing utility for the Vevo 2100. Vevo 2100 cine-images were exported as DICOM image files and converted to avi image format using Philips DICOM Viewer (Philips, Best, The Netherlands, Version R2.6L1-SP1). The converted video files of each motion test were analyzed using TEMA Version 3.7 image analysis software (Image Systems, Linköping, Sweden).

4.11.2 Image Tracking

All image tracking was done using TEMA, with the manual scaling set to the VevoStrain-determined image scale factor.

Points on the dura were tracked through the entire motion sequence for calculation of the cumulative displacement time history from initial position through acceleration and through deceleration. For synchronization with kinematic data, time zero was identified by determining (1) the first frame in which motion was visible, and (2) the lateral position at which motion appeared to start in the frame. Since the time at which each point is imaged is proportional to its lateral position in the frame (Equation 3.2) the point in the frame at which motion is first visible can be used to estimate the time of the start of motion.

Points throughout the image, from the dura through the visible depth of the brain tissue, were tracked for the acceleration phase of the high-rate tests and for the deceleration phase of the low-rate tests. The motion of these points was used to estimate the displacement of the arachnoid and cortex relative to the dura during the period of interest for each test.

4.11.3 Calculation of Dura Cumulative Displacement

The positions of points on the dura were used to calculate the cumulative displacement of the dura through the entire motion sequence for both high-rate and low-rate tests. Using the methods described in Chapter 3, the time at which each point was imaged was calculated as a function of the image frame's start time and the position of the point across the width of the image frame (Equation 3.2). After each new tracked point was added, the time-displacement of all previously-tracked points was curve-fit using the Matlab weighted linear least-squares "loess" smoothing function, which uses local regression on a quadratic model. The starting displacement of each tracked point

was calculated by interpolating from the time-displacement history estimated from all previously tracked points. After all points had been tracked and a final time-displacement curve estimated, tracking error (e) was estimated for each tracked point as the difference between the point-estimated displacement and the final time-displacement curve interpolated at the same time point. Mean and variance (σ_e^2) of the tracking error were calculated for each test.

4.11.4 Comparison of Dura Motion to Skull Motion

Rotation angle of the head about the fixture's Y-axis was estimated from the dura time-displacement history by dividing the cumulative displacement of the dura by the radius of rotation (the distance from the fixture's rotation axis to the dura). The radius of rotation was estimated from the radius of curvature of the dura measured during subject preparation, since the head was positioned such that the fixture's rotation shaft (Y-axis) was located at the center of dura curvature. The rotation angle time-history calculated from the ultrasound-tracked dura was then compared for each test to the head angle about Y calculated using the skull-mounted angular rate sensors.

4.11.5 Evaluation of Strain in the Dura

For every pair of adjacent tracked dura points visible in two consecutive frames during the entire motion sequence, the change in distance (Δ_{Dist}) between the points over the two frames was calculated. If strains in the dura were negligible, so that the dura could be assumed to be moving essentially as a rigid body, the distances between pairs of points in consecutive frames would not change and Δ_{Dist} would be zero throughout the motion sequence.

The approach used to determine if strain in the dura was negligible was to plot Δ_{Dist} versus time for all pairs of adjacent points visible in two consecutive frames. This time-history was used to identify any periods of time where Δ_{Dist} deviated from zero in a non-random pattern. In particular, the acceleration time-period in high-rate tests and the deceleration time-period in low-rate tests were scrutinized for any indication of between-frame stretch of the dura.

4.11.6 Displacement of Arachnoid and Cortex Relative to Dura

For a time sequence including the primary deceleration in low-rate tests, points were tracked across the tissue layers identified from dura down through the cortex. Cortex points were selected as close as possible to the cortical surface, and at approximately 1 mm increments through the image.

For every pair of consecutive frames during the deceleration phase, absolute between-frame displacement of each tracked point was calculated relative to the x (lateral) and y (axial or vertical) dimensions of the ultrasound frame and shown in displacement field plots.

For each tissue layer tracked, the motion relative to the dura was estimated by estimating the cumulative displacement of the tissue layer relative to the displacement of the dura in both x and y dimensions of the image. The time of each relative displacement point in the arachnoid or cortex was determined based on the image frame's start time, and the position of the point across the width of the image frame (Equation 3.2). The starting displacement for each point was calculated as described in Section 3.2.4.

Chapter 5: Results of Head Rotation Study

5.1 Subjects

Full motion testing was performed on two female *post mortem* subjects, both of whom died of thoracic cancer. Subject characteristics are listed in Table 5.1. Characteristics of the prepared heads, and the combined head and cage for each test, are shown in Table 5.2. For both subjects, the estimated radius of curvature along the dura in the area to be imaged was 8 cm, so that the head was positioned with the center of rotation at a targeted 8 cm from the dural surface during rotation.

Table 5.1. *Post mortem* test subject characteristics

Subject	Number	Sex	Age	Height	Weight	Cause of Death
PM01	#6683	Female	75	160 cm	83 kg	Lung cancer
PM02	#6704	Female	49	165 cm	67 kg	Mediastinal Myxofibrosarcoma

Table 5.2. Dimensions and mass properties of subject heads

	Head Width At Tragions	Weight Head and Neck (grams)	Moment of Inertia Head & Cage about Rotation Axis
PM01	14.7 cm	4538	0.074 kg-m^2
PM02	11.6 cm	3950	0.058 kg-m^2

Subject availability was confirmed 9.6 hours after death for subject PM01 and 29.5 hours after death for subject PM02. Testing was complete at 59 and 86 hours respectively for the two subjects. Timing of other test procedures, relative to time of death, is shown in Table 5.3.

Table 5.3. Time elapsed after death (hours) for test procedures

Subject	MRI complete	CSF perfusion initiated	Rotation testing start	Rotation testing complete	Post-test pressure check	Post-test dissection complete
PM01	13.5	18.2	41.5	59	81	100.5
PM02	35.0	38.6	81.4	85.7	106	107.2

5.2 Tests Performed on Subjects PM01 and PM02

Rotation tests with ultrasound imaging were performed on both subjects at low and high rates of acceleration. Acceleration in high-rate tests was produced by the pretensioner configuration. In the low- and mid-rate tests, the head and test fixture were dropped with gravity and deceleration was controlled by a padded brake-stop. On subject PM01, four low-rate tests were run, followed by one high-rate test, then two more low-rate tests (Table 5.4). On subject PM02, the test sequence was six low-rate tests, followed by 3 high-rate tests, and one repeat low-rate test. A final "mid-rate" deceleration test was run on subject PM02 in the low-rate configuration (gravity-drop onto a padded brake-stop) using a larger drop angle and less padding than in low-rate tests.

Table 5.4. Summary of tests performed on subjects PM01 and PM02

Subject	Test Number	Loading Mode	Loading direction	Test Conditions
PM01	PM01LOW01	Padded brake stop	Posterior to Anterior	Varied padding to match deceleration in previous low-rate volunteer tests
	PM01LOW02			
	PM01LOW03			
	PM01LOW04			
	PM01ROTATE01	Pretensioner acceleration	Anterior to Posterior	High-rate acceleration
	PM01LOW05	Padded brake stop	Posterior to Anterior	Repeated under conditions used in PM01LOW02
	PM01LOW06			
PM02	PM02LOW01	Padded brake stop	Anterior to Posterior	Varied padding to match deceleration in previous low-rate volunteer tests
	PM02LOW02			
	PM02LOW03			
	PM02LOW04			
	PM02LOW05			Repeated under conditions used in PM02LOW04
	PM02LOW06			
	PM02ROTATE01	Pretensioner acceleration		High-rate acceleration
	PM02ROTATE02			
	PM02ROTATE03			
	PM02LOW07	Padded brake stop		Repeated under conditions used in PM02LOW04
	PM02LOW08			Mid-rate deceleration

On subject PM01, attempts to cut the skull window without damage to the dura failed on both the left and right side of the vault. The damaged dura in the opening on the *left* side of the head was repaired as described in Section 4.3.6 and all ultrasound imaging was performed on the left side of the head. However, in spite of attempts to seal the damaged dura, it appeared that fluid penetrated the interface between the dura and arachnoid during test procedures. Therefore, relative motion results for PM01 are shown for comparison but not presented in detail.

On subject PM02, the dura was damaged during preparation of a window on the left side of the head, but preparation of a window on the right side of the head was

successful, leaving the dura fully intact. Ultrasound imaging on PM02 was performed through the skull opening on the *right* side of the head. Ultrasound images for low-rate test PM02LOW04 (the first low-rate test run on subject PM02 that was within the targeted deceleration range to match previously reported volunteer test results) were processed and analyzed in detail. The results for that test, along with summary information on the remaining tests, are presented in this chapter.

5.3 MR Images for Atrophy Estimation

MR images of both subjects' heads were collected for quantification of atrophy. Qualitative comparison of sample coronal slices of T1 MR images showed that 74 year-old subject PM01 (Figure 5.1) had substantially larger ventricles and more pronounced sulci than 49 year-old subject PM02 (Figure 5.2), indicative of more atrophy in PM01.

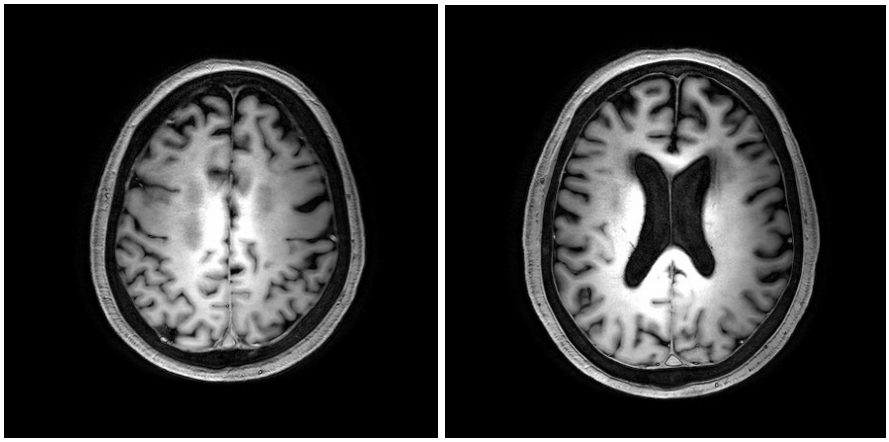

Figure 5.1. Coronal T1 slices of MR image of subject PM01.

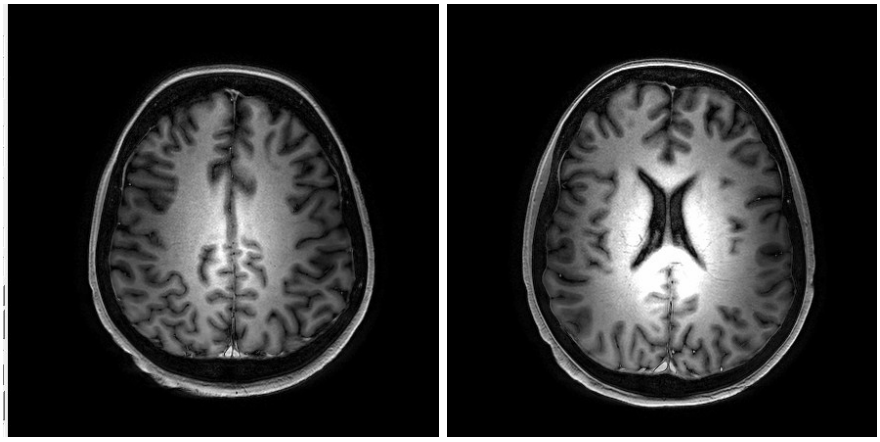

Figure 5.2. Coronal T1 slices of MR image of subject PM02.

However, although the MR images for both subjects were collected under the same image settings and conditions and on the same 7-Tesla MR machine, segmentation of the images to distinguish the proportional areas of brain and atrophy resulted in inconsistent identification of CSF in the two sets of images. This inconsistency suggested that the *post mortem* T1 images were not suitable for processing with conventional SPM8 procedures. As a result, direct comparison between the levels of atrophy in the two subjects could not be made.

5.4 Identification of Meningeal Layers in Ultrasound Images

In subject PM01, post-test ultrasound images of the meninges were recorded at the start location for high-rate testing. After testing, a strip of dura was resected across the width of the window and in an adjacent location both dura and arachnoid were resected (Figure 5.3) in order to document the appearance of the tissue in ultrasound images to better identify dura and arachnoid in images of intact tissue. Ultrasound images with dura removed (Figure 5.4) show a bright line on the surface of the cortex that is not visible in Figure 5.5. This bright line is the arachnoid in this location. The dura is visible at the edge of the opening in both sets of images.

Images from tests showed a less distinct boundary between the dura and underlying meningeal layers (Figure 5.6). While an interface layer was visible between the dura and cortex, it could not be definitively identified as the arachnoid and will be referred to as the dura/cortex interface throughout the analysis.

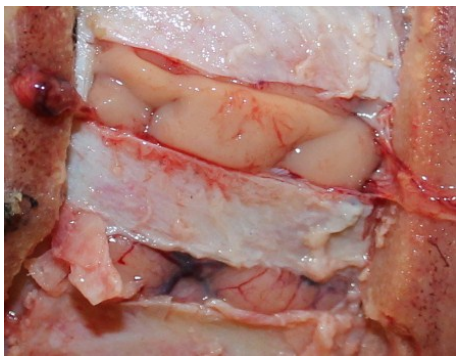

Figure 5.3. Post-test resection of strip of dura and arachnoid (top) and dura only (bottom).

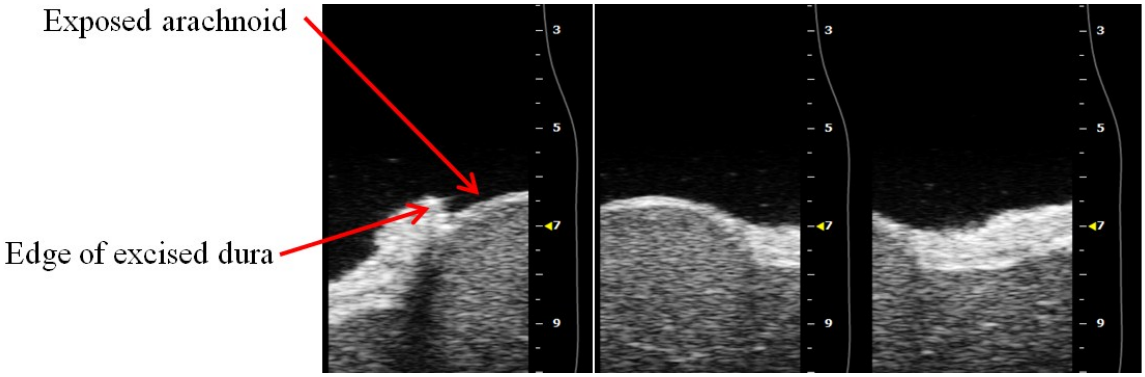

Figure 5.4. Ultrasound images across window with dura removed (intact arachnoid visible in opening).

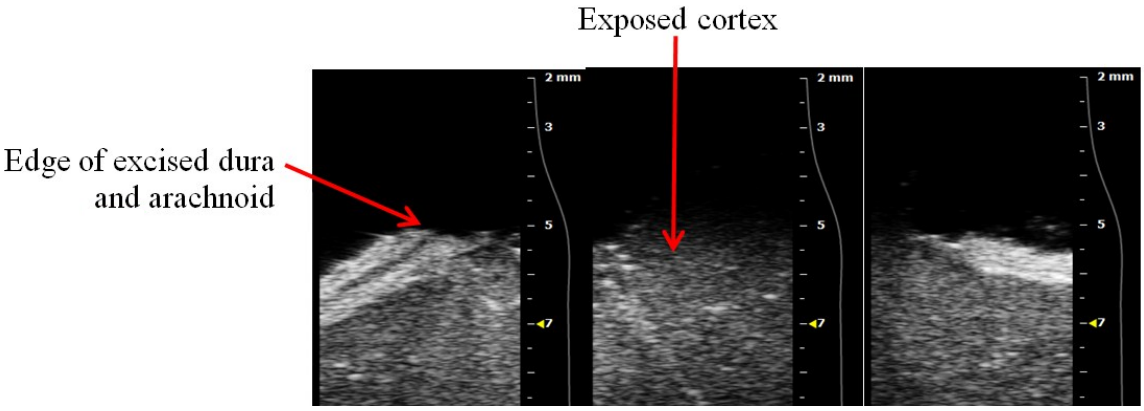

Figure 5.5. Ultrasound images across window with dura and arachnoid removed (exposed cortical surface visible in opening).

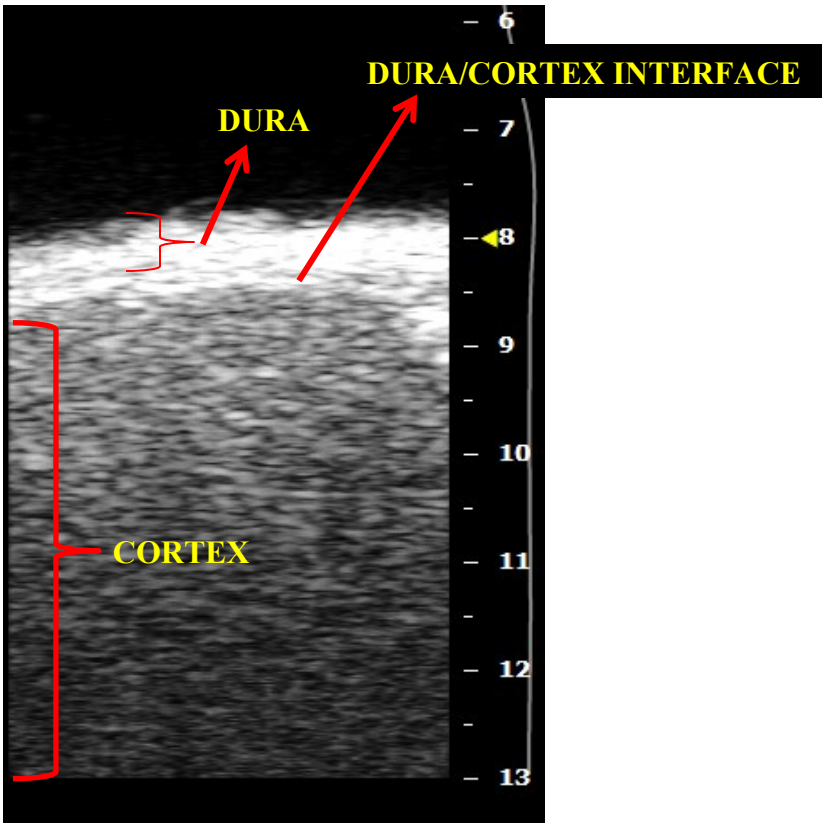

Figure 5.6. Sample ultrasound image frame from PM02LOW04 .

5.5 Low-Rate Rotation Tests

5.5.1 Head Kinematics in Low-Rate Rotation

With each subject, multiple low-rate rotation tests were performed in order to achieve the target kinematic conditions tested previously by Feng et al. in volunteer testing (2010). The target conditions were a rotational velocity at impact of greater than 120 degrees/sec and peak deceleration between 124 and 143 rad/sec^2. In the Feng et al. tests, the head rotated in a posterior-anterior direction before being decelerated to simulate a frontal impact. For subject PM01, the closest test to these conditions was PM01LOW04 in which the anterior-posterior motion was braked after 23 degrees of

rotation by braking arm contact with 12.5 mm thickness Ensolite ALC closed cell foam (contact area 25 mm x 25 mm). However, since breach of the dura during preparation of subject PM01 appeared to have allowed fluid between the dura and arachnoid, relative motion between the meningeal layers was not expected to be comparable to *in vivo* motion. For subject PM02, the first test to fall in the target corridor was PM02LOW04 in which posterior-anterior rotation was braked after an 18.5 degree rotation drop by braking arm contact with 15 mm thickness 2-pound density ethylene vinyl acetate (EVA) foam (contact area 25 mm x 50 mm). The test was repeated on subject PM02 under the same conditions for a total of 3 repeats *prior* to high-rate testing (PM02LOW04, PM02LOW05 and PM02LOW06) and one repeat *after* high-rate testing (PM02LOW07). Peak rotational velocity of the head, measured by skull-mounted angular rate sensors, and peak deceleration of the cage, calculated from cage mounted linear accelerometers, are listed in Table 5.5 for all tests close to the target kinematics from the Feng et al. tests.

Table 5.5. Peak rotational kinematics of head and cage in low-rate tests

Subject	Test No.	Direction of Initial Rotation	Peak Rotational Velocity of Head (deg/sec)	Peak Deceleration of Cage (rad/sec^2)
Target corridors from Feng et al.			>120	124-143
PM01	LOW04	Anterior-to-posterior	112	154
PM02	LOW04	Posterior-to-anterior	121	130
	LOW05	Posterior-to-anterior	125	135
	LOW06	Posterior-to-anterior	126	138
	LOW07*	Posterior-to-anterior	118	130

*PM02LOW07 was performed after high-rate testing and all others were performed prior to high-rate testing.

Full analysis was performed on PM02LOW04, since it was representative of the tests where motion fell in the corridor reported in Feng et al.'s volunteer tests, and resulted in the same direction of deceleration as in Feng's testing. Summary results are shown for the remaining low-rate tests. The kinematic time histories of the motion of the head and cage are shown for test PM02LOW04 in Figure 5.7. At a peak rotational velocity of 121 degrees per second, the estimated linear velocity of the dura at a nominal distance of 8 cm from the center of rotation was 0.17 m/s.

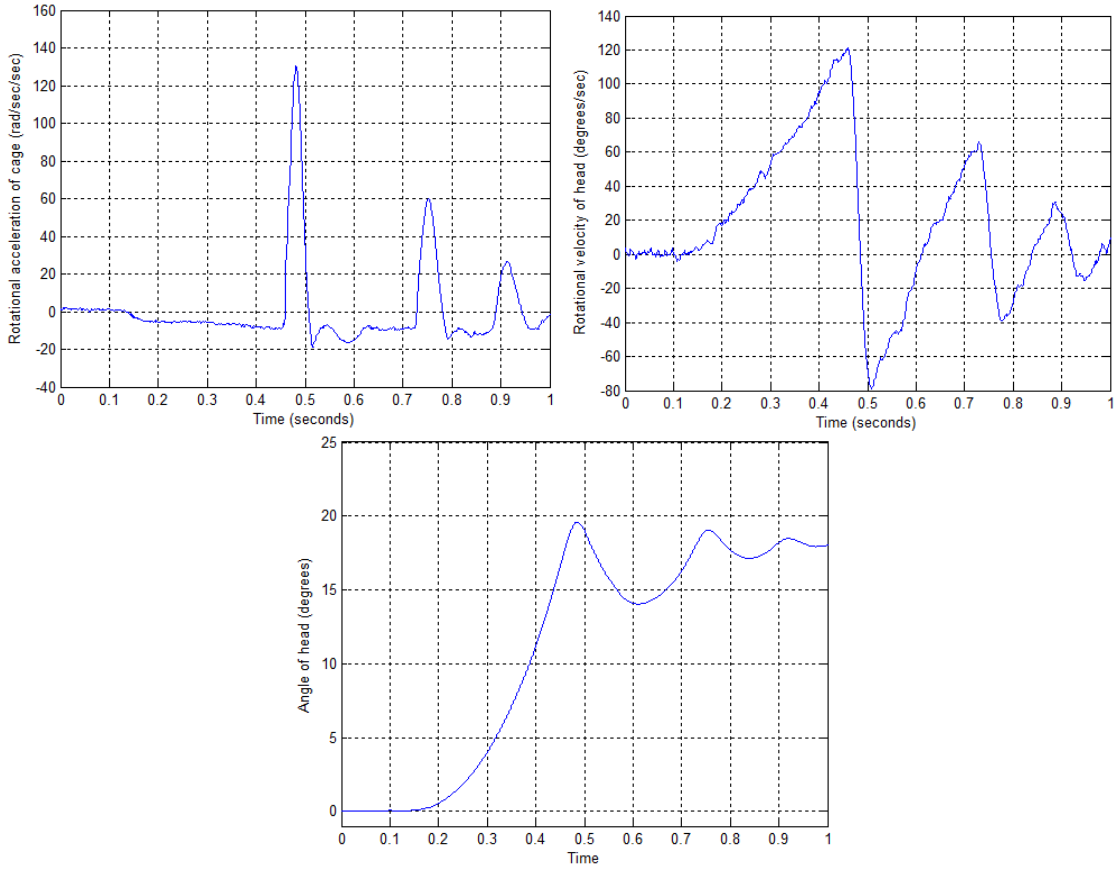

Figure 5.7. Rotational kinematics of head and cage about Y: PM02LOW04.

5.5.2 Motion Analysis in Low-Rate Rotation

Dura displacement was tracked with ultrasound for the entire acceleration and deceleration time sequence through PM02LOW04, and compared to the expected dural displacement estimated from the time history of the rotation angle of the skull about Y, multiplied by the radius of rotation, i.e. the distance from the center of the rotation shaft to the dural surface (Figure 5.8). This radius of rotation was nominally 8 cm as determined from the curvature of the dura in the area to be imaged using the procedure described in Chapter 4. Although the displacement estimated from angular displacement of the skull is sensitive to the precise measurement of radius of rotation[1], the similarity of dura displacement measured from ultrasound and estimated from skull rotation suggest that the dura and skull were moving essentially together throughout the deceleration sequence.

[1] An approximately 2 mm adjustment of the nominal radius of rotation results in a near-exact match between the dura displacement measured by ultrasound tracking and estimated from skull rotation.

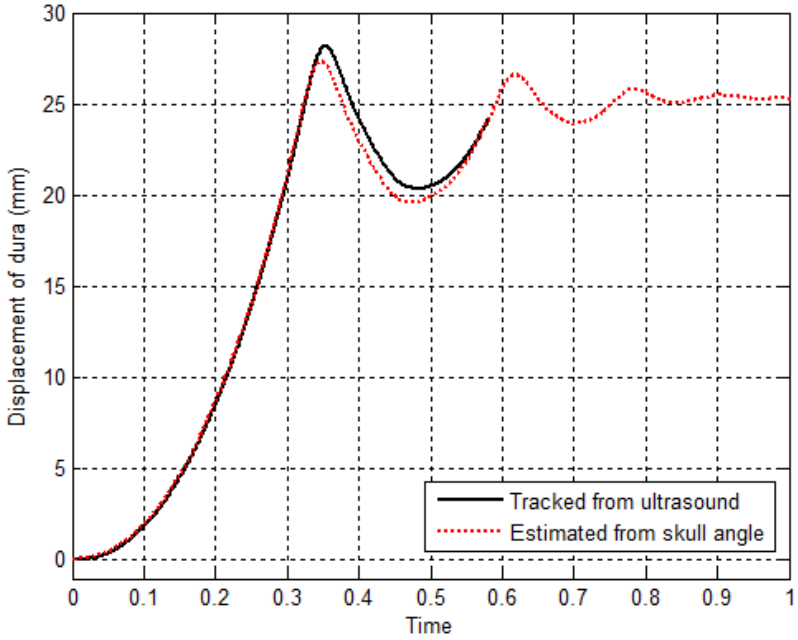

Figure 5.8. Displacement of dura past the ultrasound probe in PM02LOW04, calculated from tracking of ultrasound images and estimated from head rotation angle at nominal radius of rotation of 8 cm.

Potential stretch of the dura was evaluated by estimating how much the distance changed between pairs of adjacent points that were tracked in consecutive ultrasound image frames (Δ_{Dist}). If there was no stretch, Δ_{Dist} would be expected to be close to zero throughout the motion sequence. Any periods of time where Δ_{Dist} deviated from zero in a non-random pattern would suggest potential stretch, or normal strain, in the dura. Figure 5.9 shows the distribution of Δ_{Dist} for low-rate test PM02LOW04. The mean initial distance between the pairs of points used to track Δ_{Dist} was 0.37 mm. Mean Δ_{Dist} over the entire motion sequence was -0.00059 mm, with a standard deviation of 0.088 mm. Outliers beyond two standard deviations from the mean indicate pairs of points that moved farther apart or closer together between consecutive frames, but these appear scattered through the entire motion sequence suggesting tracking error rather than periods

of true tissue stretch or distortion. In particular, there does not appear to be any sustained distortion of the tissue during the period of deceleration when head rotation is arrested by padding at approximately 0.35 seconds.

Based on this analysis of change in distance between adjacent tracked points in consecutive image frames, normal strain of the dura in PM02LOW04 was determined to be negligible and the dura was treated as a rigid body for the remainder of the analysis.

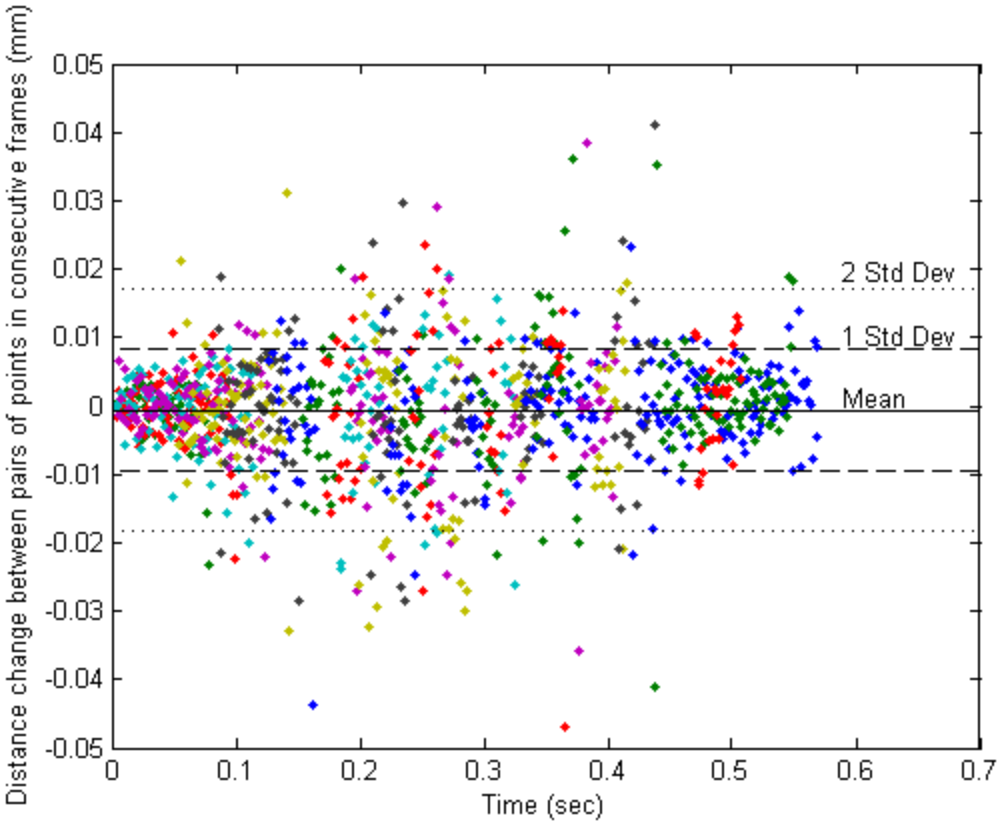

Figure 5.9. Change in distance (Δ_{Dist}) between adjacent tracked dura points in consecutive frames.

Displacement of tissue during the deceleration phase of the low-rate tests was calculated for test PM02LOW04. Tissue points throughout the image (Figure 5.10) were

tracked for the entire deceleration phase. The frame-to-frame displacement results during the deceleration phase were plotted as displacement fields for all frames during the deceleration phase of the head. Every fifth frame of the resulting displacement field plots are shown in Figure 5.11. Each arrow in each displacement plot shows the displacement of a single point between two consecutive image frames. For example, the first plot in Figure 5.11 shows the displacement of all points tracked between the ultrasound frame at 0.3290 seconds and the subsequent frame at 0.33045 seconds as shown in Figure 5.10. In the displacement field plots, tracked tissue points on the dura, dura/cortex interface layer, and cortex were identified.

Points were tracked at approximately 1, 2, 3 and 4 mm below the surface of the cortex. Deeper points were more difficult to track and to differentiate from surrounding tissue. At 3 to 4 mm below the surface of the cortex, there was significantly more artifact and "noise" in the tissue image making it difficult to visually confirm the position of automatically tracked points in each frame. Therefore, although these deeper points are illustrated in displacement field plots, they are not included in subsequent analyses.

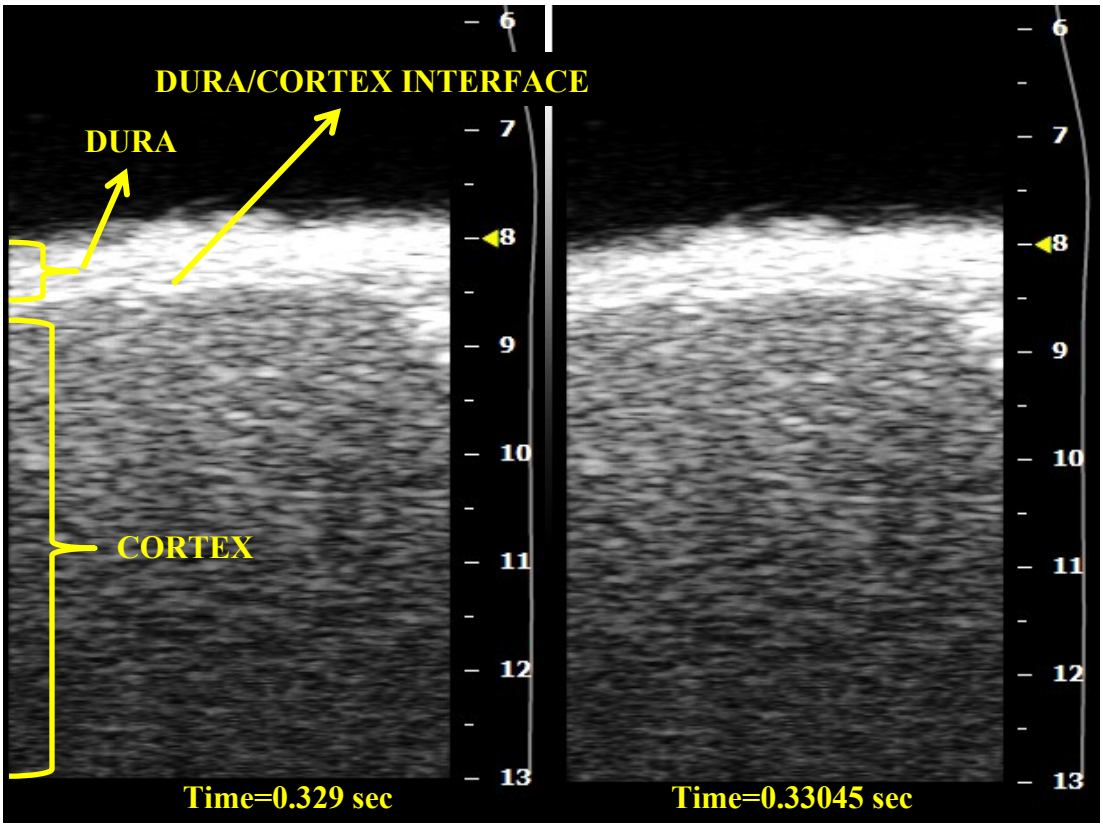

Figure 5.10. Sample ultrasound image frames from PM02LOW04.
The first displacement field plot in Figure 5.11 represents displacement of tissue points between these two frames.

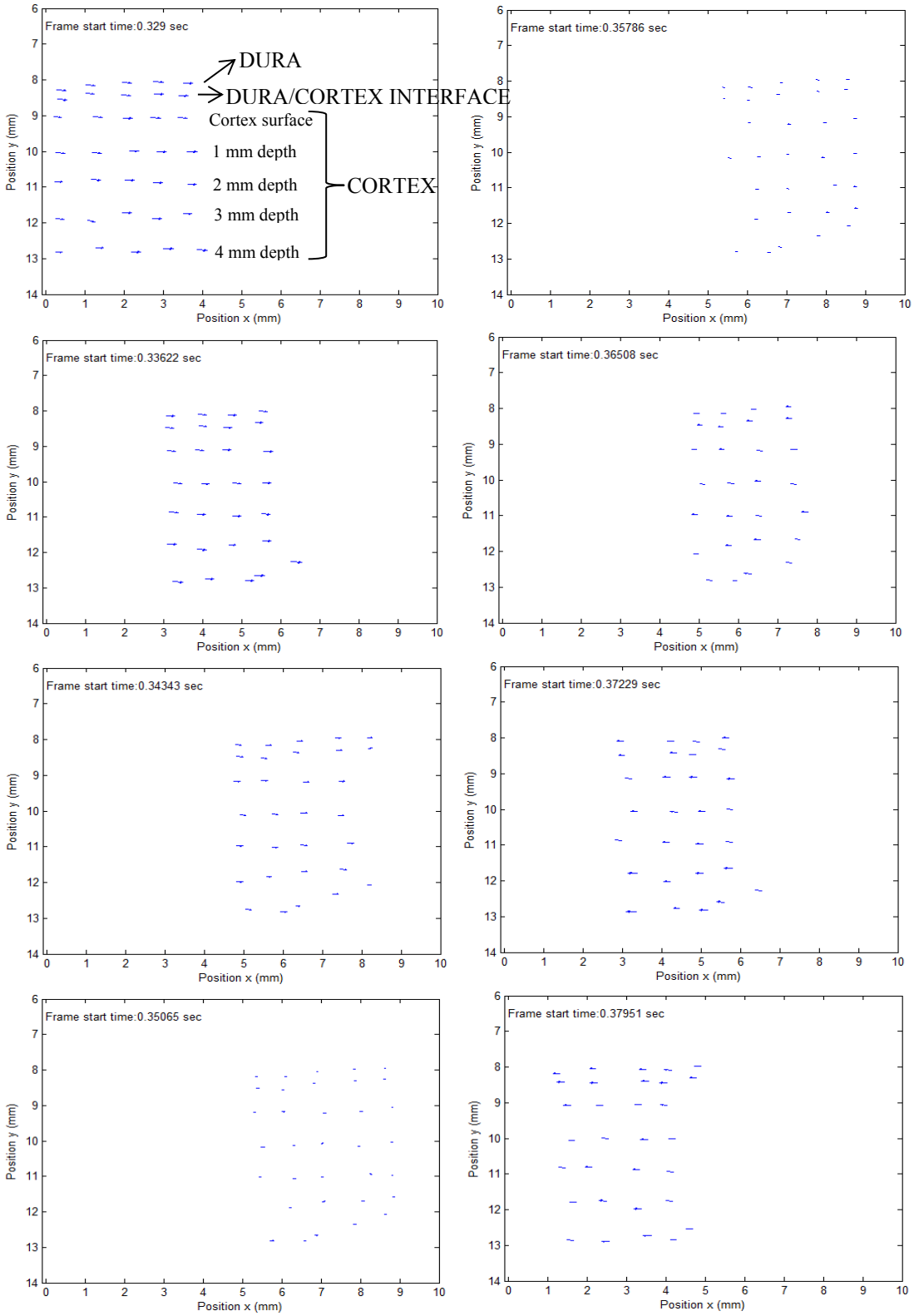

Figure 5.11. Displacement field plots of between-frame displacement for PM02LOW04.

The between-frame displacements in Figure 5.11 show little difference in cumulative displacement among each of the tracked layers during the deceleration phase. To better visualize displacement differences between the dura and the adjacent tissues, Figure 5.12 shows the cumulative displacement of each visible "layer" in the tissue, down to 2 mm below the surface of the cortex. Starting at a displacement equal to the displacement of the dura, as tracked in ultrasound from the beginning of motion (Figure 5.8), cumulative displacement of each tissue layer is estimated through the deceleration phase of head rotation in Figure 5.12 and plotted relative to the cumulative displacement of the dura in Figure 5.13. Note that any tracking error in these plots is cumulative. The dura/cortex interface layer at the anatomical location of the arachnoid shows negligible motion relative to the dura. All motion relative to the dura is in the cortex, primarily between the cortex surface and the dura, suggesting shear strain between these layers. None of the layers tracked displaces more than 0.2 mm relative to the dura. Since motion between the dura and skull was shown to be negligible, the motion relative to the dura reflects an estimate of motion relative to the skull.

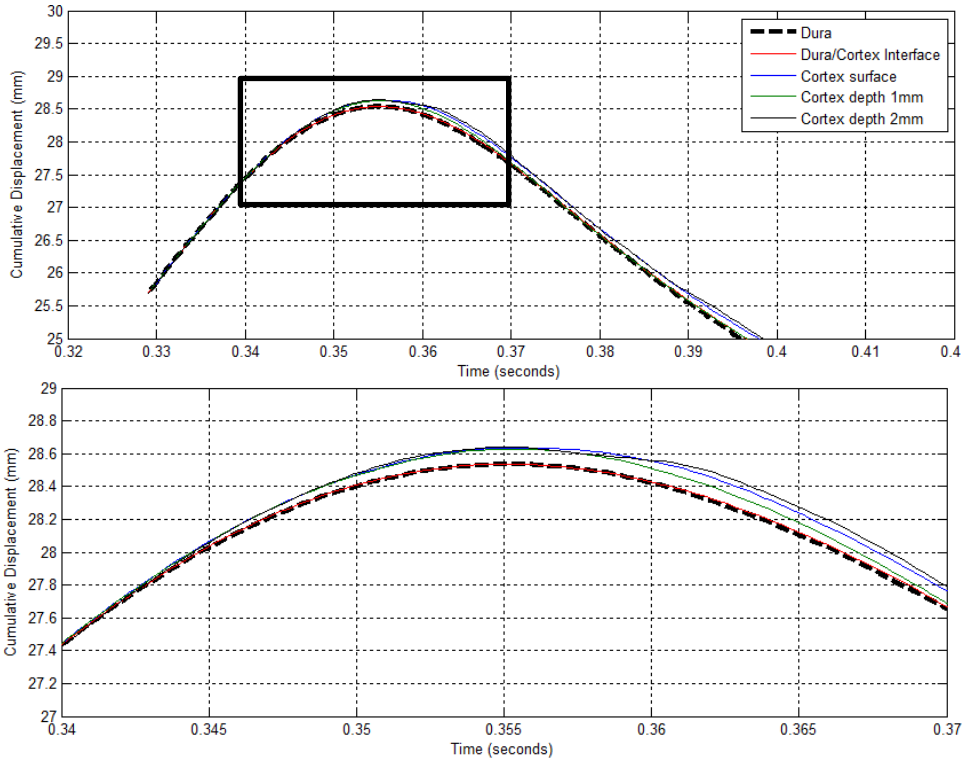

Figure 5.12. Cumulative displacement of layers of tissue during deceleration phase in PM02LOW04.
(Lower plot zooms in on period of peak displacement marked by box in upper plot).

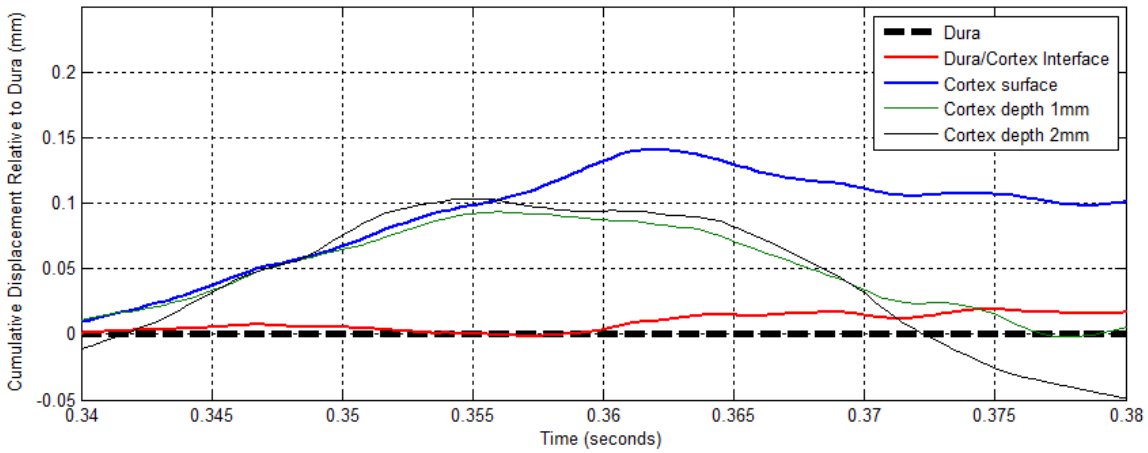

Figure 5.13. PM02LOW04 cumulative displacement of layers of tissue during deceleration phase relative to cumulative displacement of the dura.

The drop test conditions used for PM02LOW04 were repeated for PM02LOW05 and PM02LOW06. The cumulative displacement plots for these repeated tests are shown in Figure 5.14 and Figure 5.15. Among these repeated tests, there is consistently negligible motion between the dura and the dura/cortex interface layer, and less than 0.2 mm of relative motion in the superficial cortex relative to the dura.

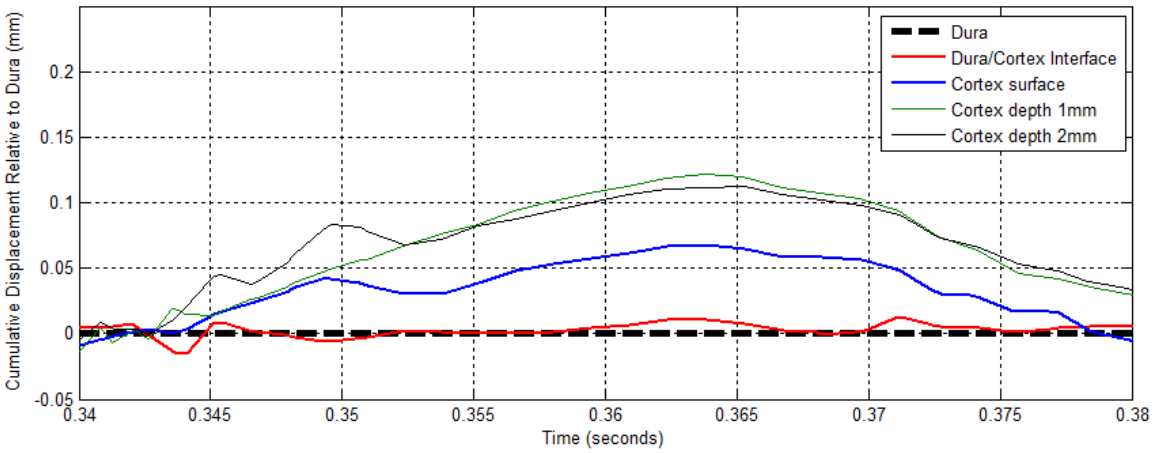

Figure 5.14. PM02LOW05 cumulative displacement of layers of tissue during deceleration phase relative to cumulative displacement of the dura.

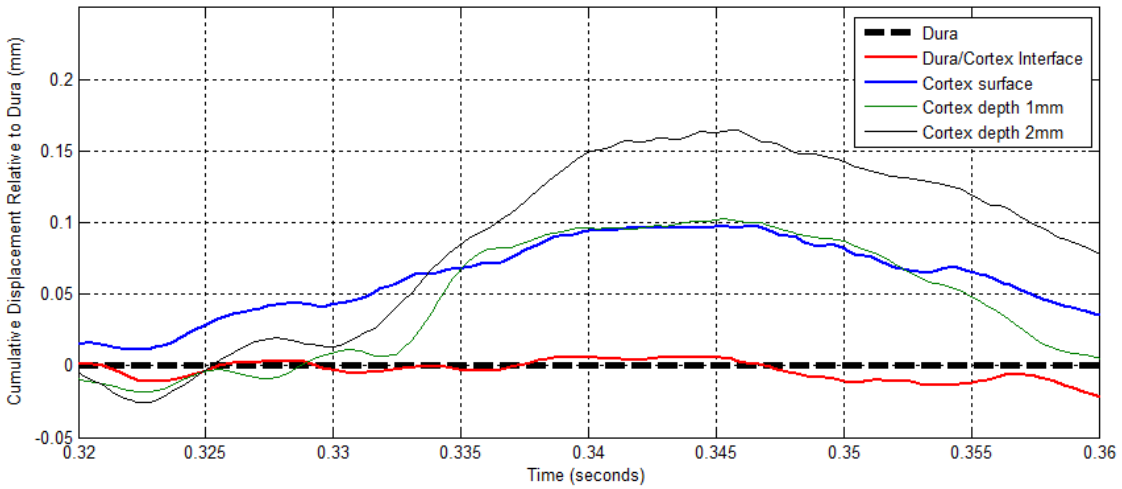

Figure 5.15. PM02LOW06 cumulative displacement of layers of tissue during deceleration phase relative to cumulative displacement of the dura.

The cumulative displacement of tracked layers of tissue was also estimated in low-rate test PM01LOW04 (Figure 5.16). As in low-rate tests on subject PM02, the cortex surface moved relative to the dura. However, in contrast to subject PM02, the interface layer in the PM01 test also showed limited motion, appearing to slide approximately 0.05 mm relative to the dura early in the deceleration phase. This relative motion may have been the result of the laceration in the dura of subject PM01, which likely allowed fluid between the dura and arachnoid during testing. Relative motion of tissue layers in this test should therefore be interpreted cautiously and is presented here for comparison with results from intact subject PM02, rather than as an estimate for *in vivo* meningeal motion.

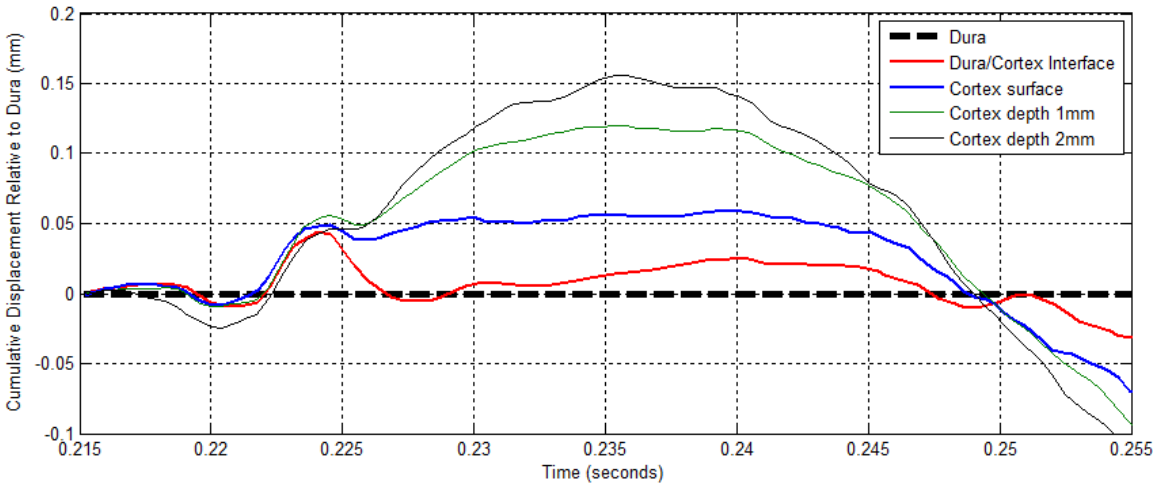

Figure 5.16. PM01LOW04 cumulative displacement of layers of tissue during deceleration phase relative to cumulative displacement of the dura.

5.6 Mid-Rate Rotation

For subject PM02 only, an additional mid-rate test was run using the low-rate test configuration but allowing the head to reach a higher rotational impact velocity than targeted in low-rate testing and maximizing cage deceleration by using less padding to brake head motion. This test was performed *after* high-rate testing when tissue damage was possible. Therefore, the mid-rate rotation test results are summarized here qualitatively in order to explore the effectiveness of ultrasound motion tracking in this range of rotational acceleration and velocity. Absolute relative displacements are not reported.

5.6.1 Head Kinematics in Mid-Rate Rotation

In mid-rate test PM02LOW08, the head and cage were allowed to rotate through an approximately 42 degree arc onto a thin layer of foam rubber, resulting in peak deceleration of the cage over 1200 rad/sec^2 (Table 5.6). The kinematic time history of the motion of the head and cage is shown for this mid-rate test in Figure 5.17.

Table 5.6. Peak rotational kinematics of head and cage in mid-rate test

Subject	Test No.	Peak Rotational Velocity of Head (deg/sec)	Peak Rotational Deceleration of Cage (rad/sec^2)
PM02	LOW08	173	1230

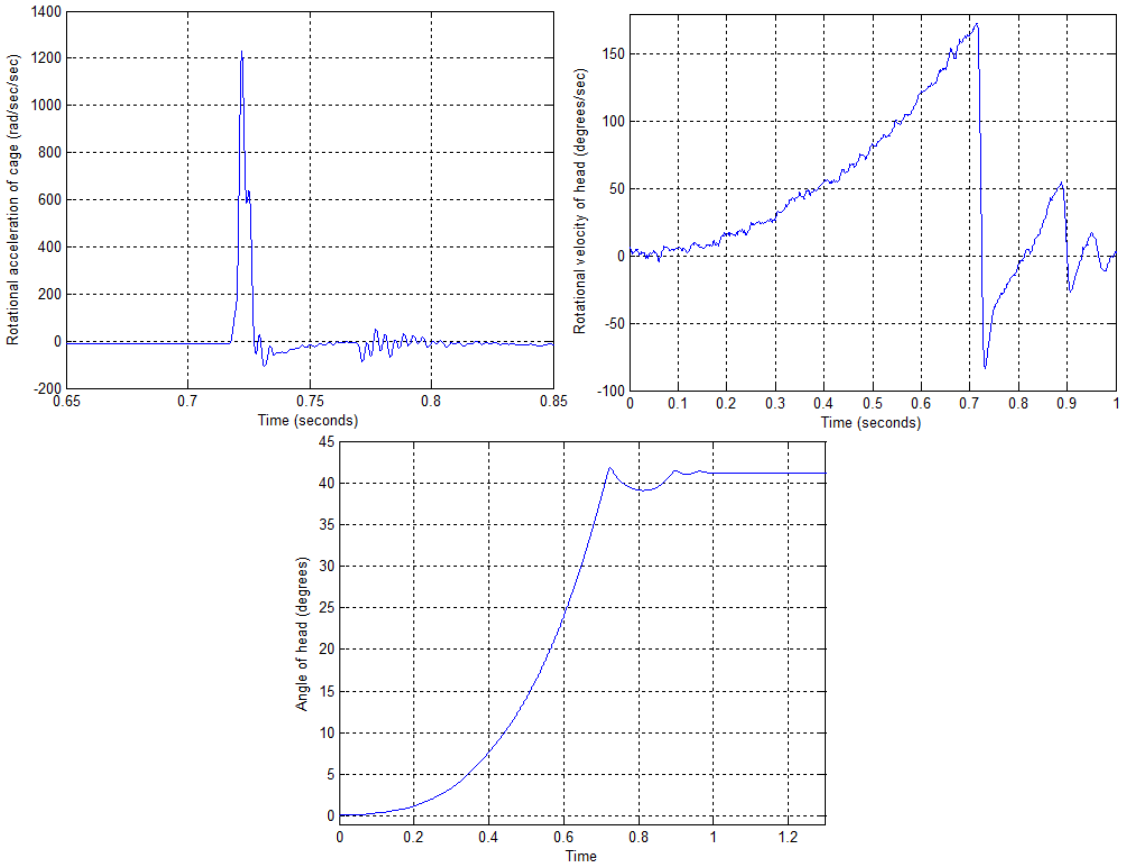

Figure 5.17. Rotational kinematics of head and cage about Y: PM02low08.

5.6.2 Motion Analysis in Mid-Rate Rotation

Although the mid-rate rotation test was performed after high-rate testing and therefore cannot be used for motion analysis of undamaged tissue, the mid-rate rotation results can be used to evaluate whether ultrasound collection procedures and image tracking procedures would be effective at higher speeds. The motion of the dura and cortex in mid-rate testing is easily visualized throughout the acceleration with gravity and deceleration on impact with the padded brake stop except for brief periods when artifact obscures the cortex, or cortex and dura. The primary period of interest during the

deceleration of the head shows little artifact and was easily tracked using semi-automated image tracking techniques. Figure 5.18 shows two sample points tracking motion in the cortex during deceleration.

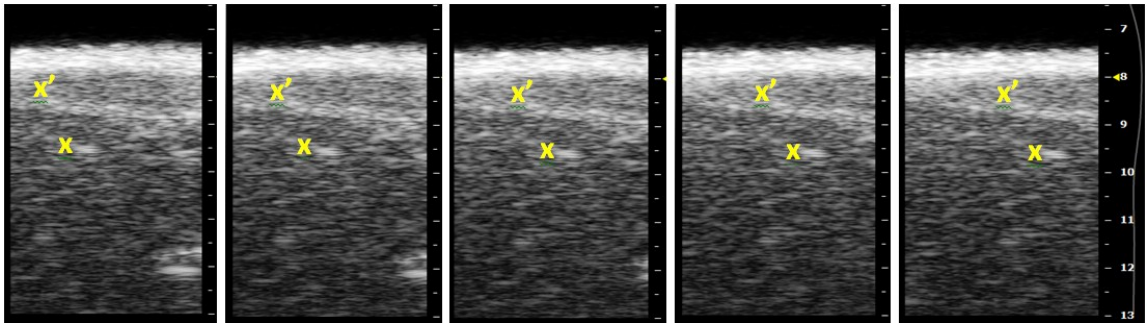

Figure 5.18. Sample consecutive images during deceleration period in PM02LOW08. (Scale at right in mm).

5.7 High-Rate Rotation

High-rate rotation tests were run for both subjects. In both tests, pretensioner loading lead to an initial rotational acceleration with a peak between 7 and 8 krad/sec^2 and duration of approximately 5 milliseconds, followed by a period of rapid deceleration (Figure 5.19 to Figure 5.21). This acceleration-deceleration pulse resulted in an initial peak rotational velocity "overshoot" approximately 50% higher than the final steady-state rotational velocity.

While the resulting rotational velocities were within the range that was predicted to be analyzable by ultrasound tracking methods, individual tracking points on the visible tissue did not stay in view for consecutive frames during the initial acceleration-deceleration period, preventing quantitative image analysis. This section summarizes the

kinematics of the head and cage during high-speed tests and describes the resulting ultrasound images qualitatively.

5.7.1 Head Kinematics in High-Rate Rotation

Rotational kinematics peak values are summarized in Table 5.7, and time histories for high-speed tests with both subjects are shown in Figure 5.19 to Figure 5.21. The targeted maximum rotational velocity was 1360 degrees per second, calculated as a function of the maximum trackable linear velocity of the dura of 1.9 m/s at a distance of 8 cm from the center of rotation, as discussed in Section 4.9.1. No results are included for test PM02ROTATE01, the first high-rate test run with subject PM02 because an ultrasound trigger failure prevented collection of any ultrasound images.

Table 5.7. Peak rotational kinematics of head and cage in high-rate tests

Subject	Test No.	Peak Rotational Velocity Head (deg/sec)	Steady State Rotational Velocity Head (deg/sec)	Peak rotational Acceleration Cage (rad/sec/sec)	Duration Primary Accel Pulse (msec)
PM01	ROTATE01	1125	700	7404	5
PM02	ROTATE02	1225	890	7709	5
	ROTATE03	1260	820	7717	5

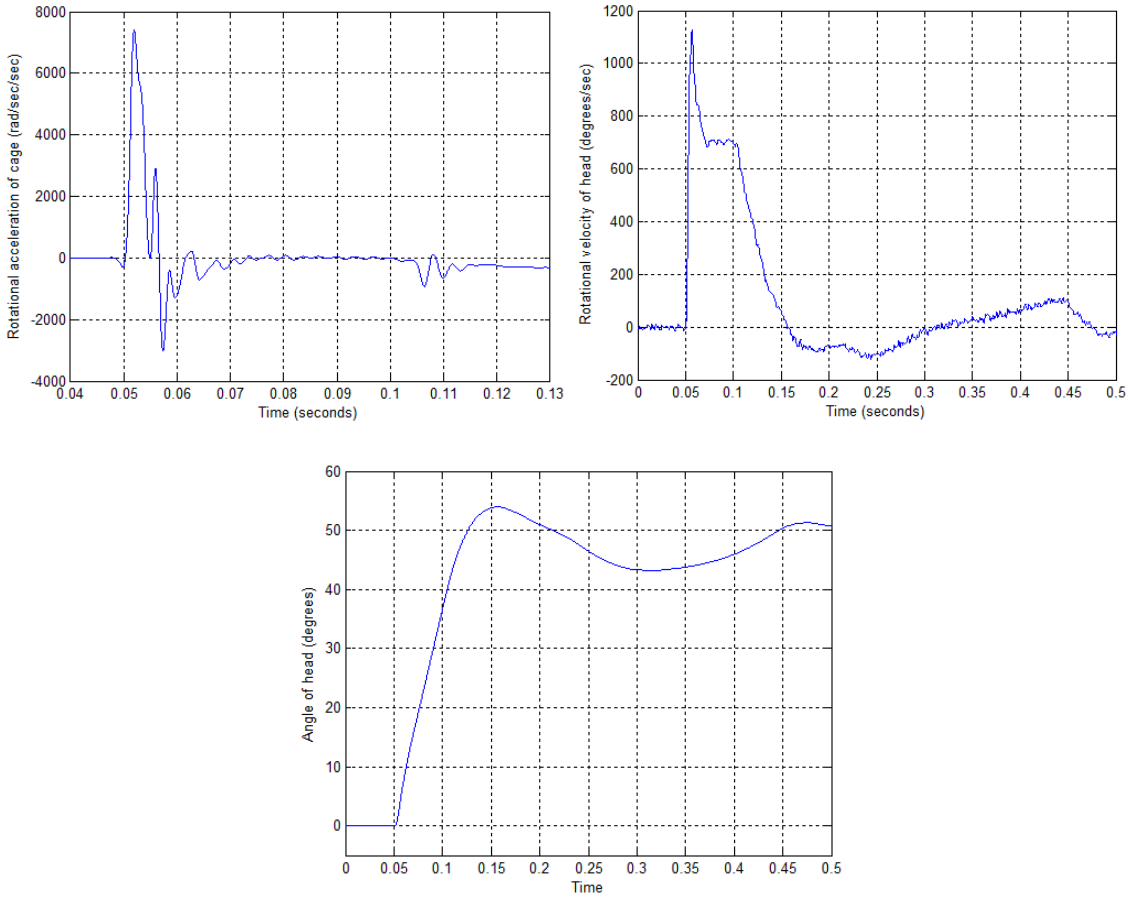

Figure 5.19. Rotational kinematics of cage and head about Y axis: PM01rotate01.

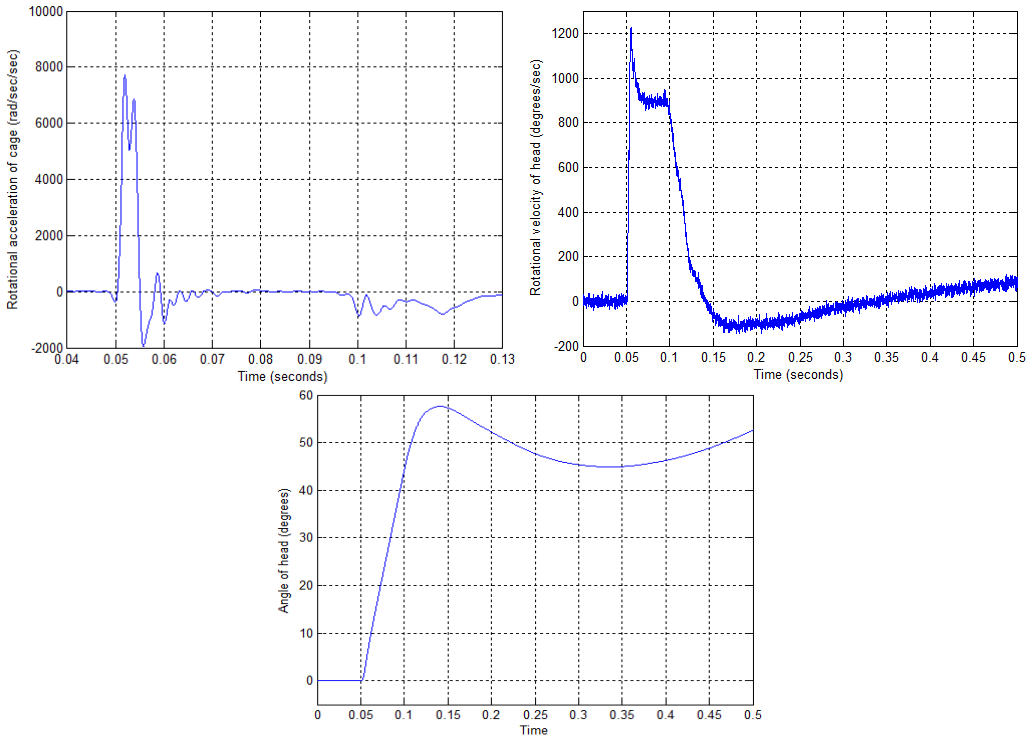

Figure 5.20. Rotational kinematics of cage and head about Y axis: PM02rotate02.

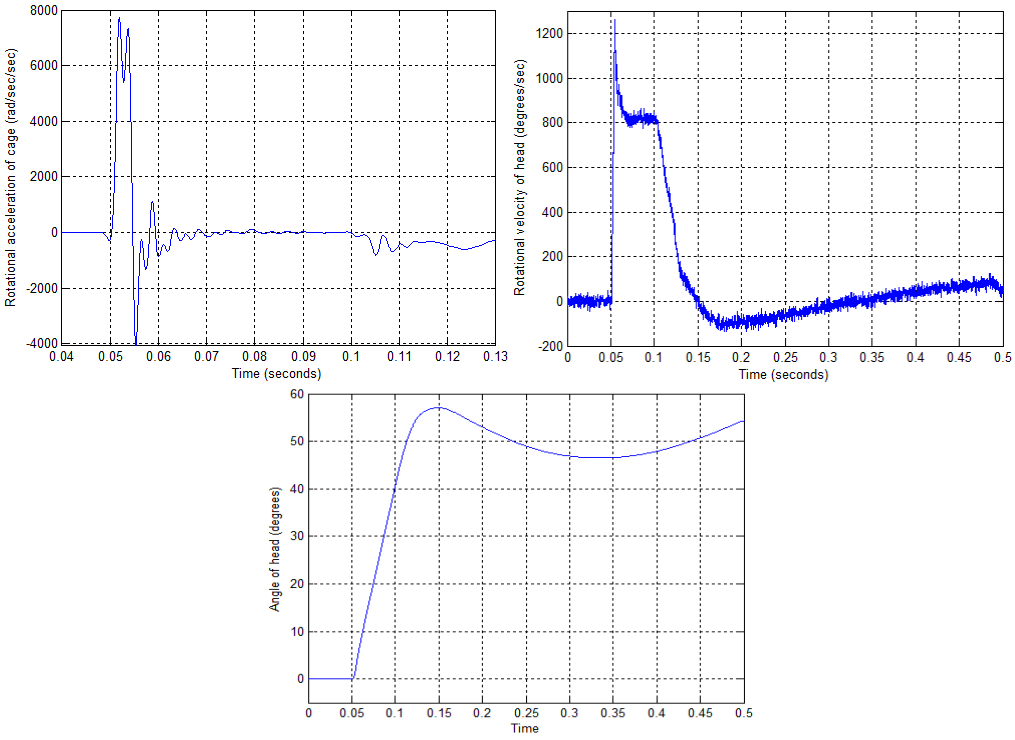

Figure 5.21. Rotational kinematics of cage and head about Y axis: PM02rotate03.

5.7.2 Motion Analysis in High-Rate Rotation

In high-rate tests, tissue motion could not be tracked from ultrasound images during the initial acceleration period by either manual or semi-automatic methods. Since tracking is performed by registering the position of identifiable locations or features on the tissue in consecutive frames, points need to be visible for at least 2 frames in order to track frame-by-frame motion. During the period of interest for tracking relative motion in the initial 10 millisecond period of acceleration and deceleration, individual points in each tissue layer could not be identified in consecutive frames for tracking, although the dura velocities were below the 1.9 m/s maximum where motion of tissue points were expected to stay in view for at least 3 frames. Therefore no ultrasound motion tracking is reported for the high-rate tests and motion is described only qualitatively.

In the high-rate rotation test with subject PM01 (PMO1ROTATE01), image frames in the initial acceleration period showed 1 to 2 mm of radial tissue motion (i.e. motion toward the ultrasound probe). In subject PM02, for which efforts were made to reduce axial motion by narrowing the lateral width of the window opening in the skull and buttressing the dura at the edges of the window with epoxy (for details see Section 4.3.6), the radial motion of the dura was reduced to approximately 1 mm. However, in both subjects, individual points on the tissue could not be tracked from frame-to-frame during the initial acceleration period, suggesting that the direction of motion of the tissue was not aligned with the plane imaged by the ultrasound probe.

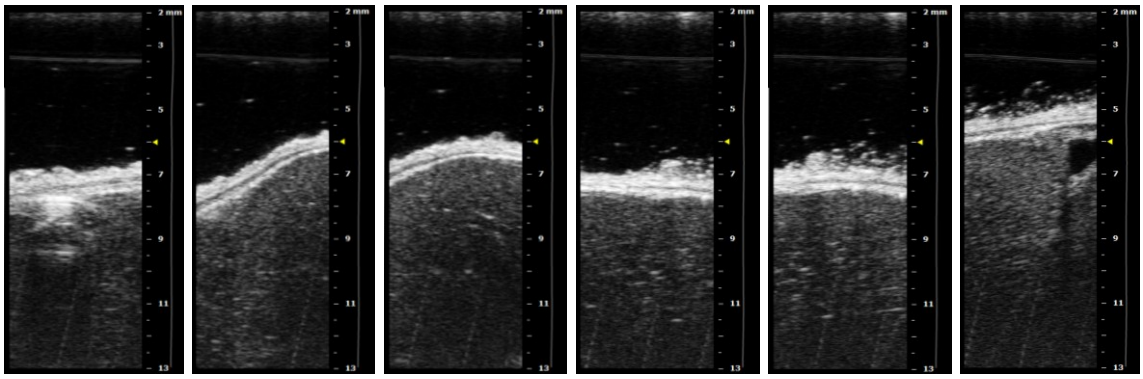

Figure 5.22. Ultrasound frames from initial acceleration in PM01ROTATE01.

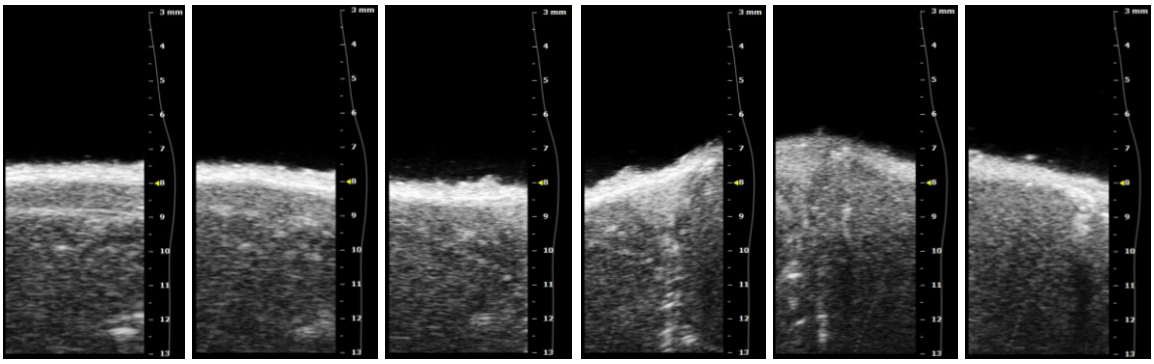

Figure 5.23. Ultrasound frames from initial acceleration in PM02ROTATE02.

5.8 Post-Test Verification of Pressure and Dissection

5.8.1 Verification Testing of Intracranial Pressure (ICP)

In order to estimate the ICP present during testing, a post-test evaluation was run to invasively measure ICP in each test head using an intraparenchymal Codman Microsensor ICP Transducer, under the pressurization conditions used in testing for that subject.

For subject PM01, arterial and venous fluids were pressurized by gravity at water-column heights of approximately 400 mm and 600 mm respectively above the fixture

shaft. Vascular fluid valves were open to allow pressurization approximately 2 to 4 minutes prior to rotation testing and turned off after each test. Measured intracranial pressures in post-test evaluation under these conditions (Table 5.8) varied more with the duration of vascular pressurization than with the fluid height. Pressurization values immediately after connection and after pressurization was suspended were within normal physiological limits of 5 to 15 mmHg (Raboel, Bartek et al. 2012). After extended periods of connection to pressurization fluid, intracranial pressure exceeded normal limits.

For subject PM02, arterial and venous fluids were pressurized by gravity at water-column heights of approximately 370 mm and 590 mm respectively above the fixture shaft. Vascular fluid valves were open to allow pressurization for approximately 15 seconds prior to testing, then closed and allowed to stabilize for 90 to 150 seconds prior to each rotation test. Measured intracranial pressures in post-test evaluation under the same conditions are shown in Table 5.9. Under all conditions, the measured intracranial pressured exceeded the normal physiological reference range.

Table 5.8. Post-test intraparenchymal ICP measurements for subject PM01

Head Position	CSF Perfusion	Vascular Pressurization	ICP (mmHg)
Head upright	On	Not connected	2
Head inverted	On	Not connected	0
Head inverted	On	Immediately after connection	10
Head inverted	On	After 3 minutes vascular pressurization	16
Head inverted	On	2 minutes after pressurization stopped	11
Head inverted	On	4 minutes after pressurization stopped	10

Table 5.9. Post-test intraparenchymal ICP measurements for subject PM02

Head Position	CSF Perfusion	Vascular Pressurization	ICP (mmHg)
Head upright	On	Not connected	21
Head inverted	On	Not connected	27
Head inverted	On	Immediately after connection	28
Head inverted	On	After 15 seconds vascular pressurization	29
Head inverted	On	Immediately after pressurization stopped	27
Head inverted	On	2 minutes after pressurization stopped	26
Head inverted	On	3 minutes after pressurization stopped	26

5.8.2 Dissection

Arterial perfusion. Since the arterial saline was not dyed, arteries that have been rinsed of blood and show evidence of clear fluid are indicative of effective saline perfusion. Both subjects PM01 and PM02 showed evidence of good arterial perfusion in arteries over the surface of the cortex (Figure 5.24). Subject PM01 also showed effective perfusion of the vessels in the Circle of Willis (Figure 5.25).

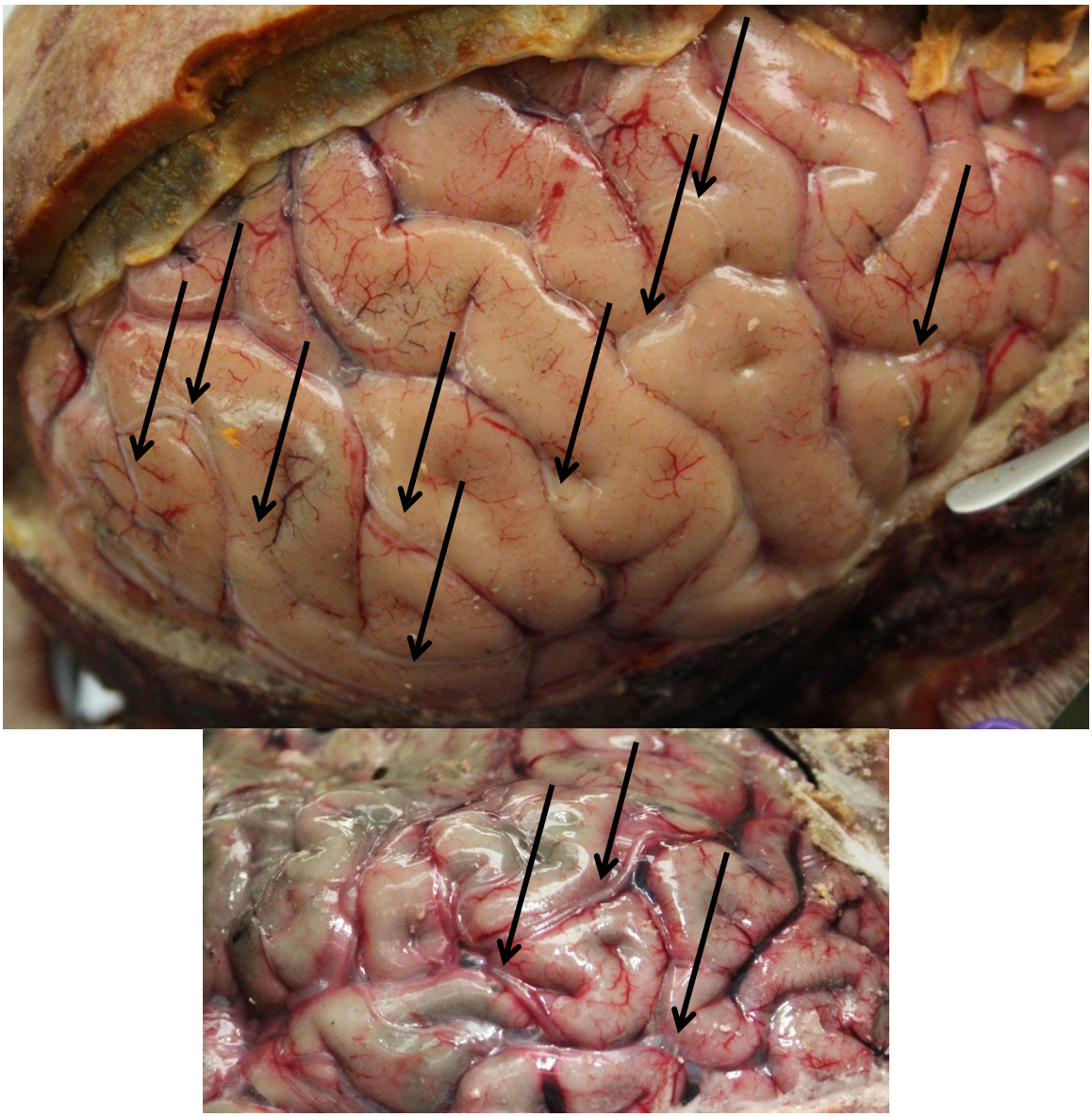

Figure 5.24. Arteries on the surface of the cortex (PM01 above, PM02 below) showing evidence of good perfusion by clear saline.

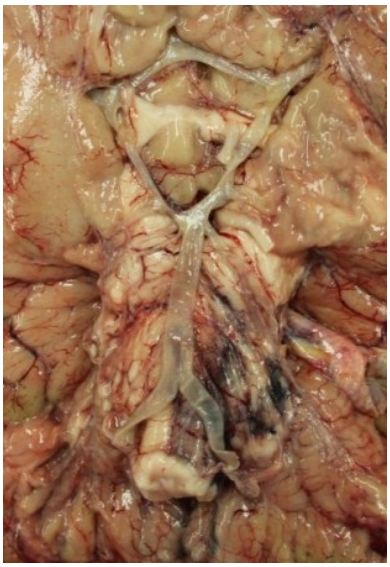

Figure 5.25. Circle of Willis (PM01) showing evidence of good perfusion by clear saline.

Venous perfusion. Subject PM01 showed some evidence of venous perfusion on autopsy, reflected in light staining of the superior sagittal sinus with orange-dyed saline (Figure 5.26). No definitive evidence of orange dye was identified in the bridging veins in subject PM01 although blood was identified in some bridging veins. In subject PM02, at least one bridging vein was severed on the non-tested (left) side of the head when initial efforts to cut the skull opening resulted in laceration of the underlying dura. As a result, orange dyed saline leaked from the skull opening on the non-test side throughout testing, and stained tissues orange over both sides of the vault. As in subject PM01, fluid blood was also identified in some bridging veins. Although leakage of dye from the lacerated bridging vein supports that venous saline was effectively perfused into the superior sagittal sinus and bridging veins, as does staining of the interior of the superior sagittal sinus, the extent of bridging vein perfusion could not be evaluated because of extensive staining of tissues with leaked orange dye.

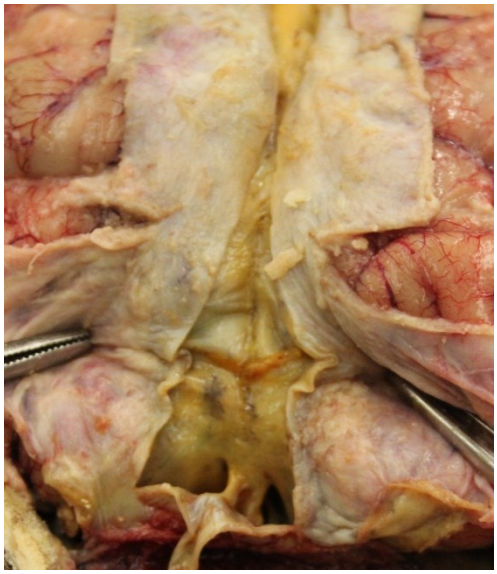

Figure 5.26. Superior sagittal sinus, opened on autopsy, stained with orange-dyed saline (PM01).

Cerebrospinal fluid perfusion. According to test procedures, CSF perfusion was established immediately after separation of the head to allow at least 20 hours of perfusion prior to testing. While this perfusion duration target was achieved with subject PM02, a closed valve in the subarachnoid catheter was discovered immediately after testing on subject PM01 at the time that post-test green dye was added to the perfusate. It is likely that little or no artificial CSF was perfused into the subarachnoid space on subject PM01 prior to testing. As a result, subject PM01 showed limited evidence of artificial CSF perfusion on autopsy. The dark green dye injected into the CSF post-test left dark stains on the subarachnoid tissues of the posterior spinal cord (Figure 5.27), as well as more subtle staining of the subarachnoid surface of the inferior surfaces of the brain, particularly on the left (tested) side (Figure 5.28). It is suspected that this evidence of artificial CSF dispersion was a result of post-test perfusion. There was no definitive

evidence of subarachnoid dye over the superior surface of the left hemisphere where ultrasound motion testing was performed.

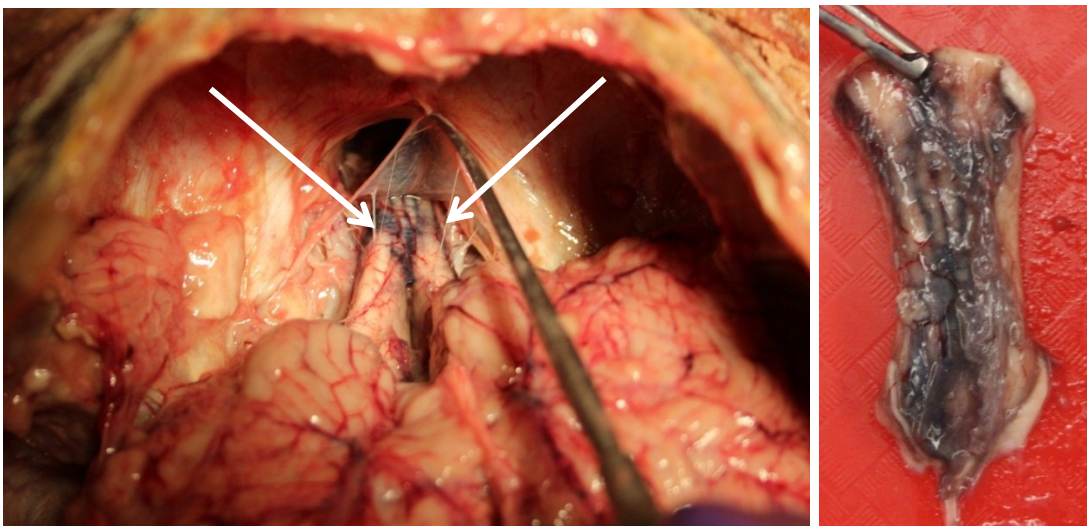

Figure 5.27. Staining of the subarachnoid tissues of the superior posterior aspect of the spinal cord with dark green-dyed artificial CSF (PM01).

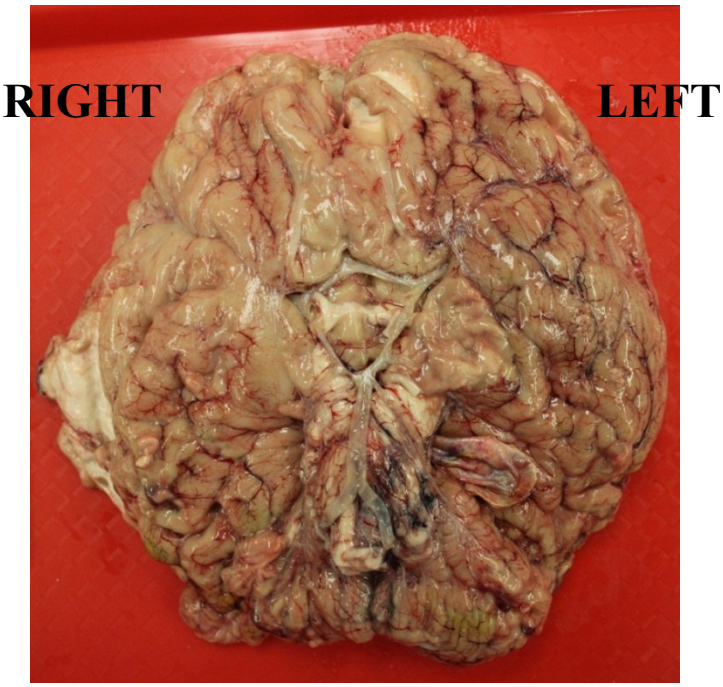

Figure 5.28. Staining of the subarachnoid surface of the cortex on the inferior surfaces of the brain (PM01).

In PM02, there was subtle evidence of green staining over the inferior brain and over the superior surface of the brain on the test side (Figure 5.29), but it was not possible to determine whether the staining was subarachnoid or whether leakage and overflow at the cervical entry point of the catheter had allowed dye to permeate through the dura onto the arachnoid. Deterioration and softening of the brain tissue in subject PM02 prevented removal of the arachnoid to inspect the intact subarachnoid space.

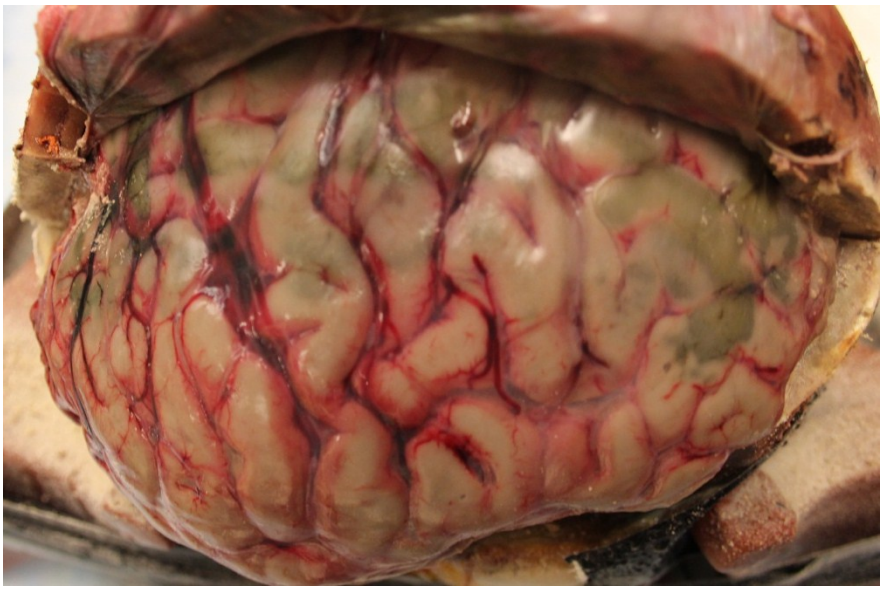

Figure 5.29. Subtle green staining over the surface of the brain on the tested side (PM02).

To summarize, perfusion of artificial CSF in subject PM01 appeared to have been prevented prior to testing by an inadvertently closed valve in the CSF plumbing system. Evidence of CSF dispersion through the subarachnoid space in PM02 was also limited, but definitive examination of the subarachnoid space for evidence of artificial CSF was limited by the advanced deterioration of brain tissue present at the time of dissection.

Chapter 6: Discussion of Head Rotation Study

6.1 Low-Rate Rotation Testing

6.1.1 Effectiveness of Ultrasound Methods in Low-Rate Testing

Ultrasound imaging of the meninges and peripheral brain during low-rate rotation testing demonstrated the effectiveness of using B-mode ultrasound to capture motion of peripheral tissues during head rotation. Qualitatively, the dura and superficial cortex could be visualized throughout the low-rate motion sequences, and quantitatively the ultrasound-tracked cumulative displacement of the dura matched the measured motion of the skull.

Identification of the arachnoid during motion was less certain than for dura or cortical tissue. Although static images with dura removed or with dura *and* arachnoid removed clearly show a bright and distinct signal associated with the arachnoid meningeal layer (Figures 5.4 and 5.5), the arachnoid was difficult to distinguish from the dura in ultrasound images of intact meningeal layers (Figure 5.6). A dura/cortex interface layer of tissue was tracked along the bright inferior edge of the visible dura, although it could not be definitively identified as arachnoid. In low-rate *post mortem* testing (PM02LOW04), there was little relative motion between the dura and this dura/cortex interface layer, but approximately 0.15 mm of motion between the interface layer and the surface of the cortex. This pattern of relative motion is consistent with the

bright dura-cortex interface layer being identified as the arachnoid since anatomically, the arachnoid would not be expected to move relative to the dura in non-injury motion, but would be expected to move slightly relative to the cortex as a result of tethering by the arachnoid trabeculae between those surfaces. A more effective method of identifying the arachnoid in ultrasound images of motion testing is needed in order to definitively track the relative motion of each meningeal layer.

The accuracy of tracked motion data is affected by the potential sources of error discussed in Section 3.4.2: (1) limitations in initial ultrasound image spatial resolution, (2) image degradation in image file type conversion from the VEVO 2100 to the image analyzed by TEMA, (3) inaccurate feature-based tracking, and (4) misalignment of the ultrasound probe and the motion of the tissue leading to changes in shape and appearance of tissue features between frames. The magnitude of potential error from (1) spatial resolution, corresponds to manufacturer's reported lateral resolution of 80 μm for the 550D ultrasound probe (Visualsonics 2009). Reduction of error in motion tracking results from the remaining three sources may be possible.

Elimination of error from (2) image degradation, and (3) feature-based tracking may be possible by tracking tissue motion in the ultrasound images directly with speckle-tracking techniques rather than with semi-automatic techniques using TEMA point-tracking software. While the TEMA point-tracking results allowed for gross evaluation of tissue motion, tracking procedures were labor-intensive and relatively subjective. Since tracking error was cumulative in relative displacement results, even small magnitude errors may have had a significant effect on relative motion results, particularly

late in the motion sequence. Speckle-tracking techniques may offer improved accuracy as well as additional information on field displacement and strain in the tissues. In future testing, tissue deformation analysis using speckle-tracking techniques should be compared to TEMA point-tracking methods in order to evaluate the efficiency, inter-operator repeatability, and accuracy of each method.

Error from misalignment of the ultrasound probe (4) could be further minimized by improving precise perpendicular alignment of the ultrasound probe and the axis of rotation.

6.1.2 Comparison to Previous Low-Rate Results

Comparison of the displacements measured in low-rate rotation tests with results from previous tests on volunteers (Feng, Abney et al. 2010) offers an opportunity to contrast motion in *post mortem* subjects to motion in the *in vivo* peripheral brain. Feng et al. used dynamic tagged MR imaging of three human volunteers to track motion of the brain during a mild frontal impact to the head. Peak linear acceleration of the head in the volunteer impacts was 14.3 to 16.3 m/s^2 (1.46 to 1.66 g) and peak angular accelerations ranged from 124 to 143 rad/sec^2. This level of angular acceleration is within the range measured in volunteers for daily activities such as jumping down from a 60 to 90 cm step, plopping down in a rigid chair, or skipping rope (Vijayakumar, Scher et al. 2006; Funk, Cormier et al. 2011). The imaged sagittal plane in these anterior-posterior accelerations was approximately 1 cm lateral to mid-sagittal.

In comparison, the lateral position of the ultrasound probe in the current study was aligned with the dura 3 to 3.5 cm from mid-sagittal. The low-rate tests in the current

series targeted the same range of rotational acceleration as in the Feng et al. tests, but without any linear acceleration. Rotational velocity on impact in the low-rate rotation tests was targeted to match the slope in the volunteer angular displacement time-histories. The resulting angular displacement time-histories are compared for test PM02LOW04 in the current study and the three volunteers in the Feng study (Figure 6.1). Although the low-rate tests in the current study did not produce any linear acceleration, the rotational kinematics in the previously-reported volunteer tests are comparable to those produced in low-rate *post mortem* tests in the current series up to approximately peak displacement.

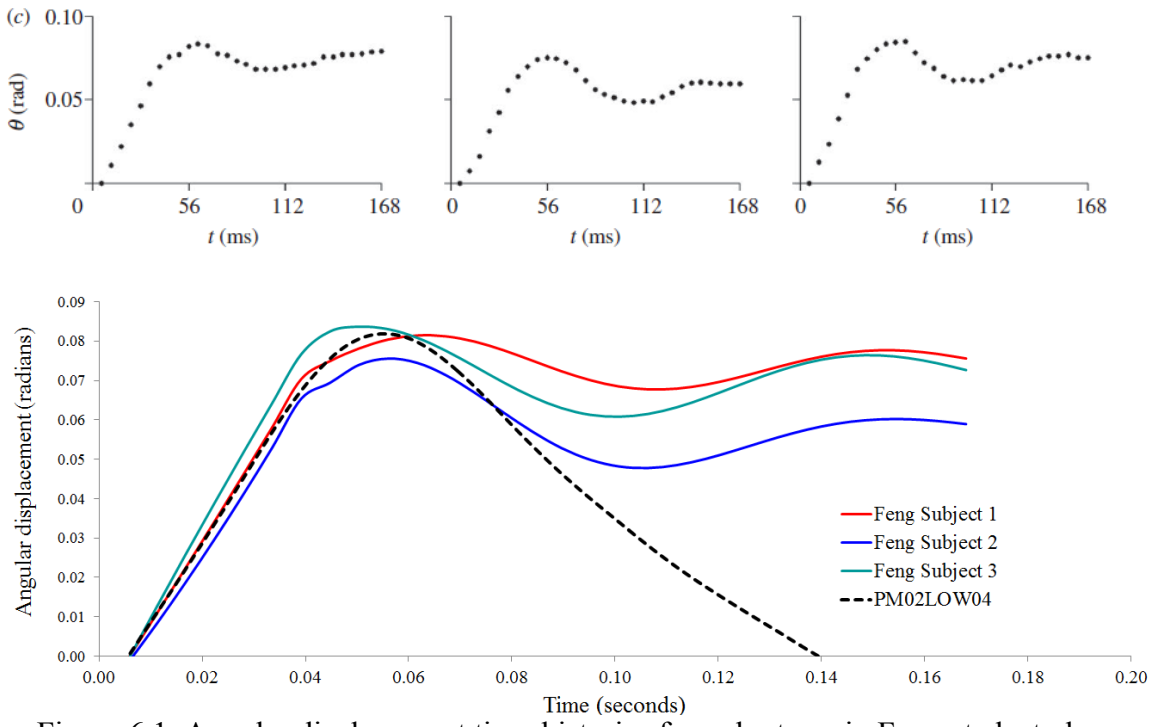

Figure 6.1. Angular displacement time-histories for volunteers in Feng et al. study (above) and compared to PM02LOW04 in current study (below) (Feng, Abney et al. 2010).

Displacement reported *near* the surface of the cortex in Feng's tests was substantially more than the displacement observed *at* the surface of the cortex in PM02LOW04. In Figure 6.2, displacement plots taken from Feng et al. at a time point between the maximum peak angular deceleration and peak angular displacement shows surface displacement near the cortical surface of 2 mm or more. In contrast, maximum displacement of visible tissue at the surface of the cortex in *post mortem* test PM02LOW04 up to the time of maximum angular displacement of the skull was less than 0.2 mm (Figure 5.13). However, one major difference between the two measurements is that the displacements measured in the current tests describe only tissue immediately adjacent to the skull. In contrast, the minimum voxel dimension of 1.3 mm in the Feng et al. study, combined with the difficulty collecting MR data immediately adjacent to the skull, make it likely that the measurements of peripheral displacements in volunteers apply to tissue deeper in the cortex than the measurements in the current *post mortem* study.

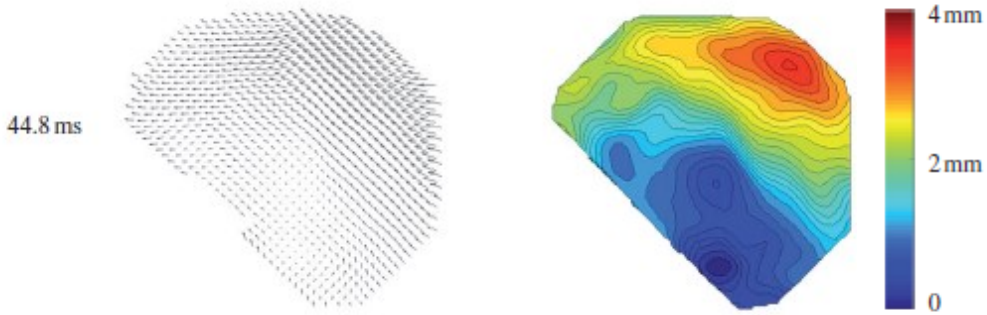

Figure 6.2. Displacement relative to skull as vector field (left) and magnitude field (right, with color scale) for subject 1 in Feng et al (2010).

If it is assumed that the Feng et al. volunteer tests are sufficiently similar to the *post mortem* tests in the current study, the results in the two studies can be combined to better understand motion of intracranial tissue relative to the skull peripherally and deep to the surface of the cortex. Taken in combination with the results from Feng et al., the preliminary low-rate ultrasound displacement results suggest that in low-rate, non-injurious rotation, there is very little motion of the meninges and cortical surface relative to the dura and skull (less than 0.2 mm), but that tissue distortion deep to the surface of the cortex can allow up to 2 to 4 mm of motion relative to the skull. The very limited motion between the cortical surface and the skull would be consistent with the anatomical connections in this region. The connections between the skull-dura, dura-arachnoid, and arachnoid-cortex vary in strength, but separation of these layers would require damage that would not be expected in non-injurious head rotation. Anatomically, the meningeal layer most likely to allow motion is between the surface of the cortex and the arachnoid, where arachnoid trabeculae crossing the CSF-lubricated subarachnoid space could be expected to allow limited relative motion without damage. For PM02LOW04 (Figure 5.13), the majority of tissue motion relative to the skull occurred between the surface of the cortex and the dura/cortex interface layer, presumed to be the arachnoid. These results suggest that there is shear strain between the arachnoid and the cortex, as well as shear strain deeper in the cortex.

However, before definitive conclusions can be made regarding the combined results of *post mortem* motion at the extreme periphery of the brain and volunteer motion slightly deeper in the cortex, additional work is needed to confirm the similarity between

these two experimental models. The major differences between Feng et al.'s volunteer MR experimental model and the *post mortem* rotation experimental model are changes in the material properties of the head associated with death and *post mortem* delay before testing, and the absence of linear acceleration in the currently reported series of *post mortem* rotation tests.

To address *post mortem* changes in the properties of the head, the efforts made to minimize *post mortem* effects are evaluated in Section 6.3.1 to Section 6.3.3, and several strategies are proposed for further reduction in differences between the experimental *post mortem* model and *in vivo* conditions.

With regard to the effect of different kinematics of the compared series of low-rate tests, evaluating the effect of comparing combined rotation and translation in Feng's volunteer tests to isolated rotation in the *post mortem* tests would ideally be done by repeating the volunteer tests in a rotation-only configuration, or by introducing translational acceleration into the *post mortem* rotation test setup. However, either of these options represents a major research effort involving considerable experimental challenges.

Alternatively, the combined effects of the differences between the two experimental models could be more efficiently evaluated by repeating *post mortem* rotation testing with a deeper ultrasound field of view than used in the currently reported tests. The image dimensions and settings were selected for the current study to allow tracking to maximize the speed of measurable tissue motion, ultimately allowing tissue tracking at speeds up to 1.9 m/s. Since tissue motion in low-rate tests did not exceed 0.2

m/s, future tests could be run with a lower-frequency ultrasound probe and a narrower field of view (smaller x image dimension) to allow a deeper field of view (larger y image dimension), maximizing the depth of cortical tissue imaged rather than the maximum tissue velocity. Thus, deeper ultrasound images of *post mortem* rotation tests could be used to capture both the relative motion of the meningeal layers as observed in the currently reported tests as well as the deeper cortical tissues for direct comparison to the data collected in the volunteer tests by Feng et al.

In summary, preliminary combination of the current superficial results with the deeper results reported by Feng et al. suggest that low-rate, non-injurious rotation results in minimal relative motion between the cortical surface and the skull but that shear strains deeper in the cortex can produce up to 2 to 4 mm of cortical motion relative to the skull. The very limited relative motion of the cortical surface and meningeal layers relative to the skull are consistent with the anatomical connections between these layers, suggestive that the meningeal layers do not slide relative to each other in low-rate rotation, but that relative motion of the peripheral brain results from deformation deeper in the cortex. However, definitive comparison or combination of the relative motion response in the volunteer test results of Feng et al., and the *post mortem* relative motion response in the current low-rate rotation tests is prevented mainly by (1) known differences in tissue condition, intracranial pressure, and subarachnoid perfusion between the *post mortem* tests and the *in vivo* Feng et al. tests, and (2) Feng's motion results applying to tissue *near* the cortical surface, while the current results describe more superficial tissue *at* the cortical surface. Additional testing is proposed to allow a more direct comparison of *post*

mortem response using the procedures developed in this study and previously reported *in vivo* response from volunteer studies. The proposed testing involves repeating low-rate *post mortem* rotation testing with a deeper ultrasound image field of view than used in the tests reported in the current study in order to capture the motion of both the meningeal and cortical surface layers seen in initial *post mortem* tests, as well as the deeper cortical tissue comparable to that tracked by Feng et al. in *in vivo* volunteer tests. Such testing would allow an evaluation of the effectiveness of the *post mortem* model in representing *in vivo* brain motion in rotation, and also allow definitive combination of the results from ultrasound rotation testing with the MR volunteer results for a full picture of the motion produced at the periphery of the brain in low-rate head rotation.

6.2 High-Rate Rotation Testing

High-rate tests accelerated with pyrotechnic seat-belt pretensioners targeted a rotational acceleration pulse simulating a frontal head impact, while limiting peak rotational velocity such that the linear velocity of the tissues of interest at the surface of the brain would be below the maximum trackable velocity for B-mode ultrasound images. Based on the ultrasound image settings used in these tests, the maximum trackable velocity was estimated to be 1.9 m/s as discussed in Section 4.9.1. This linear velocity at a radius of 8 cm from the center of rotation corresponds to a rotational velocity of 1360 degrees per second. Although the rotational velocity did remain below this targeted maximum value in high-rate rotation tests, tissues could not ultimately be tracked during the initial acceleration phase of the high speed tests. This failure to track motion in the high-rate tests was most likely because the tissue motion was not solely in

the plane imaged by the ultrasound probe. In this section, reasons for the failure to track motion during the acceleration phase of motion will be discussed and procedural modifications to ensure tracking of tissue in future test efforts will be proposed. The ultimate potential for this type of test to effectively measure meningeal motion during high-rate anterior-posterior acceleration is evaluated.

Two factors are proposed to explain why points in high-rate ultrasound images failed to stay in the plane imaged by the ultrasound probe so that individual points on the tissue could be tracked for consecutive images.

The first factor for out-of-plane motion of points on the tissue was radial acceleration of the tissue resulting from high rotational velocity. This radial motion likely deformed the tissues bi-directionally, resulting in motion of the tracked tissue points out of the imaging plane. This problem may have been exacerbated by the angled position of the probe (Figure 6.3): the radial acceleration of tissue resulting from rotation of the head about the fixture shaft would be directed perpendicular to the shaft rather than directly toward the ultrasound probe. Modifications were made to the test procedure for the second subject tested in the current test series in order to reduce the outward motion of the tissue, including narrowing of the lateral width of the skull opening and buttressing of the dura at the edges of the dura with molded epoxy. Radial motion of the dura toward the ultrasound probe was reduced by approximately half (Figures 5.18 and 5.19), but out-of-plane tissue motion still likely occurred, evidenced by the failure of individual tissue points to stay in the imaging plane in consecutive images.

Further reduction of radial motion of the tissues might be accomplished with replacement of the removed bone in the skull opening with stiff replacement material across the entire width of the opening. Currently, there is no known material that could serve as a replacement for bone to hold the tissue in place during high-rate rotation and behave transparently with respect to ultrasound waves to allow imaging of the underlying tissue. However, identification or development of such a material would prevent the out-of-plane motion that results from outward acceleration of the tissue. Alternatively, if the ultrasound probe could be mounted to the skull so it could rotate with the head, the probe face itself could prevent radial motion of the dura in a small skull window. Short of development of a novel ultrasound-transparent bone replacement material or ruggedization of the ultrasound probe such that it could be mounted to the skull during acceleration, other methods of physically holding the dura in place such as mesh covering of the opening or further narrowing of the skull opening should be developed and evaluated. The feasibility of returning the ultrasound probe to a vertical position, perpendicular to the axis of rotation, should also be assessed.

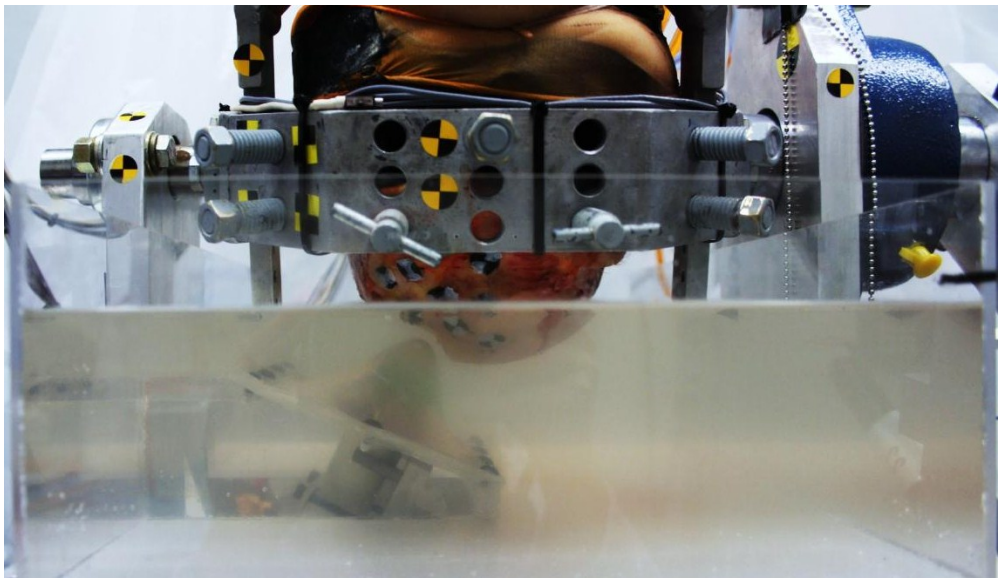

Figure 6.3. Ultrasound probe angled perpendicular to dura surface, not in plane perpendicular to fixture rotation shaft.

The second factor proposed to explain why points on the tissue moved out of the plane imaged by the ultrasound probe in high-rate testing is out-of-plane motion of the entire head and cage during the acceleration phase. The shock-loading delivered by the pyrotechnic pretensioner, combined with potential motion of the shaft within the fixture bearings, deformation of the aluminum cage, or motion of the head within the cage could allow the head to move out of plane relative to the ultrasound probe image plane during the initial moments of head and fixture acceleration. Additional testing of the fixture is needed to isolate the source and extent of out-of-plane motion of the head and cage during acceleration. Such testing can be performed with an anthropomorphic test dummy head, and should incorporate additional instrumentation of the head and cage to evaluate out-of-plane motion. Alternative methods of accelerating the test fixture should be developed and evaluated.

While the ultimate potential for B-mode ultrasound to be used to track motion of the meninges and surface of the brain relative to the skull in high-rate testing remains unproven, the preliminary testing in this study supports that it will be possible to use the basic methods developed in this study to track gross tissue motion in injury-level head accelerations. Lower-rate tests confirmed that dura and cortex could be reliably tracked and analyzed using the developed methods in sub-injury head accelerations. Mid-rate testing with decelerations over 1200 rad/sec^2 further demonstrated that tissue features could be easily visualized in B-mode ultrasound images, supporting that tissue motion could be tracked and analyzed at higher rates. This mid-rate level of rotational acceleration is between the average rotational accelerations in soccer ball impacts to the forehead measured at impact speeds of 5 m/s and 8.5 m/s (Funk, Cormier et al. 2011). Isolated testing of dura motion in controlled motion testing (Chapter 3) confirmed the effectiveness of the developed B-mode ultrasound collection and tracking techniques at tissue speeds exceeding 2.0 m/s. It was predicted in Section 4.1.9 that the developed tracking methods would theoretically work for tissue speeds of at least 1.9 m/s with the ultrasound configuration used in rotation tests. At these tissue speeds, a head with the same radius of rotation as those used in this preliminary study could be effectively tested with ultrasound imaging with a peak rotational head acceleration of 10 krad/sec^2 for a triangular pulse with a 5 millisecond duration, which is within ranges previously associated with subdural hematoma (Ommaya, Goldsmith et al. 2002; Depreitere, Van Lierde et al. 2006).

Therefore, although procedural and mechanical test issues prevented effective measurement of tissue motion relative to the skull in preliminary high-rate rotation efforts in the current study, whole-head rotation tests at lower levels of rotational acceleration and planar tests of dura samples at high speeds confirmed the potential for the developed methods to ultimately measure gross tissue motion of the peripheral brain relative to the dura. With improved tracking procedures that allow tracking of field displacements rather than semi-automated tracking of individual points in the tissue, it may also ultimately be possible to develop more detailed mappings of tissue displacements within the ultrasound frame, potentially offering the opportunity to measure strain within the tissues and across the interfaces between layers of tissues, rather than just gross motion of individual layers of tissue.

6.3 *Post Mortem* Subjects as Model for Study of Meningeal Motion

While the experimental use of an *in vivo* human model of intracranial tissue motion may offer the most accurate predictions of human response to skull motion, living humans can obviously not be used for high-rate testing at injurious levels. For higher-rate experimental motion testing, options include *in vivo* animal models or *post mortem* human models. Although living primate tests have been used in previous studies of intracranial motion in rotational loading, for ethical reasons they are no longer used in the United States for injury-level testing. While the meningeal anatomy and meningeal connections of several domestic animals including horses, cattle, goats, and pigs have been identified as similar to humans (Sisson, Grossman et al. 1975; DeLahunta and Glass 2009), the dissimilarity in craniospinal angle and brain shape between humans and other

gyrencephalic species is a major limitation in studies of brain motion in rotation (Figure 6.4). Therefore, in the current rotation study where the experimental setup requires testing of an isolated head, a human *post mortem* model was used. However, acknowledging possible differences in *in vivo* and *post mortem* response, the limitations of testing with *post mortem* human subjects need to be addressed.

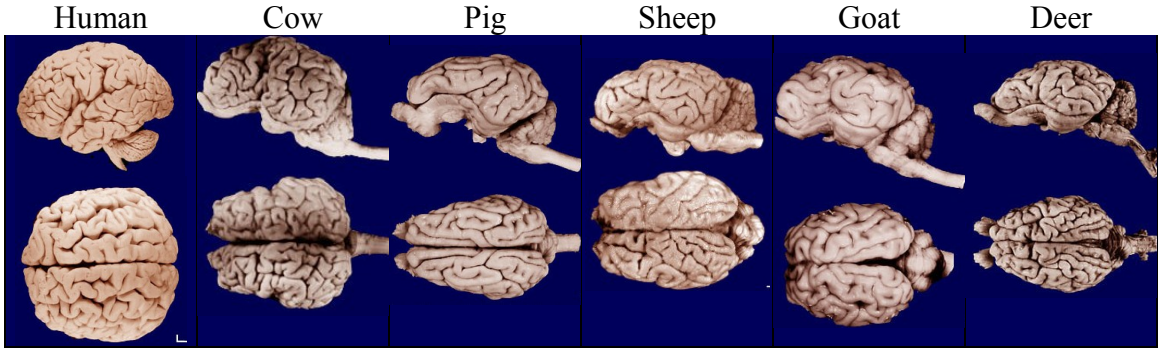

Figure 6.4. Brain shape compared by species.
(Images from the Comparative Brain Collections of the University of Wisconsin and Michigan State, www.brain museum.org).

This section will describe the differences between an *in vivo* and *post mortem* model that are expected to contribute most to differences in motion response in the peripheral brain and meninges: pressurization and perfusion differences between the *post mortem* and *in vivo* head, and degradation of brain tissue, vessels, and meningeal connections in the *post mortem* model. The effectiveness of procedures used in the current study to minimize these differences is evaluated and further improvements recommended.

6.3.1 Pressurization of the Vascular System

Intravascular and intraparenchymal pressure have been reported to affect overall relative skull-brain motion (Stalnaker, Melvin et al. 1977; Viano, Aldman et al. 1997; Depreitere, Van Lierde et al. 2006; Monea, Verpoest et al. 2012). Local properties of veins associated with subdural hematoma are also reported to change with pressure: experimental studies of the porcine superior sagittal sinus and attached bridging veins showed that the vessels were relatively extensible at low pressure, with the stiffness gradually increasing at higher pressure, concluding that vessels were less likely to be damaged under loading when pressurized (Pang, Lu et al. 2001). These previously reported results establish the importance of maintaining intracranial pressure and bridging vein perfusion during motion testing. In this section, previous efforts to pressurize the vascular system are discussed, along with procedures used in the current study and proposed improvements on those methods.

Previous efforts to pressurize the cranial vascular system. *Post mortem* pressurization of the head via the vasculature has been accomplished previously. With whole body post-mortem subjects, several researchers reported on methods to insert a balloon catheter into the common carotid arteries with pressure monitors inserted past the balloon to monitor fluid pressure in the vessel (Stalnaker, Melvin et al. 1977; Nusholtz, Lux et al. 1984; Trosseille, Tarriére et al. 1992). In post-mortem isolated head testing, Hardy additionally connected fluid input to the jugular veins with pressurization fluids at a pressure equivalent to average mean arterial and venous blood pressure (Hardy 2007).

While Nusholtz et al. ligated the vertebral arteries to maintain fluid pressure in the head, Hardy left the severed vertebral arteries patent to bleed gases from the system.

Current efforts to pressurize the vascular system. While previous efforts that have measured the success of cranial pressurization have focused on bringing fluid pressure in range of physiological ranges of blood pressure, the goals in the current study were (1) to bring the brain tissue into the range of normal ICP of 5 to 15 mmHg (Raboel, Bartek et al. 2012) and (2) to perfuse the parasagittal bridging veins with fluid. The focus on maintaining physiological *intracranial* pressure instead of *vascular* pressure is a new approach, motivated by the premise that intracranial pressure has a more direct effect on brain motion than vascular pressure. Efforts to perfuse the bridging veins were motivated by Pang's findings on the properties of these veins under pressure, which suggest that the stiffness of these supporting structures are affected by perfusion (2001).

With regard to efforts to return the head to physiological levels of intracranial pressure, post-test verification testing for subject PM01 showed that the fluid pressures used during testing were consistent with intracranial pressures in the normal physiological range, except when pressurization fluids were left connected for extended periods of time. Post-test pressure verification testing on PM02, however, suggested that applied fluid pressures had resulted in intracranial pressures exceeding normal physiological levels even when fluids were connected briefly, then disconnected prior to testing. While pressurization procedures in both tests initially appeared to be effective, demonstrating fluid throughput when first flushed, the second test appeared to result in over-perfusion of the cranial space, suggesting possible leakage from vessels into the

brain tissue. Given the very soft and deteriorated nature of the brain tissue observed during preparation and dissection of subject PM02, it is possible that leaked perfusion fluid may have contributed to the softness of the brain tissue, or that post-mortem breakdown of the tissues may have contributed to failure of the blood-brain barrier, allowing the perfusion fluids to be absorbed into the brain tissue, thus leading to the increased intracranial pressure. Thus, the deterioration of brain tissue appeared to interfere with the effectiveness of pressurization, as well as affecting brain motion as previously discussed. Additionally, these results demonstrate that intracranial pressure does not vary directly with applied vascular pressure, supporting the experimental strategy to control physiological intracranial pressure rather than vascular pressure.

In addition to minimizing *post mortem* delay before testing to reduce the effect of brain tissue deterioration on pressurization, future testing should incorporate a method to estimate *pre-test* intracranial pressure so that fluid pressures can be corrected prior to testing. Methods for pre-test intracranial pressure measurement that warrant evaluation include epidural pressure monitoring or placement of a clinical intraparenchymal pressure sensor either through the dura on the non-test side of the brain or inserted into the test side parenchyma via the spinal cord.

With respect to efforts to perfuse the parasagittal bridging veins with fluid, post-test dissection showed only trace evidence of the dyed venous saline in the superior sagittal sinus or bridging veins. Presumed leakage of orange dyed saline from severed bridging veins on the non-tested side in subject PM02 provided only indirect evidence of venous perfusion. However, since fluid blood was observed in several of these veins on

dissection, the possible lack of saline perfusion to these vessels may not have had a substantial effect on the results. In order to improve the effective perfusion and pressurization of these vessels, access to the sinus through the skull at the sinus confluence may be a more effective location to perfuse the venous system or potentially for use as an exit port to flush the venous system initially. Methods for venous pressurization at this location have been successful previously (Depreitere, Van Lierde et al. 2006).

6.3.2 Perfusion of Artificial CSF

In vivo, CSF is contained in the subarachnoid space, over the surface of the brain and in sulci, as well as in the ventricles. In order to test motion of the meningeal layers in a post-mortem subject, it is imperative to keep the relationships between these layers as close to the physiological *in vivo* condition as possible. To that end, efforts to keep the post-mortem subarachnoid space in a perfused state are important in studies of meningeal motion.

Previous efforts to perfuse CSF. Nusholtz et al. reported on a cerebrospinal re-pressurization procedure performed via the lumbar spine of whole body post-mortem subjects (1984). A small hole was cored into the second lumbar vertebra and a Foley catheter inserted under the dura and directed superiorly until the catheter balloon reached the mid-thoracic spine. Saline was injected until fluid was observed at pressure transducer couplings located in openings that that had been bored in the skull vault, perforating the dura without cutting into the brain. In tests with post-mortem heads, Hardy developed a method to perfuse artificial CSF via the spinal canal by disarticulating

the head between the third and fourth thoracic vertebrae and then removing the T3 vertebra in order to access the dural sheath at this level (Hardy 2007). Approximately 2 cm of spinal cord was excised from the exposed dural sheath, and artificial CSF was perfused into the opening via a barbed fitting within the dura sheath. Fluids were drained from the head via openings in the skull.

Based on the descriptions provided by Nusholtz and Hardy, it appears that previous efforts to re-introduce CSF in cadaver specimens have perfused the subdural space, rather than the subarachnoid space. Both the input and output locations for CSF described by Nusholtz are described as subdural without mention of efforts to access the subarachnoid space (Nusholtz, Lux et al. 1984). Furthermore, the relative ease with which insertion of the catheter up the spine and flushing of fluid from the spinal entry point to the cranial exit point are described are also more consistent with subdural injection of fluids rather than subarachnoid. Hardy's description indicates perfusion directly into the dural sheath without efforts to block the flow of fluid between the dura and the arachnoid (Hardy 2007).

Current efforts to perfuse CSF. The current study is the first known reported effort to perfuse the *subarachnoid* space of a post-mortem subject in trauma testing. While dissection showed that the perfusion procedures seemed to be effective in keeping fluids out of the dura-arachnoid interface, the success of efforts to re-introduce CSF into the cranial subarachnoid space in the two subjects reported in this dissertation was limited. Perfusion of CSF in subject PM01 appeared to have been prevented prior to testing by a closed valve in the CSF plumbing system. CSF identified in the

subarachnoid space at autopsy was likely perfused to this location after testing was complete. Evidence of CSF dispersion through the subarachnoid space in PM02 was also limited, but definitive examination of the subarachnoid space for evidence of CSF was limited by the advanced deterioration of brain tissue present at the time of dissection.

While the arachnoid can be peeled from the surface of the brain on a very fresh *post mortem* subject (Figure 1.3) to expose the subarachnoid space, the arachnoid cannot be easily separated from the surface of the brain after an extended *post mortem* delay. Whether this change occurs as a result of brain tissue softening or because drainage of CSF from this space leaves the arachnoid adhered to the surface of the brain is unknown, but it is likely that this *post mortem* adhesion of the arachnoid to the surface of the cortex essentially seals the subarachnoid space and prevents re-perfusion with artificial CSF. Considering the already-deteriorated state of the spinal cord of subject PM02 at the time artificial CSF was introduced into the spinal subarachnoid space, it is suspected that passage of CSF through the subarachnoid space may have been blocked throughout the test preparation period by the *post mortem* adhesion of the arachnoid and cortex in the spinal and cranial subarachnoid spaces.

In preliminary method development trials prior to the current test series, artificial CSF was successfully infused into the cranial subarachnoid space using the same methods later applied to PM01 and PM02 in the current test series (Figure 6.5). The previous success of this method suggests that, if used before *post mortem* deterioration results in the effective "sealing" of the subarachnoid space, efforts to perfuse the cranial subarachnoid space via the spinal subarachnoid space should be continued with artificial

CSF. However, for more effective evaluation of subarachnoid perfusion, dye should be added to perfusion fluids used throughout the perfusion process, rather than added post-test. Although the addition of dyes to the artificial CSF prior to testing will require confirmation that the fluid is still isotonic to physiological CSF (thus preventing diffusion into adjacent tissues), the extent of dyed CSF perfusion will be more definitively determined in post-test dissection.

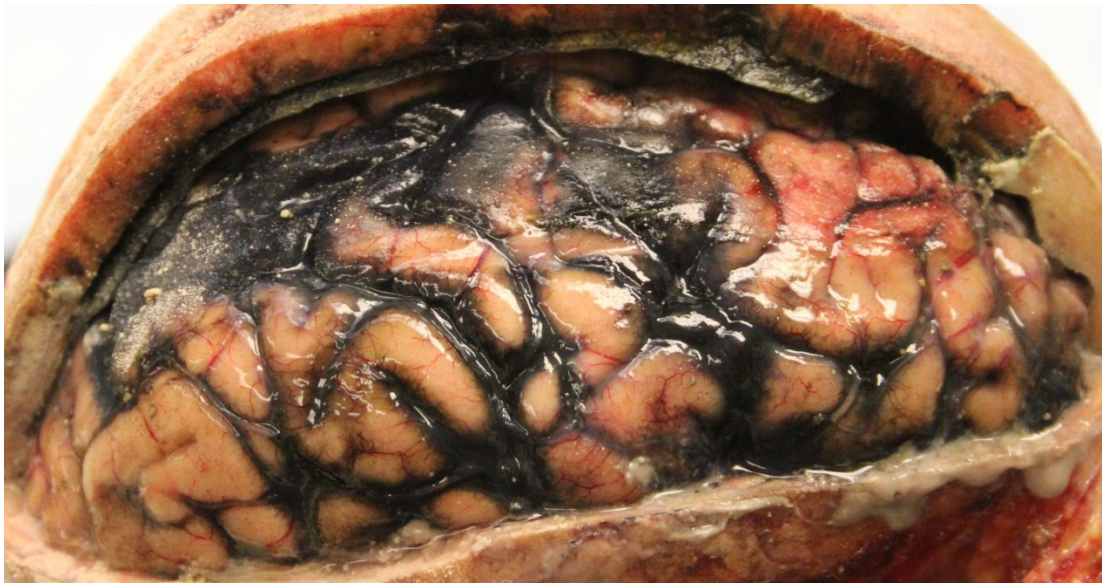

Figure 6.5. Introduction of dyed artificial CSF into the cranial subarachnoid space in a *post mortem* subject used for development of methods prior to the current test series.

In summary, maintaining CSF in the subarachnoid space is especially vital for the current test effort because of its likely effect on motion at the periphery of the brain. Based on the results of efforts to perfuse the subarachnoid space on two subjects at different stages of *post mortem* decay, improvement of subarachnoid perfusion success may ultimately depend on the freshness of the *post mortem* specimen. Extended *post mortem* delays lead to deterioration of the brain tissue and drying of the subarachnoid

space such that the spinal and cranial subarachnoid space become essentially "sealed", preventing flow of artificial CSF through this space.

While the methods developed in preparation for the current test effort were demonstrated to effectively perfuse the subarachnoid space with artificial CSF, experimental complications prevented consistent success of the procedures in subject PM01 and PM02. It is imperative that future test efforts should focus on reducing *post mortem* delay prior to perfusion of the subarachnoid space. Improved methods for evaluating the extent of perfusion of the subarachnoid space with artificial CSF should incorporate isotonic dye in the fluid, introduced throughout the perfusion process.

6.3.3 Degradation of Cranial Tissues

Degradation of brain tissue. Properties of parenchymal tissues are known to change after death, varying with *post mortem* time elapsed. In reports of whole-body human *post mortem* testing, stiffness of brain tissue has been reported to decrease after death, leading to increased brain motion. Stalnaker, Melvin et al. described noticeable brain property degradation evidenced by excessive brain motion during impact after periods longer than 4 days (1977). In contrast, studies of isolated brain tissue in the hours soon after death showed that brain tissue stiffened in in the first hours *post mortem* (Rang, Lippert et al. 2001; Garo, Hrapko et al. 2007), while showing softening or little difference over longer *post mortem* delays between 6 hours to 16 days (Darvish and Crandall 2001; Nicolle, Lounis et al. 2004; Bentil 2013). While these and other reported tests of isolated brain tissue were performed under widely varying conditions with different test techniques and with different species of mammalian brain tissue, they are

generally consistent with stiffening in the hours immediately after death followed by subsequent softening as the brain tissue deteriorates in the days following death.

In the current study, the spinal cord material observed when the head was separated from the body was clearly less degraded in PM01 at 17 hours after death than in PM02 at 37.5 hours after death. At autopsy, subject PM02's brain tissue had begun to liquefy such that it could not hold its shape without support from the skull. In contrast, subject PM01's brain had begun to soften but maintained its shape even after removal from the skull.

Additional differences between levels of degradation of the two brains were reflected in the increased evidence of trapped intracranial air in subject PM02. The artifact visible in sample images from high-rate tests (Figure 6.6) demonstrates evidence of gas beneath the dura in subject PM02, since the ultrasound signal is unimpeded through the more superficial tissues, but is blocked beyond the location of the gasses below the dura. Although the comparison image from subject PM01 shows scattered artifact in the imaging medium, no evidence of trapped gases in the tissue is visible. Such trapped gases can be a byproduct of *post mortem* cell death. Not only do these gases lead to image artifact in ultrasound images, but they have been suggested to be associated with changes in coupling of the brain and skull (Hardy 2007).

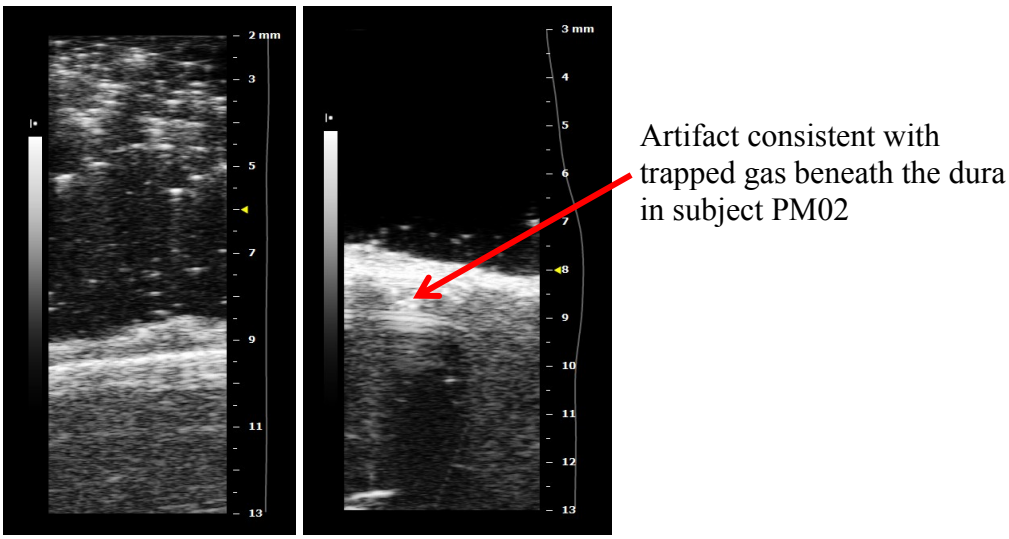

Figure 6.6. Sample ultrasound frames from PM01ROTATE01 (left) and PM02ROTATE02 (right).

Degradation of bridging veins. The properties of bridging veins have a potential effect on motion of the tissue at the periphery of the brain in *post mortem* testing, but testing has shown that the mechanical properties of cranial veins are not affected by *post mortem* delays of 5 to 8 days (Monson, Goldsmith et al. 2005).

Degradation of connection between the dura and arachnoid. In *post mortem* subjects used in this study and in *post mortem* subjects examined in preparation for this test series between 1 and 7 days *post mortem*, no definite perceptible connection between the dura and arachnoid was observed on manual removal of segments of skull and dura (Figure 6.7). Additional dissection studies of fresh bovine and porcine heads also failed to demonstrate definite evidence of adhesion at the dural border cell layer, even within 1 to 3 hours *post mortem*. It was not clear whether these findings indicated that the dural border cell layer had separated immediately *post mortem* or if the methods used to cut

and separate the removed segments of overlying bone had simply separated this weak connecting layer before it could be observed or tested.

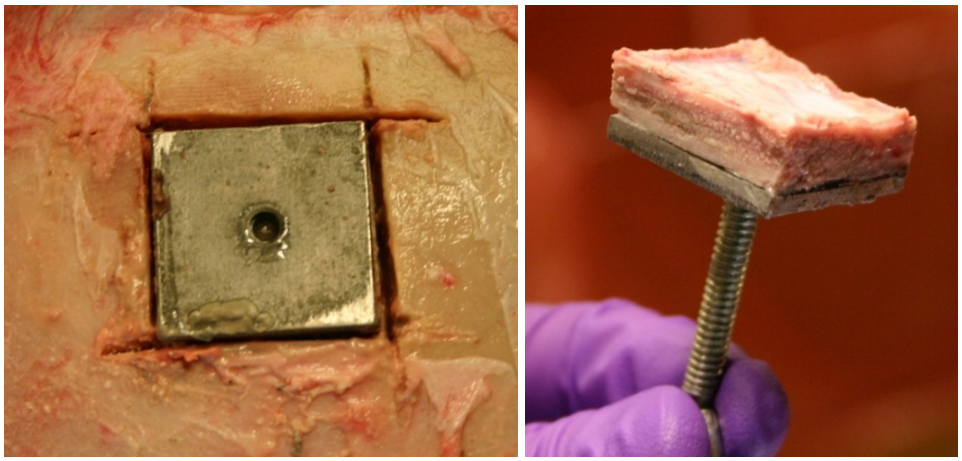

Figure 6.7. Removed segment of skull and attached dura from parietal vault of *post mortem* human subject examined in preparation for the current test series.

Post mortem deterioration or separation of the dural border cell layer in test subjects would be expected to lead to increased relative motion at this interface in *post mortem* testing compared to *in vivo*. Since the peripheral relative motion imaged in the current low-rate rotation testing was minimal, it is concluded that any *post mortem* changes in the dura border cell layer did not contribute to motion in rotation testing at non-injurious levels of acceleration. However, *post mortem* deterioration of the dura border cell layer is still poorly understood and its effect at higher rates unknown. This phenomenon could be explored by any method that allows direct comparison of the *in vivo* versus *post mortem* condition of this layer. Given the known fragility of the layer, testing should be performed *in situ,* rather than by removing the tissues from the head. Testing of animals with similar meningeal properties to humans, such as bovine or

porcine subjects, to compare *pre* and *post mortem* mechanical properties of this layer using minimally invasive methods such as MR elastography could potentially provide valuable information on how the dural border cell layer changes at death and at periodic *post mortem* times. A comparison of the *in vivo* and *post mortem* human dural border cell layer could be made by comparing high-resolution static ultrasound images of the meningeal layers through the dura. Specifically, *in vivo* images could be collected during surgical craniotomy procedures prior to opening of the dura, and *post mortem* transdural images could be collected using the same ultrasound images settings in *post mortem* subjects prepared with the pressurization and perfusion techniques developed in the current study.

Summarizing, the importance of minimizing *post mortem* delay to reduce tissue degradation is supported by previous reports that brain tissue degradation alters the motion of the brain relative to the skull in *post mortem* testing (Stalnaker, Melvin et al. 1977; Hardy 2007). These previous conclusions are consistent with the current results that showed trapped gases under the dura in the subject with more advanced tissue degradation. The urgency of reducing tissue degradation associated with *post mortem* delay is reinforced by observations made in the current study demonstrating that tissue degradation interfered with effective pressurization and perfusion of the head during testing.

6.3.4 Potential Use of *Post Mortem* Subjects for Rotation Testing

Testing with *post mortem* heads is the best alternative for high-rate rotation testing since *in vivo* human heads cannot be used for injury-level testing and non-primate

animals with human-like meningeal structure are too dissimilar to humans in brain shape and craniocervical angle for simulation of brain motion with rotation. Primate brains are more similar in shape to human brains, but differ in size and cannot be used for injury-level testing for ethical reasons. However, while *post mortem* heads may be the best experimental model for measuring head motion in high-rate tests, the ways in which they differ from *in vivo* heads need to be understood and minimized to increase their usefulness in experimental results. Procedures to minimize the *post mortem* changes expected to have the greatest effect in the current test series have been developed and evaluated in the current preliminary test series.

Cranial vascular pressurization was established in an effort to return intracranial pressure to physiological levels and to fill the parasagittal bridging veins. The role of intracranial pressure and perfused bridging veins in simulating *in vivo* motion in *post mortem* testing was established based on previous testing efforts reported in the literature.

Post-test evaluation in the current test series suggested that the fluid pressures used during testing were sufficient to maintain the head at physiological intracranial pressure for subject PM01 but not for PM02. Efforts should be made in the future to monitor intracranial pressure non-invasively *prior* to testing so that fluid pressures can be corrected if necessary. Methods for non-invasive pre-test intracranial pressure measurement include epidural pressure measurement or parenchymal measurement either on the side of the head not being tested or via a sensor inserted through the spinal cord into the cranial parenchyma. Post-test dissection showed that perfusion of venous saline into the parasagittal bridging veins may have been limited. Future efforts to pressurize

the vasculature should access the venous system via an opening in the skull to the sinus confluence to access the superior sagittal sinus and bridging veins more directly.

Perfusion of the cranial subarachnoid space with artificial CSF was attempted in order to return this meningeal interface to its *in vivo* condition. Perfusion of CSF in the subarachnoid space is vital for the current test effort because of its potential effect on motion of the meningeal layers during rotation.

It appeared that *post mortem* changes essentially sealed the subarachnoid space before artificial CSF could be re-introduced into that space in subject PM02. Given the success of perfusion procedures during development testing, it is expected that reducing *post mortem* delay in future testing will improve the effectiveness of the perfusion procedures used. However, use of dye in the artificial CSF throughout the perfusion procedure will improve the post-test evaluation of perfusion procedures.

To reduce the effect of *post mortem* deterioration of the cranial tissue, potential subjects were accepted for testing only if available within 48 hours after death and test procedures were streamlined so that rotation testing was complete within 4 days after death. Marked deterioration of brain tissue, effective sealing of the subarachnoid space, and evidence of intracranial gasses were observed for subject PM02, in spite of meeting the planned *post mortem* timing limits. These effects of *post mortem* decay likely interfered with establishing normal intracranial pressure, introduction of CSF into the subarachnoid space, and ultrasound imaging of brain tissue, and may also have affected the motion of the brain tissue. It appears that the limits placed on subject acceptance and on completion of testing were insufficient to prevent tissue breakdown from interfering

with subject preparation and testing. Investigation of the *post mortem* timing of tissue decay and how it is affected by variables such as subject age or storage temperature could help set more effective limits on elapsed time between death and testing, not only for the current procedures but for all brain injury research that relies on *post mortem* experiments. Meanwhile, in the absence of clear evidence on an adequate limit for *post mortem* delay before testing, shorter timing constraints are proposed based on the results of preliminary tests. It is proposed for future rotation testing that *post mortem* delay be further limited with subjects only being accepted for testing within 24 hours after death and that testing be completed within 3 days after death. These targets reflect the minimum practical time required to complete testing, while reducing the opportunity for tissue degradation.

Overall evaluation of biofidelity of post mortem model. While comparison of motion measured in the current *post mortem* low-rate test series with the previously reported results from the *in vivo* MR study by Feng et al. offered the potential to evaluate whether a *post mortem* model could effectively match *in vivo* motion at the periphery of the brain, it was unclear whether differences in cortex motion in the volunteer tests and the current isolated head testing resulted from *post mortem* changes or from the fact that the current *post mortem* results showed motion only between the meninges and the very outer surface of the cortex while Feng's *in vivo* results measured deeper cortical motion. Therefore, questions remain regarding the use of *post mortem* subjects to predict *in vivo* motion of the meninges and peripheral brain relative to the skull.

Once modifications have been made as proposed above to further minimize the effects of intracranial pressurization, perfusion differences between the *post mortem* and volunteer models, and brain tissue degradation, low-rate rotation testing should be repeated to evaluate the biofidelity of the *post mortem* rotation model relative to the *in vivo* results. A more direct comparison than the one made in the current study could be made using a deeper field of view in ultrasound imaging in order to compare cortical tissues at the same location relative to the skull for the *in vivo* and *post mortem* tests.

6.4 Analysis by Atrophy

The increase in bridging-vein associated subdural hematoma with age has been associated with age-related brain atrophy. Atrophy may allow increased relative motion between the skull and brain, leading to bridging vein tension and risk of failure (Yamashima and Friede 1984; Meaney 1991; Kleiven and von Holst 2002; Hanif, Abodunde et al. 2009). Therefore, the risk of subdural hematoma from bridging vein bleeding as a function of head motion would be expected to vary not only with age, but more directly with the extent of brain atrophy. Experimentally determining the relationship between skull motion and relative brain motion by age would require a very large number adult test subjects across broad age range, since the relationships between age and atrophy and between atrophy and resulting relative motion are both statistical rather than deterministic relationships. A more efficient approach is to account for the effect of atrophy on experimental motion test results, and use existing data on the statistical relationship between age and brain atrophy (Gur, Mozley et al. 1991; Good, Johnsrude et al. 2001; Resnick, Pham et al. 2003) to ultimately characterize the age-

dependent relationship between skull motion, relative brain motion, and the resulting risk of subdural hematoma from torn bridging veins. To that end, efforts were made in the current series of tests to develop a procedure for MR scanning and atrophy estimation of test subjects prior to testing so that all future test subjects could be evaluated by the same procedure. MR imaging was selected for the evaluation of atrophy because it is the imaging method most frequently reported for clinical evaluation of atrophy so that test results could ultimately be compared to clinical ranges of atrophy as a function of age.

Measures of brain atrophy are typically relative: measurements on individual patients are made periodically using the same technology and conditions to monitor changes over time, and studies comparing individuals typically involve measurements made using the same imaging settings and protocol. However, in the current study, although the same 7-Tesla MR equipment and collection sequences were used for both studies, the resulting tissue signal from the two subjects appeared to vary. Using the same protocol for segmentation of the T1 images resulted in inconsistent identification of CSF, grey matter, and white matter in the scans of the two subjects. The primary difference between the scans of the two subjects was that subject PM01 was imaged approximately 13.5 hours *post mortem* while subject PM02 was imaged approximately 35 hours *post mortem*. From preliminary analysis of the scans, it is suspected that *post mortem* changes may have modulated the response of CSF and tissue characteristic parameters in T1 and T2 images. These changes may have altered CSF, gray matter and white matter tissue contrast and led to variability in the analysis of tissue volume using SPM8 software procedures. Prior to continuing to test *post mortem* subjects to establish

the relationship between skull rotation and relative brain motion, reliable methods to consistently measure atrophy in the tested *post mortem* subjects must be developed and confirmed.

Future work to understand how brain tissue and CSF fluid MRI characteristics vary with elapsed *post mortem* time would be valuable for any study involving *post mortem* MR imaging, and may provide valuable insights on the timing of changes in the brain following death. Additionally, understanding the effects of *post mortem* changes on MR images may make MR imaging a valuable tool to non-invasively study changes in the brain following death. For example, if the presence of gases resulting from brain decomposition had an effect on MR signal characteristics that could be quantified, MR imaging could be used to non-invasively track the buildup of such gasses in the hours and days after death. Such a study would ideally involve serial MR images of a *post mortem* subject head at periodic times after death.

More urgent for the current research effort, however, is the identification of a method of measuring brain atrophy that is independent of *post mortem* delay so that consistent measurements of atrophy can be compared for each test subject. Alternative methods to explore include the use of different image segmentation techniques, image sequences and use of lower-magnetic field equipment.

6.5 Application of Developed Methods to Understand the Mechanism of Subdural Hematoma

This experimental rotation study was an effort to develop methods to track the motion of the meninges and peripheral brain during head rotation. While the ultimate

goal of this line of research is the development of an age-dependent relationship between whole-head motion and risk of subdural hematoma from bridging vein bleeding, tools are not available to experimentally determine this relationship. Therefore, experimental procedures were developed in the current study as a first step in a multi-stage process to quantify the risk of subdural hematoma as a function of head kinematics for adults of varying ages. Several research steps remain to apply the developed measurement procedures toward the ultimate goal of predicting risk of subdural hematoma from whole-head motion.

(1) Refinement of developed experimental procedures. The next step is to modify and finalize the procedures developed in the current study according to the recommendations made in this dissertation. As described in this chapter, additional work is needed to improve subject preparation, confirm effectiveness of a *post mortem* model in reproducing accurate intracranial motion during rotation, and to improve mechanical rotation methods so that tissue motion remains in the ultrasound imaging plane.

(2) High-rate rotation testing of subjects over range of brain atrophy. Subsequently, the refined procedures for measuring relative motion with ultrasound in rotation tests can be used to track meningeal and cortical motion in high-rate rotation tests of subjects with a range of levels of brain atrophy. Testing should be configured for anterior-posterior rotational acceleration consistent with frontal impact. Varying acceleration pulse durations and peak values, while limiting peak rotational velocity to the level that can be measured using available ultrasound technology will provide both *qualitative* insight into which tissue layers separate or deform to allow tissue motion

relative to the skull, as well as *quantitative* relationships between skull motion and relative tissue motion as a function of brain atrophy. The strength of these relationships can be used to determine the kinematic parameter (e.g. rotational acceleration, velocity, duration, or combination of these) that is most closely linked with the magnitude of intracranial relative motion in head rotation.

(3) Comparison of experimentally-determined relative motion to failure properties of bridging veins. Since parasagittal bridging veins originate in the cortical tissue then cross through the meningeal layers before emptying into the superior sagittal sinus, the motion of the cortex and meningeal layers relative to the skull and sinus can be used to estimate the resulting stretch in the bridging veins. The tensile failure properties of isolated bridging veins can then be used to predict the probability of bridging vein failure at a given level of relative intracranial motion. Thus, by combining the probabilistic relationships between skull motion and intracranial motion at a given level of brain atrophy and between the resulting bridging vein stretch and risk of rupture, estimates of the risk of bridging vein rupture can be made as a function of the kinematics of the skull.

The developed relationship between skull rotation and risk of subdural hematoma from bridging vein rupture is not expected to cover risk levels up to 100% since the current ultrasound technology procedures used are limited to effective tissue tracking at rotation rates consistent with the lower end of previously predicted ranges of injury thresholds for bridging vein-associated subdural hematoma. However, if the qualitative results of rotation testing can be used to refine meningeal boundary conditions in

computational models of brain motion, and the quantitative results can be used to validate those models, the relationship between skull motion and the resulting motion of the cortex and meningeal layers can be extended to predict risk of bridging vein rupture and subdural hematoma at higher rotation rates than can be tested experimentally.

(4) Development of relationship between skull rotation and risk of bridging vein-associated subdural hematoma by age. The final step in defining an age-dependent prediction of subdural hematoma risk is to replace the brain atrophy variable with age based on the probabilistic relationship between age and atrophy.

Chapter 7: Implications and Future Work

7.1 Epidemiology of Head Injury in Older Motor Vehicle Crash Occupants

Motor vehicle crash data shows that older occupants with head injury are more likely to sustain bleeding injuries than younger occupants (Mallory 2010). Subdural hematoma is of particular importance among the bleeding injuries that increase with age because of the double risk presented by increased frequency of subdural hematoma with age and the increased rate of mortality for subdural hematoma with age. More detailed analyses of subdural hematoma cases in motor vehicle crash data showed that the increase in the rate of isolated subdural hematoma with age among adult crash occupants likely reflects an increase in the frequency of subdural hematoma caused by bridging vein bleeding, particularly in frontal head impacts (Mallory, Herriott et al. 2011).

The results of these epidemiological studies motivate exploration of the mechanism of subdural hematoma in older crash occupants and, ultimately, the development of age-adjusted injury tolerance predictions so that head injury countermeasures can be developed for older occupants. Determination of age-specific injury tolerance thresholds for subdural hematoma will require evaluation of the increasing risk of bridging vein failure in aging crash victims, specifically the increased potential for stretch of the bridging veins for older individuals in anterior-posterior head motion. These ultimate goals motivated the experimental work in this dissertation to

develop methods for measuring the intracranial motion associated with bridging vein stretch in anterior-posterior head rotation.

Future work. Epidemiological results suggest that the head loading required to produce subdural hematoma from bleeding sources other than bridging veins may differ significantly from the loading needed to produce subdural hematoma associated with bridging vein failure. While bridging vein associated subdural hematomas are most relevant for understanding older occupant head injury risk, future research is also needed on the mechanism of subdural hematomas that result from contusions and ruptured vessels on the surface of the brain, given the frequency of subdural hematoma from non-bridging-vein sources among occupants younger than 70.

7.2 Use of B-Mode Ultrasound to Measure High-Speed Tissue Motion

B-mode ultrasound has not previously been used to measure tissue motion in injury biomechanics research. The experimental studies in this dissertation demonstrated the effectiveness of using high-frequency, high frame-rate B-mode ultrasound to measure motion in tissue testing. Although imaging of high-speed, large-displacement motions resulted in temporal distortion of position-time histories tracked from ultrasound images, the correction algorithm developed and validated in Chapter 3 was demonstrated to successfully correct this potential source of error.

Applications for use of current high-frequency B-mode technology for high-rate tissue testing are currently limited by tissue speed limitations, very small image frame size at high speeds, ultrasound probe fragility, incompatibility with out-of-plane motion, and the need for a fluid or gel imaging medium. However, subject to these limitations,

B-mode ultrasound imaging was effectively applied to the imaging of meningeal and peripheral brain motion in rotation testing, resulting in quantification of gross motion of individual layers of tissue.

Improved accuracy of cumulative tissue motion and more detailed analysis of tissue deformation and strain may be possible with direct analysis of ultrasound images with speckle-tracking techniques in place of the semi-automatic point-tracking techniques used in the current study.

Future work. Wider application of high-frequency B-mode ultrasound technology to high-speed tissue motion in studies of brain motion and other biological applications would be possible with technical innovations that would allow simultaneous firing of multiple transducer elements. Such advances have the potential to increase the image field of view, measurable tissue speed, and the possibility of imaging out-of-plane motion. Additionally, ruggedization of high-frequency ultrasound probes so that they could be accelerated with tissues of interest could significantly improve their usefulness in higher-speed, non-planar testing and for imaging motion of deep structures rather than just superficial tissues.

For future efforts to track tissue motion using B-mode ultrasound, speckle-tracking techniques should be developed for comparison to point-tracking techniques in order to compare the efficiency, repeatability, and accuracy to the point-tracking methods used in the current study. The potential to use speckle-tracking methods to map deformation and strain within tissue, as well as gross tissue motion, should be evaluated.

7.3 Experimental Rotation Testing

Using the methods developed for this project, rotation testing was performed on two *post mortem* subjects at acceleration levels ranging from approximately 120 rad/sec^2 to 7700 rad/sec^2. The procedures were effective for measuring motion of the dura, peripheral cortex, and dura/cortex interface layer at lower acceleration levels. Although the anatomical position of this interface layer and its motion relative to the dura and cortex in motion testing were consistent with it being the arachnoid membrane, it could not be definitively identified.

At higher levels of acceleration, results showed that the methods and procedures developed have the potential to measure intracranial motion with the resolution of remaining experimental issues. Results of these preliminary tests and proposed improvements to the test procedures are summarized below.

7.3.1 Relative Motion Measured in Low-Speed Testing

Preliminary testing in the current study showed that low-rate, sub-injury head rotation resulted in less than 0.2 mm of motion of the cortical surface relative to the skull. Combining the current results with previous MR imaging results from volunteer tests with the same rotational kinematics (Feng, Abney et al. 2010) leads to the preliminary conclusion that motion of the brain relative to the skull in sub-injury rotation results from shear strain and deformation of the cortex, rather than from relative sliding of the meningeal layers.

However, definitive comparison or combination of the motion response observed in the current *post mortem* low-rate tests with the previously reported motion from the

volunteer testing by Feng et al. (2010) is prevented by the difference in tissue depths imaged in each of the studies: the current study captures high-resolution images of the meninges and cortical surface, while the Feng study images deeper brain motion that does not extend to the surface of the cortex. Additional work to strengthen conclusions that can be made from low-rate *post mortem* rotation testing includes additional *post mortem* ultrasound rotation testing to image to the same depth of cortical tissue observed in Feng's previous volunteer tests, as well as several proposed strategies for minimizing potential differences between Feng's volunteer MR study and the current study that resulted from using *post mortem* subjects.

Future work. The first step toward comparing the current low-rate rotation results directly with Feng's previous volunteer results is to repeat *post mortem* rotation tests with ultrasound using a deeper ultrasound image field of view to observe the motion of both the meningeal and cortical surface layers seen in initial *post mortem* tests, as well as the cortical tissue comparable to the depths tracked by Feng et al. in *in vivo* volunteer tests. Comparison of cortical motion at the same depth in *post mortem* and *in vivo* testing would allow evaluation of whether the *post mortem* head is a reasonable model for the *in vivo* head and whether the effects of translational acceleration in Feng's test configuration is negligible relative to the effects of rotational acceleration. If the motion measured in *post mortem* rotation tests were comparable to motion in *in vivo* rotation/translation tests, it would confirm that the deeper, courser-resolution results observed in Feng's volunteer tests could be combined with the more peripheral, finer-resolution results in the current

post mortem ultrasound rotation tests to provide a complete picture of motion from the meninges to the central brain in low-rate rotation.

In order to definitively track the relative motion of the arachnoid, as well as the dura and cortex in rotation testing, a more effective method of identifying the arachnoid in ultrasound images is needed.

Additional future work to specifically evaluate and minimize the effect of *post mortem* changes in the head on relative motion in the meninges and periphery of the brain are summarized in Section 7.3.3.

7.3.2 Potential for B-Mode Ultrasound to Measure Meningeal Motion in High-Rate Testing

The results reported in this study confirm the potential effectiveness of using high-speed, high-frequency B-mode ultrasound to track tissue motion at the periphery of the brain relative to the skull in lower-rate rotation testing. While the preliminary tests run at higher rates, approaching the range of rotational acceleration previously associated with subdural hematoma, could not be used for motion analysis because of tissue motion out of the ultrasound image plane, it is expected that such out-of-plane motion can be prevented with modifications to the test procedure and rotation fixture. Planar validation tests to evaluate the ultrasound imaging and tracking procedures on high-rate motion of dura samples established the effectiveness of the developed methods at high speed such that it can be concluded that the B-mode ultrasound methods developed to image peripheral motion of the brain relative to the skull in head-impact levels of rotation will

be effective once rotation procedures are improved to eliminate out-of-plane motion of the imaged tissues.

Future work. Resolution of out-of-plane tissue motion in high-rate rotation tests is essential to testing at rotation rates sufficient to compare to injury-level rotations. Two potential sources of out-of-plane motion of the tissue need to be addressed. The first source of out-of-plane motion is the axial acceleration of tissue that results from high rotational velocity. Potential solutions include development of an ultrasound-transparent material stiff enough to replace the removed skull in holding the tissue in place during rotation; ruggedization of the ultrasound probe so it could be mounted to the skull during acceleration and the probe face could prevent radial tissue motion; narrowing of the window cut into the skull with additional buttressing of the exposed tissue; and vertical placement of the ultrasound probe. Development of solutions for the second source of out-of-plane motion, associated with motion of the entire head during acceleration, will require evaluation of motion resulting from the pyrotechnic pretensioner, motion of the shaft within the fixture bearings, deformation of the aluminum cage, or displacement of the head within the cage.

7.3.3 Use of *Post Mortem* Subjects to Evaluate Meningeal Motion

Post mortem human heads were selected as models for intracranial motion in the current study because the high-rate, destructive test procedures precluded use of human volunteers, and available non-human animal models were insufficiently similar to humans in brain shape and craniospinal angle to be effective in rotation testing.

The effectiveness of efforts to prepare the *post mortem* subjects to minimize the differences between the *post mortem* head the and *in vivo* human head was evaluated and future improvements to *post mortem* preparation procedures recommended. The potential for a *post mortem* model to ultimately be effective in the measurement of meningeal and peripheral intracranial motion is discussed.

Softening of brain tissue in the days after death and buildup of intracranial gases developing as a byproduct of *post mortem* cell death can contribute to altered motion of the brain parenchyma, difficulties re-pressurizing the head to normal intracranial pressure, prevention of perfusion of the subarachnoid space with artificial CSF, and artifact in ultrasound images, and may be associated with changes in the coupling of the brain and skull. Thus degradation of brain tissue over the time needed to prepare subjects in the current test series is a major concern.

While the subjects used for preliminary testing in this dissertation were accepted only if available within 48 hours after death, and all testing was completed within 4 days of death, the subject received almost 30 hours *post mortem* (PM02) showed significantly more evidence of *post mortem* deterioration than the subject received less than 10 hours *post mortem* (PM01). It was concluded that *post mortem* deterioration in PM02 was associated with preventing effective pressurization to normal intracranial pressure and perfusion of the cranial subarachnoid space with artificial CSF, and with intracranial image artifact in ultrasound images. While no definitive post-mortem delay before intracranial motion testing has been defined as acceptable, minimization of post-mortem

test time is clearly desirable and should be limited to shorter *post mortem* times than the limits used in preliminary testing.

While maintaining the integrity of tissues by reducing *post mortem* delay is likely the most important improvement to subject preparation procedures, all efforts to bring the *post mortem* heads closer to an *in vivo* state were evaluated.

Methods to use pressurization of the vascular system to return the head to physiological *intracranial* pressure differed from previous efforts to return *vascular* pressure to normal physiological levels. Use of this strategy to control intracranial pressure directly in future testing is supported by the results of preliminary tests that showed that measured intracranial pressure did not vary directly with applied vascular pressure. Although modifications to the procedure are recommended in order to monitor intracranial pressure prior to testing rather than after testing, the success of the developed methods in maintaining normal intracranial pressure was demonstrated for subject PM01. Changes to the venous pressurization system should be developed to improve perfusion of the superior sagittal sinus and bridging veins.

Procedures used to introduce artificial CSF into the cranial subarachnoid space via the spinal subarachnoid space represent the first known effort to specifically re-perfuse this space in a *post mortem* head. Although plumbing and *post mortem* deterioration issues in the two subjects reported in this dissertation prevented effective re-perfusion of CSF using these methods, pre-test trials to perfuse this space were successful. Given the importance of returning the relationships between the meningeal

layers to their *in vivo* state when measuring peripheral intracranial motion during rotation, continued use of these re-perfusion procedures is essential.

Overall, preliminary results show good potential for improving subject preparation techniques to minimize the differences between *post mortem* and *in vivo* models for brain motion in rotation. Once preparation techniques are improved and *post mortem* delay can be minimized, additional low-rate rotation testing in the same acceleration range tested previously with human volunteers (Feng, Abney et al. 2010) will allow a more definitive comparison of *in vivo* and *post mortem* response. Using a deeper ultrasound image field of view will allow more direct comparison of *post mortem* motion with the previous volunteer results. Differences between *post mortem* and *in vivo* response in high-rate rotation may also be affected by *post mortem* deterioration of the dural border cell layer. Ultimately, research to explore *post mortem* changes in this connection between the dura and the arachnoid may be needed to understand potential differences in *post mortem* and *in vivo* results. Potential methods for studying these *post mortem* differences are proposed in Section 6.3.3.

Future work. While immediate changes to test procedures have been recommended to improve intracranial re-pressurization and CSF perfusion and to reduce *post mortem* delay before testing, longer term research on the effects of *post mortem* timing on degradation of intracranial tissues and buildup of intracranial gases would be of great benefit for all experimental head injury work relying on *post mortem* material. The effects of storage conditions and temperature should be explored as well. Additional

research is needed to understand and quantify *post mortem* changes in the dural border cell layer between the dura and the arachnoid.

7.3.4 Evaluation of Brain Atrophy in Test Subjects

Pre-test MR scanning of the heads of *post mortem* subjects offers an opportunity to compare the relative atrophy in each subject for use in the development of motion predictions as a function of atrophy, and ultimately as a function of age. However, analysis of the pre-test 7-Tesla MR images of the subjects in this study suggested that *post mortem* changes in brain tissues and fluids affected the resulting images such that atrophy was not consistently calculated for subjects scanned after different durations of *post mortem* delay using SPM8 segmentation techniques on T1 images.

Future work. Prior to the continuation of *post mortem* motion testing, methods need to be identified to reliably measure brain atrophy pre-test so that it can be incorporated into predictions of the relationship between skull motion and brain motion. If MR imaging is used to make clinically-relevant estimates of brain atrophy, segmentation methods for *post mortem* MR images need to be improved to provide consistent estimates of atrophy, even for subjects imaged at varying times *post mortem.*

Additional research to understand how tissue and fluid response in MR imaging vary with elapsed *post mortem* time would be more broadly useful for any study involving *post mortem* MR imaging, and could be particularly useful in studying the timing of deterioration in the *post mortem* brain. The first steps of such a study would involve analysis of serial MR images of a *post mortem* subject head at periodic times after death.

7.4 Prediction of Subdural Hematoma Risk with Developed Methods

The immediate goal of the experimental work in this dissertation was targeted at the development of methods to measure the relative motion of the meninges and peripheral brain during head rotation. Testing with *post mortem* human subject heads successfully confirmed the potential of the developed test procedures for this purpose.

Once refined and finalized, these methods are expected to be effective in demonstrating *qualitatively* which tissue layers are moving relative to each other in impact-level rotations to better understand the mechanism of bridging vein stretch and failure associated with subdural hematoma. Quantifying this motion in tests of *post mortem* subjects demonstrating a range of brain atrophy will allow development of relationships between skull motion and bridging vein stretch as a function of brain atrophy. In turn, the probabilistic relationships between bridging vein stretch and risk of failure and between brain atrophy and age can be used to develop predictions of the risk of bridging vein failure and associated subdural hematoma as a function of skull motion and occupant age. Additionally, results of meningeal motion testing could be used to better define and validate boundary conditions among the meningeal layers in computational models to improve the biofidelity of head impact models for adults of all ages.

The methods developed in this study to track motion of the meninges during head rotation using high-frequency, high frame-rate B-mode ultrasound represent a first essential step in the development of age-dependent risk estimates for subdural hematoma from bridging vein bleeding.

References

AAAM (1990). "The Abbreviated Injury Scale, 1990 Revision", Des Plaines, IL.

AAAM (1998). "The Abbreviated Injury Scale, 1990 Revision Update 98", Des Plaines, IL.

Abney, T. M., Y. A. Feng, R. Pless, R. J. Okamoto, G. M. Genin and P. V. Bayly (2010). "Principal Components of Brain Deformation in Response to Skull Acceleration: The Roles of Sliding and Tethering between the Brain and Skull." 26th Southern Biomedical Engineering Conference.

Al-Bsharat, A. S., W. N. Hardy, K. H. Yang, T. B. Khalil, S. Tashman and A. I. King (1999). "Brain/Skull Relative Displacement Magnitude Due to Blunt Head Impact: New Experimental Data and Model." Stapp Car Crash Conference.

Anata, K., Y. Miyazaki, T. Nishi, H. Tachiya, A. Hojo and Y. Sakamoto (2010). "Constructions of a Head Physical Model with Actual Human Shape for Clarification of Brain Injury Mechanism and the Deformation Measurement." Transactions of the Japan Society of Mechanical Engineers 76(762): 233-240.

Bayly, P. V., T. S. Cohen, E. P. Leister, D. Ajo, E. C. Leuthardt and G. M. Genin (2005). "Deformation of the Human Brain Induced by Mild Acceleration." Journal of Neurotrauma 22(8): 845-56.

Bentil, S. A. (2013). "A Fractional Zener Constitutive Model to Describe the Degradation of Swine Cerebrum with Validation from Experimental Data and Predictions Using Finite Element Analysis." Ph.D. Dissertation, Mechanical Engineering, Ohio State University.

Cheng, J., I. C. Howard and M. Rennison (2010). "Study of an Infant Brain Subjected to Periodic Motion Via a Custom Experimental Apparatus Design and Finite Element Modelling." Journal of Biomechanics 43(15): 2887-96.

Chieregato, A., E. Fainardi, A. M. Morselli-Labate, V. Antonelli, C. Compagnone, L. Targa, J. Kraus and F. Servadei (2005). "Factors Associated with Neurological Outcome and Lesion Progression in Traumatic Subarachnoid Hemorrhage Patients." Neurosurgery 56(4): 671-80; discussion 671-80.

Claessens, M., F. Sauren and J. Wismans (1997). "Modeling of the Human Head under Impact Conditions: A Parametric Study." 41st Stapp Car Crash Conference, SAE, Inc.

Coats, B., S. A. Eucker, S. Sullivan and S. S. Margulies (2012). "Finite Element Model Predictions of Intracranial Hemorrhage from Non-Impact, Rapid Head Rotations in the Piglet." International Journal of Developmental Neuroscience.

Coronado, V. G., K. E. Thomas, R. W. Sattin and R. L. Johnson (2005). "The CDC Traumatic Brain Injury Surveillance System: Characteristics of Persons Aged 65 Years and Older Hospitalized with a TBI." Journal of Head Trauma Rehabilitation 20(3): 215-228.

Darvish, K. and J. Crandall (2001). "Nonlinear Viscoelastic Effects in Oscillatory Shear Deformation of Brain Tissue." Medical Engineering and Physics 23(9): 633-645.

DeLahunta, A. and E. Glass (2009). "Veterinary Neuroanatomy and Clinical Neurology." St. Louis, Mo., Saunders Elsevier.

Delye, H., J. Goffin, P. Verschueren, J. Vander Sloten, G. Van der Perre, H. Alaerts, I. Verpoest and D. Berckmans (2006). "Biomechanical Properties of the Superior Sagittal Sinus-Bridging Vein Complex." Stapp Car Crash Journal 50: 625-636.

Depreitere, B., C. Van Lierde, J. V. Sloten, R. Van Audekercke, G. Van der Perre, C. Plets and J. Goffin (2006). "Mechanics of Acute Subdural Hematomas Resulting from Bridging Vein Rupture." Journal of Neurosurgery 104(6): 950-6.

Depreitere, B., C. Van Lierde, P. Verschueren, H. Delye, D. Berckmans, I. Verpoest, J. Vander Sloten, G. Van der Perre and J. Goffin (2005). "Cerebral Bridging Vein Rupture in Humans: An Experimental Evaluation." In IUTAM Symposium on Impact Biomechanics, M. D. Gilchrist, Springer: 305-12.

Feng, Y., T. M. Abney, R. J. Okamoto, R. B. Pless, G. M. Genin and P. V. Bayly (2010). "Relative Brain Displacement and Deformation During Constrained Mild Frontal Head Impact." Journal of the Royal Society Interface 7(53): 1677-88.

Funk, J. R., J. M. Cormier, C. E. Bain, H. Guzman, E. Bonugli and S. J. Manoogian (2011). "Head and Neck Loading in Everyday and Vigorous Activities." Annals of Biomedical Engineering 39(2): 766-776.

Garo, A., M. Hrapko, J. Van Dommelen and G. Peters (2007). "Towards a Reliable Characterisation of the Mechanical Behaviour of Brain Tissue: The Effects of Post-Mortem Time and Sample Preparation." Biorheology 44(1): 51-58.

Gennarelli, T. A., G. M. Spielman, T. W. Langfitt, P. L. Gildenberg, T. Harrington, J. A. Jane, L. F. Marshall, J. D. Miller and L. H. Pitts (1982). "Influence of the Type of

Intracranial Lesion on Outcome from Severe Head Injury." Journal of Neurosurgery 56(1): 26-32.

Gennarelli, T. A. and L. E. Thibault (1982). "Biomechanics of Acute Subdural Hematoma." Journal of Trauma-Injury Infection & Critical Care 22(8): 680-6.

Good, C. D., I. S. Johnsrude, J. Ashburner, R. N. Henson, K. Fristen and R. S. Frackowiak (2001). "A Voxel-Based Morphometric Study of Ageing in 465 Normal Adult Human Brains." Neuroimage 14: 21-36.

Gosch, H. H., E. Gooding and R. C. Schneider (1970). "The Lexan Calvarium for the Study of Cerebral Responses to Acute Trauma." Journal of Trauma-Injury Infection & Critical Care 10(5): 370-6.

Graham, D. I. (1996). "Neuropathology of Head Injury." In Neurotrauma, R. K. Narayan, J. E. Wilberger and J. T. Povlishock (Eds.), New York, McGraw Hill: 43-59.

Greene, K. A., F. F. Marciano, B. A. Johnson, R. Jacobowitz, R. F. Spetzler and T. R. Harrington (1995). "Impact of Traumatic Subarachnoid Hemorrhage on Outcome in Nonpenetrating Head Injury. Part I: A Proposed Computerized Tomography Grading Scale." Journal of Neurosurgery 83(3): 445-52.

Gur, R. C., P. D. Mozley, S. M. Resnick, G. L. Gottlieb, M. Kohn, R. Zimmerman, G. Herman, S. Atlas, R. Grossman and D. Berretta (1991). "Gender Differences in Age Effect on Brain Atrophy Measured by Magnetic Resonance Imaging." Proceedings of the National Academy of Sciences 88(7): 2845-2849.

Haines, D. E., H. L. Harkey and O. Al-Mefty (1993). "The "Subdural" Space: A New Look at an Outdated Concept." Neurosurgery 32(1): 111-120.

Han, H., W. Tao and M. Zhang (2007). "The Dural Entrance of Cerebral Bridging Veins into the Superior Sagittal Sinus: An Anatomical Comparison between Cadavers and Digital Subtraction Angiography." Neuroradiology 49(2): 169-175.

Hanif, S., O. Abodunde, Z. Ali and C. Pidgeon (2009). "Age Related Outcome in Acute Subdural Haematoma Following Traumatic Head Injury." Irish Medical Journal 102(8): 255-7.

Hardy, W. N. (2007). "Response of the Human Cadaver Head to Impact." Ph.D. Dissertation, Biomedical Engineering, Wayne State University, Detroit, Michigan.

Hardy, W. N., C. D. Foster, M. Mason, K. H. Yang, A. I. King and S. Tashman (2001). "Investigation of Head Injury Mechanisms Using Neutral Density Technology and High-Speed Biplanar X-Ray." Stapp Car Crash Journal 45: 1-32.

Hardy, W. N., M. J. Mason, C. D. Foster, C. S. Shah, J. M. Kopacz, K. H. Yang, A. I. King, J. Bishop, M. Bey, W. Anderst and S. Tashman (2007). "A Study of the Response of the Human Cadaver Head to Impact." Stapp Car Crash Journal 51: 17-80.

Haselsberger, K., R. Pucher and L. M. Auer (1988). "Prognosis after Acute Subdural or Epidural Haemorrhage." Acta Neurochirurgica 90(3-4): 111-116.

Hodgson, V. R., E. S. Gurdjian and L. M. Thomas (1966). "Experimental Skull Deformation and Brain Displacement Demonstrated by Flash X-Ray Technique." Journal of Neurosurgery 25(5): 549-52.

Holbourn, A. H. S. (1943). "Mechanics of Head Injuries." Lancet 2: 438-441.

Horgan, T. J. and M. D. Gilchrist (2004). "Influence of FE Model Variability in Predicting Brain Motion and Intracranial Pressure Changes in Head Impact Simulations." International Journal of Crashworthiness 9(4): 401-418.

Hukkelhoven, C. W., E. W. Steyerberg, A. J. Rampen, E. Farace, J. D. Habbema, L. F. Marshall, G. D. Murray and A. I. Maas (2003). "Patient Age and Outcome Following Severe Traumatic Brain Injury: An Analysis of 5600 Patients." Journal of Neurosurgery 99(4): 666-73.

Ibrahim, N. G., R. Natesh, S. E. Szczesny, K. Ryall, S. A. Eucker, B. Coats and S. S. Margulies (2010). "In Situ Deformations in the Immature Brain During Rapid Rotations." Journal of Biomechanical Engineering 132(4): 044501.

Jamieson, K. G. and J. D. Yelland (1972). "Surgically Treated Traumatic Subdural Hematomas." Journal of Neurosurgery 37(2): 137-49.

Jane, J. A. and P. C. Francel (1996). "Age and Outcome of Head Injury." In Neurotrauma, R. K. Narayan, J. E. Wilberger and J. T. Povlishock, McGraw-Hill: 793-804.

Ji, S., D. W. Roberts, A. Hartov and K. D. Paulsen (2009). "Brain-Skull Contact Boundary Conditions in an Inverse Computational Deformation Model." Medical Image Analysis 13(4): 659-72.

Ji, S., Q. Zhu, L. Dougherty and S. S. Margulies (2004). "In Vivo Measurements of Human Brain Displacement." Stapp Car Crash Journal 48: 227-37.

Kahane, C. J. (2013). "Injury Vulnerability and Effectiveness of Occupant Protection Technologies for Older Occupants and Women". Report No. DOT HS 811 766, National Highway Traffic Safety Administration, Washington, DC.

King, A. I., J. S. Ruan, C. Zhou, W. N. Hardy and T. B. Khalil (1995). "Recent Advances in Biomechanics of Brain Injury Research: A Review." Journal of Neurotrauma 12(4): 651-658.

Kleiven, S. (2006). "Evaluation of Head Injury Criteria Using a Finite Element Model Validated against Experiments on Localized Brain Motion, Intracerebral Acceleration, and Intracranial Pressure." International Journal of Crashworthiness 11(1): 65-79.

Kleiven, S. and W. N. Hardy (2002). "Correlation of an FE Model of the Human Head with Local Brain Motion--Consequences for Injury Prediction." Stapp Car Crash Journal 46: 123-44.

Kleiven, S. and H. von Holst (2002). "Consequences of Head Size Following Trauma to the Human Head." Journal of Biomechanics 35(2): 153-60.

Kleiven, S. and H. von Holst (2002). "Consquences of Reduced Brain Volume Following Impact in Prediction of Subdural Hematoma Evaluated with Numerical Techniques." Traffic Injury Prevention 3: 303-310.

Lee, M. C. and R. C. Haut (1989). "Insensitivity of Tensile Failure Properties of Human Bridging Veins to Strain Rate: Implications in Biomechanics of Subdural Hematoma." Journal of Biomechanics 22(6-7): 537-42.

Lee, M. C., J. W. Melvin and K. Ueno (1987). "Finite Element Analysis of Traumatic Subdural Hematoma." 31st Stapp Car Crash Conference, SAE.

Löwenhielm, P. (1974). "Dynamic Properties of the Parasagittal Bridging Veins." Zeitschrift fur Rechtsmedizin. Journal of Legal Medicine 74(1): 55-62.

Löwenhielm, P. (1974). "Strain Tolerance of the Vv. Cerebri Sup. (Bridging Veins) Calculated from Head-on Collision Tests with Cadavers." Zeitschrift fur Rechtsmedizin. Journal of Legal Medicine 75(2): 131-44.

Maier, S. E., C. J. Hardy and F. A. Jolesz (1994). "Brain and Cerebrospinal Fluid Motion: Real-Time Quantification with M-Mode MR Imaging." Radiology 193(2): 477-83.

Mallory, A. (2010). "Head Injury and Aging: The Importance of Bleeding Injuries." Annals of Advances in Automotive Medicine 54: 51-60.

Mallory, A., R. Herriott and H. Rhule (2011). "Subdural Hematoma and Aging: Crash Characteristics and Associated Injuries." 22nd International Technical Conference on the Enhanced Safety of Vehicles (ESV). Washington, DC: Paper Number 11-0399.

Margulies, S. S. (1987). "Biomechanics of Traumatic Coma in the Primate." Ph.D. Dissertation, University of Pennsylvania.

Margulies, S. S., L. E. Thibault and T. A. Gennarelli (1990). "Physical Model Simulations of Brain Injury in the Primate." Journal of Biomechanics 23(8): 823-36.

Marshall, L. F., T. Gautille, M. R. Klauber, H. M. Eisenberg, J. A. Jane, T. G. Luerssen, A. Marmarou and M. A. Foulkes (1991). "The Outcome of Severe Closed Head Injury." Journal of Neurosurgery 75: S28-S36.

Mattioli, C., L. Beretta, S. Gerevini, F. Veglia, G. Citerio, M. Cormio and N. Stocchetti (2003). "Traumatic Subarachnoid Hemorrhage on the Ct Scan Obtained at Admission: A Multicenter Assessment of the Accuracy of Diagnosis and the Potential Impact on Patient Outcome." Journal of Neurosurgery 98(1): 37-42.

Maxeiner, H. (1997). "Detection of Ruptured Cerebral Bridging Veins at Autopsy." Forensic Science International 89(1-2): 103-10.

Maxeiner, H. (1998). "Subdural Hematomas in Victims with and without Cerebral Contusions - Comparision of Two Types of Head Injuries." Rechtsmedizin 9(1): 14-20.

Maxeiner, H. and M. Wolff (2002). "Pure Subdural Hematomas: A Postmortem Analysis of Their Form and Bleeding Points." Neurosurgery 50(3): 503-509.

Meaney, D. F. (1991). "Biomechanics of Acute Subdural Hematoma in the Subhuman Primate and Man." Ph.D. Dissertation, Bioengineering, University of Pennsylvania.

Miller, D. J., I. R. Piper and P. A. Jones (1996). "Pathophysiology of Head Injury." In Neurotrauma, R. K. Narayan, J. E. Wilberger and J. T. Povlishock (Eds.), New York, McGraw Hill: 61-69.

Miller, J. D. and P. F. X. Statham (2000). "Surgical Management of Traumtic Intracranial Hematomas." In Operative Neurosurgical Techniques, H. H. Schmidek (Eds.), Philadelphia, PA, W.B. Saunders Company. 1: 83-90.

Monea, A. G., I. Verpoest, J. Vander Sloten, G. Van der Perre, J. Goffin and B. Depreitere (2012). "Assessment of Relative Brain-Skull Motion in Quasistatic Circumstances by Magnetic Resonance Imaging." Journal of Neurotrauma 29(13): 2305-2317.

Monson, K. L., W. Goldsmith, N. M. Barbaro and G. T. Manley (2005). "Significance of Source and Size in the Mechanical Response of Human Cerebral Blood Vessels." Journal of Biomechanics 38(4): 737-744.

Moore, K. L. (1992). "Clinically Oriented Anatomy." Baltimore, MD, Williams & Wilkins.

Mosenthal, A. C., R. F. Lavery, M. Addis, S. Kaul, S. Ross, R. Marburger, E. A. Deitch and D. H. Livingston (2002). "Isolated Traumatic Brain Injury: Age Is an Independent

Predictor of Mortality and Early Outcome." Journal of Trauma-Injury Infection & Critical Care 52(5): 907-11.

Newman, J. A. (1998). "Kinematics of Head Injury." In Frontiers of Head and Neck Trauma: Clinical and Biomechanical, N. Yoganandan, F. A. Pintar, S. J. Larson and A. Sances (Eds.), Burke, Virginia, IOS Press Inc.: 200-214.

Nicolle, S., M. Lounis and R. Willinger (2004). "Shear Properties of Brain Tissue over a Frequency Range Relevant for Automotive Impact Situations: New Experimental Results." Stapp Car Crash Journal 48: 239.

Nusholtz, G. S., P. Lux, P. Kaiker and M. A. Janicki (1984). "Head Impact Response - Skull Deformation and Angular Accelerations." Stapp Car Crash Conference, Society of Automotive Engineers: 41-74.

Ommaya, A. K., F. Faas and P. Yarnell (1968). "Whiplash Injury and Brain Damage: An Experimental Study." JAMA: Journal of the American Medical Association 204(4): 285-9.

Ommaya, A. K., W. Goldsmith and L. Thibault (2002). "Biomechanics and Neuropathology of Adult and Paediatric Head Injury." British Journal of Neurosurgery 16(3): 220-242.

Pang, Q., X. Lu, H. Gregersen, G. von Oettingen and J. Astrup (2001). "Biomechanical Properties of Porcine Cerebral Bridging Veins with Reference to the Zero-Stress State." Journal Of Vascular Research 38(1): 83-90.

Perel, P., I. Roberts, O. Bouamra, M. Woodford, J. Mooney and F. Lecky (2009). "Intracranial Bleeding in Patients with Traumatic Brain Injury: A Prognostic Study." BMC Emergency Medicine 9(1): 15.

Poncelet, B. P., V. J. Wedeen, R. M. Weisskoff and M. S. Cohen (1992). "Brain Parenchyma Motion: Measurement with Cine Echo-Planar MR Imaging." Radiology 185(3): 645-51.

Pudenz, R. H. and C. H. Shelden (1946). "The Lucite Calvarium; a Method for Direct Observation of the Brain; Cranial Trauma and Brain Movement." Journal of Neurosurgery 3(6): 487-505.

Raboel, P., J. Bartek, M. Andresen, B. Bellander and B. Romner (2012). "Intracranial Pressure Monitoring: Invasive Versus Non-Invasive Methods—a Review." Critical care research and Practice 2012.

Raju, S., D. K. Gupta, V. S. Mehta and A. K. Mahapatra (2004). "Predictors of Outcome in Acute Subdural Hematoma with Severe Head Injury - a Prospective Study." Indian Journal of Neurotrauma 1(2): 37-44.

Rang, E. M., S. A. Lippert and M. J. Grimm (2001). "The Degradation of Material Properties of Brain Tissue as a Function of Time Postmortem." ASME Bioengineering Conference. Snowbird, Utah.

Resnick, S. M., D. L. Pham, M. A. Kraut, A. B. Zonderman and C. Davatzikos (2003). "Longitudinal Magnetic Resonance Imaging Studies of Older Adults: A Shrinking Brain." The Journal of Neuroscience 23(8): 3295-3301.

Sabet, A. A., E. Christoforou, B. Zatlin, G. M. Genin and P. V. Bayly (2008). "Deformation of the Human Brain Induced by Mild Angular Head Acceleration." Journal of Biomechanics 41(2): 307-315.

SAE (2007). "J211/1 200707: Instrumentation for Impact Test Part 1 - Electronic Instrumentation." Warrendale, PA.

Sass, D. J., P. Corrao and A. K. Ommaya (1971). "Brain Motion During Vibration of Water Immersed Rhesus Monkeys." Journal of Biomechanics 4(5): 331-4.

Sawauchi, S. and T. Abe (2008). "The Effect of Haematoma, Brain Injury, and Secondary Insult on Brain Swelling in Traumatic Acute Subdural Haemorrhage." Acta Neurochirurgica 150(6): 531-6; discussion 536.

Seelig, J. M., D. P. Becker, J. D. Miller, R. P. Greenberg, J. D. Ward and S. C. Choi (1981). "Traumatic Acute Subdural Hematoma: Major Mortality Reduction in Comatose Patients Treated within Four Hours." New England Journal of Medicine 304(25): 1511-8.

Servadei, F. (1997). "Prognostic Factors in Severely Head Injured Adult Patients with Acute Subdural Haematomas." Acta Neurochirurgica 139(4): 279-85.

Servadei, F., G. D. Murray, G. Teasdale, M. Dearden, F. Iannotti, F. Lapierre, A. Maas, A. Karimi, J. Ohman, L. Persson, N. Stocchetti, T. Trojanowski and A. Unterberg (2002). "Traumatic Subarachnoid Hemorrhage: Demographic and Clinical Study of 750 Patients from the European Brain Injury Consortium Survey of Head Injuries." Neurosurgery 50(2): 261-269.

Shatsky, S. A., W. A. Alter, III, D. E. Evans, V. Armbrustmacher and G. Clark (1974). "Traumatic Distortions of the Primate Head and Chest: Correlation of Biomechanical, Radiological and Pathological Data." Stapp Car Crash Conference, Society of Automotive Engineers: 351-381.

Shatsky, S. A., D. E. Evans, F. Miller and A. N. Martins (1974). "High-Speed Angiography of Experimental Head Injury." Journal of Neurosurgery 41(5): 523-30.

Sheldon, C. H., R. H. Pudenz, J. S. Restarski and W. M. Craig (1944). "The Lucite Calvarium - a Method for Direct Observation of Hte Brain. I. The Surgical and Lucite Processing Techniques. ." Journal of Neurosurgery 1(1): 67-75.

Sisson, S., J. D. Grossman and R. Getty (1975). "Sisson and Grossman's the Anatomy of the Domestic Animals." Philadelphia, Saunders.

Stalnaker, R. L., J. W. Melvin, G. S. Nusholtz, N. M. Alem and J. B. Benson (1977). "Head Impact Response." Stapp Car Crash Conference, Society of Automotive Engineers: 305-335.

Stitzel, J. D., P. D. Kilgo, K. A. Danelson, C. P. Geer, T. Pranikoff and J. W. Meredith (2008). "Age Thresholds for Increased Mortality of Three Predominant Crash Induced Head Injuries." Annual proceedings of the Association for the Advancement of Automotive Medicine 52: 235-44.

Sugawara, O., Y. Atsuta, T. Iwahara, T. Muramoto, M. Watakabe and Y. Takemitsu (1996). "The Effects of Mechanical Compression and Hypoxia on Nerve Root and Dorsal Root Ganglia. An Analysis of Ectopic Firing Using an in Vitro Model." Spine 21(18): 2089-94.

Taussky, P., H. R. Widmer, J. Takala and J. Fandino (2008). "Outcome after Acute Traumatic Subdural and Epidural Haematoma in Switzerland: A Single-Centre Experience." Swiss Med Wkly 138(19-20): 281-5.

Toyama, Y., T. Kobayashi, Y. Nishiyama, K. Satoh, M. Ohkawa and K. Seki (2005). "Ct for Acute Stage of Closed Head Injury." Radiation Medicine 23(5): 309-16.

Trosseille, X., C. Tarriére, F. Lavaste, F. Guillon and A. Domont (1992). "Development of a F.E.M. Of the Human Head According to a Specific Test Protocol." Stapp Car Crash Conference.

Viano, D., B. Aldman, K. Pape, J. van Hoof and H. von Holst (1997). "Brain Kinematics in Physical Model Tests with Translational and Rotational Acceleration." International Journal of Crashworthiness 2(2): 191-205.

Vijayakumar, V., I. Scher, D. Gloeckner, J. Pierce, R. Bove and D. Young (2006). "Head Kinematics and Upper Neck Loading During Simulated Low-Speed Rear-End Collisions: A Comparison with Vigorous Activities of Daily Living". 2006-01-0247, SAE Transactions.

Visualsonics (2009). "Vevo2100 Transducers V1.9." VisualSonics. Toronto, Ontario.

Vollmer, D. G., J. C. Torner, J. A. Jane, B. Sadovnic, D. Charlebois, H. M. Eisenberg, M. A. Foulkes, A. Marmarou and L. F. Marshall (1991). "Age and Outcome Following Traumatic Coma: Why Do Older Patients Fare Worse." Journal of Neurosurgery 75: S37-S49.

Ward, C. C. and R. B. Thompson (1975). "The Development of a Detailed Finite Element Brain Model." Stapp Car Crash Conference, San Diego, California, Society of Automotive Engineers.

Wiener, J. M. and J. Tilly (2002). "Population Ageing in the United States of America: Implications for Public Programmes." International Journal of Epidemiology 31(4): 776-781.

Yamashima, T. and R. L. Friede (1984). "Why Do Bridging Veins Rupture into the Virtual Subdural Space?" Journal of Neurology, Neurosurgery and Psychiatry 47(2): 121-127.

Yaşargil, M. G. (1984). "Microsurgical Anatomy of the Basal Cisterns and Vessels of the Brain, Diagnostic Studies, General Operative Techniques and Pathological Considerations of the Intracranial Aneurysms." Thieme.

Zhong, X., C. H. Meyer, D. J. Schlesinger, J. P. Sheehan, F. H. Epstein, J. M. Larner, S. H. Benedict, P. W. Read, K. Sheng and J. Cai (2009). "Tracking Brain Motion During the Cardiac Cycle Using Spiral Cine-Dense MRI." Medical Physics 36(8): 3413-9.

Zou, H., J. P. Schmiedeler and W. N. Hardy (2007). "Separating Brain Motion into Rigid Body Displacement and Deformation under Low-Severity Impacts." Journal of Biomechanics 40(6): 1183-91.